THE
PHYSICAL REVIEW

A journal of experimental and theoretical physics established by E. L. Nichols in 1893

SECOND SERIES, VOL. 73, No. 8 APRIL 15, 1948

Low Energy Yield of $D(D,p)H^3$ and the Angular Distribution of the Emitted Protons†

E. BRETSCHER,* A. P. FRENCH,* AND F. G. P. SEIDL,** ††
Los Alamos Scientific Laboratory, Los Alamos, New Mexico

(Received January 9, 1948)

The thick target yield $N(E)$ of the reaction

$$D^2+D^2\rightarrow H^3+H^1+4.0 \text{ Mev}$$

has been studied using a heavy ice target, and the angular distribution of the protons observed. Experiments have been carried out from 15 to 105 kev incident deuteron energy. There is evidence that even for very small bombarding energies the angular distribution of protons in the c.g. system does not become isotropic. Evaluation of the cross sections $\sigma(E)$ from $N(E)$ involves an estimate of the energy loss of deuterons in heavy ice. The variation of cross section $\sigma(E)$ with energy E can only approximately be represented by a Gamow function, i.e.,

$$\sigma(E) \propto (1/E) \exp[-c/(E)^{\frac{1}{2}}].$$

INTRODUCTION

A STUDY of the D−D reaction at small bombarding energies was considered to be of general interest, especially in view of the anisotropic angular distribution of the reaction products.[1,2,3] The present work concerns the reaction

$$D^2+D^2\rightarrow H^3+H^1+4.0 \text{ Mev} \quad (1)$$

which is only one of two possible reactions, the other being[4]

$$D^2+D^2\rightarrow He^3+n^1+3.3 \text{ Mev}. \quad (2)$$

The experimental arrangement was as follows: A well-collimated monoenergetic beam of deuterons was directed onto a freshly formed D_2O ice target. The intensity of the incident beam was measured by the charge transferred to the target per unit time, and the number of protons emitted from the target per unit time was counted as a function of their angle θ with the direction of the incident beam and as a function of incident deuteron energy E between 15 and 105 kev.

APPARATUS

The experimental apparatus used in these investigations was mostly of a conventional type

* Present address: Atomic Energy Research Establishment, Harwell, Berks, England.

** Now at Brookhaven National Laboratory, Upton, Long Island, New York.

† This document is based on work performed at Los Alamos Scientific Laboratory of the University of California under Government Contract W-7405-eng-36 and the information contained therein will appear in Division V of the National Nuclear Energy Series (Manhattan Project Technical Section) as part of the contribution of the Los Alamos Laboratory.

†† Professor H. Staub, now at Stanford University, joined in the direction of this research in its later stages. Considerable contributions have also been made by M. J. Poole and H. L. Wiser.

[1] H. P. Manning, R. D. Huntoon, F. E. Myers, and V. J. Young, Phys. Rev. 61, 371 (1942).

[2] R. D. Huntoon, A. Ellett, D. S. Bayley, and J. A. Van Allen, Phys. Rev. 58, 97 (1940).

[3] W. E. Bennett, C. E. Mandeville, and H. T. Richards, Phys. Rev. 69, 418 (1946).

[4] T. W. Bonner, Phys. Rev. 59, 237 (1941).

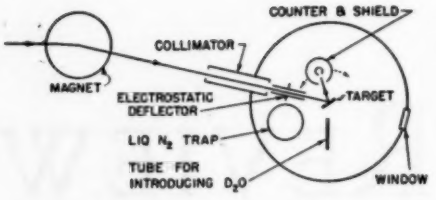

FIG. 1. Experimental arrangement (diagrammatic).

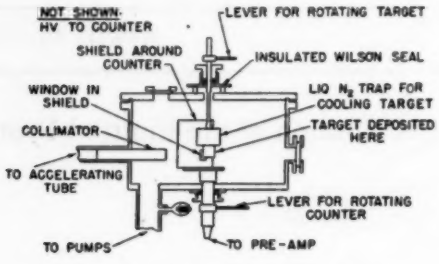

FIG. 2. Vacuum tank (sectional view).

and, consequently, we shall give a cursory description dwelling only on the points where special care was taken.

A full-wave kenotron rectifier was constructed to produce a deuteron beam of from 15 kev to 50 kev energy. At the *HV* end a small electron-arc ion source was mounted, having a cylindrical permanent magnet to lengthen the electron paths for ionizing collisions. Later a second *HV* set was built for voltages up to 125 kv, and again the ion source was of the arc type which was surrounded by a solenoidal electromagnet with an adjustable field. Adjustment of the magnetic field was desirable for obtaining optimum beam currents.

Accurate measurements of the bombarding voltages were essential; e.g., a change of incident deuteron energy of 1 kev at 20 kev produces a 30 percent change in reaction yield. Consequently, care was taken to measure the bombarding voltage to ± 1 percent. On the 50-kev set a 1-milliamp. meter was put in series with two 20-megohm precision resistors, and a further 10 megohms was later added in extending the measurements up to the full 50 kev. For the 125-kev set, a stack of 300 1-megohm precision resistors was made, and the leakage current down this stack was measured by a 30-microampere meter arranged in a potential-divider circuit across the bottom megohm of the stack. The ratio of the arms of the potential divider was measured by a Wheatstone-bridge circuit and was found to vary by less than 0.3 percent under full load. Furthermore, the calibrations of both the 1-milliamp. and the 30-microampere meters were checked.

After acceleration the deuteron beam was magnetically analyzed in order to select D_1^+, or D_2^+ ions. The beam was then collimated and entered the target chamber along a horizontal radius. It passed between a pair of electrostatic analyzer plates (used to investigate neutralization of incident beam but normally kept grounded) and impinged upon the target. The target chamber is illustrated by Figs. 1 and 2.

The target was deposited on a copper plate whose plane was vertical. It was soldered to the under side of a liquid-nitrogen container, which in turn was supported on a thin-walled steel tube passing through a Wilson seal in the lid of the chamber. The target could thus be rotated. The axis of rotation coincided with the vertical axis of the chamber itself, and was carefully arranged to lie in the front face of the target plate. Under these circumstances the spot produced at the front face of the target by a radial beam lay always on the axis of the chamber, and did not change its position as the target rotated.

After the cooling trap had been filled, a layer of heavy ice could be deposited on the target, which could then be turned to any desired orientation for carrying out a measurement.

The protons from the nuclear reaction were detected in a proportional counter having a mica window of about 8-cm air equivalent. (The proton range was about 14 cm; all other charged-particle ranges were less than 2 cm.) A small solid angle ($\sim 4\pi/1000$) was subtended at the target spot by the counter window. The arrangement was therefore one having "good" geometry. The counter could be rotated in a horizontal plane about a vertical axis passing through the target spot. Adjustment was made through a Wilson seal at the bottom of the tank (Fig. 2), so that the position of the counter could be altered without breaking the vacuum. The setting of the counter θ, defined as the angle between the direction of the incident beam and the radius joining target spot to counter window, could be varied from 40° to 150°. Moreover, the counter

was electrostatically shielded against strong disturbances from the target.

The glass windows were provided in the chamber to permit an optical check on the alignment of the system.

A determination of the incident deuteron intensity was accomplished by measuring the beam current on the target and, in order to measure this current, a current integrator for use in the range 0.01 to 2.5 microamperes was, designed and built by W. J. Poole. The circuit is shown in Fig. 3. Charge was accumulated on a 0.005-μf silver mica condenser which was automatically discharged when the potential reached 110 v; and, to ensure proper functioning of this circuit, care was taken that the leakage resistance across the condenser from target to ground was higher than 10^5 megohms. The calibration was effected with a galvanometer and the change in sensitivity of the circuit was tested at intervals during the investigation.

The target was held at a positive potential of 100 v so as to eliminate influences of secondary electrons on the recorded target current. However, there was some concern as to whether secondaries produced at the second slit of the beam collimator (Fig. 1) were attracted to the target. To test this point, a hollow, cylindrical, permanent magnet was mounted coaxially around the collimator. The field of this magnet was chosen so as to cause electrons to spiral away from the target without appreciably affecting the deuterons. Nevertheless, the reaction yield per microcoulomb of effective beam current was found to be the same before and after inserting the magnet.

At low energies a beam of charged particles tends to suffer neutralization. Since the number of deuterons reaching the target was measured in terms of the positive charge collected, any neutralization in the incident beam, occurring between the analyzing magnetic field and the target, could well invalidate these measurements. Therefore, an attempt was made to achieve as low a pressure as possible in this region by pumping it from both ends. A 4-in. oil diffusion pump and a liquid-nitrogen trap were located in front of the magnetic analyzer; another such pumping system was mounted below the target chamber behind the analyzer and a third liquid-nitrogen trap was suspended in the target tank itself. To test the efficiency of the system, the electrostatic deflector (Fig. 1) was used on a 17-kev deuteron beam. The conclusion was that only about 1.5 percent of this beam was neutralized, and at higher energies the neutralization would, of course, be less.

A high vacuum was also essential to reduce any target contamination; e.g., traces of oil become attached to the surface and are carbonized by the beam. Since the target was cooled by liquid nitrogen, this possibility could have been very

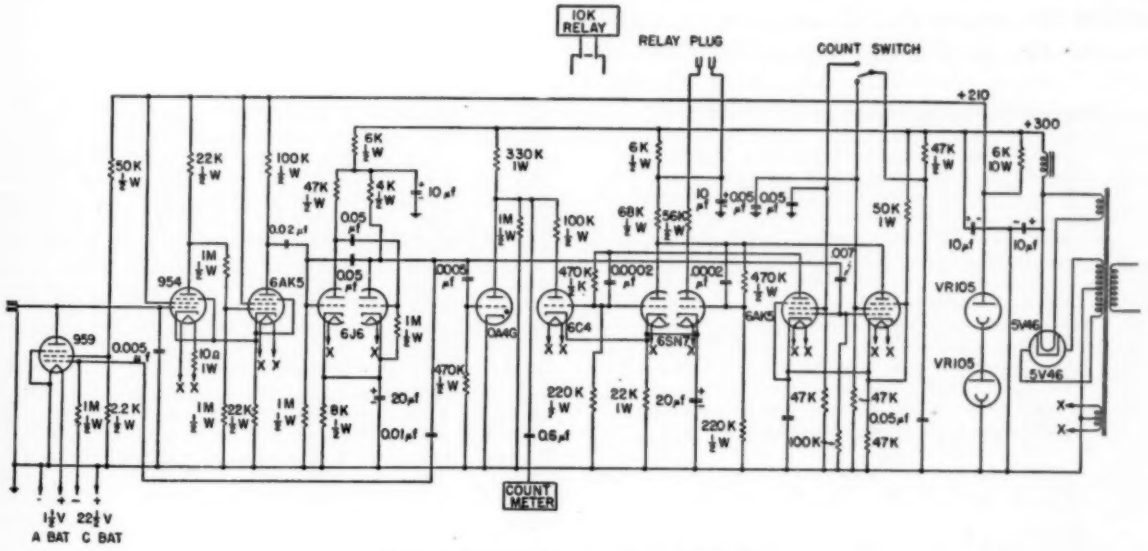

FIG. 3. Automatic current integrator.

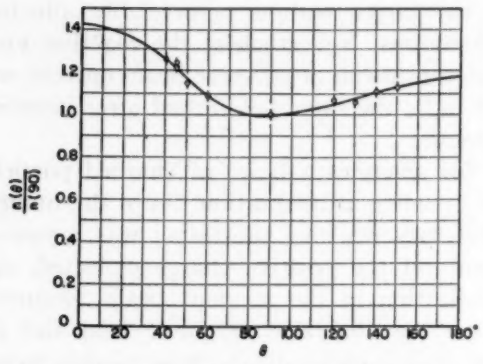

FIG. 4. Angular distribution D+D 50 kev. Laboratory system. $A=0.30\pm0.03$.

marked, in which case some energy would be lost from the incident beam before it actually reached the D_2O. To remove condensable material at the start of a run, the three liquid-nitrogen traps were kept filled for several hours before the target trap itself was cooled. Two checks were possible on the effect of target contamination: an observation of the change with time of the reaction yield at a given bombarding voltage and a search at a given deuteron energy for any dependence of yield on the angle of the target face relative to the incident beam. Upon applying these checks the contamination problem was found to be negligible.

ANGULAR DISTRIBUTION MEASUREMENTS

In Fig. 4 is shown a typical experimental result of the angular distribution measurements. A curve has been drawn through the experimental points corresponding to the relations:

$$n'(\theta')=n'(90°)[1+A(E)\cos^2\theta'], \quad (3)$$

$$n'(\theta')=g(\theta)\cdot n(\theta). \quad (4)$$

$n(\theta)/n(90°)$ has been plotted, where $n(\theta)$ is the number of protons per microcoulomb of beam observed in the counter at setting θ for the bombarding energy E. $n'(\theta')$ denotes the hypothetical count at an angle θ' in the c.g. frame corresponding to the observed count $n(\theta)$ in the laboratory system and $g(\theta)$ is the functional factor connecting the two distributions. The quantities in (3) and (4) refer to thick target yields. $g(\theta)$, which in the case of a thin target may be evaluated from the incident deuteron energy E and heat of reaction Q, has been taken as the weighted mean value corresponding to a thick target and can be arrived at from an

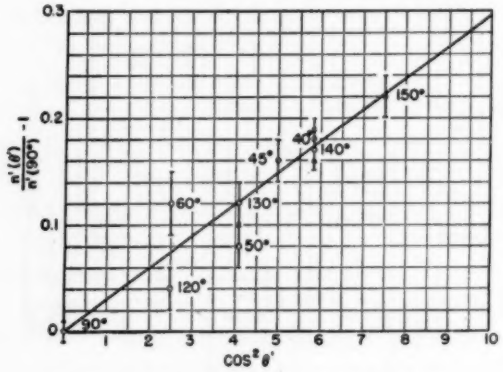

FIG. 5. D+D 50 kev. Test of $\cos^2\theta'$ law. $\left[\frac{n'(\theta')}{n'(90)}-1\right]$ *vs.* $\cos^2\theta'$. $A=0.30\pm0.03$.

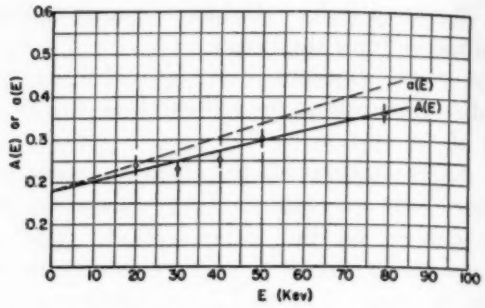

FIG. 6. $A(E)$ and $a(E)$ *vs.* E. ∤ Observed values of $A(E)$ $A(E)=0.175+0.0023E$; $a(E)=0.175+0.0031E$. (The bottom symbol marking the ordinate should be 0.1.)

TABLE I.

E kev	$E^{-\frac{1}{2}}$ (Mev)$^{-\frac{1}{2}}$	$(1/F)n(125°)$ counts	$g(125°)$*	$N(E)$ per microcoulomb
15.4	8.05	2.47×10^2	1.025	2.53×10^2
18.1	7.45	6.24×10^2	1.028	6.40×10^2
20.5	7.00	1.18×10^3	1.030	1.21×10^3
23.0	6.60	2.29×10^3	1.031	2.36×10^3
23.8	6.47	2.71×10^3	1.032	2.79×10^3
26.4	6.15	4.30×10^3	1.033	4.43×10^3
30.6	5.67	8.60×10^3	1.035	8.88×10^3
31.6	5.60	9.90×10^3	1.037	1.03×10^4
35.6	5.25	1.73×10^4	1.040	1.80×10^4
39.6	5.02	2.32×10^4	1.042	2.41×10^4
40.9	4.92	2.81×10^4	1.044	2.93×10^4
45.6	4.68	4.13×10^4	1.046	4.32×10^4
47.7	4.56	4.90×10^4	1.047	5.13×10^4
52.8	4.35	6.29×10^4	1.050	6.59×10^4
63.2	3.97	1.11×10^5	1.055	1.17×10^5
79.2	3.56	2.19×10^5	1.061	2.32×10^5
95.0	3.25	3.60×10^5	1.070	3.85×10^5
105.6	3.08	4.45×10^5	1.075	4.78×10^5

* Thick target values of $g(125°)$.

approximate knowledge of the excitation curve. The value of $A(E)$ has been obtained by a best fit of the data. A more exacting test of the validity of (3) consists in plotting

$$\frac{n'(\theta')}{n'(90°)}-1$$

against $\cos^2\theta'$; since the degree of anisotropy is small, experimental errors are thus magnified (Fig. 5).

The angular distribution has been studied for five bombarding energies E (20 kev to 80 kev)

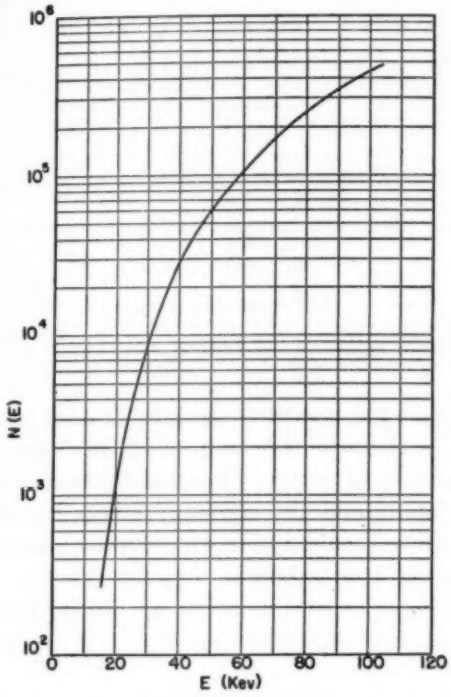

FIG. 7. Complete excitation curve, 15 kev to 105 kev. $N(E)$ *vs.* E. $N(E)$ is in units of protons per microcoulomb of incident deuteron beams.

and in each case plots similar to Figs. 4 and 5 have been prepared. During these investigations the angle ϕ between the target face and forward direction of the incident beam was set about 20°; but variations in ϕ apparently did not modify the angular distribution, provided the protons being counted did not leave the target surface at too slight an angle. $A(E)$ as a function of E is given by Fig. 6. The corresponding thin target quantities††† $a(E)$ were calculated and are indicated

††† I.e., in the c.g. frame $\eta'(\theta')=\eta'(90°)[1+a(E)\cos^2\theta']$, where the number of protons emitted per solid angle $\sin\theta' d\theta' d\phi'$ is given by $\eta'(\theta')\sin\theta' d\theta' d\phi'$.

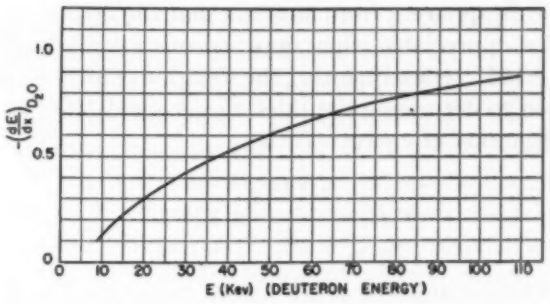

FIG. 8. Energy loss of deuterons in D_2O. dE/dX in kev per cm in D_2O vapor at 1-mm pressure, 15°C.

by the dashed line (Fig. 6). When these results for $a(E)$ are plotted against E together with values for $a(E)$ as have been obtained (cf. reference 1) in the region 89 to 246 kev by workers at New York University, all the points appear to fall on the same straight line. Using our data only, empirical *linear* relations between $A(E)$ and $a(E)$ and energy E were computed by a least square fit, although the results in themselves are not accurate enough to completely justify this assumption of linearity. It is interesting that the asymmetry coefficient $a(E)$ shows no sign of tending to zero at zero bombarding energy.

EXCITATION-CURVE MEASUREMENTS

If (3) is obeyed, the total yield $N(E)$ can be found from observations at a single angle, without a knowledge of the asymmetry coefficient $A(E)$. This statement may be demonstrated as follows: If $n(\theta)$ is the number of protons observed per microcoulomb of beam by a counter of effective solid-angle factor F, then the number per unit solid angle is $n(\theta)/4\pi F$ and

$$N(E)=\frac{1}{2F}\int n(\theta)\sin\theta d\theta=\frac{1}{2F}\int n'(\theta')\sin\theta' d\theta',$$

where $n'(\theta')$ is given by (3). Using (3) we may show that

$$N(E)=\frac{1}{F}n'(\theta_0'), \qquad (5)$$

provided $\cos^2\theta_0'=\frac{1}{3}$, i.e., $\theta_0'=54°44'$ or $125°16'$. The corresponding angles θ_0 in the laboratory system depend on E; in this work $E\lesssim 105$ kev, so that values of θ_0 never differ from angles in the c.g. system by even as much as 3°.

It is apparent from analysis that the errors are least appreciable when observations are made at $\theta_0 = 125°$; consequently, the relation which was used to determine the thick target yield $N(E)$ as a function of energy (E) is

$$N(E) = \frac{g(125°)}{F} n(125°). \qquad (6)$$

Observations of $n(125°)$ were made using both mass 4 and mass 2 beams. The mass 4 was assumed to be pure D_2^+ so that a measurement of the yield per microcoulomb of target current led directly to the number of protons produced by the nuclear reaction per incident deuteron. With mass 4, however, only half the maximum bombarding energy could be obtained. The full energy was obtainable with mass 2 which contained H_2^+ as well as D_1^+. To find the absolute yield of the mass 2 beam a correspondence was made between respective curves for mass 2 and mass 4 of the form $\log N(E)$ *vs.* $E^{-\frac{1}{2}}$, $N(E)$ representing here either apparent yield by mass 2 or absolute yield by mass 4. For both cases such a plot was found to give a straight line within experimental error, and the lines were parallel.

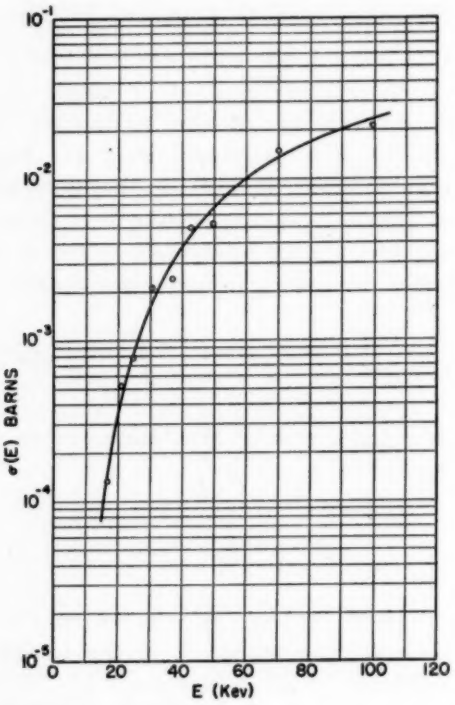

FIG. 9. D+D cross section for proton emission, 15 kev to 105 kev.

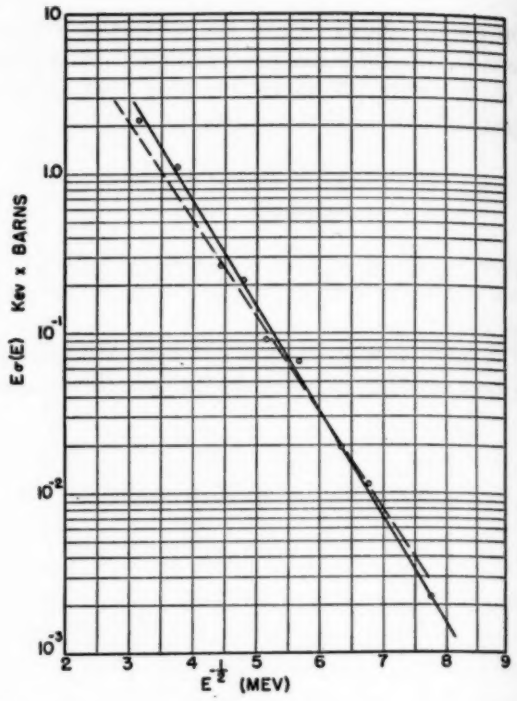

FIG. 10. ——— experimental curve. ·-·-·-·- theoretical slope. Gamow plot: $\log[E \cdot \sigma(E)]$ *vs.* $E^{-\frac{1}{2}}$. Theoretically, $\sigma(E) = \text{const.}\ 1/E.\ \exp[-1.408E^{-\frac{1}{2}}]$.

Moreover, the resulting straight line for mass 2 indicates that the H_2^+ content of this beam was independent of energy. The distance between the lines determined the constant factor by which the observed mass 2 yields were to be multiplied to give the true values.

The experimental data are set out in Table I. $N(E)$ *vs.* E is shown in Fig. 7.

CROSS SECTION

The cross section for reaction (1) may be found from the data in Table I by using the relation

$$\sigma(E) = 1/A \cdot dN/dE \cdot dE/dx, \qquad (7)$$

where A contains the product of the number of incident deuterons per unit of beam current and the number of deuterium nuclei per cm^3 in the target and dE/dx is the rate of energy loss of incident deuterons in the D_2O ice target.

dN/dE as a function of energy E has been evaluated by two closely related methods. According to the first, $\Delta N/\Delta E$ was taken from the differences of the yield $N(E)$ for adjacent energies E_1, E_2, and the energy E associated with

each $\Delta N/\Delta E$ was obtained as‡

$$E^{-\frac{1}{2}}=\tfrac{1}{2}(E_1^{-\frac{1}{2}}+E_2^{-\frac{1}{2}}),$$

which is an average along the experimentally straight line $\log N(E)$ *vs.* $E^{-\frac{1}{2}}$. According to the second, the data in Table I were fitted to the form

$$\log_{10}N(E)=A-BE^{-\frac{1}{2}} \qquad (8)$$

which was then differentiated.

However, in absence of suitable experimental work, the evaluation of dE/dx in D_2O ice for deuterons between 10 and 100 kev gives trouble. An endeavor has been made to estimate this quantity on the basis of certain experiments[5–8] by Gerthsen and his co-workers, concerning the energy loss of slow protons in various media (air, hydrogen, and celluloid). Their results are applicable to our case through the following assumptions: (a) that the rates of energy loss of a proton and a deuteron having the same velocity are identical in any given medium; (b) that the atomic stopping powers of H and D are nearly identical; (c) that the molecular stopping power of D_2O can be found by adding the atomic stopping powers of two atoms of H and one atom of O, and (d) that the stopping power of D_2O is roughly independent of its physical state.[9] By subjecting to least square analyses the data from the various experiments by Gerthsen, Eckardt, and Reusse through the energy region 5–50 kev, expressions for the rate of energy loss dE/dx of protons in air, hydrogen, and celluloid were obtained. These values of dE/dx were combined according to assumptions (a) to (d) into the variation with E of dE/dx for deuterons in D_2O, and the result is given in Fig. 8. This curve was used in the derivation of $\sigma(E)$.

The resulting dependence of $\sigma(E)$ for reaction (1) upon E is shown by Figs. 9 and 10. The individual points were derived from $\Delta N/\Delta E$; while the full curves correspond to values obtained by differentiating (8). It may be seen that the Gamow plot of Fig. 10 is a straight line, but with a slightly different slope from the theoretical curve.

ERRORS

During most measurements the counting errors did not exceed 1 percent, except at the lowest energies (~15 kev) where the intensities were weak. The bombarding energy was known to within 1 percent. Determinations of beam current by the integrator should be good to ±2 percent. And as far as could be discovered, errors resulting from target contamination or secondary-electron emission were together not more than 1 percent. The error due to observing at 125° in the laboratory system instead of 125° in the c.g. system was always less than 1.5 percent. The presence of neutral particles in the beam amounted to less than 1 percent, except at the lowest energies employed. Geometrical errors, as arise from measurements of the counter solid-angle factor F, are considered to be ±2 percent. Combination of these considerations leads to an aggregate error in the thick target yield $N(E)$ amounting to ±4 percent at most energies, but reaching ±8 percent at 15 kev.

CONCLUSIONS

The experiments described here appear to be a reliable measure of the thick target yield of reaction (1) for bombarding energies 15 to 105 kev. However, if these thick target yield measurements are to be translated with any certainty into values for cross sections, a far better knowledge of dE/dx for deuterons in heavy ice is required.

‡ It may be more correct to use $E=\frac{1}{2}(E_1+E_2)$, although it makes no practical difference.

[5] Chr. Gerthsen, Ann. d. Physik **5**, 657 (1930).
[6] Chr. Gerthsen, Physik. Zeits. **31**, 948 (1931).
[7] A. Eckardt, Ann. d. Physik **5**, 401 (1930).
[8] W. Reusse, Ann. d. Physik **15**, 256 (1932).
[9] Some discussion of assumptions (c) and (d) as concerns α-particles appears in a paper by L. H. Gray, Proc. Camb. Phil. Soc. **40**, 72 (1944).

Theoretical Considerations Concerning the $D+D$ Reactions

E. J. KONOPINSKI, *Indiana University, Bloomington, Indiana*

AND

E. TELLER, *University of Chicago, Chicago, Illinois*

(Received January 12, 1948)

Some possibilities are explored for the theoretical explanation of the angular distribution of $D+D$ reaction products. The variation with energy is ascribed entirely to differences in the centrifugal barriers encountered by the bombarding particles responsible for the isotropic and non-isotropic components. The detailed data on the proton distributions at low energies appear to be explained in terms of an asymmetric part produced by P-waves superposed on isotropic emissions caused by S-waves. However, ordinary extrapolation of this to higher energies gives much less symmetric distributions than experimentally found at such energies for the emission of neutrons. If the experiments are correct as interpreted, then they appear to show that spin-orbit coupling plays a large part in the reactions. In that case, an isotropic component produced by incoming P-waves grows in importance with energy and accounts for the increasingly parallel growth of the isotropic and asymmetric emissions.

1. INTRODUCTION

THEORETICAL treatments of the reactions of deuterons with deuterons have been offered by Dolch,[1] Schiff,[2] Flügge,[3] and Myers.[4]

The first three authors made attempts to to derive an absolute value for the reaction cross section from the magnitude of the nuclear forces. Flügge improved on the others in that he included the effect of the nuclear forces on the relative motion of the two deuterons (a Hartree-Fock approximation), instead of assuming that motion to be influenced only by the electrostatic repulsion (a modified Born approximation). He succeeded in obtaining the right order of magnitude (cross section $\sim 10^{-26}$ cm^2 at ~ 150 kev). Difficulties of calculation caused Flügge to consider only the production of particles without relative orbital angular momentum. With the type of nuclear forces assumed, such emissions can arise only from singlet collisions. This resulted in the introduction of a weight factor 1/9, representing the fraction of the collisions in which the deuterons come together in a singlet state.

Schiff, using the modified Born approximation, was able to consider particles with non-vanishing angular momenta. This made possible a discussion of the angular distribution of the product particles. No spin changes during the reaction were permitted by the types of nuclear forces assumed, these types being the same as those considered by Dolch and Flügge.

Myers made a tentative application of the Breit-Wigner resonance theory. He argues that, in general, symmetry of the angular distribution with respect to a plane normal to the direction of incidence indicates the formation of a compound nucleus. This argument is not binding here, where such a symmetry follows from the identity of the collision partners.

None of the work mentioned discusses the *energy-dependence* of the asymmetry in the angular distribution. This is the primary object of the present paper.

The experiments give for the angular distribution of the product protons the form:

$$1+A(E)\cos^2\theta, \tag{1}$$

where θ is the angle of emission relative to the incident deuteron beam, in the center of mass system (CMS), and $A(E)$ is the "asymmetry coefficient," which depends on the deuteron bombarding energy, E. Extensive measurements of $A(E)$ for protons were carried out at New York University,[5] for E between 90 kev and 250 kev. Bretscher, French, and Seidl[6] supplemented

[1] H. Dolch, Zeits. f. Physik **100**, 401 (1936).
[2] L. T. Schiff, Phys. Rev. **51**, 783 (1937).
[3] S. Flügge, Zeits. f. Physik **108**, 545 (1938).
[4] R. D. Myers, Phys. Rev. **54**, 361 (1938).
[5] H. P. Manning, R. D. Huntoon, F. Myers, and V. Young, Phys. Rev. **61**, 371 (1942); also R. D. Huntoon, A. Ellett, D. S. Bayley, and J. Van Allen, Phys. Rev. **58**, 97 (1940).
[6] E. Bretscher, A. French, and F. Seidl, Phys. Rev. **73**, (1948).

these with points between $E=20$ kev and 80 kev. Both sets of data are represented by the experimental points in Fig. 1. Bennett, Mandeville, and Richards[7] made measurements of the relative dependence of A on energy for neutrons. This was for E in the range from 0.5 Mev to 2 Mev. Their results are shown in Fig. 2, in which the data already in Fig. 1 are included for comparison.

In exploring the possibilities for explaining the results for A, it is helpful to consider also the integral cross section, including all angles. Experimental data[6,8] on this are represented by the points in Fig. 3. Actually plotted is the quantity $\sigma E/(1+\frac{1}{3}A)$ where σ is the total proton production cross section in barns (1 barn $=10^{-24}$ cm^2) and E is the energy in kev. The abscissa of Fig. 3 is $E^{-\frac{1}{2}}$, with E expressed in Mev.

The present theoretical treatment proceeds on the assumption that the relative penetrability of the electrostatic and centrifugal force barriers can entirely account for the energy dependence of the asymmetry coefficient, A. Thus, no effort will be made to find absolute magnitudes dependent on the interactions between particles after their penetration within the barriers. Usually, the only strong variation with energy which results from the specifically nuclear interactions within the barriers is due to resonance effects. The observed[6,8] dependence of yield on energy shows no resonance in the D−D process, at least in the energy range of interest here (in which the reliable measurements of A have been made). Moreover, Flügge seems to have shown that a "first-order," non-resonance reaction should have the observed order of magnitude.

In treating the penetration of the barriers, one may consider using the precise solutions of the Schrödinger equation with a Coulomb potential. To justify such precision, care would have to be taken with the fitting of the "regular" and "irregular" solutions at the nuclear surface. The conditions for such fitting are at least as obscure as the current status of the nuclear forces. We shall be content with the usual (WKB) approximations for the penetration probabilities.

2. THE PENETRABILITY

The distance R to which two deuterons may approach before nuclear forces take hold will be given the value:

$$R=7\times10^{-13}\text{ cm}. \qquad (2)$$

This is compounded from a deuteron diameter ($\sim4.2\times10^{-13}$ cm) plus the range of nuclear forces ($\sim2.8\times10^{-13}$ cm). The value here leads to a Coulomb barrier of height $e^2/R=205$ kev in the CMS equivalent to a bombarding energy

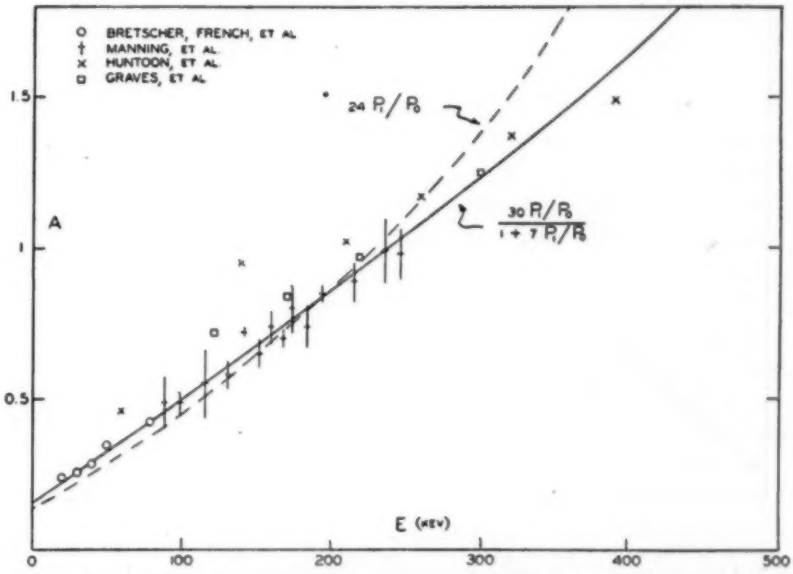

FIG. 1. The asymmetry coefficient A for proton emission as a function of bombarding energy, E. The experimental points are due to the groups indicated.[5,6,8] The numerical coefficient "24" for the steeper theoretical curve was adjusted to the data at ~200 kev. This represents the case 4(a) in which all the isotropic emission is presumed to be due to incident S-waves. The second theoretical curve has had the coefficients "30" and "7" chosen so that the data at 40 kev and 200 kev are fitted. It represents case 4(c), in which some of the isotropic emission is ascribed to incident P-waves, indicating spin-orbit coupling in the transition.

[7] W. E. Bennett, C. Mandeville, and H. T. Richards, Phys. Rev. **69**, 418 (1946).
[8] A. Graves, E. Graves, J. Coon, and J. Manley, Phys. Rev. **70**, 101 (1946).

$E_B=410$ kev. The centrifugal barrier has the height

$$l(l+1)\hbar^2/2\mu R^2=2.05l(l+1)e^2/R\approx 420l(l+1) \text{ kev.}$$

Here l is the orbital angular momentum quantum number ($l=0, 1, 2, \cdots$), and μ is the reduced mass of the two deuterons.

Usually, centrifugal barriers are of great importance only for neutrons. Charged particles with moderate angular momentum, such as are responsible for most of the observed nuclear reactions, are most affected by electrostatic repulsion outside the nucleus. The $D+D$ reactions present a peculiar case in that the centrifugal barrier is higher than the Coulomb barrier even for P-waves ($l=1$). Actually, a comparison of the barrier heights is not quite fair because the centrifugal barrier is thinner ($\sim 1/r^2$) than the electrostatic barrier ($\sim 1/r$). The centrifugal barrier will be dominant if it manages to equal the Coulomb barrier even at the distance to which the electrostatic repulsion by itself would allow particles to approach:

$$r_0=e^2/W, \tag{3}$$

$W=\frac{1}{2}E$ being the relative kinetic energy of the two deuterons. This leads to

$$E=2W>(4\mu e^4/\hbar^2)/l(l+1)=200/l(l+1) \text{ kev}$$

for the energies at which the Coulomb barrier is negligible compared to the angular momentum barrier.

The penetration probability P_l for a pair of deuterons possessing the relative orbital angular momentum $[l(l+1)]^{\frac{1}{2}}\hbar$ is given by:

$$P_l=e^{-2C_l},$$

$$C_l=\frac{(2\mu)^{\frac{1}{2}}}{\hbar}\int_R^{r_l}\left[\frac{e^2}{r}+\frac{l(l+1)\hbar^2}{2\mu r^2}-W\right]^{\frac{1}{2}}dr. \tag{4}$$

The radius r_l is the "classical distance of closest

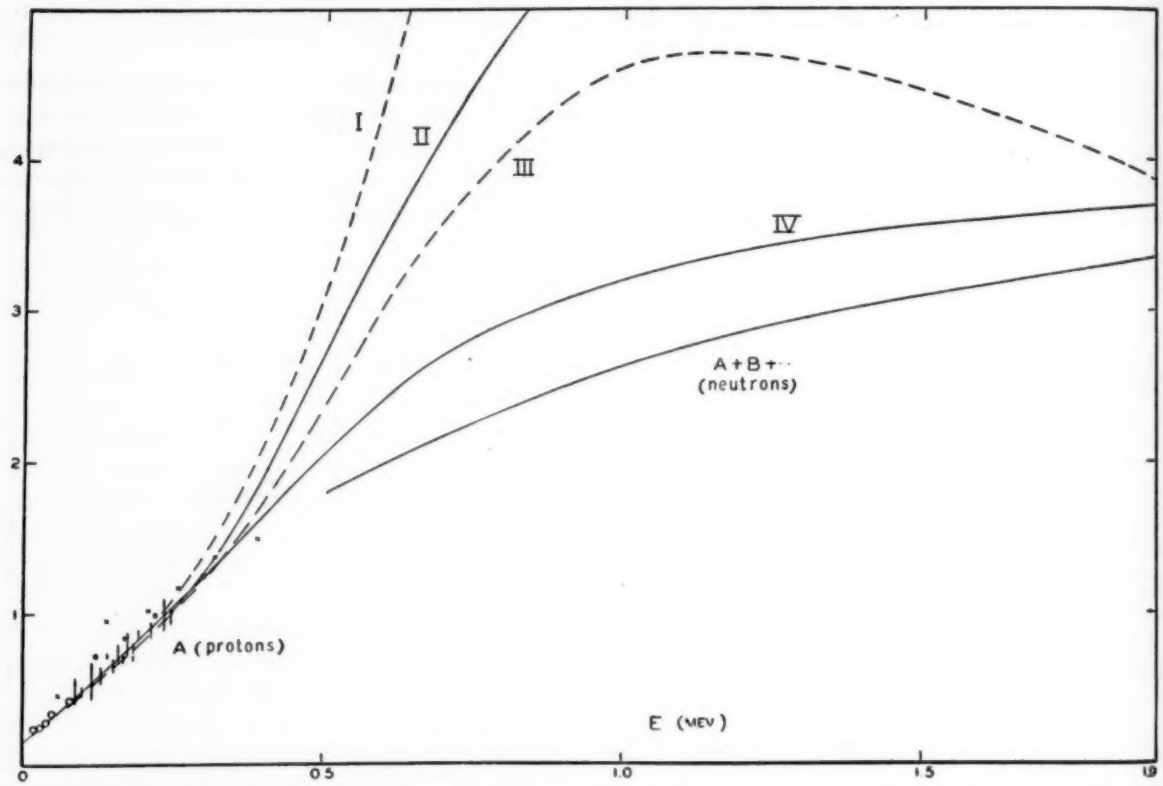

FIG. 2. The experimental points are repeated from Fig. 1. The solid curve starting at 0.5 Mev represents $A+B+\cdots$ (see 4) as measured[7] for neutron emission. The theoretical curves I and IV are extensions from Fig. 1. Curve III is A, curve II is $A+B$, according to the assumption 4(b). These two curves involved the adjusting of three parameters to fit the data at 40 kev, 250 kev and to give as low $A+B$ values at high energies as is consistent with the experimental upper limit on B at 246 kev.

approach" and is the root of the integrand. If one introduces the de Broglie wave-length (divided by 2π) $\lambda\!\!\!^{-}=\hbar/(2\mu W)^{\frac{1}{2}}$, and the collision parameter $b=[l(l+1)]^{\frac{1}{2}}\lambda\!\!\!^{-}$, one has

$$C_l=\int_R^{r_l}[(r_0/r)+(b/r)^2-1]^{\frac{1}{2}}(dr/\lambda\!\!\!^{-}),$$
$$r_l=\tfrac{1}{2}[r_0+(r_0^2+4b^2)^{\frac{1}{2}}]. \tag{5}$$

The integrated form of C_l may be found in Bethe's article.[9] It has the well-known value $\pi e^2/\hbar v$, with v the relative velocity, for vanishingly small energy and $l=0$.

It is illuminating to notice that when the Coulomb barrier is negligible and if

$$E\ll l(l+1)\hbar^2/\mu R^2=840l(l+1)\text{ kev},$$
$$P_l\approx(\epsilon/2l+1)^{2l+1}(R/\lambda\!\!\!^{-})^{2l+1}\sim E^{l+\frac{1}{2}}. \tag{6}$$

Here ϵ is the base of the natural logarithms. (6) exhibits the well-known dependence on energy of the l-wave intensity near the nucleus, which is thus seen to be automatically included by the present procedure.

The penetration formulae presented here can be applied also to the outgoing particles, with an appropriate change of the reduced mass μ. The energy release is high enough (4 Mev) so that the Coulomb barrier for the protons can be neglected. The outgoing S-, P-, and D-waves surmount their respective barriers. The F-waves have a penetrability: $P_3\approx0.55$, the G-waves: $P_4\approx0.07$, values which will change little with deuteron energy.

3. CHARACTER OF THE TRANSITIONS

Two deuterons may collide in singlet, triplet, or quintet states. The triplet is antisymmetric in the deuteron spins, the others are symmetric. Thus the Bose statistics will have the consequence that the initial triplet states are odd (as to orbital quantum number) while the singlet and quintet states are even, thus: ^1S, ^5S, ^3P, ^1D, ^5D, ^3F, $\cdots$. The states ^5S and ^5D will be omitted since, in order to get reaction in these states, close approach of neutrons (and protons) with parallel spins is required.

The final states contain pairs of unlike particles of spin $\frac{1}{2}$, so that singlet and triplet states of arbitrary orbital angular momentum may be formed (the state ^3S, which requires the close approach of parallel protons or neutrons will be omitted).

If one assumes that spins must be conserved (see 1) in addition to parity and total angular momentum, the following transitions ($l\leq2$) may occur:

$$^1S_0\rightarrow{}^1S_0;\quad {}^3P\rightarrow{}^3P;\quad {}^1D_2\rightarrow{}^1D_2. \tag{7a}$$

Quintet collisions would be totally ineffective; odd-singlet and even-triplet final states would not be formed.

Spin conservation is only approximate at best, since there is evidence for spin-orbit coupling in nuclear interactions (e.g., the quadrupole moment of the deuteron). If spin changes are admitted, one has in addition to (7a), the following possibilities:

$$^3P_1\rightarrow{}^1P_1;\quad {}^3P_2\rightarrow{}^3F_2;\quad {}^1D_2\rightarrow{}^3D_2. \tag{7b}$$

These might be expected to be weak in comparison to the transitions (7a).

No initial orbital quantum numbers higher than $l=2$ are included in the lists (7). Particles with higher l have greater centrifugal barriers to penetrate, and it can be shown that this fact makes it impossible already for $l=2$ to account for more than a small fraction of the observed reactions, as follows. The cross section for penetration to the nuclear surface is given by

$$\sigma_l=\pi\lambda\!\!\!^{-2}(2l+1)P_l \tag{8}$$

for particles with orbital quantum number l. The highest energy for which fairly reliable measurements on both the neutron producing and proton producing cross section have been made is $E\approx300$ kev. There the total is found to be about 0.08 barn, with the proton production accounting for 0.034 barn of this. For 300 kev, $\pi\lambda\!\!\!^{-2}=\pi\hbar^2/\mu E=4.32$ barns, $P_0=0.845$, $P_1=0.0488$, and $P_2=0.00108$. This makes $\sigma_0=3.66$ b and $\sigma_1=0.634$ b. Thus, even though only $\frac{1}{4}$ of the S collisions are in the required singlet state, only $\frac{1}{3}$ of the P collisions triplet, still only a fraction of either need be effective in producing reaction to yield the observed cross section. On the other hand, $\sigma_2=0.0234$ b, so that ^1D collisions could not account for more than $0.0026/0.08\approx3$ per-

[9] H. A. Bethe, Rev. Mod. Phys. 9, 178 (1937).

cent of the observed cross section, while ^5D collisions could only give 15 percent of the observed magnitude if every one led to a reaction. These figures are based on what is regarded as a generous nuclear radius ($R=7\times10^{-13}$ cm) which would tend to exaggerate the importance of high l-values.

Of course, the effective fraction of D collisions becomes larger relative to S and P with increasing energies. Raising the energy gives a greater increase in the penetration of the higher barrier. For this reason, the D collisions will not be left entirely out of consideration, and are included in the lists (7). An even more important reason is that S, D interference makes the D-waves more effective.

It is of interest that A is an increasing function of E (Figs. 1 and 2). This suggests that the collisions responsible for the asymmetry probably have to penetrate greater barriers than the ones giving rise to the isotropic emissions.

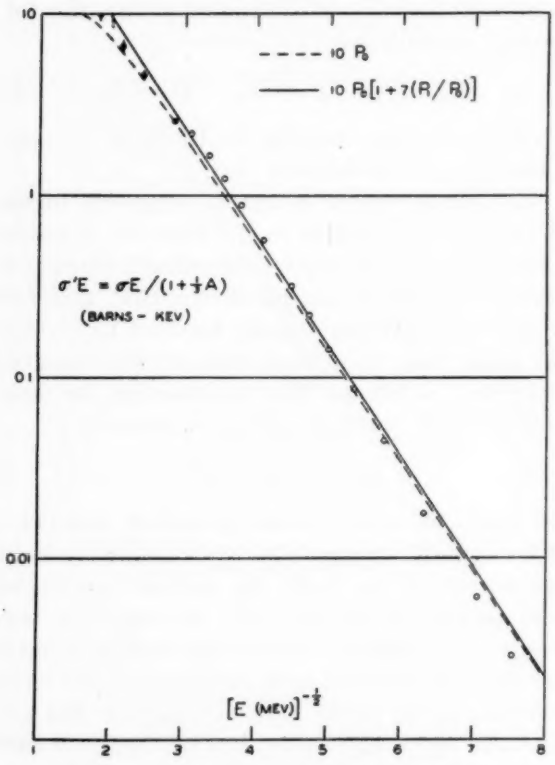

FIG. 3. The product of bombarding energy E in kev and isotropic cross section σ' in barns (10^{-24} cm^2) plotted logarithmically *vs.* $E^{-\frac{1}{2}}$ with E in Mev. The open circles (○) represent experimental points due to Bretscher, French, and Seidl.[6] The dots (●) are due to Graves, *et al.*[8] The dashed curve (---) represents the theoretical penetrability P_0 for S-waves adjusted to the data at 80 kev. The second theoretical curve represents the superposed penetration of S- and P-waves also fitted at 80 kev. The coefficient "7" indicated was obtained from an adjustment in Fig. 1.

4. THE ANGULAR DISTRIBUTION

The S, P, $D\cdots$ states formed in the reaction are represented by de Broglie wave components having amplitudes proportional, respectively, to spherical harmonics of order $l'=0, 1, 2, \cdots$. The resultant wave intensity determines the angular distributions of the outgoing particles.

A first general statement which can be made concerning the outgoing intensity is that it cannot contain interference terms between harmonics of even (l') and odd (l') order. Such an interference would result in asymmetry with respect to the plane which is equidistant from the two deuterons. No such distinction between the forward and backward directions can arise from the reaction of two identical deuterons, which approach each other symmetrically from opposite directions in the center of mass system. Reflection through the center of mass changes the phase difference between the initial odd and even waves by π. Accordingly, with each phase difference between the odd and even states another phase difference greater by π must occur. These states give rise to product waves with similar pairs of phase differences between their odd and even components. There will result a cancellation of interference effects just as in the initial configuration.

A second general statement concerning the product angular distribution can be made when one considers the effect of the incoming wave component described by the lth spherical harmonic and when the incoming spins can be regarded as oriented at random. In that case, one can show that the outgoing intensity is described by the spherical harmonics of order $2l$, $2l-2$, $2l-4$, etc., or any superposition of these.[10]

First conservation of spin will be assumed. This assumption leads to disagreement with experiments.

Next we shall investigate how much spin-orbit coupling must be admitted to obtain agreement with the observed facts.

[10] R. G. Sachs and E. Eisner, Phys. Rev. 72, 680 (1948).

If the spin is conserved, the orbital angular momentum vector also remains unchanged. It will have the same magnitude ($l'=l$) and the same orientation ($m=0$) in the initial and final states (7a). Accordingly, the differential cross section for the emission of reaction products into the solid angle $d\omega$ will have the form:

$$d\sigma=|\sum_l \alpha_l\sigma_l^{\frac{1}{2}}g_l^{\frac{1}{2}}Y_{l0}|^2d\omega. \quad (9)$$

The Y's are normalized spherical harmonics, appropriate to the various components of the outgoing wave amplitude. A component with quantum number l is expected to have an amplitude proportional to $\sigma_l^{\frac{1}{2}}$, since it arises from an initial l-wave having a cross section for reaching the nucleus as given by (8). g_l is a weight factor determined by the initial spin configuration; $g_l=1/9$ for the singlet collisions, 3/9 for the triplet states. The α's are coefficients, possibly complex, which determine the relative magnitudes of the outgoing wave components. Integration of $d\sigma$ over all directions of emission gives

$$\sigma=\sum_l \sigma_l g_l|\alpha_l|^2. \quad (10)$$

From the significance of σ_l and g_l it is clear that if σ is to be interpreted as the total reaction cross section then $|\alpha_l|^2\leq 1$ for each l. An appropriate name for $|\alpha_l|^2$ may be "the intrinsic reaction probability" for l-waves.

(a) $^1S_0\rightarrow{}^1S_0$ plus $^3P\rightarrow{}^3P$

If only the first two of the transitions (7a) are taken into account, the expression

$$d\sigma=(d\omega/4\pi)(\pi\lambda^2/9)|\alpha_0|^2P_0 \times[1+27|\alpha_1/\alpha_0|^2(P_1/P_0)\cos^2\theta] \quad (11)$$

is obtained for the differential cross section. The consequent expression for the asymmetry coefficient is $A=27|\alpha_1/\alpha_0|^2(P_1/P_0)$. In order to evaluate $|\alpha_1/\alpha_0|^2$, this expression is compared with the experimental values in Fig. 1. One sees that $A=24(P_1/P_0)$ may be regarded as fitting the experimental points within the possibly large uncertainties. This corresponds to

$$|\alpha_1|^2=0.89|\alpha_0|^2.$$

To evaluate $|\alpha_0|^2$, one compares the isotropic part of the cross section resulting from (11), $\sigma'=(\pi\lambda^2/9)|\alpha_0|^2P_0$, with the isotropic part of the proton producing cross section shown in Fig. 3. A fair fit with the experimental points occurs if $\sigma'E=10P_0$ barns-kev. This leads to $|\alpha_0|^2=0.0694$ and $|\alpha_1|^2=0.063$. Each of these quantities is expected to be less than $\frac{1}{2}$, since about half the reactions may be expected to produce neutrons instead of protons.

A striking feature of the fair agreement between the low energy experimental points and the present theoretical standpoint (a) is the comparatively large finite value of the asymmetry coefficient A for vanishing energy. One might have expected A to vanish for vanishing energy, since a vanishing velocity might be considered incapable of establishing a direction relative to which asymmetry could appear. The theory, however, gives for $E\rightarrow 0(r_0/\lambda^2\rightarrow 2\mu e^2/\hbar^2\equiv K)$:

$$P_l/P_0\rightarrow\exp -2\int_R^\infty\{[(K/r)+(l+\tfrac{1}{2}/r)^2]^{\frac{1}{2}} -[K/r]^{\frac{1}{2}}\}dr\approx[\epsilon^2KR/(2l+1)^2]^{2l+1}$$

if

$$KR\ll(2l+1)^2. \quad (12)$$

This is non-vanishing only in the presence of a Coulomb field ($K\neq 0$). Without it, the S-waves would predominate completely because an l-wave of vanishing energy requires an infinite "lever arm" to maintain its angular momentum of $l\hbar$, and would miss collision with the nucleus. When the Coulomb repulsion acts, r_0 becomes greater than the lever arm for low energies. The S-, P-, D-, $\cdots$ waves are all treated alike for $r<r_0$, since the centrifugal potential is there negligible in comparison to the electrostatic barrier.

Two points concerning the standpoint represented by (a) may be regarded as unsatisfactory. In the first place, the experimental values of $\sigma'E$ in Fig. 3 seem to change more rapidly with energy than can be expected from the penetrability, P_0, for S-waves. This lack of agreement persists to the lowest energies investigated by Bretscher, French, and Seidl, where the variation of the penetrability is quite insensitive to the choice of nuclear radius.

The second point at which the present theoretical explanations (a) may be unsatisfactory is concerned with the behavior of the asymmetry

coefficient $A(E)$ beyond the range of energies included in Fig. 1. According to (11), the coefficient $A \sim P_1/P_0$ continues to increase rapidly (up to the top of the P-barrier, $\sim$1.7 Mev) as shown by curve I in Fig. 2. There are no measurements on the angular distribution of protons at these energies. However, one might expect them to differ little from the neutron data shown in Fig. 2, especially since the latter appear to be a smooth continuation of the proton data. We shall therefore seek other possibilities than (a), in order to explain the leveling off exhibited by the neutron data.

One precaution is necessary in dealing with the neutron data presented in Fig. 2. These data are based on measurements at two angles only, with $\cos\theta \approx 0$ and 1. The distribution (1) was assumed so that the ratio of observed intensities was equated to $1:(1+A)$. If the true distribution had been $1+A\cos^2\theta+B\cos^4\theta+\cdots$ instead, this ratio would be $1:(1+A+B+\cdots)$. Thus the measurement can be considered to have given $A+B+\cdots$ rather than A, as indicated in Fig. 2.

(b) $^1S \rightarrow S^1$ plus $^3P \rightarrow {}^3P$ plus $^1D \rightarrow {}^1D$

The contribution of the $^1D \rightarrow {}^1D$ transition to the angular distribution may be important because of the interference between the S- and D-waves. If this is taken into account, a term proportional to $(\sigma_2\sigma_0)^{\frac{1}{2}}$ appears in the expression for the differential cross section. The quantity $(\sigma_2\sigma_0)^{\frac{1}{2}}$ differs little in its energy dependence from σ_1 over most of the range; at low energies the σ_1 vanishes less rapidly.

In this case the differential cross section (9) becomes:

$$\begin{aligned} d\sigma &= (d\omega/4\pi)(|\alpha_0|^2/9)\{\sigma_0+9\sigma_1\rho_1^2\mu^2 \\ &\quad +(5\sigma_0\sigma_2)^{\frac{1}{2}}\rho_2\cos\chi(3\mu^2-1) \\ &\quad +\sigma_2\rho_2^2(5/4)(3\mu^2-1)^2\} \\ &= (d\omega/4\pi)\sigma'\{1+A\mu^2+B\mu^4\}. \end{aligned} \tag{13}$$

Here $\rho_1^2=|\alpha_1/\alpha_0|^2$, $\rho_2 e^{i\chi}=(\alpha_2/\alpha_0)$, $\mu \equiv \cos\theta$, and the isotropic cross section $\sigma'=(|\alpha_0|^2/9)C\sigma_0$. Thus:

$$\begin{aligned} A &= [27(P_1/P_0)\rho_1^2+15(P_2/P_0)^{\frac{1}{2}}\rho_2\cos\chi \\ &\quad -(75/2)(P_2/P_0)\rho_2^2]/C, \end{aligned} \tag{14a}$$

$$B=(225/4)(P_2/P_0)\rho_2^2/C, \tag{14b}$$

with

$$\begin{aligned} C &= 1-5(P_2/P_0)^{\frac{1}{2}}\rho_2\cos\chi \\ &\quad +(25/4)(P_2/P_0)\rho_2^2. \end{aligned} \tag{14c}$$

When a matching of the formula (14a) for A to the experimental data is attempted by giving as arbitrary values as possible to the intrinsic probabilities $|\alpha|^2$, the following facts become plain. The magnitude of $|\alpha_2|^2$ is most severely limited through the second asymmetry coefficient, B, as given by (14b). The detailed angular distribution measurement[5] of highest energy ($E \approx 246$ kev) showed no definite trace of B, but it appears that $B \leq 0.2$ at that energy could not be excluded. Now, any value of $|\alpha_2|^2$ consistent with this turns out to be too small (even though it approached the largest possible value $\sim\frac{1}{2}$) to affect much the low energy values predicted for A. This means that $|\alpha_0|^2$ and $|\alpha_1|^2$ are not significantly changed from the values found in Part (a). The small value which $|\alpha_2|^2$ must be given also limits its influence at the high energies regardless of the value of the phase χ. In Fig. 2 are shown the theoretical curves (II and III) for A and $A+B$ according to formulae (14), when $|\alpha_0|^2=1/15$, $|\alpha_1|^2=1/10$, $|\alpha_2|^2=1/10$ and $\cos\chi=-1$. These are the values which make $A+B$ a minimum at $E=600$ kev when it is required that A be fitted at the energies below 246 kev and that the value of B at 246 kev be not more than 0.2.

The conclusion is that transitions in which spin is conserved cannot account for the small value of the asymmetry coefficient, $A+B$, apparently observed for high energies, as against the comparatively large values of A at low energy. There is still the possibility that spin-orbit coupling plays a large part in the transitions.

(c) ^1S and ^3P, with Spin-Orbit Coupling

It seems plausible that the spin-orbit corrections to the D-transitions, having the status of "corrections upon corrections," cannot play an important role. Accordingly, we attempt to find how large the coupling of spin and orbit must be for S and P collisions alone in order to achieve an explanation of the apparent experimental facts.

In the present case, the differential cross sec-

tion, replacing (9), will be

$$d\sigma=|\alpha_0(\sigma_0/9)^{\frac{1}{2}}Y_{00}+(\sigma_1/3)^{\frac{1}{2}}\sum m\alpha_{1m}Y_{1m}|^2d\omega$$
$$=(d\omega/4\pi)(|\alpha_0|^2/9)\{\sigma_0+9\sigma_1[\rho_{10}{}^2\mu^2+\rho_{11}{}^2(1-\mu^2)]\} \quad (15)$$

in which

$$\rho_{10}{}^2=|\alpha_{10}/\alpha_0|^2,$$
$$\rho_{11}{}^2=\tfrac{1}{2}(|\alpha_{11}/\alpha_0|^2+|\alpha_{1-1}/\alpha_0|^2).$$

Thus,

$$A=27(P_1/P_0)(\rho_{10}{}^2-\rho_{11}{}^2)/C, \quad (16a)$$

$$C=1+27(P_1/P_0)\rho_{11}{}^2. \quad (16b)$$

Ostensibly, only ${}^1S\rightarrow{}^1S$ and ${}^3P\rightarrow{}^{1,3}P$ transitions are so far included. The P-waves can also give rise (7b) to ${}^3P_2\rightarrow{}^3F_2$ transitions which are *a priori* expected to be somewhat weaker for two reasons: only the particular initial configuration with $j=2$ can produce them (thus a factor 5/9) and, further, the F-waves must penetrate an outgoing barrier (a factor $\sim$0.5, see **2**). According to the argument presented above, the $P\rightarrow F$ transitions cannot alter the type of resultant angular distribution (15); such transitions will only contribute both to the isotropic and μ^2 terms. The expressions (16) for A and C would then be retained with somewhat altered meanings for ρ_{10} and ρ_{11}.

The curve IV in Fig. 2 has the form (16a) with $\rho_{10}{}^2=1.37$ and $\rho_{11}{}^2=0.26$. These values were adjusted to give the very good agreement at low energies shown both in Fig. 2 and in Fig. 1. Thus the rapid leveling off of the values of A at higher energies is a characteristic of the assumption (c). Better agreement with the experimental curve shown at high energy could have been obtained by making use of the wide margin of error permissible at the low energies. As the concluding discussion will show, it is doubtful that a closer agreement would have more significance than the present comparison.

The consequences for the isotropic cross section are shown by Fig. 3. With the present assumptions, it is found that $\sigma'E\approx 10P_0\cdot(1+7P_1/P_0)$ barns-kev fits the data somewhat better than was the case when the S-wave alone was made responsible for the isotropic part of the product distribution. This is a result of the steeper energy dependence of the P contribution, which deals with a higher barrier. The curve calculated on the basis of (c), shown in Fig. 3, is based on the value $|\alpha_0|^2\approx 1/15$, for the intrinsic reaction probability of the S-wave. The intrinsic probability for the P reactions is the sum of $|\alpha_{10}|^2=0.09$, and $|\alpha_{11}|^2=0.017$ and $|\alpha_{1,-1}|^2=0.017$.

5. CONCLUSION

The large asymmetry of the $D+D$ reaction product angular distribution *at low energies* is almost certainly due largely to the effects of P-waves superposed on isotropic emissions resulting from the incident S-waves. The *a priori* probabilities are such that the intrinsic reaction probability of P-waves need not be greater in order of magnitude than that of S-waves in order to account for the striking results. These facts hold whether assumptions 4(a) or 4(c) are made, that is, without or with the contribution of the P-wave to the isotropic component which may come from spin-orbit coupling. The presence of the spin-orbit coupling, as in 4(c), seems to provide somewhat the better agreement (Fig. 1) at the low energies inasmuch as the margins of error need not be strained.

The incident D-wave can have little effect in the low energy region because of its small penetration to the nuclear surface. It has greater effect in the region above 0.5 Mev but still much too small to account for the leveling off in the asymmetry observed for neutrons, as shown in 4(b). To produce this observed result it seems essential to assume rather large spin-orbit coupling, as done in 4(c).

The assumption 4(c), which ascribes a substantial part of the isotropic emission to incident P-waves, seems to be able to account for all the known experimental facts within their margins of error. The result shown in Fig. 2 as curve IV was produced with no attempt to fit the high energy data through the evaluation of the two parameters available with assumption 4(c). If such an attempt were regarded as significant in connection with the available experimental data, then either the wide margins of error at the low energies or the small effects of D-waves at high energies could be made use of in providing complete agreement. Such a procedure is, however, probably without significance because of the uncertainty in the relation between proton and neutron angular distributions and because of the

lack of separation of the angular distribution into $\cos^2\theta$, $\cos^4\theta$, etc., terms in the high energy experiments.

A measurement of the value of B, the coefficient for the $\cos^4\theta$ asymmetry, would have the greatest significance for determining the magnitude of the spin-orbit coupling in the nuclear interactions. It would determine just how large the spin-orbit coupling must be made to account for results such as those of Fig. 2.

The authors are grateful to Mr. Geoffrey Chew for helpful calculations in connection with this work.

This document is partially based on work begun at the Los Alamos Scientific Laboratory under Government Contract W-7405-eng-36.

PHYSICAL REVIEW VOLUME 73, NUMBER 8 APRIL 15, 1948

The Diffraction of Neutrons by Crystalline Powders

E. O. WOLLAN AND C. G. SHULL
Oak Ridge National Laboratory, Oak Ridge, Tennessee

(Received January 5, 1948)

The powdered crystal technique, which has been shown for the case of x-rays to be best suited for accurate, integrated intensity measurements, has been applied to neutron diffraction. Neutrons from the Clinton pile are monochromatized by reflection from a single crystal and the diffraction patterns produced when these neutrons fall on specimens of crystalline powders have been studied. These studies have given (a) a check on some aspects of the diffraction theory, (b) the magnitude and sign of the scattering amplitudes from various nuclear species from which information is obtained on the spin dependence of the scattering, which has a bearing on the magnitude and range of nuclear forces, and (c) an improvement in the techniques and a better understanding of the problems involved so that results can be more readily obtained on the diffraction by other crystals, such as those containing hydrogen or deuterium.

Diffraction measurements have been obtained on diamond, graphite, Al, Na, NaBr, NaCl, and NaF in which all intensity measurements were standardized against diamond to which a definite cross section was assigned on the basis of total cross-section measurements. The scattering of carbon, Al, and F was found to have no measurable spin dependence. The scattering by Na, however, shows a considerable spin dependence as evidenced by a Bragg scattering cross section of 1.51 barns as against a total scattering cross section of 3.7 barns. Measurements have been made on a number of other crystals with the purpose of determining the phase of scattering. A table showing the scattering phase for a number of elements is given.

1. INTRODUCTION

EXPERIMENTAL work on the diffraction of neutrons by crystals, directed towards obtaining information about the diffraction process and its dependence on the crystal and nuclear properties of various substances, was started at Clinton Laboratories in 1945 by E. O. Wollan and R. B. Sawyer. The first measurements along this line were made with single crystals; the results gave information regarding the phase of nuclear scattering. It was found, however, that with single crystals it would be difficult to make measurements of the diffracted intensity with sufficient accuracy to permit reliable conclusions to be drawn regarding the effect on the intensity of various factors such as nuclear spin, presence of more than one isotope, characteristic temperature of the crystals, crystal structure, etc.

By using the powdered crystal method one can almost completely eliminate the effects of extinction and of crystal distortion and, as has been shown in the case of x-rays, accurate intensity measurements can be made if a sufficiently intense source of monochromatic radiation is available. The flux from the Clinton pile was found to be just sufficient to permit one to use the powder diffraction method. However, since no monochromatic lines are available with neutron sources, it is necessary to first reflect

the neutrons from a single crystal (or use a mechanical velocity selector) to obtain a monoenergetic beam and this fact also increases the difficulty of obtaining sufficient intensity for the application of this method. The low intensity encountered in this work has made progress less rapid than would be desired, but recent changes in the apparatus have gone far in the direction of improving the situation.

The recently published experimental work of Fermi and Marshall[1] and Fermi, Sturm, and Sachs[2] performed at the Argonne National Laboratory have been directed along the same lines as the present research. Fermi and Marshall have studied Bragg reflections from a variety of single crystals, thereby obtaining information on the relative phase of scattering and the coherent scattering cross sections for various elements. On the other hand, Fermi, Sturm, and Sachs have observed the variation of total scattering cross section by crystalline powders as a function of neutron energy. For materials possessing a favorably large ratio of scattering to capture cross section, pronounced changes in the crystal scattering cross section as a function of changing neutron wave-length should result from crystal diffraction effects as Halpern, Hamermesh, and Johnson[3] have predicted. The information available from the present diffraction experiments duplicates in many respects that from the above procedures.

2. EXPERIMENTAL ARRANGEMENT

The data which are being reported here were taken during the past year with an experimental arrangement which was accepted at the time as being satisfactory. The long hours of readings which were required to produce data with good statistical accuracy, however, led recently to the incorporation of improvements in the technique which have materially increased the efficiency of the work, and all the data have been retaken with the present experimental arrangement.

The arrangement of the apparatus, including the monochromator, the spectrometer for holding the powder specimens, the counter and the associated shielding, is shown in Fig. 1. A beam of neutrons emerges from the pile through a 1 in. ×1 in. square hole in a one-foot long shielding block. The neutrons emerging from the pile through this hole have a maximum angular divergence of about one degree. The monochromating crystal (NaCl), on which the neutrons fall, is located on a turntable attached to the pile face, and the region around the crystal is heavily shielded with borated paraffin and lead. In our earlier work the cleavage face (200 plane) of the NaCl crystal was used as the reflecting surface. The face of the crystal has now been cut so that it makes an angle of 6° with the (200) reflecting planes and this permits the primary neutron beam of 1-in. width to give a diffracted beam of $\frac{3}{8}$-in. width. The situation can be understood from the enlarged drawing of the crystal shown in Fig. 1. This method of cutting a crystal to permit the use of a wide primary beam was first suggested for x-ray work by Fankuchen.[4] The method has proved effective with neutrons, our beam strength having been improved by a factor of about two. The monochromatic beam from this crystal passes out through the shield through a long boron carbide lined slit, 1 in. high by $\frac{3}{8}$ in. wide, and passes over the center of a spectrometer table on which the powder crystal specimens are held.

The crystal powders are contained in flat cells with thin aluminum windows (which give negligible scattering) and these cells are held on the spectrometer table in the conventional position for diffraction by transmission. The counter has an active length of 18 inches and is filled with BF_3 gas in which the boron is enriched in the B^{10} isotope. The counter is shielded with four inches of paraffin and $\frac{1}{2}$ in. of B_4C. It is arranged to rotate about the center of the spectrometer table; the heavy load caused by shielding, is supported by cables leading to a bearing above the spectrometer table in line with the axis of rotation.

The process of taking data is now on an automatic basis. The electrical impulses from the proportional counter are fed to an amplifier and scaler and to a printing recorder. The counter

[1] E. Fermi and L. Marshall, Phys. Rev. **71**, 666 (1947).
[2] E. Fermi, W. J. Sturm, and R. G. Sachs, Phys. Rev. **71**, 589 (1947).
[3] O. Halpern, M. Hamermesh, and M. H. Johnson, Phys. Rev. **59**, 981 (1941).
[4] I. Fankuchen, Nature **139**, 193 (1937).

and the powder specimen are rotated by a motor at a low angular velocity (the counter at 15′ and the specimen at 7½′ of arc per four minutes of time) and at four-minute time intervals the printing recorder stamps the number accumulated on a mechanical counter and then resets the counter to zero. Alternate four-minute intervals are taken with and without cadmium in the beam, this being accomplished automatically with a solenoid. Adjustable microswitches for reversing the motor drive can be set to keep the spectrometer operating within any desired angular range. The advantage of automatic operation cannot be overestimated since the best data can be taken during the evening and night shifts.

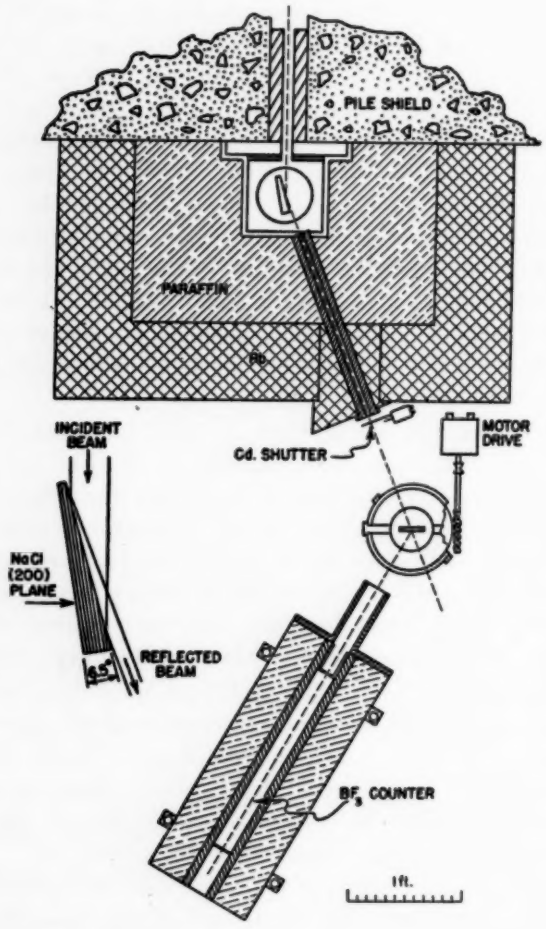

FIG. 1. Arrangement of apparatus, showing the monochromating crystal (detailed in left center) collimating slits, shielding, second spectrometer with location of powder specimen and counter.

3. ANALYSIS OF RADIATION FROM FIRST CRYSTAL

In the study of the diffuse scattering from crystals it is important to know the energy distribution of the neutrons incident on the crystals or crystal powders being investigated.

The quality of the neutron beam reflected from the first crystal depends on the energy spectrum, the angular divergence of the neutrons falling on the crystal, and on the perfection of and the amount of diffuse scattering from the monochromating crystal.

To analyze this beam we have made rocking curves on both sides of the beam with a second crystal set in the transmission position on the spectrometer table. When the reflecting planes of the first and second crystal are parallel, one obtains a narrow rocking curve (width at half-maximum = 10 min. of arc) with a high peak intensity. This rocking curve is a measure of the imperfection of the two crystals and its width is practically independent of the energy in the incident beam for the neutrons which have been Bragg reflected from the first crystal. On the other hand, the rocking curve, taken in the non-parallel position, is a measure of the energy spread in the neutron beam falling on it. The energy distribution in the beam can then be obtained from the shape of the intensity distribution in the non-parallel position. A plot of the energy distribution thus obtained is shown in Fig. 2 without correction for crystal imperfection which, if made, would narrow the curve by about 10 percent.

The amount of radiation diffusely scattered from the first crystal was determined by measuring the intensity through the slit when the first crystal was set at an angle of 2° off the maximum of the Bragg peak. In this position the measured intensity was found to be about 3 percent of that obtained with the monochromator in the optimum position for Bragg reflection.

A further test of the quality of the radiation from the monochromating crystal was made by taking rocking curves with the second crystal at various angles both inside and outside of the first-order peak. At no other angular position was there evidence of radiation outside of the energy range shown in Fig. 2, except that cor-

responding to second-order reflection of radiation of $\frac{1}{2}\lambda_0$, $(4E_0)$, where λ_0, (E_0) are the wave-length and energy of the main first-order reflection from the monochromating crystal. The strength of this second-order contamination as determined from a rocking curve at $\sin\theta=\frac{1}{2}\sin\theta_0$ was found to be 1.6 percent of the first-order peak.

We feel that the above analysis shows our monochromatic beam to be of sufficient purity to introduce no appreciable errors in our diffraction measurements.

4. THEORETICAL CONSIDERATIONS

Although the scattering of slow neutrons and the scattering of x-rays are in many respects very similar problems, there are some distinct differences which make the scattering of slow neutrons a field in itself.

With x-rays, the atomic electrons are the scattering entities and the cross section for scattering by a single electron can be accurately calculated. On the basis of classical theory one obtains the well-known Thomson formula which is valid for bound electrons. A free electron, however, takes up momentum from the incident photon and in this case one must apply quantum theory which leads to the Klein-Nishina Compton scattering formula. The scattering by an atom is obtained by summing the scattering amplitudes of all the electrons with respect to their relative positions in the atom and this gives the atomic scattering factor which is defined in terms of the relative scattering by the whole atom to that of a single bound electron. With x-rays these atomic scattering factors can be determined experimentally, and they can also be approximately determined theoretically by the method of self-consistent fields.

With neutrons the scattering is almost entirely nuclear and, since so little is known about nuclear structure, it cannot be expected that scattering cross sections, in general, can be determined theoretically. Aside from this fundamentally different mechanism of scattering, there exist a number of other basic differences between neutron and x-ray diffraction which will be of interest in connection with the experimental data and a general review of these is given in the following sections. Details on these discussion points can be found in earlier papers.[3, 5–14]

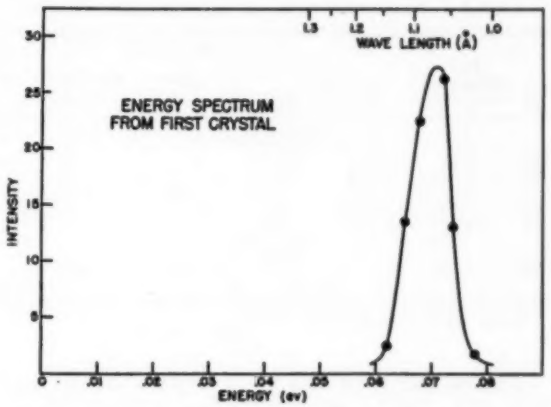

FIG. 2. Energy and wave-length distribution of neutrons reflected from monochromating crystal.

5. SCATTERING THEORY

The theory of the scattering of neutrons by nuclei gives a relation between the scattering amplitude and the nuclear potential. For the case of slow neutrons the theory is simplified by the fact that there is only s scattering which is spherically symmetric.

The wave equation representing the interaction of a neutron with a nucleus is

$$\nabla^2\psi+k'^2\psi=0 \qquad (1)$$

where

$$k'=\left(\frac{2m'(E-V)}{\hbar^2}\right)^{\frac{1}{2}}$$

is the wave number inside the nucleus whose potential function is $V(r)$ and m' is the reduced mass of the system. Correspondingly, the incident wave is represented by the same equation with $V=0$ and then $k=(2mE/\hbar^2)^{\frac{1}{2}}=2\pi/\lambda$, where λ is the wave-length of the incident neutrons and m is the neutron mass.

---

[5] E. Fermi, Ricerca Scient. **7**, 13 (1936).
[6] G. C. Wick, Physik. Zeits. **38**, 403 (1937).
[7] J. Schwinger and E. Teller, Phys. Rev. **52**, 286 (1937).
[8] H. A. Bethe, Rev. Mod. Phys. **9**, 69 (1937).
[9] I. Pomeranchuk, Physik. Zeits. Sowjetunion **13**, 65 (1938).
[10] R. J. Seeger and E. Teller, Phys. Rev. **62**, 37 (1942).
[11] R. Weinstock, Phys. Rev. **65**, 1 (1944).
[12] H. Feshbach, D. C. Peaslee, and V. F. Weisskopf, Phys. Rev. **71**, 145 (1947).
[13] M. L. Goldberger and F. Seitz, Phys. Rev. **71**, 294 (1947).
[14] R. J. Finkelstein, Phys. Rev. **72**, 907 (1947).

TABLE I. Scattering data for diamond and graphite.

hkl	P_{hkl} (integrated counts/min.)	e^{2W}	k^2/ϵ^2	f_0 (10^{-12} cm)	$\sigma_B=4\pi f_0^2$ (barns)	σ
			Diamond			
111	253	1.018	10.5	0.64	5.2	5.2*
220	272	1.048	9.5			
311	216	1.067	9.7			
331	151	1.119	9.9			
			Graphite			
002	135		10.6	0.66	5.5	

* From our transmission measurements.

The solution of the wave equation[15] at large distances r from the nucleus (neglecting absorption) can be represented as the sum of an incident plane wave (along z) and a radially scattered wave

$$\psi=e^{ik'z}+fe^{ikr}/r, \tag{2}$$

where f is the complex amplitude of the scattered wave.

It can be readily shown that f depends on the phase shift of the total wave with respect to the incident wave and this phase shift depends on the nuclear potential $V(r)$. For slow neutrons there is only s scattering and, in this case, only the spherically symmetric part of the solution need be considered. The spherically symmetric part of the incident plane wave can be represented as the sum of an incoming and an outgoing wave

$$(\sin kr)/kr=(e^{ikr}-e^{-ikr})/2ikr. \tag{3}$$

The corresponding spherically symmetric part of the total wave with the nuclear potential turned on will be given by the same function with different phase,

$$\frac{A\sin(kr+\eta_0)}{kr}=\frac{Ae^{i(kr+\eta_0)}-Ae^{-i(kr+\eta_0)}}{2ikr}. \tag{4}$$

The difference between Eqs. (3) and (4) will then represent the scattered wave

$$f\frac{e^{ikr}}{r}=\frac{(Ae^{i\eta_0}-1)e^{ikr}-(Ae^{-i\eta_0}-1)e^{-ikr}}{2ikr}. \tag{5}$$

In the scattered wave, however, there must be no incoming wave and for this condition to be satisfied, $A=e^{i\eta_0}$. Substituting this value for A back into Eq. (5) gives

$$f=(e^{2i\eta_0}-1)/2ik, \tag{6}$$

and the cross section for scattering will be

$$\sigma_{scat}=4\pi|f|^2=4\pi\sin^2\eta_0/k^2. \tag{7}$$

The phase shift η_0 is very small except in the near vicinity of a resonance level and hence in most cases only the first power of η_0 in the ex-

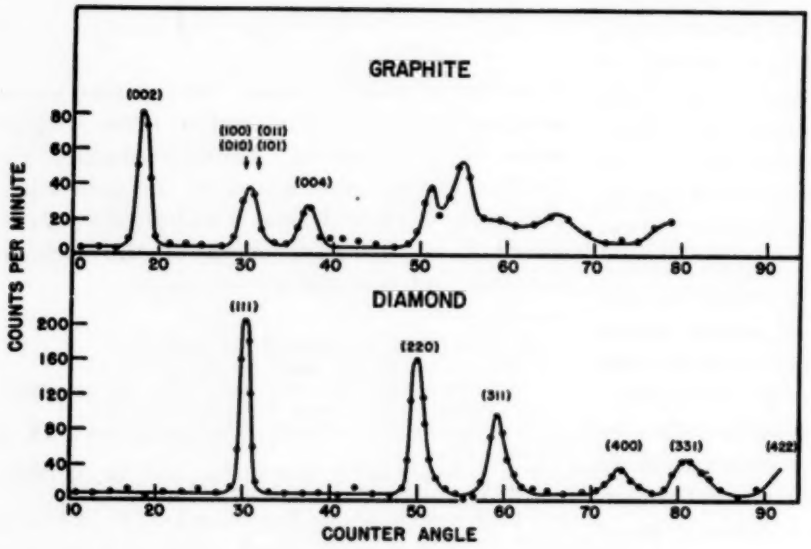

FIG. 3. Powder diffraction patterns for diamond and graphite. The major part of the diffuse scattering in these patterns arises from multiple scattering in the samples.

[15] See for example N. F. Mott and H. S. W. Massey, *The Theory of Atomic Collisions* (Oxford University Press, 1933).

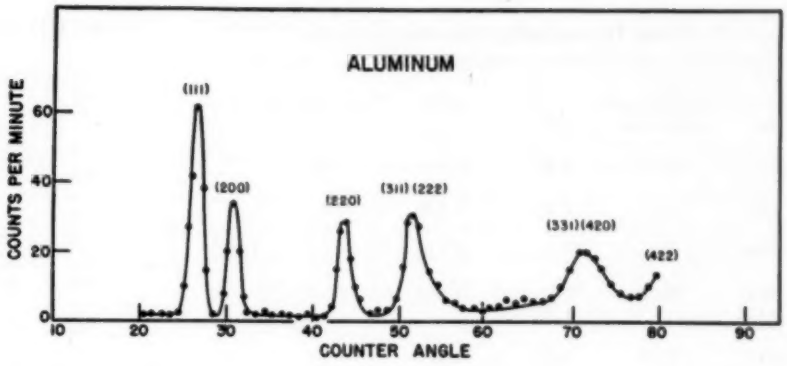

FIG. 4. Powder diffraction pattern for aluminum. The diffuse scattering at small angles arises primarily from multiple scattering. At the larger angles it is mostly temperature diffuse scattering.

pansion of Eq. (7) need be considered so that

$$f=\eta_0/k, \tag{8}$$

and

$$\sigma=4\pi\eta_0^2/k^2. \tag{9}$$

Positive or negative phase shifts correspond to positive or negative scattering amplitudes and, hence, the corresponding scattered waves for these two cases will be 180° out of phase with each other. Positive phase shifts occur only in the vicinity of a resonance and, hence, they will be less common than negative phase shifts.

The measurement of phase shifts or scattering amplitudes will constitute a good check on any theory of nuclear structure, since, for such a theory to be satisfactory it must be capable of yielding these quantities.

For hydrogen the scattering cross section can be evaluated in terms of the binding energy and the range of forces in the triplet and singlet state of the deuteron. With heavy elements for which the nucleus behaves in most cases as an impenetrable sphere, rough estimates of the cross section can be made by taking $\sigma=4\pi a^2$ where the radius a is approximately equal to the nuclear radius as obtained from other sources of information.

6. BINDING, ISOTOPE, AND SPIN EFFECTS

The scattering cross section for a given nucleus depends on whether the nucleus is in a free or a bound state. The cross section for scattering by a rigidly bound nucleus will be greater than for the same nucleus in a free state by the square of the ratio of the neutron mass to the reduced mass for the neutron and the scattering nucleus, i.e., $[(A+1)/A]^2$ where A is the mass number of the scattering nucleus. Between the extremes of completely free scattering centers and completely bound centers there will be a region which may be loosely referred to as that of partial binding for which the reduced mass effect will lie somewhere between $[(A+1)/A]^2$ and 1. The coherent scattering by crystals will always correspond to rigidly bound scattering centers.

When scattering measurements are made on an element containing more than one isotope the results will correspond to an average of the scattering by these isotopes. If the measurements are made with free nuclei, the total scattering cross section averaged over the isotopes will be

$$\sigma_f=4\pi(p_1a_1^2+p_2a_2^2+\cdots), \tag{10}$$

where the p's are the isotopic abundances and the a's are the free nuclear scattering amplitudes for the respective isotopes. If the atoms are bound but still act independently as far as interference effects are concerned, the corresponding cross section will be

$$\sigma_{\text{bound}}=\sigma_f[(A+1)/A]^2 =4\pi(p_1f_1^2+p_2f_2^2+\cdots), \tag{11}$$

where the f's are the scattering amplitudes for bound scattering centers.

The coherent scattering by the various isotopes of an element randomly distributed in a crystal will be

$$\sigma_{\text{coh}}=4\pi(p_1f_1+p_2f_2+\cdots)^2, \tag{12}$$

since here the isotopic amplitudes must be combined algebraically into a total amplitude before squaring to obtain the intensity.

A situation similar to that of the isotope effect arises from the fact that neutron scattering may depend on the relative orientation of the spins

TABLE II. Scattering data for aluminum.

hkl	P_{hkl} (integrated counts/min.)	e^{2W}	f_0 (10^{-12} cm)	$\sigma_B=4\pi f_0^2$ (barns)	σ
111	82.0	1.08	0.330	1.38	
200	47.5	1.11	0.338	1.43	
220	20.3	1.23	0.334	1.40	1.48*
311	91.2	1.35	0.350	1.54	
222		1.37			
331	73.9	1.67	0.345	1.50	
420		1.71			
		averages	0.340	1.46	

* σ_{free} taken from literature as 1.37 barns.

TABLE III. Scattering data for sodium containing crystals.

Crystal	hkl	P_{hkl} (integrated counts/min.)	f_0 (10^{-12} cm)		$4\pi f_0^2$ (barns)		σ^* (barns)	
			Na	X	Na	X	Na	X
Na	110	11.3	0.345		1.50		3.7	
NaBr	111	10.2	0.335	Br 0.65	1.41	Br 5.3		Br 7.5
	200	48.5						
NaCl	111	30.5	0.358	Cl 1.01	1.61	Cl 12.8		Cl 15
	200	72.5						
NaF	111	13.7	0.348	F 0.65	1.52	F 5.2		F 4.5
	200	88.5						
		averages	0.346		1.51			

* Literature values $\times[(A+1)/A]^2$.

of the neutron and the scattering nucleus. There will then be two amplitudes associated with each nucleus, one for parallel and one for antiparallel spins. The measured scattering cross section for a given nuclear species will then correspond to an average, weighted with respect to the probability for the two spin states. For scattering by free nuclei then

$$\sigma_f=4\pi\left[\frac{i+1}{2i+1}a_{i+\frac{1}{2}}^2+\frac{i}{2i+1}a_{i-\frac{1}{2}}^2\right], \qquad (13)$$

where i is the spin of the scattering nucleus and the a's are the free scattering amplitudes for parallel and antiparallel spin. For the coherent scattering by bound nuclei

$$\sigma_{coh}=4\pi\left[\frac{i+1}{2i+1}f_{i+\frac{1}{2}}+\frac{i}{2i+1}f_{i-\frac{1}{2}}\right]^2. \qquad (14)$$

These equations apply to the case where the nuclear spins are randomly oriented. In the case of ortho- and parahydrogen the situation is different since the spins of the two nuclei in the molecule have a definite orientation.

7. THE SCATTERING OF NEUTRONS BY CRYSTALS

The equations describing the intensity pattern of neutron diffraction by a crystalline powder are exactly similar to those characteristic of x-ray diffraction except for the absence of the polarization factor in the present case. As mentioned earlier, the present data have been taken with a flat plate of crystalline powder arranged in the transmission orientation and for this case, the power P_{hkl} diffracted in a selected Bragg peak is given by

$$\frac{P_{hkl}}{P_0}=\frac{\lambda^3 l}{4\pi r}\frac{h\rho'}{\rho}\frac{e^{-\mu h\sec\theta}}{\sin^2 2\theta}j_{hkl}N^2F_{hkl}^2, \qquad (15)$$

where P_0 is the power in the primary beam, λ is the wave-length of the neutrons, l is the height of the slit in front of the counter, r is the distance from sample to counter slit, ρ' is the density of the powder, ρ is the density of the solid crystal, $e^{-\mu h}$ is the transmission of specimen of thickness, h, θ is the glancing angle of reflection, j_{hkl} is the multiplicity factor, N is the number of unit cells per cm^3 of crystal, and F_{hkl} is the Bragg scattering amplitude per unit solid angle per unit cell of the crystal. F_{hkl} corresponds to the usual crystal structure factor in x-rays, except that here it is a true amplitude with the dimension of length. It is a linear combination of effective nuclear scattering amplitudes which we will designate by f_T, the subscript T being used to designate the amplitude obtained from direct measurement of a Bragg peak for a crystal at a given temperature T. For neutrons, as for x-rays, the loss in Bragg scattering due to the interaction of the neutrons with the lattice vibrations can be corrected for by the Debye-Waller temperature factor as Weinstock[11] has shown, and the true nuclear scattering amplitude f_0 for a given nucleus will be

$$f_0=f_T e^W,$$

where

$$W=M\frac{\sin^2\theta}{\lambda^2},\quad M=\frac{6h^2}{mk\Theta}\left(\frac{\varphi(x)}{x}+\frac{1}{4}\right). \quad (16)$$

$x=\Theta/T$, $\varphi(x)$ is the Debye function and Θ is the Debye characteristic temperature.

If the crystal specimen is monatomic, measurement of the absolute intensity of a single peak, plus a knowledge of the characteristic temperature of the crystal will suffice for the determination of f_0^2. With polyatomic crystals, two or more peaks must be measured to obtain values of f_0^2 for the individual atoms and even then the assignment of f_1^2 and f_2^2 to the nuclei 1 and 2 is only possible if it is known which of these cross sections is the larger. This may be determined without previous information by making measurements with a given element in several compounds. In x-rays this difficulty never arises since atomic scattering factors are known to increase with the atomic number.

In addition to the Bragg scattering, it is important to consider also the intensity of the neutrons diffusely scattered by a crystal. With x-rays the diffuse scattering consists of the Compton inelastic scattering and the temperature diffuse scattering some of which may also be inelastic. According to the Debye theory, the temperature diffuse scattering is given for a single crystal by $(1-e^{-2W})f_0^2$, where f_0 is the atomic structure factor. This theory has been extended by Zachariasen[16] to include the quantized interaction of the radiation with the Debye waves of the crystal. For the neutron case the corresponding theory has been developed by Weinstock[11] and extended by Seitz and Goldberger[13] and by Finkelstein.[14]

In the case of neutrons there will also be diffuse scattering arising from the spin and isotope effects. The over-all scattering by a crystal will then be made up of the coherent Bragg scattering plus the diffuse scattering arising from various sources. The over-all scattering cross section for a crystal as measured, for example, by a transmission experiment with correction for the effects of absorption, can then be written as

$$\sigma_{\text{crystal}}=\sigma_{\text{Bragg}}+\sigma_{DS}+\sigma_{DI}+\sigma_{DT}, \quad (17)$$

where σ_{Bragg} is the total scattering in the Bragg peaks and σ_{DS}, σ_{DI}, and σ_{DT} are the diffuse scattering cross sections for the spin, isotope, and temperature effects, respectively.

As an example of the diffuse scattering arising from the spin effect, consider a crystal containing an element of one isotope ($\sigma_{DI}=0$) and having a high characteristic temperature ($\sigma_{DT}\sim 0$) and if, in addition, A is large, then $[(A+1)/A]^2\sim 1$ and we obtain

$$\begin{aligned}\sigma_{DS}&=\sigma-\sigma_{\text{Bragg}}\\&=4\pi\left[\frac{i+1}{2i+1}f_{i+1}^2+\frac{i}{2i+1}f_{i-1}^2\right]\\&\quad-4\pi\left[\frac{i+1}{2i+1}f_{i+1}+\frac{i}{2i+1}f_{i-1}\right]^2\\&=4\pi\frac{i(i+1)}{(2i+1)^2}[f_{i+1}-f_{i-1}]^2. \quad (18)\end{aligned}$$

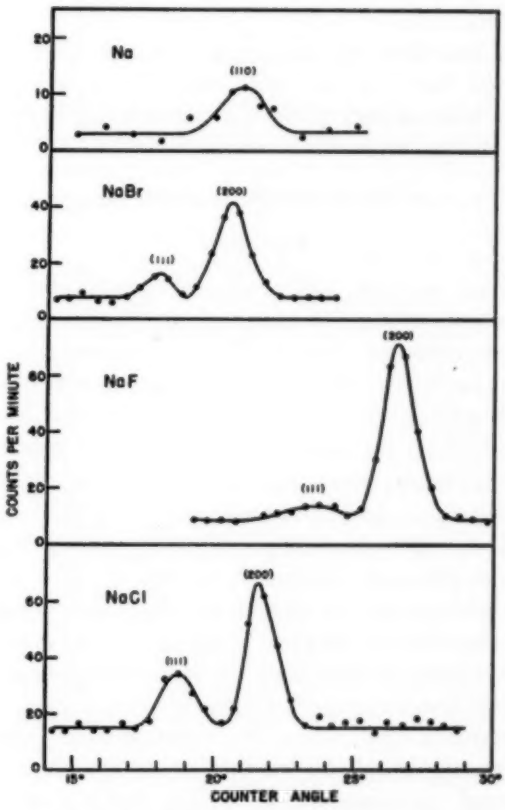

FIG. 5. Powder diffraction patterns for four Na containing crystals. The fact that the (111) peaks are smaller than the (200) peaks shows that Na, Br, F, and Cl all scatter with the same phase.

[16] W. H. Zachariasen, *Theory of X-Ray Diffraction in Crystals* (John Wiley and Sons, Inc., New York, 1945).

TABLE IV. Scattering amplitudes for two spin states of sodium.

	$f_{+\frac{1}{2}}$	$f_{-\frac{1}{2}}$	
either	+0.88	+0.02	$\times 10^{-12}$ cm
or	−0.20	+0.67	

It will be seen from this equation that the diffuse scattering due to the spin dependence will be zero when the scattering amplitudes for parallel and antiparallel spins are equal. This will be the case for a nucleus with zero spin. The other extreme is reached when the two weighted spin amplitudes are equal in magnitude but opposite in sign in which case there will be no Bragg peaks from a crystal, all the scattering will be diffuse.

For a crystal containing a light element, such as hydrogen, the spin diffuse scattering (for our wave-length $\lambda \sim 1$A) will be considerably reduced by the lack of complete binding (see following paper).

A situation similar to the one we have discussed here for the spin dependence will also exist with respect to the scattering by an element containing more than one isotope.

8. EXPERIMENTAL RESULTS

Diamond

The neutron diffraction measurements for diamond (800-mesh powder) are shown by the lower curve of Fig. 3. The measurements correspond to the difference in counting rates with and without a cadmium shutter in the beam incident on the specimen, the incident neutrons being monochromatic, as we have already pointed out, and of wave-length $\lambda = 1.057$A.

From the integrated intensities of the Bragg peaks one can determine values of F_{hkl}^2 from Eq. (16) except for a constant, k^2, which depends on the effective incident neutron intensity which it has not yet been possible to measure directly. From the measured values of $k^2F_{hkl}^2$ one can determine $k^2f_T^2$, where f_T is the effective Bragg scattering amplitude of the carbon atoms at the crystal temperature at which these measurements are made.

By applying the usual Debye-Waller temperature factor e^{2W} (Eq. (16)) to the measured values of $k^2f_T^2$ the effects of the lattice vibrations are eliminated and one obtains numbers proportional to the true Bragg scattering amplitudes for the carbon atoms in the crystal. The values of $k^2f_0^2 = k^2f_T^2e^{2W}$ are listed in Table I for four diamond peaks.

TABLE V. Sign of scattering amplitudes for various elements.

Positive scattering amplitude			Negative scattering amplitude
O	Pb	Na	Mn
Fe	N	K	Li
Mg	C	Cl	H
Ba	Be	Br	
Ca	Al	I	
S	Sr	D	
F			

Whether or not k^2f^2 is proportional to the total nuclear scattering cross section of carbon can be determined by measuring both the Bragg scattering and the diffuse scattering by the crystal. If there are no spin or isotope effects with diamond, then one would expect no diffuse scattering other than that arising from the effects of lattice vibrations. Since C^{12} has zero spin, any spin diffuse scattering would have to be associated with C^{13}. Since this isotope is present in normal carbon to the extent of only 1.1 percent, one would expect its contribution to the total scattering to be very small.

The actual measured diffuse background from diamond, as shown in Fig. 4, is, however, quite appreciable even at small angles where the temperature diffuse scattering should be immeasurably small. This extra diffuse background can, however, be accounted for on the basis of multiple scattering by the sample. Although the attenuation of the neutron beam in traversing the sample was in this case only 20 percent, the fact that there is no true absorption by the sample makes multiple scattering important. In x-ray work this problem does not enter since the attenuation of the beam arises primarily from true absorption of the radiation. The effects of multiple scattering of neutrons in the sample can only be eliminated by making the sample very thin and then the peaks become too small to measure with the present available neutron intensities. We have, however, made approximate calculations of the amount of multiple scattering to be expected from our diamond sample and

it agrees closely with the observed excess scattering.

On this basis then, it can be concluded that there is no measurable spin or isotope effect arising from the presence of the small amount of C^{13} in normal carbon and that the true diffuse scattering by the sample arises from the effects of lattice vibrations which can be corrected for by the usual Debye-Waller temperature factor which Weinstock[9] has shown to apply also to the case of neutron diffraction.

The Bragg scattering by diamond, when corrected for the lattice vibration effects, constitutes within the accuracy of our measurements the total scattering by carbon atoms. On this basis the measurements can be normalized to the true scattering cross section of carbon.

It seemed advisable in this connection to make an independent measurement of the total scattering cross section of the diamond powder by the transmission method. These measurements gave a value of 4.9 barns for the total scattering cross section by diamond powder at our particular neutron wave-length of 1.057A. This value is related to the scattering cross section for bound carbon atoms σ, according to the expression

$$\sigma_{\text{transmission}}=\frac{\lambda^2 N}{8}\sum_{hkl} jd\sigma e^{-2W}R, \qquad (19)$$

with the summation carried over all Bragg reflections and where

$$R_{hkl}=\sum_{\substack{\text{unit}\\ \text{cell}}}\exp[2\pi i(hx+ky+lz)],$$

summed over all atomic positions (x, y, z) in the unit cell. N is the number of unit cells per cm^3, j the multiplicity value, and d the interplanar spacing value. Upon insertion of appropriate numerical values into Eq. (19) one obtains $\sigma=5.2$ barns. Since this corresponds to bound carbon atoms, the scattering cross section for free carbon centers is smaller by the reduced mass factor and thus $\sigma_f=4.4$ barns. This value is lower than the usually accepted carbon cross section of 4.8 barns, but it agrees well with the results of Rainwater and Havens.[17] The measured quantities $k^2f_0^2$ in Table I can now be normalized in terms of a bound carbon scattering cross section of 5.2 barns and thus k^2, which is a constant of our experimental arrangement, is evaluated. The average value of $k^2f_0^2$ for the measured peaks has been taken for use in determining k^2 in terms of the above cross section of carbon. Any later measurements can then be evaluated in terms of absolute cross sections by comparison with diamond which is taken as standard.

Graphite

Diffraction measurements with powdered graphite are shown in the upper part of Fig. 3. The scattering cross section for carbon (see Table I) has been determined from the (002) reflection alone, since the other peaks are less accurately measured. The intensity of this peak corresponds to a slightly higher carbon scattering cross section than the average value obtained from diamond, but the difference is within the experimental error.

Aluminum

The diffraction results for aluminum are shown in Fig. 4. The sample on which the measurements were made consisted of a $\frac{1}{2}$-in. thick plate of pure rolled aluminum which was several times heated to near the melting point and then quenched. This process was found to remove preferred orientations in the sample and by using a solid sample more material can be exposed to the neutron beam and hence greater accuracy can be achieved.

The results of the measurements standardized against diamond are shown in Table II. The characteristic temperature for Al is sufficiently low (398°K) so that a very appreciable lattice vibration effect is observed over the angular range measured. One observes, however, that after application of the factor e^{2W} the Bragg scattering amplitudes f_0 are very nearly constant as is to be expected if the Weinstock treatment of the elastic scattering of neutrons is substantially correct.

The measured Bragg scattering cross section for aluminum agrees closely with the nuclear scattering cross section ($\sigma=1.48$ barns) and, since Al has only one isotope, it can be concluded

[17] L. J. Rainwater and W. W. Havens, Jr., Report No. CP-1962, Manhattan District Plutonium Project.

that the scattering by aluminum has, if any, only a small dependence on spin.

Sodium Containing Crystals

In connection with the work on NaH and NaD reported in the following paper in this journal it is important to have an independent determination of the Bragg scattering amplitude of Na. Diffraction measurements on Na, NaBr, NaF, and NaCl, from which the Bragg scattering amplitude for sodium as well as for the other elements in the crystals can be determined, are reported here. Less extensive measurements have been made on these crystals than on those discussed above. The intensity patterns are shown in Fig. 5 and the results are listed in Table III. For NaBr, NaCl, and NaF the (111) and (200) reflections suffice to determine the amplitudes for the two elements in the crystal and for Na only one reflection (110) is required. With the compound crystals the usual powder sample was used. The measurements on Na were made with two samples; one consisted of the solid metal and the other consisted of small beads obtained by shaking the molten metal in xylene. The measurements from the two samples were in good agreement.

Fluorine

The measured Bragg scattering cross section for fluorine is found to be somewhat higher than the total bound nuclear scattering cross section, as taken from the literature. Actually, this cannot be the case and it must be ascribed to error in one or the other of the measurements. Since our measurements have been made on the first two peaks of a single fluorine compound, an uncertainty of 15 percent is not unreasonable. The results indicate, therefore, that there is only a small spin dependence, if any, for the scattering by fluorine.

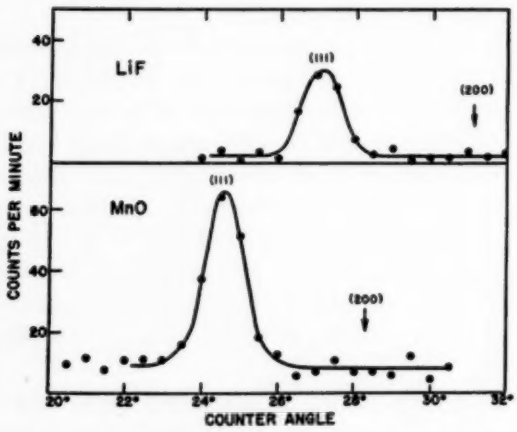

FIG. 6. Powder diffraction patterns for LiF and MnO. The absence of measurable (200) peaks shows that Li and F and also Mn and O scatter with opposite phase.

Bromine and Chlorine

Bromine and chlorine each have two isotopes and hence it is not expected that the Bragg scattering cross section should equal the nuclear scattering cross section.

From the values of σ and f with its proper sign and the isotopic abundances, the scattering amplitudes for the individual isotopes could be calculated by solving Eqs. (14) and (15) for f_1 and f_2. It is felt, however, that the measurements are of insufficient accuracy at present to warrant carrying out such a calculation.

Sodium

The scattering amplitude for Na is determined independently from each of the four crystals. The values of f_0 and $\sigma_B=4\pi f_0^2$ for Na listed in Table III are seen to be in good agreement and they give an average value of $f_0=0.346\times10^{-12}$ cm and $\sigma_B=1.51$ barns. The fact that σ_B is considerably smaller than the nuclear scattering cross section, $\sigma=3.7$ barns, shows that the scattering by Na is spin dependent. The separate amplitudes for parallel and antiparallel spin can be calculated by solving Eq. (14) and Eq. (13), modified to the case of bound nuclei,* for $f_{i+\frac{1}{2}}$ and $f_{i-\frac{1}{2}}$, which gives

$$f_{i+\frac{1}{2}}=f_0\pm\left(\frac{\sigma-\sigma_B}{4\pi}\times\frac{i}{i+1}\right)^{\frac{1}{2}},$$

and (20)

$$f_{i-\frac{1}{2}}=f_0\mp\left(\frac{\sigma-\sigma_B}{4\pi}\times\frac{i+1}{i}\right)^{\frac{1}{2}}.$$

The data for sodium including the spin ($i=\frac{3}{2}$) when substituted into these equations give the

* *Note:* σ_{coh} of Eq. (14) is the same as σ_B ($B\equiv$Bragg) of Eq. (20). σ is used to designate the total scattering cross section by bound nuclei and σ_f is used for free scattering centers.

scattering amplitudes for the two spin states which are listed in Table IV. There is nothing in the experiments that permits one to make a choice between the two sets of values, but it might be argued that the set in which both amplitudes are positive is more apt to be the correct one.

The above value of 1.51 barns for the Bragg scattering cross section of sodium is not in agreement with the value of 3.5 barns reported by Fermi and Marshall.[1] Their measurements were made on the Bragg reflections from single crystals of NaCl with the chlorine cross section being arbitrarily adjusted to the total scattering cross section. Their intensity measurements were made by comparing peak heights rather than determining integrated intensities, and they have assumed that their crystals behave as if they were perfect (intensity proportional to first power of scattering amplitude). It would seem that these procedures might introduce considerable error in the calculated cross section values.

Phase of Nuclear Scattering

The sign of the phase shift of the total neutron wave relative to the incident wave determines the sign of the scattering amplitude. The relative sign of the scattering amplitudes for two elements can be readily determined by diffraction measurements on a crystal containing the two elements. With simple crystals such as NaCl, LiF, etc. a comparison of the intensities of the (111) and (200) peaks suffices for a comparison of the scattering phases since these two peaks correspond to a difference and a sum, respectively, of the scattering amplitude of the two elements. For more complicated crystals it may be necessary to measure more than two peaks to determine the relative scattering phases of two elements. Where an element consists of more than one isotope, the phase of scattering by the element will be determined by the predominant amplitude.

The powder patterns for the (111) and (200) peaks of LiF and MnO are shown in Fig. 6. The fact that the (200) peaks are smaller than the (111) peaks in LiF shows that Li and F have opposite scattering phases. The same is true of Mn and O, while for the Na compounds, shown in Fig. 5, the phases are all the same. Although one cannot from such comparisons alone determine the absolute sign of the phase shift, one can from other information readily identify the phase shift for Li and Mn as being positive.

Fermi and Marshall[1] have already published phase determinations for a number of elements. They use the convention of associating a positive scattering amplitude with a negative phase shift. Table V gives a list of elements for which the scattering phase has been measured either by us or by Fermi and Marshall; their terminology is used with respect to sign.

ACKNOWLEDGMENTS

We are indebted to our colleagues Drs. M. E. Rose, G. Goertzel, and W. G. Pollard for many helpful discussions on questions of theoretical interpretation and for the opportunity of seeing some of their unpublished calculations on the interaction of neutrons with crystals. Mr. M. C. Marney assisted greatly in the task of data accumulation.

Neutron Diffraction Studies of NaH and NaD

C. G. SHULL, E. O. WOLLAN, G. A. MORTON,* AND W. L. DAVIDSON**
Oak Ridge National Laboratory, Oak Ridge, Tennessee

(Received January 5, 1948)

Neutron diffraction patterns for NaH and NaD are given from which it is established that the crystal structure is analogous to that of NaCl with the hydrogen centers replacing chlorine. It is shown that both sodium and deuterium scatter neutrons with a positive scattering amplitude whereas hydrogen scattering is characterized by a negative scattering amplitude. The coherent scattering cross sections for hydrogen and deuterium are determined as 2.0 ± 0.3 and 4.1 ± 1.2 barns, respectively. Using this value of the coherent scattering cross section for hydrogen and Melkonian's value of 20 barns for the total scattering cross section by a free proton, the scattering amplitudes characteristic of the two proton spin states have been evaluated, and these are in good agreement with the latest data on the scattering of neutrons by *o*- and *p*-hydrogen. The range of nuclear forces present in the neutron-proton triplet interaction is evaluated as $1.6\pm0.2\cdot10^{-13}$ cm.

INTRODUCTION

THE preceding paper[1] has described in some detail the general problem of neutron diffraction as related to the nuclear properties and the structural array of atoms in crystalline materials. The present paper is concerned with studies which have been made on hydrogen and deuterium containing crystals by use of the techniques described in the previous paper, which for convenience will be referred to as I.

The diffraction of neutrons by hydrogen and deuterium containing crystals is of interest for two reasons; (1) this technique offers a promising method of obtaining information on the location of hydrogen positions in crystalline and molecular structures whereas similar analyses by the diffraction of x-rays or electrons can only rarely give such information, and (2) the scattering of neutrons by protons or deuterons is of importance from a theoretical physics point of view since these simplest of nuclear reactions can be treated theoretically for comparison with experiment. Information pertinent to both of these items has been obtained.

EXPERIMENTAL RESULTS

Perhaps the simplest of hydrogen-containing crystals from the structural point of view are the alkali hydrides. X-ray diffraction studies have shown that the metallic atoms in LiH, NaH, KH, CsH, etc. are arrayed in a face-centered cubic structure. However, it is only in the case of LiH, where the x-ray structure factors of the two atoms are sufficiently the same, that the hydrogen positions have been located.[2] For this case the hydrogen centers are also found to be at face-centered cubic positions and the structure is identical to that occurring in NaCl with hydrogen replacing chlorine. By analogy to LiH the other simple hydrides are suspected also to crystallize in the NaCl structure.

NaH was selected for the present study because of (1) its commercial availability, (2) it could be prepared in the laboratory thereby permitting the preparation of the deuteride, and (3) the absorption cross section is low in contrast to the relatively high absorption cross section of LiH samples. In the laboratory preparation of the hydride (or deuteride) the product was formed by the direct reaction of molten sodium with hydrogen catalyzed by a small amount of stearic acid. The hydrogen was obtained by electrolysis of water after which it was cleansed of (1) residual oxygen by passage over copper at 300°C and (2) residual water vapor by passage through a liquid nitrogen trap. The reaction was then performed by bubbling the hydrogen gas through molten sodium contained in a stainless steel tube and maintained at a temperature of 380°C.

* On leave (July 1946–Aug. 1947) from R.C.A. Laboratories, Princeton, New Jersey.

** On leave (July 1946–Aug. 1947) from B. F. Goodrich Company, Akron, Ohio.

[1] E. O. Wollan and C. G. Shull, Phys. Rev. **73**, 830 (1948).

[2] E. Zintl and A. Harder, Zeits. f. physik. Chemie **B14**, 265–284 (1931).

Since the reaction rate is rather low, recirculation of the unreacted gas was found desirable and was accomplished by means of a thermal pump.

Three batches of the material were used for examination: (1) commercially prepared NaH,[3] (2) laboratory-prepared NaH, and (3) laboratory-prepared NaD. X-ray diffraction analyses[4] were obtained on these preparations and showed the presence of minor impurities, mostly metallic sodium, in (1) and (2) whereas a considerable impurity of sodium and sodium hydroxide or deuteroxide was indicated in preparation (3). Since some of the diffraction lines for sodium and sodium hydroxide fall at or near to the positions of the principal NaD lines, a certain ambiguity in the relative intensities of the latter lines is introduced through the presence of the impurities. The effect of this upon the quantitative interpretation of the NaD pattern will be discussed in a later section.

Physically, sodium hydride is a grey or white powder with a solid density of 1.37 g/cm³. It is extremely active towards water or water vapor and, consequently, must be handled in a controlled atmosphere and kept in sealed containers. The sample holder was similar to that described in I with thin aluminum windows for air-tight construction. Samples of different thicknesses ranging from about 0.5 g/cm² to 0.8 g/cm² were used in evaluating the intensity of the diffraction pattern.

Typical diffraction patterns for NaH and NaD covering the inner diffraction peaks are shown in Fig. 1. A pronounced (111) peak and a very weak or absent (200) peak is to be noted for NaH in contrast to the reversed intensities of these peaks for NaD. If sodium were the only element contributing to the pattern (as is the case in x-ray diffraction analysis) one would expect a (111) peak about twice as strong as the (200) peak. Since neither the NaH nor NaD pattern shows this ratio of peak intensities, it is immediately concluded that both hydrogen and deuterium are contributing to the coherent scattering. Moreover, the reversal of intensities in the two patterns suggests that the hydrogen and deuterium centers are scattering in opposite phase with respect to each other. These data do not, however, permit a conclusion as to the relative phase of scattering of hydrogen (or deuterium) with respect to sodium because of the uncertainty in the crystal structure of sodium hydride. Before this can be accomplished it is necessary to establish without ambiguity the correct structure.

TABLE I. Experimental intensities and values calculated for possible structures of NaH.

Diffraction peak	Experimental intensity	Calculated for ZnS structure	Calculated for NaCl structure
(111)	37	$f_{Na}^2+f_H^2$	$(f_{Na}-f_H)^2$
(200)	<2	$(f_{Na}-f_H)^2$	$(f_{Na}+f_H)^2$
(220)	0	$(f_{Na}+f_H)^2$	$(f_{Na}+f_H)^2$
(311)	25	$f_{Na}^2+f_H^2$	$(f_{Na}-f_H)^2$
(222)	0	$(f_{Na}-f_H)^2$	$(f_{Na}+f_H)^2$
(400)	<5	$(f_{Na}+f_H)^2$	$(f_{Na}+f_H)^2$
(331)	15	$f_{Na}^2+f_H^2$	$(f_{Na}-f_H)^2$
(420)	0	$(f_{Na}+f_H)^2$	$(f_{Na}+f_H)^2$

Among the several structures of face-centered cubic type which are known to exist, there are

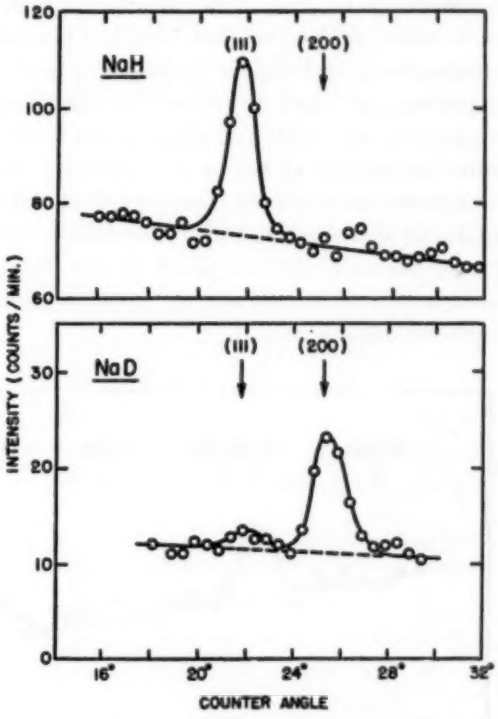

FIG. 1. Powder diffraction patterns over the (111) and (200) peaks of NaH and NaD. The diffuse scattering for NaH is seen to be much larger than that for NaD.

[3] Available from the Electrochemicals Department, E. I. duPont deNemours and Company, Niagara Falls, New York.

[4] We are indebted to Mr. A. C. Eckert of the Carbide and Carbon Chemical Corporation who supplied some of the analyses for us.

only two (B-1 type, NaCl and B-3 type, ZnS) which are possible structures for NaH. Other structures are ruled out because of unit cell size. Fortunately it is possible to determine rather easily the correctness of either the NaCl or the ZnS structure on the basis of the relative intensities of some of the outer diffraction peaks. Figure 2 shows additional diffraction data for some of the higher index peaks of NaH. Peaks at the (311) and (331) locations are to be observed while the (220), (400), and (420) are either too weak for measurement or are absent.

A comparison of the measured intensities with those calculated for the two possible structures is given in Table I. The squares of the crystal structure factors (approximately proportional to the diffraction peak intensities) are given here in terms of the individual nuclear scattering amplitudes. Either the ZnS structure with a common sign for f_{Na} and f_H or the NaCl structure with opposite signs for the amplitudes would satisfy the experimental data for the (111) and (200) peaks but the relative intensities of the (220), (311), (420), and (331) eliminate the ZnS structure from consideration. For instance, the (220) reflection of the ZnS structure should exhibit a strength close to that of the (111) and (311) reflections, and this is in contradiction to the experimental data. Similar considerations with respect to the (420) and (331) peaks lead to the same conclusion. *Thus it is established that sodium hydride possesses the same type of structure as* NaCl *and that sodium and hydrogen are scattering neutrons with opposite phase. It also follows that sodium and deuterium are scattering neutrons with common phase.*

EVALUATION OF THE COHERENT SCATTERING CROSS SECTIONS FOR HYDROGEN AND DEUTERIUM

The intensities of the diffraction peaks, illustrated in Figs. 1 and 2, can be used to evaluate coherent scattering cross sections just as has been performed in I. Equation (15) of I has been used along with the diamond calibration data in evaluating the crystal structure factor F_{hkl} for several of the diffraction peaks, and this permits a determination of the individual nuclear scattering amplitudes.

For the case of NaH, values of F_{111} and F_{200} will, in principle, determine values of f_{Na} and f_H since two independent expressions in terms of the nuclear scattering amplitudes are available. In practice, however, it is found that the resultant values of f_{Na} and f_H are quite sensitive to the value of F_{200}, which is in turn dependent upon the intensity of the unmeasurably weak (200) peak in the NaH pattern. Such a procedure yields a hydrogen cross section with a considerable probable error because of the uncertainty in the measurement of the (200) peak intensity. For this reason an alternative procedure has been used which combines values of F_{hkl} for NaH with previously obtained data on the nuclear scattering amplitude for sodium.

A further difficulty in the analysis of the hydrogen scattering data arises because of the lack of information on the magnitude of the thermal oscillations in the NaH crystal, and hence of the uncertainty in the temperature corrections to be applied to the data. No direct experimental data on the characteristic temperature of NaH are available but a comparison of

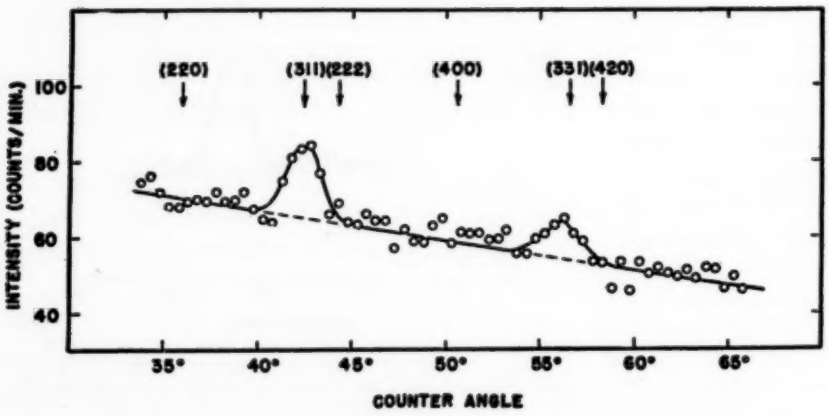

FIG. 2. Powder diffraction pattern for NaH showing some of the higher indexed peaks.

the characteristic temperatures of other alkali compounds suggests the value of 650°K as is shown in Fig. 3. Since the masses of the sodium and hydrogen centers are so different it is not feasible*** to apply a temperature correction factor based upon a single characteristic temperature. Fortunately it has been found possible to obtain a unique value of the hydrogen scattering amplitude from values of F_{111} and F_{311} without having a detailed knowledge of the hydrogen thermal oscillations.

In the NaH diffraction pattern there are three peaks of measurable intensity, namely, (111), (311), and (331). The first two are of comparable intensity and can be measured with an accuracy better than ten percent while the third peak is quite weak and cannot be determined with any significant accuracy. The crystal structure factors for these two peaks can be written as

$$\begin{aligned} F_{111} &= \exp[-\alpha \sin^2\theta_{111}] f_{\mathrm{Na}} \\ &\quad - \exp[-\beta \sin^2\theta_{111}] f_{\mathrm{H}} \\ F_{311} &= \exp[-\alpha \sin^2\theta_{311}] f_{\mathrm{Na}} \\ &\quad - \exp[-\beta \sin^2\theta_{311}] f_{\mathrm{H}}. \end{aligned} \tag{1}$$

In these equations, the algebraic sign of f_{Na} is considered to be positive in keeping with the convention discussed in I, while that of f_{H} is to be considered negative since hydrogen is scattering out of phase with respect to sodium. The exponential coefficients are temperature correction factors necessary to correct for thermal motion of the scattering centers and these are not necessarily the same for the two scattering atoms. Values of the crystal structure factors have been obtained experimentally, giving

$$\begin{aligned} F_{111} &= 0.69_5 \cdot 10^{-12}, \\ \text{and} \qquad & \qquad (2) \\ F_{311} &= 0.59_1 \cdot 10^{-12} \text{ cm}. \end{aligned}$$

When use is made of the previously obtained (see I) value for f_{Na} of $0.345 \cdot 10^{-12}$ cm, one has

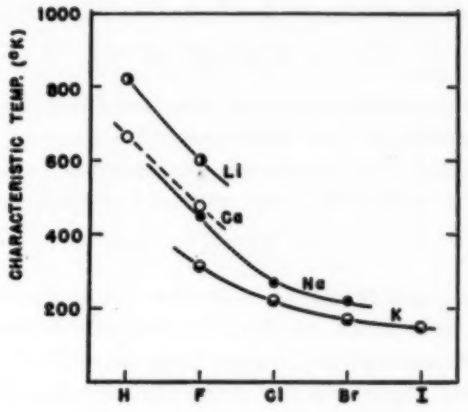

FIG. 3. Values of the Debye characteristic temperature for various alkali metal compounds.

available two equations containing the three unknowns α, β, and f_{H}. Under these conditions a unique solution is, of course, not possible but nevertheless considerable information on the value of f_{H} can be obtained. Table II lists several sets of consistent solutions to Eq. (1) covering a wide range of possible values for the sodium temperature correction factor in the (111) peak. It is seen that the resultant values of f_{H} are very insensitive to the temperature correction factors as long as these are consistent with the data indicated in Eq. (1) and in the range indicated on Table II. Some information on the latter point is obtained from a study of the (111) peak intensity at liquid nitrogen temperature as compared to room temperature. Measurements of the effect of specimen temperature upon the (111) intensity indicate that

$$\frac{F_{111}(78°K)}{F_{111}(300°K)} = 1.00 \pm 0.02 \tag{3}$$

and this implies that the sodium temperature correction factor in Table II lies between 0.96 and 1.00. Thus it is established that the coherent

TABLE II. Various sets of consistent solutions to Eq. (1).

$\exp[-\alpha\sin^2\theta_{111}]$	$\exp[-\beta\sin^2\theta_{111}]$	f_H
0.990	0.890	$0.398 \cdot 10^{-12}$ cm
0.980	0.902	0.396
0.960	0.922	0.395
0.940	0.941	0.395
0.920	0.958	0.395
0.900	0.972	0.396

*** We are indebted to Professor O. Halpern for pointing this out to us in a private communication. In an earlier report [Phys. Rev. 73, 262 (1948)] an erroneous temperature correction factor based upon the conventional Debye-Waller expression with the above characteristic temperature was used, and this led to a value for the coherent scattering cross section for hydrogen which differs somewhat from the present value. The procedure described here requires no advance knowledge of the characteristic temperature or of the thermal oscillations but rather these are determined, in effect, from the consistency of the intensity data.

scattering amplitude for hydrogen is given by

$$f_H = -0.39_6 \pm 0.02 \cdot 10^{-12} \text{ cm} \quad (4)$$

with the suggested error obtained from the uncertainties in the experimental values of F_{111} and F_{311}. This amplitude corresponds to a coherent scattering cross section for hydrogen of

$$\sigma_H^{coh} = 2.0 \pm 0.3 \text{ barns.} \quad (5)$$

Such a scattering cross section for hydrogen is seen to be much smaller than the total scattering cross section for bound protons, namely, 80 barns. The reason for this difference lies in the pronounced spin dependence of scattering in hydrogen, as will be discussed in a later section.

The experimental data for NaD have been treated in the same fashion as those for NaH. The crystal structure factor F_{200} can be written

$$F_{200} = 0.978 f_{Na} + 0.934 f_D, \quad (6)$$

where the temperature correction factors have been obtained from information suggested by the above analysis of the hydrogen data. When use is made of the earlier value of f_{Na} and the experimental data on the intensity of NaD (200) peak it is obvious that the scattering amplitude for deuterium can be obtained. However, because of the considerable impurity in the NaD preparation and the uncertainty in the quantitative composition of the NaD sample, there is a fairly large possible error in the value of F_{200}. This turns out to be $0.87 \cdot 10^{-12}$ cm with an estimated error of possibly $0.07 \cdot 10^{-12}$ cm. Substitution into Eq. (6) leads to

$$f_D = +0.57 \pm 0.08 \cdot 10 \text{ cm}, \quad (7)$$

and hence,

$$\sigma_D^{coh} = 4.1 \pm 1.2 \text{ barns.} \quad (8)$$

Thus deuterium shows a coherent scattering cross section about twice that of hydrogen.

SCATTERING BY THE SPIN STATES OF HYDROGEN AND DEUTERIUM

The coherent scattering amplitudes for hydrogen and deuterium can be used in conjunction with the total scattering amplitudes of the free nuclei to evaluate the scattering amplitudes characteristic of the two spin states of scattering for each of these nuclei. It can be shown that the coherent scattering amplitude for hydrogen f_H can be expressed as

$$f_H = 2(\tfrac{3}{4}a_1 + \tfrac{1}{4}a_0), \quad (9)$$

where a_1 and a_0 are the triplet and singlet scattering amplitudes of a free proton for which the spins of the proton and the incident neutron are, respectively, parallel and antiparallel. The fractional multipliers of a_1 and a_0 are the spin weighting factors characteristic of the two states, and the common factor 2 is the reduced mass factor (see I). Also from Eq. (13) of I, the total scattering cross section of the free proton σ_f can be expressed as

$$\sigma_f = 4\pi(\tfrac{3}{4}a_1^2 + \tfrac{1}{4}a_0^2). \quad (10)$$

Using the coherent hydrogen scattering amplitude of $-0.396 \cdot 10^{-12}$ cm and a free proton scattering cross section[6] of 20 barns results in

$$\begin{aligned} a_1 &= +0.520 \cdot 10^{-12} \text{ cm}, \\ a_0 &= -2.35 \cdot 10^{-12} \text{ cm}. \end{aligned} \quad (11)$$

The value of the singlet scattering amplitude a_0 is determined almost completely by the free proton scattering cross section. On the other hand, the triplet scattering amplitude a_1 is sensitive about equally to errors in both the coherent scattering cross section and the free proton cross section.

These values for the scattering amplitudes of the two spin states are in good agreement with those obtained by Sutton, Hall, and others[7] from the scattering by *o*- and *p*-hydrogen, namely,

$$\begin{aligned} a_1 &= +0.522 \cdot 10^{-12}, \\ a_0 &= -2.34 \cdot 10^{-12}. \end{aligned} \quad (12)$$

It is also possible to evaluate the range of the neutron-proton force acting in the triplet interaction from the values of the scattering amplitudes. Hamermesh and Schwinger[8] have discussed this relationship and using their calculations and the amplitudes of Eq. (11), the triplet range is evaluated as

$$r_0 = 1.6 \pm 0.2 \cdot 10^{-13} \text{ cm}. \quad (13)$$

[6] E. Melkonian, Bull. Am. Phys. Soc. **23**, No. 2, AU7 (1948).
[7] R. B. Sutton, T. Hall, E. E. Anderson, H. S. Bridges, J. W. DeWire, L. S. Lavatelli, E. A. Long, T. Snyder, and R. W. Williams, Phys. Rev. **72**, 1147 (1947).
[8] M. Hamermesh and J. Schwinger, Phys. Rev. **71**, 678-680 (1947).

This is seen to be appreciably smaller than that generally attributed to the proton-proton singlet interaction (namely, $2.8 \cdot 10^{-13}$ cm), and presumably this indicates a real difference between these interactions. The present value is likewise in good agreement with the value $1.5 \cdot 10^{-13}$ cm indicated in the *ortho-para*-hydrogen experiments.[7]

For the case of neutron scattering by deuterium, the coherent scattering cross section of 4.1 barns can be used to establish the presence or absence of spin dependent forces just as has been done for hydrogen above and for sodium in I. Using 3.1 barns as the scattering cross section for free deuterium[9] one calculates the cross section for bound deuterium to be 7.0 barns. This is somewhat larger than the coherent scattering cross section of 4.1 barns. If this difference is real, then the scattering amplitudes characteristic of the two spin states must differ and there must be spin dependent forces present in the neutron-deuteron reaction. However, the present lack of precision in the evaluation of the coherent scattering cross section for deuterium does not permit significant conclusions concerning the magnitude of the spin dependent effects. Additional diffraction data taken on deuterium containing materials whose purity is better established than for the present NaD preparation must be obtained before conclusions can be assured.

DIFFUSE SCATTERING BY NaH

It will be noticed in Figs. 1 and 2 that the diffraction peaks for NaH are superimposed on a high background of diffuse scattering. This is not surprising since the total scattering cross section for hydrogen is unusually high (ranging from 20 to 80 barns depending upon the neutron energy and the conditions of binding) and the large fraction of spin incoherence for hydrogen has caused most of the scattering to appear as a diffuse component. The large spin incoherence is a consequence of the presence of opposite signs in the scattering amplitudes of the two spin states as discussed in the preceding section. Measurements of the transmission cross section (total scattering and capture cross section) have been made on a number of NaH samples and these indicate a total scattering cross section per NaH molecule of 32 barns. This value is, of course, representative for our particular neutron energy of 0.0724 ev only and would be different for other energies. Since the total Bragg scattering cross section for all of the peaks in the diffraction pattern amounts to only 1 or 2 barns, there must be 31 barns of scattering in the diffuse part of the pattern. A direct measurement of the integrated diffuse scattering would provide an interesting comparison with this value, but unfortunately the presence of multiple scattering in the specimen increases the diffuse scattering intensity sufficiently to make the integrated value considerably larger than the transmission value.

The large diffuse scattering obtained with hydrogenous compounds increases the difficulty of obtaining the Bragg scattering features from which structural analyses are derived. This complication does not arise with deuterated compounds however, so that it would appear more feasible to perform crystallographic studies with such compounds. Evidence in favor of this conclusion has already been obtained in the study of the structures of ice and water. In any event, the coherent scattering cross sections for both hydrogen and deuterium are conveniently near the values characteristic of most elements, and hence crystallographic analysis of hydrogen atom positions should be readily possible.

[9] W. W. Havens and L. J. Rainwater, Report No. CP-2293, Manhattan District Plutonium Project.

Radiations from Molybdenum (99) and Technetium (99)

C. E. MANDEVILLE AND M. V. SCHERB*
Bartol Research Foundation of the Franklin Institute, Swarthmore, Pennsylvania
(Received January 2, 1948)

The 67-hour activity was induced in Mo_2O_3 irradiated by slow neutrons in the Clinton pile. Mo^{99} emits two beta-ray spectra, one of low energy, having an end point at 0.057 g/cm² in aluminum, the other having a maximum energy of 1.03 Mev. The beta-rays of the low energy group are coupled with gamma-radiation, whereas those of the spectrum ending at 1.03 Mev are not. The gamma-rays of Mo^{99} have a maximum energy of 0.71 Mev as measured by coincidence absorption, and a small gamma-gamma coincidence rate, 0.085×10^{-3} coincidence per gamma-ray, was detected in Mo^{99}.

The electrons of the highly converted gamma-ray of the 6-hour metastable state of Tc^{99}, separated from Mo^{99}, are non-coincident with gamma-radiation. No gamma-gamma coincidences were observed in the technetium fraction. The conversion electrons have a range of 0.022 g/cm² in aluminum.

1. INTRODUCTION

IRRADIATION of molybdenum by slow neutrons gives rise to a 67-hour activity which has been assigned to molybdenum (99).[1] It has been shown[1,2] that part of the molybdenum disintegrations lead to a 6-hour metastable state of an isotope of element 43, $_{43}Tc^{99}$. A large percentage of the disintegrations go directly to the ground state of Tc^{99}, having a half-period of 4×10^6 years.[2]

For the experiments to be discussed in this paper, Mo^{99} was produced when Mo_2O_3 was irradiated by slow neutrons in the Clinton pile. Chemical separations were performed for the removal of calcium, columbium, iron, and phosphorous as possible impurities. Beta-ray energies were measured by noting the absorption in thin aluminum foils placed before a single G-M counter. Gamma-ray energies were measured by coincidence absorption of the secondary electrons. Two G-M counters in coincidence were employed for the determination of the beta-gamma and gamma-gamma coincidence rates of Mo^{99} and Tc^{99}. The accidental coincidences were calculated by the expression

$$A = N_1N_2(K\tau),$$

where $K\tau$ was 1.3 microseconds. A more detailed description of the general experimental procedure has been previously given.[3]

Mo^{99}

The hard beta-rays of Mo^{99} have been reported to have energies of 1.5 Mev[1] and 1.2 Mev.[2] A number of gamma-ray energies have been reported. Schwarz and Pool[4] have obtained evidence for the presence of gamma-rays having energies of 0.770, 0.815, and 0.840 Mev from an analysis of photoelectric lines in a semicircular focusing spectrometer. Quantum energies of 0.24 and 0.75 Mev were reported by Miller and Curtiss[5] who used a thin magnetic lens spectrometer.

The absorption curve of the primary beta-rays of Mo^{99} is shown in Fig. 1. The absorption limit is seen to occur at 0.40 g/cm², 1.03 Mev as calculated by Feather's equation.[6] Coincidence absorption of the secondary electrons of the gamma-rays of Mo^{99} yielded a maximum quantum energy of 0.71 Mev as calculated from the end point of Fig. 2. The above-quoted values of beta-ray and gamma-ray energies were present in Mo^{99} whether in equilibrium with its daughter isotope of technetium or chemically separated from it.[7]

A thin source of Mo^{99} in equilibrium with the 6-hour metastable state of Tc^{99} was placed between two G-M counters in coincidence, and the beta-gamma coincidence rate was observed

* Assisted by the Office of Naval Research.
[1] G. T. Seaborg and E. Segré, Phys. Rev. **55**, 808 (1939).
[2] Plutonium Project Report, "Nuclei formed in fission," Rev. Mod. Phys. **18**, 513 (1946).
[3] C. E. Mandeville and M. V. Scherb, Phys. Rev. **73**, 141 (1948).
[4] W. M. Schwarz and M. L. Pool, Phys. Rev. **71**, 122 (1947).
[5] L. C. Miller and L. F. Curtiss, Phys. Rev. **70**, 983 (1946).
[6] N. Feather, Proc. Camb. Phil. Soc. **34**, 599 (1938).
[7] C. Perrier and E. Segré, J. Chem. Phys. **5**, 712 (1937); *ibid.* **7**, 155 (1939).

as a function of the thickness of aluminum absorber inserted before the beta-ray counter. These data are given in Fig. 3(a) where the genuine beta-gamma coincidence rate is seen to decrease from 0.07×10^{-3} coincidence per beta-ray at zero absorber thickness to zero at an absorber thickness of 0.057 g/cm². This would indicate the presence of a group of beta-rays of low energy (about 240 kev) which is coupled with gamma-rays. It follows also that the hard beta-rays, reported in this paper as having an end point at 1.03 Mev, are non-coincident with gamma-radiation. The beta-transition of high energy then leads to the ground state of one or both of the technetium isomers. The beta-gamma coincidence rate for Mo^{99} chemically separated from its daughter isotopes of Tc^{99} is given in Fig. 3(b), where it is seen to be essentially the same as prior to separation.

The gamma-gamma coincidence rate for the molybdenum fraction was found to be 0.085×10^{-3} coincidence per gamma-ray, suggesting cascade emission of gamma-rays following the beta-ray group of low energy.

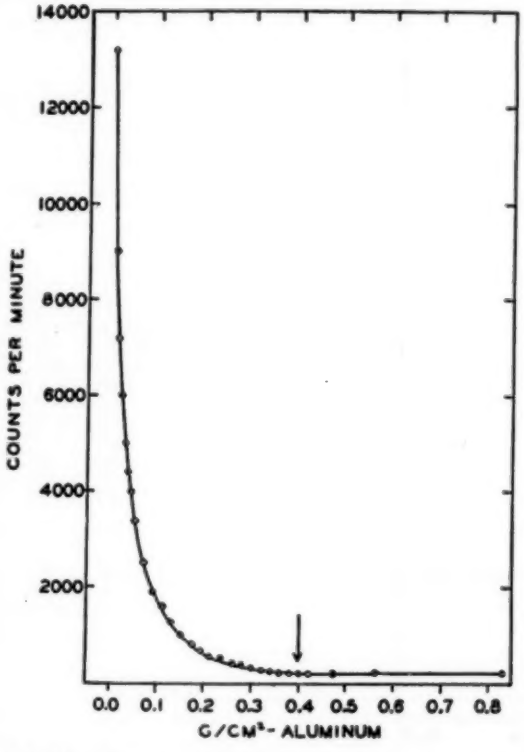

FIG. 1. Absorption in aluminum of the beta-rays of Mo^{99}.

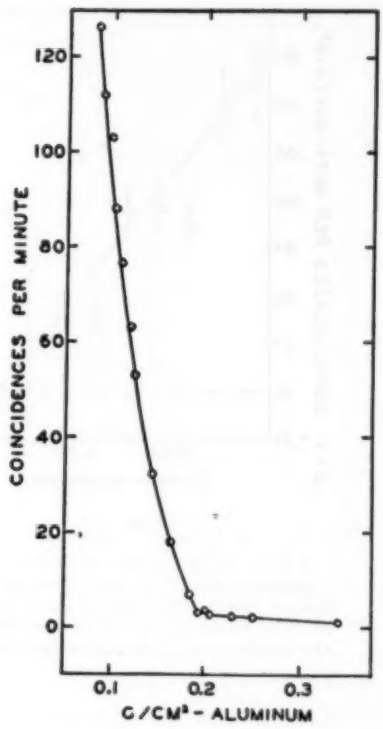

FIG. 2. Coincidence absorption of the secondary electrons of the gamma-rays of Mo^{99}. The quantum energy calculated from the end point is 0.71 Mev.

Tc^{99}

As has already been pointed out, Mo^{99} has been shown to be in equilibrium with a 6-hour daughter element,[1,2] an isomer of Tc^{99}. The 6-hour activity decays with the emission of gamma-rays and conversion electrons.[1,2] The energy of the converted gamma-ray has been measured to be 0.129 Mev.[8] Some evidence has also been obtained for the presence of gamma-rays of energy 0.18 Mev which were thought to be in cascade with the gamma-rays of the 6-hour isomeric transition.[1] No coincidences were found in the present experiment between the conversion electrons and the gamma-radiation nor were gamma-gamma coincidences observed. These results would indicate that the 6-hour Tc^{99} de-excites with emission of a single partially converted gamma-ray of energy 0.129 Mev. It should be remarked that several hundred coincidences were recorded during each of a number of different runs in the case of both beta-gamma

[8] D. C. Kalbfell, Phys. Rev. **54**, 543 (1938).

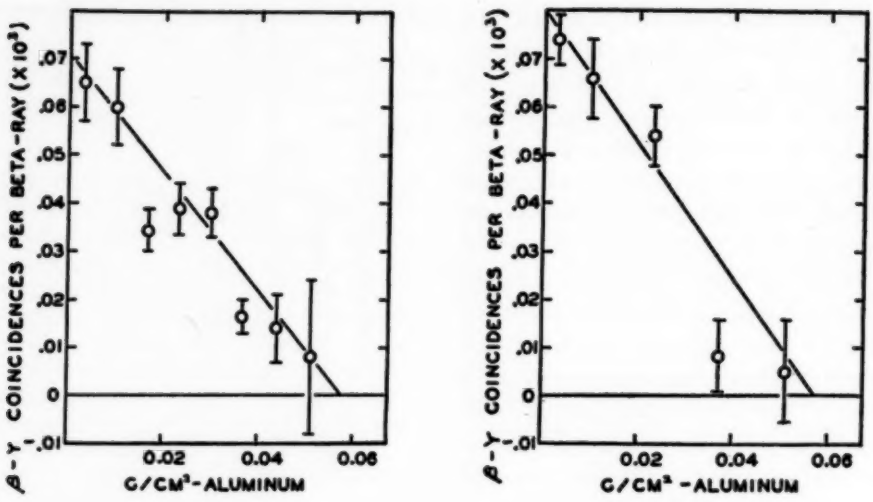

FIG. 3. Beta-gamma coincidence rate of Mo^{99} as a function of the surface density of aluminum absorber placed before the beta-ray counter. The data of 3(a) were taken before the technetium isomers were separated from their molybdenum parent, those of 3(b) immediately after the chemical separation. From the curves, it is clear that the presence of technetium had little effect on the coincidence rate.

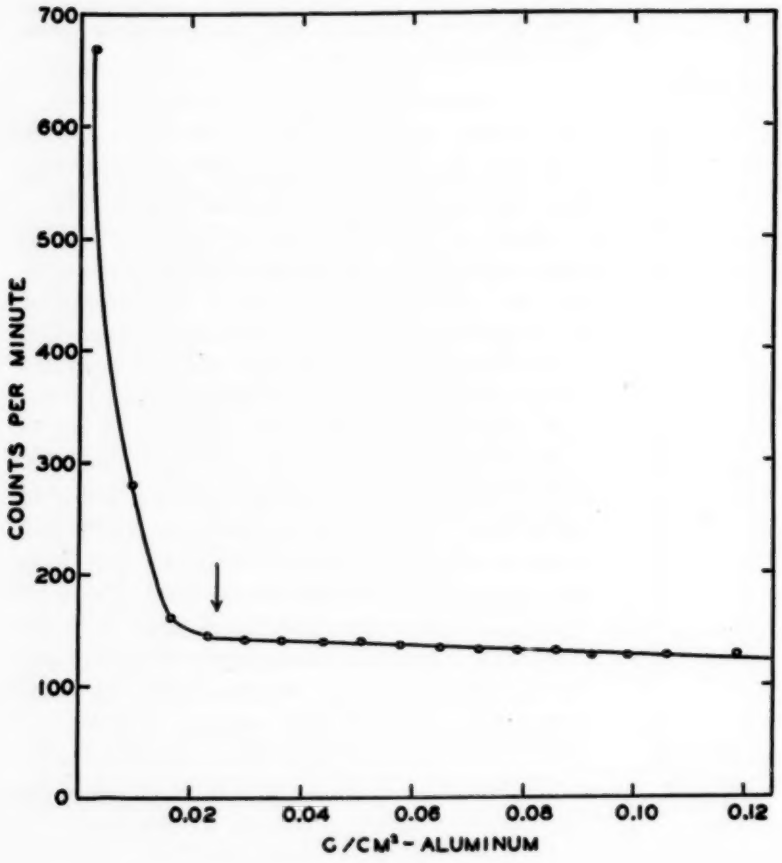

FIG. 4. Absorption in aluminum of the electrons of the converted gamma-ray of the 6-hour isomer of Tc^{99}.

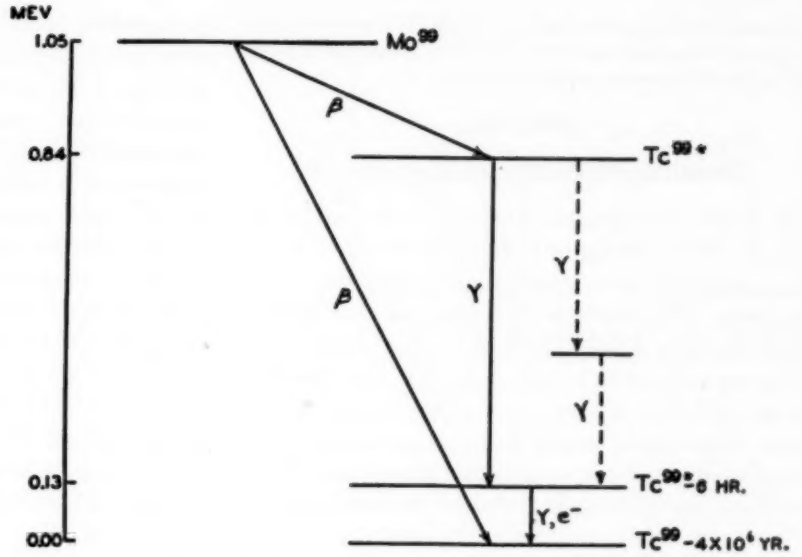

FIG. 5. Disintegration scheme for Mo^{99} and Tc^{99}. Owing to the uncertainties of absorption methods, it was not possible to construct a level diagram using *precisely* the same energy values as are given in the text.

and gamma-gamma coincidences. No† coincidences in excess of the accidental rates were observed. Coincidence experiments on elements having known disintegration schemes have indicated a net efficiency of about 0.13×10^{-3} for a quantum energy of 0.18 Mev. An efficiency of this magnitude would have given as many genuine coincidences as accidentals. The technetium fraction was found to emit no gamma-rays of sufficient energy to measure with the coincidence absorption arrangement. The range of the conversion electrons was measured in aluminum and was found to be 0.022 g/cm². These data are given in Fig. 4.

2. A DISINTEGRATION SCHEME FOR Mo^{99} AND Tc^{99}

The experimental data of this paper are summarized in the level diagram of Fig. 5. The hard beta-rays are shown to lead to the ground state of the long lived isomer of Tc^{99}, and the soft beta-rays, coupled with gamma-radiation, are assumed to lead to the 6-hour isomer. This seems reasonable, since it has been shown that only about ten percent of the molybdenum disintegrations go to the 6-hour metastable state.[2] These experiments would not reveal whether some of the hard beta-rays also go to the 6-hour level. A Fermi plot of spectrometric data might disclose the presence of two high energy spectra having end points differing by 0.129 Mev. It should be pointed out that since the measurements of this paper are subject to all of the inaccuracies of the absorption method, the hard beta-rays may actually have enough energy to permit cascade emission of the two gamma rays reported by Miller and Curtiss.[5]

ACKNOWLEDGMENTS

The writers wish to express their appreciation to Professor W. B. Keighton of Swarthmore College for having carried out the chemical separations.

Note added in proof: A second quantity of Mo_2O_3 has been irradiated by neutrons in the pile. The coincidence measurements of this paper have been repeated with coincidence resolving times of one microsecond and 0.10 microsecond with essentially the same results as reported above. In investigating the coincidence rates of the technetium fraction with the shorter resolving time, the single counting rates in either counter were adjusted so that a genuine (conversion electron)-gamma coincidence rate of 0.02×10^{-3} coincidence per conversion electron would have given four times as many genuine coincidences as accidental coincidences. A gamma-gamma coincidence rate of similar magnitude would have given about twice as many genuine coincidences as accidentals. In neither case were any genuine coincidences observed.

These new measurements would confirm the view already expressed in the text of the paper that if the 0.18 Mev

† The actual values of the coincidence rates were $(0.02\pm0.015)\times10^{-3}$ (conversion electron)-gamma-coincidence per conversion electron and $(-0.05\pm0.05)\times10^{-3}$ gamma-gamma coincidence per gamma-ray. It is possible that a small (conversion electron)-(x-ray) coincidence rate was detected, as the first coincidence rate above may indicate. X-rays would be emitted on readjustment of the extra-nuclear structure following internal conversion. Very few (conversion electron)-(x-ray) coincidences would be counted owing to the low detection efficiency of the gamma-ray counter for x-rays.

gamma-ray reported by Seaborg and Segrè is present at all, it is not in cascade with the 0.129 Mev converted gamma-ray of the 6-hour metastable state in Tc^{99}.

APPENDIX

Chemical Purification of Molybdenum

To about two grams of Mo_2O_3 were added 40 mg of Al_2O_3, 20 mg of CaO, and 20 mg of Ta_2O_5 as carriers for iron, calcium, and columbium impurities. The mixture was fused with Na_2CO_3, and the melt was leached with cold water. After filtering out calcium carbonate, 20 mg of Na_3PO_4 were added as a carrier for phosphorous, which was then precipitated from ammoniacal solution as ammonium magnesium phosphate. Most of the aluminum and tantalum should have accompanied this precipitate together with any iron and columbium impurities which might be present. After filtration, the filtrate was acidified with HCl, and most of the molybdenum was precipitated with H_2S as MoS_2. The precipitate was washed with dilute H_2SO_4 (1:99); washed with alcohol, and ignited to MoO_3.

For the separation of Mo from Tc, a second sample of Mo_2O_3 was purified as described above. The filtrate from the magnesium ammonium phosphate precipitation was neutralized and buffered with sodium acetate. Molybdenum was precipitated by 8-hydroxyquinoline. From the filtrate, about 0.5 N in HCl, technetium was precipitated as a sulfide. For details of the molybdenum-technetium separation, see reference 7.

PHYSICAL REVIEW VOLUME 73, NUMBER 8 APRIL 15, 1948

The Penetration of Gamma-Radiation through Thick Layers

I. Plane Geometry, Klein-Nishina Scattering

J. O. HIRSCHFELDER,[1] J. L. MAGEE,[2] AND M. H. HULL[3]
The Los Alamos Scientific Laboratory, Los Alamos, New Mexico

(Received December 15, 1947)

A rough method is developed for estimating the intensity of gamma-rays which have passed through thick targets. Only Klein-Nishina scattering is considered. The treatment is exact both for those gamma-rays which are unscattered and those which are scattered once. The accuracy of the results for rays which are multiple scattered depends upon the fact that most of the scattering takes place in the forward direction with only small angles of deviation. Numerical calculations are made for energies of 2, 6, and $10m_0c^2$ and all thicknesses of target. If A is the intensity of the initial beam, and I is the intensity after passing through a target of D mean-free-paths measured in terms of the initial unscattered gamma ray, it is found that:

initial energy $=2m_0c^2$,
$$I/A=(1+0.487D+0.030D^2)e^{-D},$$
initial energy $=6m_0c^2$,
$$I/A=(1+0.400D+0.0080D^2)e^{-D},$$
initial energy $=10m_0c^2$,
$$I/A=(1+0.33D+0.0040D^2)e^{-D}.$$

The contributions to the intensity are given for the gamma-rays which have been scattered a various number of times. Extensive tables are given which are generally useful for any problems in which only Klein-Nishina scattering is assumed.

I. INTRODUCTION[4]

THE general problem of multiple scattering is exceedingly difficult. However, in some special cases it is possible to develop a rough theory which gives an accurate description of the gamma-radiation that has passed through a thick target. The method presented here is applicable to a wide homogeneous monochromatic beam of gamma-rays impinging at right angles on a flat slab of material. In subsequent papers the photoelectric effect and pair production will be considered, but only Klein-Nishina scattering is considered here. This limits the energy range in which the numerical calculations are valid to a comparatively small range which

[1] Present address: Department of Chemistry, University of Wisconsin, Madison, Wisconsin.
[2] Present address: Argonne National Laboratory, Chicago, Illinois.
[3] Present address: Department of Physics, Yale University, New Haven, Connecticut.
[4] This paper is a thorough revision of and substitution for LADC-70. The method and numerical results have been changed considerably.

fortunately is important for the gamma-rays emitted by many naturally occurring and some artificially produced radioactive substances. The treatment presented here is exact for both the unscattered and the first scattered beams. Because most of the scattered radiation makes only a small angle with the forward direction, the averaging and estimating of the angles does not greatly affect the intensity and distribution of the second, third, etc., scattered components. Then, too, the contribution to the total intensity of the multiple scattered radiation is usually quite small. If the initial beam were not perpendicular to the target, our method of averaging the angles would not be permissible. And if the multiple scattered beam were hundreds of times more intense than the unscattered beam, as in some problems where pair production is included, our approach would need modification.

There are three primary processes by which gamma-radiation is absorbed:

(*a*) *Photoelectric effect.* The photoelectric effect depends primarily on resonance between the energy of radiation and the energy required to remove the K-electrons from the atom. In this process, the gamma-ray photon is completely absorbed. At energies large compared to the atomic energy terms, the cross section for this process becomes negligible compared to the Compton scattering. This occurs for Al at around 0.1 Mev and for Pb at 1.0 Mev.

(*b*) *Compton scattering.* In the Compton effect, the gamma-ray photon collides with an electron. Its energy is reduced from αm_0c^2 to $\alpha' m_0c^2$, and its direction is changed through an angle ϕ. From the conservation of momentum and energy:

$$\alpha/\alpha' = 1+\alpha(1-\cos\phi). \tag{1}$$

The cross section per electron, σ, for this process, including the relativistic corrections, is given by the Klein-Nishina formula:

$$\sigma = 2\pi r_0^2\left[\left(\frac{1+\alpha}{\alpha^2}\right)\left(\frac{2(1+\alpha)}{1+2\alpha}-\frac{1}{\alpha}\ln(1+2\alpha)\right)+\frac{1}{2\alpha}\ln(1+2\alpha)-\frac{1+3\alpha}{(1+2\alpha)^2}\right]. \tag{2}$$

Here r_0 is the classical electron radius, $r_0 = e^2/m_0c^2$. The value of σ decreases with increasing energy. The value of σ/r_0^2 as a function of α are given in Table I.

TABLE I. Cross section as function of energy.

α	σ/r_0^2	α	σ/r_0^2	α	σ/r_0^2
0.15	6.570	1.2	3.3367	3.2	2.0622
0.2	6.1739	1.3	3.2206	3.4	1.9946
0.25	5.839	1.4	3.1149	3.6	1.9322
0.30	5.5516	1.5	3.0181	3.8	1.8743
0.35	5.3021	1.6	2.9290	4.0	1.8204
0.40	5.083	1.7	2.8465	4.2	1.7700
0.45	4.8887	1.8	2.7699	4.4	1.7229
0.50	4.7148	1.9	2.6984	4.6	1.6786
0.55	4.5579	2.0	2.6315	4.8	1.6370
0.60	4.4155	2.1	2.5688	5.0	1.5977
0.65	4.2855	2.2	2.5097	5.5	1.5084
0.70	4.1661	2.3	2.4539	6.0	1.4300
0.75	4.0558	2.4	2.4012	6.5	1.3605
0.80	3.9537	2.5	2.3513	7.0	1.2984
0.85	3.8586	2.6	2.3039	7.5	1.2424
0.90	3.7698	2.7	2.2588	8.0	1.1917
0.95	3.6866	2.8	2.2158	8.5	1.1114
1.00	3.6085	2.9	2.1748	9.0	1.1032
1.1	3.4652	3.0	2.1356	9.5	1.0643
				10.0	1.0284

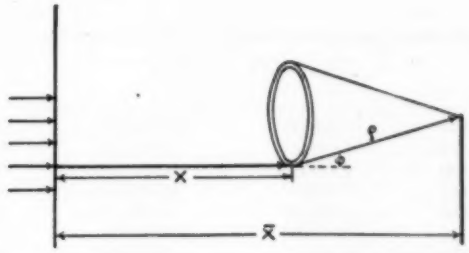

FIG. 1. Geometry of gamma-ray which is scattered through an angle ϕ after passing through the target to a distance x. Here X is the total thickness of the target. (The symbol X with a bar in the bottom of the figure should be capitalized.)

(*c*) *Pair production.* No pair production can occur if the energy of the gamma-ray photon is less than the rest energy of an electron pair, $2m_0c^2$. The cross section for this process varies as the square of the atomic number. For Pb, this cross section becomes equal to that for Compton scattering at 5 Mev; for Al, at about 15 Mev.

The total cross section for the primary processes is given by the sum:

$$\sigma_{\text{total}} = \sigma_{\text{photoelectric}} + \sigma_{\text{Compton}} + \sigma_{\text{pair}}.$$

It goes through a minimum value at energy α_m. This occurs at $2\frac{1}{2}$ Mev for Pb and 15 Mev for Al. The nature of the transmitted radiation depends on whether the energy of the primary beam is less or greater than α_m. For convenience, we

TABLE II.

(A) $\alpha=0.5(m_0c^2)$

μ	$2f(\mu)/r_0^2$	α'	σ_1/r_0^2
1.000	2.0000	0.5000000	4.7148
.995	1.9752	.4987531	4.7187
.990	1.9506	.4975124	4.7232
.985	1.9266	.4962779	4.7270
.980	1.9028	.4950495	4.7311
.975	1.8794	.4938272	4.7354
.970	1.8563	.4926108	4.7393
.960	1.8112	.4901961	4.7475
.950	1.7672	.4878049	4.7556
.940	1.7246	.4854369	4.7637
.930	1.6831	.4830918	4.7717
.920	1.6427	.4807692	4.7795
.910	1.6036	.4784689	4.7874
.900	1.5657	.4761905	4.7954
.880	1.4927	.4716981	4.8108
.860	1.4238	.4672897	4.8263
.840	1.3587	.4629630	4.8415
.820	1.2971	.4587156	4.8570
.800	1.2390	.4545455	4.8722
.780	1.1840	.4504505	4.8872
.760	1.1321	.4464286	4.902
.740	1.0830	.4424779	4.916
.720	1.0365	.4385965	4.931
.700	.99257	.4347826	4.945
.650	.89295	.4255319	4.981
.600	.80631	.4166667	5.016
.550	.73100	.4081633	5.050
.500	.66560	.4000000	5.083
.400	.55950	.3846154	5.148
.300	.47988	.3703704	5.210
.200	.42066	.3571429	5.269
.100	.37712	.3448276	5.326
.000	.34569	.3333333	5.381
−.100	.32364	.3225806	5.435
−.200	.30884	.3125000	5.486
−.300	.29966	.3030303	5.535
−.400	.29477	.2941176	5.583
−.500	.29320	.2857143	5.629
−.600	.29417	.2777778	5.673
−.700	.29700	.2702703	5.717
−.800	.30125	.2631579	5.757
−.900	.30652	.2564103	5.800
−1.000	.31250	.2500000	5.839

(B) $\alpha=1(m_0c^2)$

μ	$2f(\mu)/r_0^2$	α'	σ_1/r_0^2
1.000	2.0000	1.000000	3.6085
.995	1.9604	.9950249	3.6160
.990	1.9220	.9900990	3.6236
.985	1.8843	.9852217	3.6311
.980	1.8477	.9803922	3.6386
.975	1.8119	.9756098	3.6460
.970	1.7771	.9708738	3.6534
.960	1.7096	.9615385	3.6681
.950	1.6456	.9523810	3.6828
.940	1.5844	.9433962	3.6973
.930	1.5261	.9345794	3.7117
.920	1.4704	.9259259	3.7260
.910	1.4174	.9174312	3.7402
.900	1.3667	.9090909	3.7543
.880	1.2722	.8928571	3.7822
.860	1.1858	.8771930	3.8096
.840	1.1069	.8620690	3.8366
.820	1.0346	.8474576	3.8633
.800	.96834	.8333333	3.8896
.780	.90764	.8196721	3.9155
.760	.85183	.8064516	3.9410
.740	.80049	.7936508	3.9662
.720	.75324	.7812500	3.9911
.700	.70970	.7692308	4.0157
.650	.61502	.7407407	4.0756
.600	.53728	.7142857	4.1337
.550	.47307	.6896552	4.1900
.500	.41976	.6666667	4.2446
.400	.33813	.6250000	4.3490
.300	.28052	.5882353	4.4478
.200	.23930	.5555556	4.5414
.100	.20940	.5263158	4.6303
.000	.18750	.5000000	4.7148
−.100	.17128	.4761905	4.7954
−.200	.15914	.4545455	4.8722
−.300	.14998	.4347826	4.945
−.400	.14299	.4166667	5.016
−.500	.13760	.4000000	5.083
−.600	.13340	.3846154	5.148
−.700	.13008	.3703704	5.210
−.800	.12742	.3571429	5.269
−.900	.12525	.3448276	5.326
−1.000	.12346	.3333333	5.381

(C) $\alpha=2(m_0c^2)$

μ	$2f(\mu)/r_0^2$	α'	σ_1/r_0^2
1.000	2.0000	2.000000	2.6315
.995	1.9316	1.980198	2.6444
.990	1.8663	1.960784	2.6572
.985	1.8039	1.941748	2.6699
.980	1.7441	1.923077	2.6826
.975	1.6871	1.904762	2.6951
.970	1.6325	1.886792	2.7076
.960	1.5301	1.851852	2.7322
.950	1.4362	1.818182	2.7565
.940	1.3499	1.785714	2.7805
.930	1.2704	1.754386	2.8041
.920	1.1971	1.724138	2.8275
.910	1.1294	1.694915	2.8505
.900	1.0667	1.666667	2.8733
.880	.95505	1.612903	2.9180
.860	.85872	1.562500	2.9616
.840	.77530	1.515152	3.0042
.820	.70272	1.470588	3.0458
.800	.63932	1.428571	3.0864
.780	.58366	1.388889	3.1262
.760	.53467	1.351351	3.1652
.740	.49134	1.315789	3.2033
.720	.45290	1.282051	3.2407
.700	.41870	1.250000	3.2773
.650	.34820	1.176471	3.3658
.600	.29417	1.111111	3.4502
.550	.25205	1.052632	3.5310
.500	.21875	1.000000	3.6085
.400	.17041	.9090909	3.7543
.300	.13792	.8333333	3.8896
.200	.11519	.7692308	4.0157
.100	.098720	.7142857	4.1337
.000	.086419	.6666667	4.2446
−.100	.076981	.6250000	4.3490
−.200	.069563	.5882353	4.4478
−.300	.063610	.5555556	4.5414
−.400	.058740	.5263158	4.6303
−.500	.054688	.5000000	4.7148
−.600	.051265	.4761905	4.7954
−.700	.048334	.4545455	4.8722
−.800	.045794	.4347826	4.945
−.900	.043569	.4166667	5.016
−1.000	.041600	.4000000	5.083

TABLE II.—*Continued.*

	(D) $\alpha=6(m_0c^2)$			(E) $\alpha=10(m_0c^2)$			
μ	$2f(\mu)/r_0^2$	α'	σ_1/r_0^2	μ	$2f(\mu)/r_0^2$	α'	σ_1/r_0^2
1.000	2.0000	6.000000	1.4300	1.000	2.0000	10.000000	1.0284
.995	1.8220	5.825243	1.4563	.995	1.7211	9.523810	1.0626
.990	1.6654	5.660377	1.4822	.990	1.4945	9.090909	1.0959
.985	1.5271	5.504587	1.5077	.985	1.3083	8.695652	1.1285
.980	1.4046	5.357143	1.5327	.980	1.1538	8.333333	1.1604
.975	1.2954	5.217391	1.5574	.975	1.0243	8.000000	1.1917
.970	1.1981	5.084746	1.5817	.970	.91493	7.692308	1.2223
.960	1.0323	4.838710	1.6292	.960	.74195	7.142857	1.2818
.950	.89745	4.615385	1.6753	.950	.61310	6.666667	1.3391
.940	.78668	4.411765	1.7202	.940	.51479	6.250000	1.3943
.930	.69469	4.225352	1.7639	.930	.43825	5.882353	1.4476
.920	.61759	4.054054	1.8064	.920	.37757	5.555556	1.4992
.910	.55239	3.896104	1.8479	.910	.32868	5.263158	1.5492
.900	.49683	3.750000	1.8884	.900	.28875	5.000000	1.5977
.880	.40794	3.488372	1.9664	.880	.22811	4.545455	1.6904
.860	.34081	3.260870	2.0410	.860	.18492	4.166667	1.7782
.840	.28897	3.061224	2.1124	.840	.15306	3.846154	1.8615
.820	.24816	2.884615	2.1810	.820	.12889	3.571429	1.9408
.800	.21549	2.727273	2.2468	.800	.11012	3.333333	2.0165
.780	.18895	2.586207	2.3103	.780	.095242	3.125000	2.0890
.760	.16710	2.459016	2.3714	.760	.083241	2.941176	2.1584
.740	.14891	2.343750	2.4305	.740	.073418	2.777778	2.2252
.720	.13359	2.238806	2.4877	.720	.065272	2.631579	2.2894
.700	.12059	2.142857	2.5430	.700	.058438	2.500000	2.3513
.650	.095502	1.935484	2.6742	.650	.045484	2.222222	2.4970
.600	.077705	1.764706	2.7963	.600	.036480	2.000000	2.6315
.550	.064612	1.621622	2.9106	.550	.029957	1.818182	2.7565
.500	.054688	1.500000	3.0181	.500	.025077	1.666667	2.8733
.400	.040863	1.304348	3.2158	.400	.018376	1.428571	3.0864
.300	.031878	1.53846	3.3944	.300	.014092	1.250000	3.2773
.200	.025690	1.034483	3.5572	.200	.011181	1.111111	3.4502
.100	.021234	0.9375000	3.7069	.100	.0091100	1.000000	3.6085
.000	.017909	0.8571429	3.8455	.000	.0075815	.9090909	3.7543
−.100	.015357	0.7894737	3.9745	−.100	.0064196	.8333333	3.8895
−.200	.013352	0.7317073	4.0952	−.200	.0055152	.7692308	4.0157
−.300	.011745	0.6818182	4.2083	−.300	.0047963	.7142857	4.1337
−.400	.010434	0.6382979	4.3148	−.400	.0042154	.6666667	4.2446
−.500	.0093500	0.6000000	4.4155	−.500	.0037385	.6250000	4.3490
−.600	.0084416	0.5660377	4.5107	−.600	.0033419	.5882353	4.4478
−.700	.0076724	0.5357143	4.6012	−.700	.0030086	.5555556	4.5415
−.800	.0070146	0.5084746	4.6871	−.800	.0027253	.5263158	4.6303
−.900	.0064466	0.4838710	4.7689	−.900	.0024825	.5000000	4.7148
−1.000	.0059522	0.4615385	4.8468	−1.000	.0022728	.4761905	4.7954

shall use m_0c^2 as the unit of energy. If the primary energy, α, is less than α_m, the primary beam is more penetrating than the secondary radiation. However, if α is greater than α_m, a large fraction of the secondary radiation is more penetrating than the primary beam. After such radiation has passed through a sufficiently thick target, its energy will be degraded so that α_m becomes the maximum value of its energy spectrum. At energies of the order of 100 Mev, the problem is made considerably more complicated by the bremsstrahlung radiated from the recoil electrons.

In the remainder of this report, unless otherwise specified, only Compton scattering is considered. This limits the validity of our results to that energy range where α is sufficiently large that the photoelectric effect can be neglected and yet sufficiently small so that the cross section for pair production has not yet become appreciable. For light elements this covers a rather large range (for Al, from 0.1 to more than 10 Mev). For heavier elements the range is somewhat more restricted.

The problems of multiple scattering are still complicated for Compton scattering alone. The energy flux at any point can be broken up into a sum of components according to the number of times the photon has been scattered. If the primary beam is monochromatic and unidirectional, the first scattered beam has an anergy which is a unique function of the azimuthal

TABLE III. I_1/A.

$\alpha \backslash D$	1	2	5	10	20
0.5	0.1420	0.0878	0.00791	7.75×10^{-5}	4.82×10^{-9}
1.0	.1416	.0884	.00808	8.00×10^{-5}	5.01×10^{-9}
2.0	.1330	.0836	.00771	7.67×10^{-5}	4.83×10^{-9}
6.0	.1089	.0681	.00624	6.17×10^{-5}	3.86×10^{-9}
10.0	.0969	.0603	.00547	5.38×10^{-5}	3.35×10^{-9}

TABLE IV. $\bar{\mu}$.

$\alpha \backslash D$	1	2	5	10	20	μ_{max}
0.5	0.419	0.512	0.625	0.697	0.754	0.8050
1.0	.519	.598	.694	.754	.802	.8675
2.0	.636	.694	.767	.815	.852	.9183
6.0	.803	.834	.875	.902	.922	.9675
10.0	.861	.883	.913	.932	.946	.9797

angle. For the second and higher scattered beams, the energy spectrum is a function of both the distance and the azimuthal angle. In this report, the energy flux of the first scattered beam of a monochromatic plane wave is calculated rigorously for a number of energies and distances. At energies greater than $m_0c^2/2$, most of the photons are scattered in the forward direction with only a small angle of deflection. If all of the photons were scattered through the same angle, $\bar{\phi}$, the energy flux of the first scattered beam could be expressed in terms of a simple equation, Eq. (12). The results of the rigorous calculations can be expressed in terms of appropriate values of $\bar{\phi}$ to be used in this equation. These values of $\bar{\phi}$ are only slowly varying functions of distance as well as energy.

A rough theory is developed for the penetration of gamma-radiation through a thick target. In this theory, the values of $\bar{\phi}$ determined from calculations of single scattering are used to determine the intensity of the multiple scattered beams. As long as the values of $\bar{\phi}$ are small, this theory should give reasonably good results.

The same treatment and methods which we have applied for Compton scattering can be used when either the photoelectric effect or pair production are appreciable. In these cases, the total cross sections replace the Compton cross sections. The angular dependence of the scattered radiation remains unchanged.

II. FIRST SCATTERED BEAM, PLANE GEOMETRY

Consider a plane-parallel beam of monochromatic gamma-rays which has the intensity A when it enters the scattering medium at $X=0$. In Fig. 1, the trajectory of a photon is shown which travels a distance x before it is scattered; the angle of deflection is ϕ; and it travels the additional distance ρ without being scattered again. We wish to calculate the energy flux due to all such photons which penetrate the target to a distance X after having been scattered once.

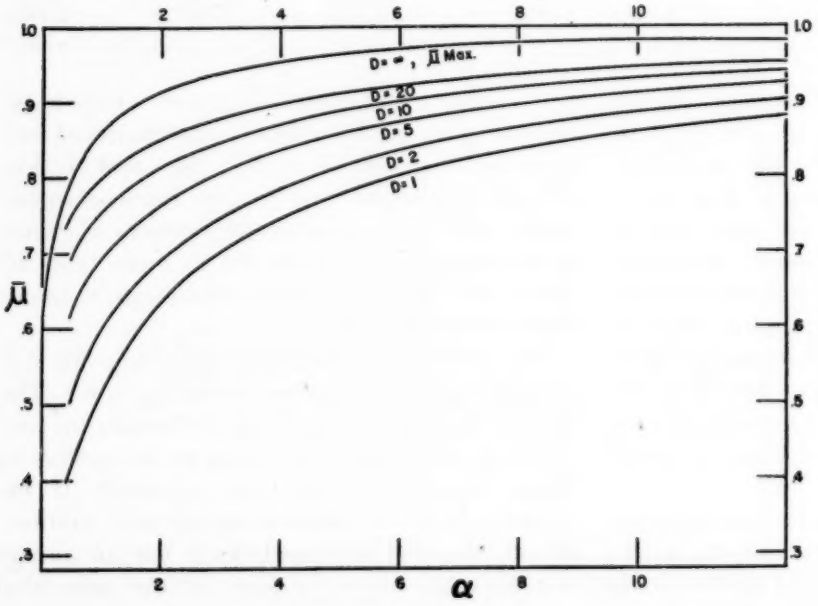

FIG. 2. The variation of $\bar{\mu}$, the cosine of the effective angle of scattering, as a function of the gamma-ray energy, αm_0c^2, for different thicknesses of target, D, measured in mean free paths for the initial gamma-rays.

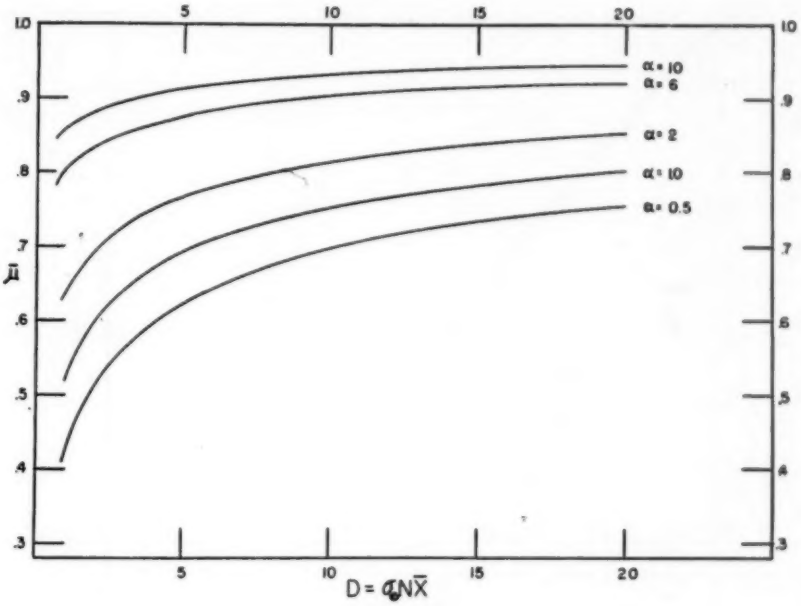

FIG. 3. The variation of $\bar{\mu}$ of the effective angle of scattering, as a function of the target thickness, D, measured in mean free paths of the initial gamma-rays. The different curves are for different values of the gamma-ray energy, αm_0c^2.

The intensity of the unscattered beam at the point, x, is

$$I_0 = A\exp(-\sigma_0 Nx) = A\exp(-\sigma_0 N(X-\rho\mu)). \quad (3)$$

Here σ_0 is the cross section for the initial beam as given in Eq. (2) and N is the density of the electrons in the target.

In order to calculate the intensity of the first scattered beam, it is necessary to introduce the function $f(\mu)$, where μ is the cosine of the angle of scattering, ϕ. Here $f(\mu)$ gives the intensity of the energy scattered in the direction corresponding to μ per unit solid angle, per unit initial intensity, and per electron. According to the Klein-Nishina formulation:

$$f(\mu) = \frac{r_0^2}{2}\left[\frac{1+\mu^2}{(1+\alpha\{1-\mu\})^3} + \frac{\alpha^2(1-\mu)^2}{(1+\alpha\{1-\mu\})^4}\right]. \quad (4)$$

The contribution to the x component of the flux due to the electrons scattered in the volume element dv is then:

$$dI_1 = I_0(Ndv)[\mu f(\mu)/\rho^2]\exp(-\sigma_1 N\rho). \quad (5)$$

Here σ_1 is the cross section given by Eq. (2) for the scattered radiation having the energy α' as given by Eq. (1). In Table II, for various values of the initial energy, α, the function $2f(\mu)/r_0^2$, together with the energy of the scattered photon α' and its total cross section are given as functions of μ, the cosine of the scattering angle. In Eq. (5) the volume element is

$$dv = 2\pi\rho^2 d\mu d\rho. \quad (6)$$

Integrating Eq. (5) gives:

$$I_1 = \int_0^1 d\mu \int_0^{X/\mu} 2\pi A N\mu f(\mu) \times\exp[-\sigma_0 N(X-\rho\mu) - \sigma_1 N\rho]d\rho \quad (7)$$

$$= [2\pi A\exp(-\sigma_0 NX)]\int_0^1 \frac{\mu f(\mu)}{\sigma_1-\sigma_0\mu} \times[1-\exp(-\{\sigma_1-\sigma_0\mu\}NX/\mu)]d\mu. \quad (8)$$

It is convenient to let

$$D = \sigma_0 NX \quad \text{and} \quad w = (\sigma_1-\sigma_0\mu)/\sigma_0\mu. \quad (9)$$

Then Eq. (8) may be written in the form:

$$\frac{I_1}{A} = \frac{2\pi e^{-D}}{\sigma_0}\int_0^1 \frac{f(\mu)}{w}[1-e^{-wD}]d\mu. \quad (10)$$

This expression has been numerically integrated for a number of distances and energies as given in Table III.

We would like to interpret these results in terms of an average angle of scattering, $\bar{\phi}$, whose cosine is given by $\bar{\mu}$. According to Eq. (1), the energy of the scattered photon is smaller than the initial photon by the factor, $1/(1+\alpha(1-\bar{\mu}))$.

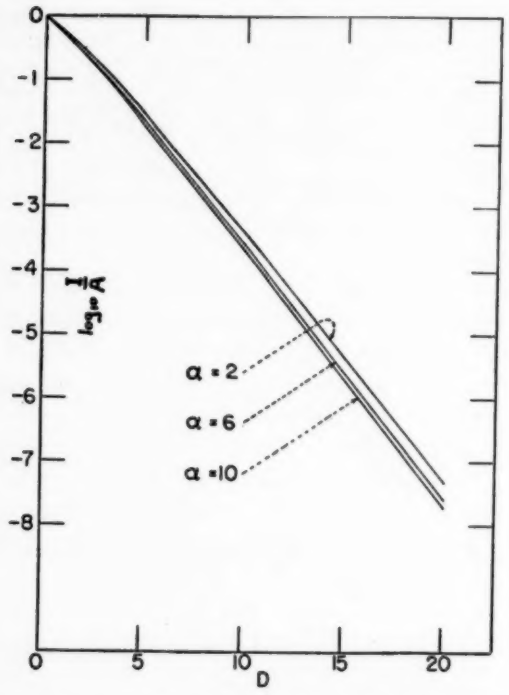

FIG. 4. The variation of the logarithm of the gamma-ray intensity with target thickness, D, measured in mean free paths of the initial gamma-rays.

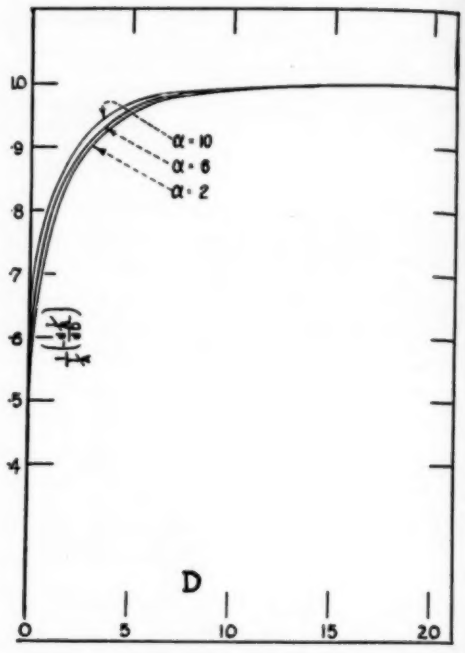

FIG. 5. The ionization produced by gamma-rays is proportional to $-(A/I)(d/dD)(I/A)$ rather than the intensity itself. After passing through a thick target, the two quantities become equal.

If all the scattered photons were deflected through the angle $\bar{\phi}$, this would correspond to having an angular dependence:

$$f(\mu)=\left(\frac{1}{2\pi}\right)\frac{\sigma_0}{1+\alpha(1-\bar{\mu})}\delta(\mu-\bar{\mu}). \qquad (11)$$

Here $\delta(\mu-\bar{\mu})$ is the Dirac delta-function. Under these conditions Eq. (10) can be integrated to give:

$$\frac{I_1}{A}=\frac{e^{-D}}{\psi(1+\alpha(1-\bar{\mu}))}[1-\exp[-\psi D]]. \qquad (12)$$

In this equation, ψ is the function defined in Eq. (9) having $\bar{\mu}$ as its argument. For each value of the energy and the distance there is some value of $\bar{\mu}$ for which Eq. (12) leads to the correct value for I_1/A. Thus, we can use the exact values of I_1/A, given in Table III, to solve for the corresponding values of $\bar{\mu}$, as shown in Table IV and Figs. 2 and 3. For distances large compared to a mean free path, $\bar{\mu}$ remains nearly constant for any given energy.

As the distance becomes very large, the value of $\bar{\mu}$ approaches μ_{max}, where μ_{max} is the value of μ for which $\mu f(\mu)$ has a maximum value. That is, μ_{max} corresponds to that angle for which the greatest amount of energy is scattered per unit angle ϕ (not per unit solid angle). The value of μ_{max} can be obtained for any energy by solving the equation:

$$(3\alpha+3\alpha^2-\alpha^3)(1-\mu_{max})^4$$
$$+(3-6\alpha-7\alpha^2+3\alpha^3)(1-\mu_{max})^3$$
$$-(9+2\alpha-5\alpha^2)(1-\mu_{max})^2$$
$$+8(\alpha+1)(1-\mu_{max})=2.$$

III. MULTIPLE SCATTERING

It would be exceedingly difficult to make an exact calculation of the multiple scattering of gamma-rays. However, the investigations of the single scattering, discussed in the previous section, suggest a method of approximation which should be fairly good. Assume that all gamma-rays of a given energy are scattered through the same angle, $\bar{\phi}$, having the cosine, $\bar{\mu}$, as given in Table IV. At each scattering, the energy of the photon is degraded by the factor $1/(1+\alpha\{1-\mu\})$. It is convenient to let the subscript n denote the number of times that the photon has been scat-

tered. The x component of the energy flux of the nth scattered beam is designated by I_n. The attenuation of the primary unscattered beam is given by the equation:

$$dI_0/dX = -\sigma_0 N I_0 \text{ or } I_0/A = \exp(-\sigma_0 N X). \quad (13)$$

The intensity of the first scattered beam can be determined from the equation:

$$dI_1/dX = \frac{\sigma_0 N I_0}{1+\alpha_0\{1-\bar{\mu}_0\}} - \frac{\sigma_1 N I_1}{\bar{\mu}_0}. \quad (14)$$

Its solution is given by Eq. (12)

It is, of course, necessarily true that the delta-function approximation for the angular dependence of the scattering (Eq. (11)) inserted into the exact integral should lead to the same result as the assumption of a single scattering angle and the differential Eq. (14). The rate of energy loss from the primary beam is given by $\sigma_0 N I_0$, and the fraction of this which goes into radiation is $[1/1+\alpha_0(1-\bar{\mu}_0)]$; the remainder goes into the recoil electrons. The cross section for attenuation of the first scattered beam in the x direction is $(\sigma_1 N/\bar{\mu}_0)$ since it is moving at an angle $\bar{\phi}$.

A new assumption must be introduced in order to estimate the intensity of the second scattered beam. Even if all of the gamma-rays are deflected through the same angle, they make various angles, χ_2, with the x direction depending on the value of their azimuthal angle, ω:

$$\cos\chi_2 = \cos\bar{\phi}_0 \cos\bar{\phi}_1 + \sin\bar{\phi}_0 \sin\bar{\phi}_1 \cos\omega. \quad (15)$$

The rate of change of I_2 can be expressed in terms of the average value of $\cos\chi_2$ (indicated by a bar):

$$\frac{dI_2}{dX} = \frac{\sigma_1 I_1}{\bar{\mu}_0[1+\alpha_1(1-\bar{\mu}_1)]} - \frac{\sigma_2 I_2}{\langle\cos\chi_2\rangle_{Av}}. \quad (16)$$

The correct method of averaging $\cos\chi_2$ in the sense required for the intensity of the multiple scattered radiation gives:

$$\exp[-\sigma_2 N X/\langle\cos\chi_2\rangle_{Av}] = \frac{1}{2\pi}\int_0^{2\pi} \exp[-\sigma_2 N X/\cos\chi_2]\, d\omega_2.$$

This integral is difficult to evaluate and the resulting expression is complicated. If the initial beam were not perpendicular to the target, this complication could not be avoided. However, in our case where the angles of scattering are small, the results are not sensitive to the method of averaging and we take

$$\langle\cos\chi_2\rangle_{Av} = \frac{1}{2\pi}\int_0^{2\pi} \cos\chi_2 d\omega_2 = \cos\bar{\phi}_0 \cos\bar{\phi}_1 = \bar{\mu}_0\bar{\mu}_1. \quad (17)$$

Equation (16) can then be integrated to give:

$$I_2/A = \left\{\frac{\sigma_0\sigma_1/\bar{\mu}_0}{[1+\alpha_0(1-\bar{\mu}_0)][1+\alpha_1(1-\bar{\mu}_1)][(\sigma_1/\bar{\mu}_0)-\sigma_0]}\right\}\left[\left(\frac{\exp[-\sigma_0 N X]-\exp[-\sigma_2 N X/\bar{\mu}_0\bar{\mu}_1]}{(\sigma_2/\bar{\mu}_0\bar{\mu}_1)-\sigma_0}\right) - \left(\frac{\exp[-\sigma_1 N X/\bar{\mu}_0]-\exp[-\sigma_2 N X/\bar{\mu}_0\bar{\mu}_1]}{(\sigma_2/\bar{\mu}_0\bar{\mu}_1)-(\sigma_1/\bar{\mu}_0)}\right)\right]. \quad (18)$$

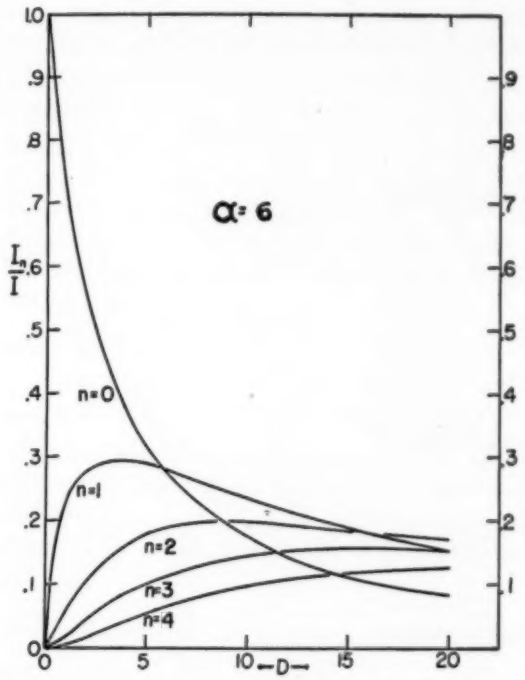

FIG. 6. For $\alpha = 6$, the relative intensity of the unscattered, singly scattered, doubly scattered, etc., beams of gamma-rays is plotted as a function of the target thickness D.

TABLE V.

	D	1	2	5	10	20
$\alpha_0=2$ $D=2.6315Nr_0^2\bar{X}$	I/A	0.5578	0.2833	0.02817	4.028×10^{-4}	4.666×10^{-4}
	$-d(I/A)/dD$	.4240	.2424	.02687	3.983×10^{-4}	4.661×10^{-4}
	I_0/I	.6596	.4776	.2392	.1127	.0442
	I_1/I	.2386	.295	.2728	.1907	.1035
	I_2/I	.0722	.136	.2064	.2002	.1448
	I_3/I	.0213	.0558	.1285	.1659	.1552
	I_4/I	.0063	.022	.0725	.1201	.1414
	I_5/I	.0018	.0085	.0389	.0802	.1159
$\alpha_0=6$ $D=1.4300Nr_0^2\bar{X}$	I/A	.5164	.2462	.02131	2.624×10^{-4}	2.516×10^{-4}
	$\dfrac{d(I/A)}{dD}$	.4067	.2156	.02054	2.604×10^{-4}	2.514×10^{-4}
	I_0/I	.7124	.5496	.3162	.1730	.0819
	I_1/I	.2109	.277	.2914	.2355	.1531
	I_2/I	.0546	.107	.1782	.1978	.1696
	I_3/I	.016	.041	.1007	.1425	.1527
	I_4/I	.0045	.016	.0549	.0953	.1255
	I_5/I	.001	.006	.0288	.0615	.0955
$\alpha_0=10$ $D=1.0284Nr_0^2\bar{X}$	I/A	.4973	.2295	.01850	2.133×10^{-4}	1.902×10^{-4}
	$-d(I/A)/dD$	.4056	.2056	.01799	2.122×10^{-4}	1.901×10^{-4}
	I_0/I	.7398	.5895	.3642	.2128	.1084
	I_1/I	.195	.262	.2937	.2518	.1761
	I_2/I	.0469	.0932	.1677	.1995	.1850
	I_3/I	.013	.034	.0851	.1301	.1526
	I_4/I	.0038	.013	.0440	.0810	.1140
	I_5/I	.001	.0048	.0226	.0504	.0824

The intensity of the higher scattered beams can be estimated in much the same way. Thus:

$$\frac{dI_n}{dX}=\frac{N\sigma_{n-1}I_{n-1}}{\langle\cos\chi_{n-1}\rangle_{Av}[1+\alpha_{n-1}(1-\bar{\mu}_{n-1})]}-\frac{N\sigma_nI_n}{\langle\cos\chi_n\rangle_{Av}}. \quad (19)$$

Here the angle χ_n that the nth scattered beam make with the x axis is given by

$$\cos\chi_n=\cos\chi_{n-1}\cos\bar{\phi}_{n-1}+\sin\chi_{n-1}\sin\bar{\phi}_{n-1}\sin\omega_{n-1}, \quad (20)$$

and the average value of its cosine is

$$\langle\cos\chi_n\rangle_{Av}=\frac{1}{2\pi}\int_0^{2\pi}\cos\chi_n d\omega_{n-1}=\langle\cos\chi_{n-1}\rangle_{Av}\bar{\mu}_{n-1}=\bar{\mu}_0\bar{\mu}_1\cdots\bar{\mu}_{n-1}. \quad (21)$$

It is convenient to define:

$$\sigma_0'=\sigma_0 \text{ and for all other values of } n,$$
$$\sigma_n'=\sigma_n/\bar{\mu}_0\bar{\mu}_1\cdots\bar{\mu}_{n-1}, \quad (22)$$

and

$$\sigma_{sn}'=\sigma_n'/[1+\alpha_n(1-\bar{\mu}_n)].$$

The intensity of the nth beam may be written in the form:

$$I_n/A=\sum_{j=0}^{n}K_{j,n}\exp(-\sigma_j'NX). \quad (23)$$

Substituting this expression back into Eq. (19)

$$-\sum_{j=0}^{n}\sigma_j'K_{j,n}N\exp(-\sigma_j'NX)=\sum_{j=0}^{n-1}\sigma'_{s(n-1)}K_{j,n-1}N\exp(-\sigma'NX)-\sum_{j=0}^{n-1}\sigma_n'NK_{j,n}\exp(-\sigma_j'NX). \quad (24)$$

Since this equation must be true for all values of X, we can equate the coefficients of each of the exponentials. This leads to the recursion formula:

$$K_{j,n}=\left(\frac{\sigma'_{s(n-1)}}{\sigma_n'-\sigma_j'}\right)K_{j,n-1}, \quad (n\neq j). \quad (25)$$

The values of $K_{n,n}$ are determined by the initial conditions. If the original beam is monochromatic, then:

$$K_{0,0}=1 \quad \text{and} \quad K_{n,n}=-\sum_{j=0}^{n-1}K_{j,n}. \quad (26)$$

These recursion formulae are sufficient to determine all of the $K_{j,n}$.

The following procedure can be used for making numerical calculations:

1. Make a table with the column headings:

n	α_n	σ_n	$\bar{\mu}_n$	$1+\alpha_n(1-\bar{\mu}_n)$	σ_n'	σ_{zn}'

For the initial beam, $n=0$, the energy α_0 is given and the corresponding value of σ_0 can be found (e.g. from Table II). The value of $D_0=\sigma_0 N\bar{X}$ follows immediately. From Table II or Figs. 2 and 3, the value of $\bar{\mu}_0$ corresponding to α_0 and D_0 can be estimated. For the subsequent values of $\bar{\mu}_n$ we take as arguments α_n and D_0. The energy in each new row is determined by the recursion formula:

$$\alpha_n=\alpha_{n-1}/[1+\alpha_{n-1}(1-\bar{\mu}_{n-1})]. \tag{27}$$

And the formation of the rest of the table is obvious.

2. The $K_{j,n}$ are easy to determine with the help of the above table. Starting with $K_{0,0}=1$, the recursion formula, Eq. (25), determines successively each of the $K_{0,n}$. Then by virtue of Eq. (26), $K_{1,1}=-K_{0,1}$ and Eq. (25) determines each of the $K_{1,n}$ successively in terms of $K_{1,1}$. Then $K_{2,2}=-K_{0,2}-K_{1,2}$, etc.

The most arbitrary feature of this treatment of multiple scattering is the assumption that $\bar{\mu}_n$ should be characteristic of the energy α_n and of the total thickness of the target in mean free paths of the primary energy $D_0=\sigma_0 N\bar{X}$. This assumption cannot be justified in a rigorous fashion, but rather we must argue that it cannot lead to a large error since $\bar{\mu}_n$ has only a slight dependence on distance.

IV. TOTAL INTENSITY OF GAMMA-RAYS

The total intensity of the gamma-rays reaching a given point is made up of the sum of the intensities of the primary, singly scattered, doubly scattered, etc., beams. This I, the x component of the total energy flux, may be written:

$$I/A=\sum_{j=0}^{\infty} c_j \exp(-\sigma_j' N\bar{X}), \tag{28}$$

where

$$c_j=\sum_{n=j}^{\infty} K_{j,n}. \tag{29}$$

From the standpoint of both the physiological effects and the measurement of radiation, the gradient of the flux rather than the flux itself is of primary interest. The gradient of the flux determines the specific ionization or roentgens per unit time. This is easily obtained by differentiating Eq. (28). Here the c_j are regarded as constants since they only depend on X very weakly through the weak dependence of $\bar{\mu}_n$ on distance. Thus:

$$-\frac{d(I/A)}{dNX}=\sum_{j=0}^{\infty} c_j\sigma_j' \exp(-\sigma_j' NX). \tag{30}$$

Usually the initial beam has a smaller cross section than the scattered beams. Thus after the radiation has passed through a sufficient thickness of target, only the terms with $j=0$ contribute and

$$I/A=c_0\exp(-\sigma_0 NX)=\frac{d(IA)}{d(\sigma_0 NX)}. \tag{31}$$

TABLE VI.

D		1	2	5	10	20
	α_1	1.1574	1.2407	1.3643	1.4599	1.5432
	α_2	.7581	.8506	.9977	1.1184	1.2329
	α_3	.5420	.6247	.7642	.8856	1.0082
	α_4	.4138	.4843	.6081	.7212	.8409
	α_5	.3314	.3912	.4993	.6016	.7138
	α_6		.3261	.4205	.5122	.6155
$\alpha_0=2$	α_7		.2784	.3617	.4437	.5381
(1 Mev)	α_8		.2422	.3164	.3901	.4761
	α_9			.2806	.3472	.4257
	α_{10}			.2517	.3123	.3842
	α_{11}			.2280	.2834	.3495
	α_{12}			.2082	.2591	.3201
	α_{13}				.2385	.2950
	α_1	2.7498	3.0060	3.4826	3.7783	4.0872
	α_2	1.4534	1.6810	2.0918	2.4755	2.8550
	α_3	.9072	1.0765	1.4129	1.7372	2.0865
	α_4	.6251	.7560	1.0276	1.2903	1.5996
$\alpha_0=6$	α_5	.4644	.5671	.7837	1.0040	1.2632
(3 Mev)	α_6	.3646	.4467	.6214	.8054	1.0254
	α_7	.2981	.3652	.5088	.6633	.8534
	α_8	.2512	.3075	.4275	.5586	.7234
	α_9	.2166	.2647	.3670	.4795	.6230
	α_{10}			.3204	.4183	.5441
	α_{11}			.2838	.3698	.4810
	α_1	4.1841	4.6083	5.3476	5.9524	6.4935
	α_2	2.0064	2.3731	3.0788	3.7495	4.4149
	α_3	1.1605	1.4074	1.9165	2.4593	3.0619
	α_4	.7596	.9423	1.3200	1.7280	2.2154
	α_5	.5429	.6794	.9702	1.2931	1.6827
$\alpha_0=10$	α_6		.5191	.7461	1.0059	1.3307
(5 Mev)	α_7		.4148	.5957	.8068	1.0799
	α_8		.3428	.4905	.6643	.8947
	α_9			.4140	.5594	.7550
	α_{10}			.3567	.4801	.6476
	α_{11}			.3125	.4187	.5635

This corresponds to a radiation spectrum which no longer depends on distance, an equilibrium having been reached between the primary and all of the successively scattered beams. If only the primary beam contributed, c_0 would equal to one. Instead, it usually has a value of the order of two.

Numerical calculations were made for α equal to 2, 6, and 10. The values for I/A and $[-d(I/A)/dD]/[I/A]$ as a function of the target thickness D are shown in Figs. 4 and 5, respectively. For $\alpha=6$, the contributions to the intensity of the gamma-rays which have been scattered a various number of times are plotted against D in Fig. 6. These results are shown in Table V for all three energies. In Table VI, the energies of the various scattered beams are given.

The numerical results can also be expressed in terms of the following formulae which were obtained by curve fitting:

$$\alpha=2 \qquad I/A=(1+0.487D+0.030D^2)e^{-D},$$

$$(D=2.6315Nr_0^2\bar{X}) \qquad -\frac{d}{dD}(I/A)=I/A-(0.527+0.073D^2)e^{-3D/2};$$

$$\alpha=6 \qquad I/A=(1+0.400D+0.0080D^2)e^{-D},$$

$$(D=1.4300Nr_0^2\bar{X}) \qquad -\frac{d}{dD}(I/A)=I/A-(0.438+0.021D+0.0343D^2)e^{-3D/2};$$

$$\alpha=10 \qquad I/A=(1+0.33D+0.0040D^2)e^{-D},$$

$$(D=1.0284Nr_0^2\bar{X}) \qquad -\frac{d}{dD}(I/A)=I/A-(0.38+0.01D+0.02D^2)e^{-3D/2}.$$

Considerable difficulty was encountered with the convergence of the contributions of the various scattered beams to the intensity when the values of μ_{max} were used corresponding to passage through an infinitely thick target.

The authors wish to thank John Von Neumann for suggesting the differential equation method for treating multiple scattering, Benedict Cassen for discussions and criticisms of the average angles of scattering, and Victor Weisskopf for many helpful discussions. The calculations presented in this report were made by Jean Patterson and Ruth Shoemaker at the University of Wisconsin.

The Penetration of Gamma-Radiation through Thick Layers

II. Plane Geometry, Iron, and Lead

JOSEPH O. HIRSCHFELDER AND EDWARD N. ADAMS II
Department of Chemistry, University of Wisconsin, Madison, Wisconsin

(Received December 15, 1947)

The method for considering the multiple scattering of gamma-rays given in Part I is extended to include the photoelectric effect and pair formation. Numerical calculations are made for the penetration of a monochromatic beam of gamma-rays through targets of either iron or lead. The thicknesses required to reduce the energy flux of factors of 2, 10, 100, 1000, and 10^6 are tabulated for gamma-rays of 1, 3, and 5 Mev passing through air, water, concrete, iron, or lead; and the corresponding absorbtion coefficients are given. The distinction between roentgen per unit time and energy flux is considered and numerical tables are given for the decrease in dosage with increasing target thickness. Rough experimental agreement is obtained with the rough experimental data now available. The need for careful measurements of the absorbtion of monochromatic gamma-rays passing through very thick targets is pointed out.

IN the paper[1] which is Part I in this series, a method was developed for considering the multiple scattering of gamma-rays in passing through a thick target. For simplicity, only Klein-Nishina scattering was considered. In the present paper we extend this method to take into account the absorbtion of gamma-radiation by the photoelectric effect for low energies and pair formation for large energies. Actual numerical calculations of both the energy flux and the roentgens are made for the penetration of 1-, 3-, or 5-Mev gammas through either iron or lead. For convenience, a table is given (see Table II) for the thicknesses required to attenuate the original beam by 0.5, 0.1, 0.01, 0.001, or 10^{-6} for not only these metals but for air, water, and concrete in which the pair formation and photoelectric effects may be ignored.

I. PAIR FORMATION

The cross section per electron for pair formation for energies less than $\alpha=10m_0c^2$ can be estimated from the relation

$$\sigma_{pf}/r_0^2=0.2545(Z/137)[\alpha-2.332]. \quad (1)$$

Here $r_0=e^2/m_0c^2$, the classical radius for the electron, Z is the atomic number, and α is the gamma-ray energy in units of m_0c^2. This expression for the cross section gives good agreement with the numerical values cited by Heitler.[2]

II. PHOTOELECTRIC EFFECT

The cross section per electron for the photoelectric effect, σ_{pe}, can be simply represented provided that the gamma-ray energy is considerably larger than α_k, the K x-ray limit. According to Gray[3]

$$\frac{\sigma_{pe}}{r_0^2}=3.45\times10^{-6}\frac{Z^5}{\alpha^3}(1+0.008Z)\times\left(1-\frac{\alpha_k}{4\alpha}-\frac{\alpha_k^2}{1.21\alpha}\right). \quad (2)$$

For iron, $\alpha_k=0.0140$; for lead, $\alpha_k=0.173$. Thus for

$$\text{iron:}\quad \sigma_{pe}/r_0^2=(0.0733/\alpha^3)[1-(0.00365/\alpha)]; \quad (3)$$

$$\text{lead:}\quad \sigma_{pe}/r_0^2=(3.151/\alpha^3)[1-(0.0678/\alpha)]. \quad (4)$$

III. INCLUSION OF PAIR FORMATION AND THE PHOTOELECTRIC EFFECT IN MULTIPLE SCATTERING EQUATIONS

The result of both pair formation and the photoelectric effect is to absorb gamma-rays but

[1] J. O. Hirschfelder, J. L. Magee, and M. H. Hull, "Penetration of gamma-radiation through thick layers. I. Plane geometry, Klein-Nishina scattering," Phys. Rev. 73, 851 (1948).

[2] W. Heitler, *Quantum Theory of Radiation* (Oxford University Press, London, 1944), 2nd edition, Appendix II, p. 259.

[3] Hulme, McDowgall, Buckingham, and Fowler, Proc. Roy. Soc. London 139, 150 (1935). Formula for photoelectric cross section is given and reference to J. A. Gray, Proc. Roy. Soc. Canada 21, 179 (1927).

not to scatter or to degrade those which are transmitted. The formulation of the equations for multiple scattering proceeds exactly as in the case where only the Klein-Nishina cross sections are considered. However, the intensity of each beam is further diminished by virtue of the absorbtion cross section.

Thus for a wide beam of gamma-rays impinging at right angles to a thick target we get the following set of equations:

$$dI_0/dX = -[\sigma_0+(\sigma_{pe})_0+(\sigma_{pf})_0]NI_0, \quad (5)$$

$$\frac{dI_1}{dX} = \frac{\sigma_0 NI_0}{1+\alpha_0(1-\bar{\mu}_0)} - \frac{[\sigma_1+(\sigma_{pe})_1+(\sigma_{pf})_1]NI_1}{\bar{\mu}_0}, \quad (6)$$

$$\frac{dI_n}{dX} = \left(\frac{\sigma_{n-1}NI_{n-1}}{\bar{\mu}_0\bar{\mu}_1\cdots\bar{\mu}_{n-2}[1+\alpha_{n-1}(1-\bar{\mu}_{n-1})]}\right) - \left(\frac{[\sigma_n+(\sigma_{pe})_n+(\sigma_{pf})_n]NI_n}{\bar{\mu}_0\bar{\mu}_1\cdots\bar{\mu}_{n-1}}\right). \quad (7)$$

Here, as in Part I, the subscript n refers to gamma-rays which have been scattered n times; N is the number of electrons per unit volume; σ_n are the Klein-Nishina cross sections corresponding to α_n, as before; $\bar{\mu}_n$ is the cosine of the effective angle of Klein-Nishina scattering, as given in Part I, and for the same values of $D=\sigma_0 NX$. The solution to these equations can be written

$$\frac{I_n}{A} = \sum_{j=0}^{n} K_{j,n} \times \exp(-[\sigma_j'+(\sigma_{pe})_j'+(\sigma_{pf})_j']D/\sigma_0), \quad (8)$$

Where the prime again has the meaning

$$\sigma_j' = \sigma_j/(\bar{\mu}_0\bar{\mu}_1\cdots\bar{\mu}_{j-1}), \quad (9)$$

$$(\sigma_{pe})_j' = (\sigma_{pe})_j/(\bar{\mu}_0\bar{\mu}_1\cdots\bar{\mu}_{j-1}), \quad (10)$$

$$(\sigma_{pf})_j' = (\sigma_{pf})_j/(\bar{\mu}_0\bar{\mu}_1\cdots\bar{\mu}_{j-1}). \quad (11)$$

The values of $K_{j,n}$ are determined as before from the boundary condition that when $X=0$

$$I_0 = A, \quad (12)$$

$$I_1 = I_2 = \cdots = I_n = 0, \quad (13)$$

or

$$K_{0,0} = 1, \quad (14)$$

and for all other values of n,

$$K_{n,n} = -\sum_{j=0}^{n-1} K_{j,n-1}. \quad (15)$$

The non-diagonal $K_{j,n}$ are determined by the recursion formula:

$$K_{j,n} = \frac{\sigma_{n-1}'K_{j,n-1}}{[\sigma_n'+(\sigma_{pe})_n'+(\sigma_{pf})_n'-\sigma_j'-(\sigma_{pe})_j'-(\sigma_{pf})_j'][1+\alpha_{n-1}(1-\bar{\mu}_{n-1})]}. \quad (16)$$

The method and the approximations are then very much the same as for the Klein-Nishina scattering alone.

IV. NUMERICAL CALCULATIONS

Numerical calculations were made for both iron and lead for values of $D=\sigma_0 NX$ equal to 1, 2, 5, 10, and 20. Notice that, because of the dependence of $\bar{\mu}_n$ on D, it is still desirable to express the unit of distance in Klein-Nishina mean free paths for the initial gamma-rays. The results are shown in Table I. The energies, α_n, are the same as for the Klein-Nishina scattering and are given in Table V of the previous paper, Part I. The total intensity of gamma-rays which have passed through either iron or lead targets may be summarized by the following equations which were obtained by curve fitting the information given in Table I.

Iron:

$$\alpha=2, \quad I/A = (1+0.2206X+0.00435X^2)e^{-0.462X}, \quad (17)$$

$$\alpha=6, \quad I/A = (1+0.1000X+0.00123X^2)e^{-0.281X}, \quad (18)$$

$$\alpha=10, \quad I/A = (1+0.0635X+0.00123X^2)e^{-0.245X}. \quad (19)$$

Lead:

$$\alpha=2, \quad I/A = [1.3222+0.0786X-(0.4027/\{1.25+0.565X\})]e^{-0.647X}, \quad (20)$$

$$\alpha=6, \quad I/A = (1+0.1159X+0.00264X^2)e^{-0.430X}, \quad (21)$$

TABLE I.

(A) Iron

X(cm)	1 Mev	$\alpha=2$		($X=2.17D$ cm)	
D	2.17 1	4.34 2	10.85 5	21.70 10	43.40 20
R/R_0	0.5597	0.2807	0.02671	3.58×10^{-4}	3.75×10^{-8}
I/A	0.5498	0.2737	0.02577	3.44×10^{-4}	3.59×10^{-8}
$-d/dD(I/A)$	0.4270	0.2382	0.02479	3.42×10^{-4}	3.60×10^{-8}
I_0/I	0.6668	0.4910	0.2570	0.1275	0.0535
I_1/I	0.2388	0.2997	0.2886	0.2121	0.1232
I_2/I	0.0699	0.1334	0.2121	0.2172	0.1686
I_3/I	0.0188	0.0510	0.1257	0.1731	0.1751
I_4/I	0.0046	0.0179	0.0654	0.1182	0.1527
I_5/I	0.0010	0.0055	0.0309	0.0725	0.1178
I_6/I		0.0015	0.0134	0.0409	0.0830
I_7/I			0.0053	0.0214	0.0543
I_8/I			0.0019	0.0104	0.0332
I_9/I				0.0047	0.0192
I_{10}/I				0.0020	0.0104
I_{11}/I					0.0053
I_{12}/I					0.0025
I_{13}/I					0.0011

X(cm)	3 Mev	$\alpha=6$		($X=4.00D$ cm)	
D	4.00 1	8.00 2	20.00 5	40.00 10	80.00 20
R/R_0	0.5105	0.2309	0.01591	12.12×10^{-5}	3.87×10^{-9}
I/A	0.4618	0.1985	0.01270	9.23×10^{-5}	2.85×10^{-9}
$-d/dD(I/A)$	0.4129	0.1935	0.01365	1.026×10^{-4}	3.20×10^{-9}
I_0/I	0.7036	0.5319	0.2853	0.1422	0.0605
I_1/I	0.2177	0.2881	0.2963	0.2254	0.1349
I_2/I	0.0570	0.1129	0.1933	0.2093	0.1689
I_3/I	0.0161	0.0430	0.1118	0.1586	0.1646
I_4/I	0.0044	0.0159	0.0608	0.1083	0.1415
I_5/I	0.0011	0.0056	0.0309	0.0698	0.1101
I_6/I		0.0019	0.0148	0.0422	0.0801
I_7/I			0.0067	0.0242	0.0558
I_8/I				0.0132	0.0370
I_9/I				0.0069	0.0236
I_{10}/I					0.0144
I_{11}/I					0.0034

X(cm)	5 Mev	$\alpha=10$		($X=5.56D$ cm)	
D	5.56 1	11.12 2	27.80 5	55.60 10	111.20 20
R/R_0	0.4165	0.1543	0.00585	1.592×10^{-5}	5.77×10^{-11}
I/A	0.3587	0.1223	0.00411	1.030×10^{-5}	3.52×10^{-11}
$-d/dD(I/A)$	0.4045	0.1465	0.00533	1.379×10^{-4}	4.77×10^{-11}
I_0/I	0.7153	0.5383	0.2709	0.1201	0.0435
I_1/I	0.2110	0.2870	0.2972	0.2130	0.1140
I_2/I	0.0533	0.1116	0.2027	0.2167	0.1640
I_3/I	0.0149	0.0416	0.1132	0.1660	0.1678
I_4/I	0.0042	0.0158	0.0612	0.1134	0.1455
I_5/I	0.0011	0.0057	0.0318	0.0741	0.1155
I_6/I			0.0157	0.0459	0.0873
I_7/I			0.0074	0.0271	0.0626
I_8/I				0.0153	0.0428
I_9/I				0.0083	0.0282
I_{10}/I					0.0179
I_{11}/I					0.0109

(B) Lead

X(cm)	1 Mev	$\alpha=2$		($X=1.77D$ cm)	
D	1.77 1	3.54 2	8.85 5	17.70 10	35.4 20
R/R_0	0.4127	0.1522	0.00659	3.00×10^{-5}	4.87×10^{-10}
I/A	0.4076	0.1495	0.00642	2.90×10^{-5}	4.69×10^{-10}
$-d/dD(I/A)$	0.4381	0.1671	0.00733	3.32×10^{-5}	5.37×10^{-10}
I_0/I	0.7810	0.6779	0.5092	0.3686	0.2436
I_1/I	0.1937	0.2649	0.3444	0.3677	0.3419
I_2/I	0.0236	0.0511	0.1187	0.1882	0.2486
I_3/I	0.0015	0.0055	0.0244	0.0604	0.1167
I_4/I	0.0001	0.0004	0.0033	0.0130	0.0383
I_5/I				0.0020	0.0091
I_6/I				0.0002	0.0016
I_7/I					0.0002

X(cm)	3 Mev	$\alpha=6$		($X=3.26D$ cm)	
D	3.26 1	6.52 2	16.30 5	32.60 10	65.20 20
R/R_0	0.3806	0.1298	0.00397	8.13×10^{-5}	1.792×10^{-11}
I/A	0.3464	0.1126	0.00321	6.30×10^{-5}	1.343×10^{-11}
$-d/dD(I/A)$	0.4104	0.1417	0.00431	8.67×10^{-5}	1.874×10^{-11}
I_0/I	0.7114	0.5393	0.2827	0.1312	0.0508
I_1/I	0.2312	0.3226	0.3610	0.2832	0.1694
I_2/I	0.0494	0.1088	0.2254	0.2825	0.2504
I_3/I	0.0073	0.0251	0.0958	0.1816	0.2360
I_4/I	0.0006	0.0036	0.0286	0.0842	0.1630
I_5/I		0.0003	0.0058	0.0288	0.0844
I_6/I			0.0008	0.0071	0.0334
I_7/I			0.0001	0.0012	0.0101
I_8/I				0.0002	0.0024
I_9/I					0.0004

X(cm)	5 Mev	$\alpha=10$		($X=4.53D$ cm)	
D	4.53 1	9.06 2	22.65 5	45.30 10	90.60 20
R/R_0	0.2073	0.04208	2.771×10^{-4}	4.123×10^{-8}	3.164×10^{-16}
I/A	0.1753	0.03197	1.831×10^{-4}	2.535×10^{-8}	1.867×10^{-16}
$-d/dD(I/A)$	0.3170	0.05897	3.519×10^{-4}	5.023×10^{-8}	3.776×10^{-16}
I_0/I	0.6721	0.4342	0.1240	0.0203	0.0014
I_1/I	0.2510	0.3541	0.3217	0.1556	0.0435
I_2/I	0.0634	0.1555	0.3023	0.2816	0.1535
I_3/I	0.0121	0.0459	0.1653	0.2647	0.2392
I_4/I	0.0015	0.0092	0.0648	0.1657	0.2378
I_5/I	0.0001	0.0011	0.0179	0.0776	0.1709
I_6/I		0.0001	0.0033	0.0265	0.0953
I_7/I			0.0004	0.0065	0.0408
I_8/I				0.0011	0.0133
I_9/I				0.0002	0.0033
I_{10}/I					0.0006
I_{11}/I					0.0001

$\alpha=10$, $I/A=(1+0.0405X+0.00461X^2)e^{-0.442X}$. (22)

For many practical purposes it is desirable to know the thickness of various types of targets which will attenuate gamma-rays to a given fraction of their initial intensity. As a result of the calculations given in this paper and its predecessor, we can estimate these thicknesses either for substances which have only Klein-Nishina cross sections such as air, water, or concrete, or iron or lead for which we have made separate calculations. In any case,

$$D=0.02392\rho(2Z/M)(\sigma_0/r_0^2)X. \quad (23)$$

For mixtures of elements, the weight average of $2Z/M$ is to be taken over all the elements. For air at N.T.P. (0°C, 1 atmos.), $\rho=0.001293$ g/cm^3 and $(2Z/M)=1$, so that

$$D=3.093\times10^{-5}(\sigma_0/r_0^2)X. \quad (24)$$

For water at 2°C, $\rho=1$ g/cm^3 and $2Z/M=(16+4)/18.016$, so that

$$D=0.02655(\sigma_0/r_0^2)X. \quad (25)$$

For concrete,[4] 1–2–4 mix, $\rho=2.29$ g/cm^3 and

[4] O. W. Eshbach, *Handbook of Engineering Fundamentals* (John Wiley and Sons, Inc., New York, 1936).

$(2Z/M)=1$, so that

$$D=0.0548(\sigma_0/r_0^2)X. \quad (26)$$

For iron, $\rho=7.86$ g/cm^3 and $(2Z/M)=0.9312$, so that

$$D=0.1750(\sigma_0/r_0^2)X. \quad (27)$$

For lead, $\rho=11.34$ g/cm^3 and $(2Z/M)=0.7915$, so that

$$D=0.2147(\sigma_0/r_0^2)X. \quad (28)$$

Thus we obtain the results shown in Table II. Here by "Klein-Nishina" is meant any substance for which pair formation and photoelectric effect are negligible.

In most treatments of gamma-ray scattering and absorbtion, the decrease in energy flux as a function of target thickness is expressed in terms of "absorbtion coefficients," a, which are defined by the relation:

$$I/A=\exp(-aX). \quad (29)$$

In Table III, the mass absorption coefficients, a/ρ, are tabulated. The column labeled "concrete" was calculated for pure Klein-Nishina scattering with $(2Z/M)=1$. For any other material for which Klein-Nishina scattering is valid

$$a/\rho=(2Z/M)(a/\rho)_{\text{concrete}} \quad (30)$$

The meaning of our absorption coefficients should be emphasized. They correspond to the total energy which has been absorbed from the beam of gamma-rays and should not be confused with the coefficients for absorption plus scattering. Our coefficients could be experimentally determined by allowing the rays to enter the counting chamber from all directions; whereas the coefficients for absorbtion plus scattering only consider the flux from the unscattered beam and require a fine slit system to insure that only the undeflected rays can enter the counter.

V. ROENTGEN

The physiological effects of gamma-rays are determined, not by the energy flux, I, but by the ionization which they produce in the body tissues. This is proportional to the dosage in roentgen units. A roentgen is defined as that amount of radiation which will produce 2.08×10^9 ion pairs per cm^3 of air under N.T.P. Since both air and the body tissues are composed of elements of small atomic number, in the energy range considered here only Klein-Nishina scattering is important and the ionization produced in the body tissues differs from the ionization produced in air only by the ratio of

TABLE II. Thickness in cm required to reduce intensity of incident beam by stated factors.

		Klein-Nishina alone				
	I/A	0.5	0.1	0.01	0.001	10^{-4}
$\alpha=2$ (1 Mev)	D	1.17	3.40	6.26	8.96	16.68
	Air (N.T.P.)	1.44×10^4	4.18×10^4	7.70×10^4	1.10×10^5	2.05×10^5
	Water (2°C)	16.7	48.6	89.5	128.	239.
	Concrete (1–2–4 mix)	8.1	23.6	43.4	62.2	116.
$\alpha=6$ (3 Mev)	D	1.05	3.15	5.90	8.51	16.07
	Air (N.T.P.)	2.37×10^4	7.12×10^4	1.33×10^5	1.92×10^5	3.63×10^5
	Water (2°C)	27.6	82.8	155.	224.	423.
	Concrete (1–2–4 mix)	13.4	40.3	75.5	109.	206.
$\alpha=10$ (5 Mev)	D	0.98	3.01	5.71	8.30	15.79
	Air (N.T.P.)	3.08×10^4	9.45×10^4	1.79×10^5	2.61×10^5	4.96×10^5
	Water (2°C)	35.9	110.	209.	304.	578.
	Concrete (1–2–4 mix)	17.3	53.3	101.	147.	279.

		Klein-Nishina plus pair production and photoelectric effect				
	I/A	0.5	0.1	0.01	0.001	10^{-4}
$\alpha=2$ (1 Mev)	Iron	2.49	7.22	13.31	19.08	35.63
	Lead	1.40	4.23	8.11	11.91	23.12
$\alpha=6$ (3 Mev)	Iron	3.61	11.11	21.00	30.46	57.68
	Lead	2.15	6.88	13.27	19.45	37.26
$\alpha=10$) (5 Mev)	Iron	3.77	12.14	23.54	34.52	66.05
	Lead	1.76	5.98	12.19	18.35	36.13

TABLE III. Mass absorbtion coefficients.

		a/ρ cm²/g				
	I/A	0.5	0.1	0.01	0.001	10^{-4}
$\alpha=2$ (1 Mev)	Water	0.0415	0.0474	0.0514	0.0540	0.0578
	Concrete	0.0374	0.0426	0.0463	0.0485	0.0520
	Iron	0.0354	0.0406	0.0440	0.0460	0.0494
	Lead	0.0437	0.0480	0.0501	0.0512	0.0527
$\alpha=6$ (3 Mev)	Water	0.0251	0.0278	0.0297	0.0308	0.0327
	Concrete	0.0226	0.0249	0.0266	0.0277	0.0293
	Iron	0.0244	0.0263	0.0279	0.0289	0.0305
	Lead	0.0284	0.0295	0.0306	0.0313	0.0327
$\alpha=10$ (5 Mev)	Water	0.0193	0.0209	0.0220	0.0227	0.0239
	Concrete	0.0175	0.0189	0.0199	0.0205	0.0216
	Iron	0.0234	0.0242	0.0249	0.0254	0.0266
	Lead	0.0348	0.0340	0.0333	0.0332	0.0337

the electron densities in the two cases. This is why the roentgen is a satisfactory unit for physiological dosage. Unfortunately, Geiger counters are not constructed to measure roentgens, but rather the ionization produced in metal foils. However, they are calibrated in roentgens with different calibration curves corresponding to different energies of incident gamma-rays.

The energy absorbed in 1 cm³ of air N.T.P. is equal to $3.69\times10^{-5}I(\sigma_a/r_0^2)$. Here 3.69×10^{-5} is the product of the number of electrons per cm³ in air times the square of the classical electron radius r_0, in cm; I is the energy flux in Mev per cm²; and (σ_a/r_0^2) is the Klein-Nishina cross section for energy absorption per electron in units of r_0^2. A formula for σ_a is given in Rutherford, Chadwick, and Ellis,[5] and its numerical value is given in Table IV. The number of roentgens is simply proportional to the energy absorbed in 1 cm³ of air. Since 1 Mev of energy absorbed produces $10^6/33.2$ ion pairs, and 1 roentgen unit corresponds to 2.08×10^9 ion pairs, the number of roentgens per unit time, R, is given by

$$R=5.34\times10^{-10}I(\sigma_a/r_0^2), \tag{31}$$

and for a beam of gamma-rays having many energy components

$$R=5.34\times10^{-10}\sum_n I_n\times(\sigma_a/r_0^2)_n. \tag{32}$$

Since (σ_a/r_0^2) is not independent of energy, the ratio of R/R_0, where R_0 is the roentgens per unit time of the initial gamma rays before passing through the target, is not equal to I/A.

[5] Rutherford, Chadwick, and Ellis, *Radiations from Radioactive Substances* (The Macmillan Company, New York, 1930), p. 464.

TABLE IV. σ_a/r_0^2.

α	σ_a/r_0^2	α	σ_a/r_0^2
0.25	0.9548	1.5	1.2150
0.30	1.0217	2.0	1.1659
0.35	1.0729	2.5	1.1134
0.40	1.1132	3.0	1.0625
0.50	1.1695	4.0	0.9711
0.60	1.2035	5.0	0.8941
0.75	1.2313	6.0	0.8289
1.00	1.2431	8.0	0.7258
		10.0	0.6478

Numerical values are given for R/R_0 for iron and lead in Table I. Similar calculations were made for substances in which only the Klein-Nishina scattering occurred. The ratio

$$(R/R_0)/(I/A)$$

is almost unity for 1-Mev gammas, and becomes large of the order of 1.52 for 5-Mev gammas which have plowed through a large thickness of target. This ratio can be expressed in the form:

$$R/R_0=(I/A)\exp(bX)=\exp[(b-a)X]. \tag{33}$$

Here the calculated values of b have been curve-fitted in the form:

$$b=c/(d+X). \tag{34}$$

The values of c and d are given in Table V for water, concrete, iron, and lead. For any substances for which only the Klein-Nishina scattering occurs

$$c=(c)_{\text{concrete}},\quad d=\frac{d_{\text{concrete}}}{(\rho/2.29)(2Z/M)}. \tag{35}$$

VI. CONCLUSIONS

There are no adequate experimental data with which to make a quantitative comparison with the theoretical results presented here. Most of the experimental work on the scattering and absorption of gamma-rays has been designed to study single rather than multiple scatterings, and when a target of many mean free paths has been used, a slit system has been incorporated to insure "perfect geometry" and eliminate the scattered rays. The review articles such as Gentner's[6] and Hall's[7] do not even mention the

[6] W. Gentner, Physik. Zeits. **38**, 836 (1937).
[7] Harvey Hall, Rev. Mod. Phys. **8**, 358 (1936).

problems of multiple scattering. Kohlrausch[8] and the earlier workers were troubled by scattered radiation but their targets were not thick enough to furnish useful data for our purposes and their radiation was not monochromatic. Sizoo and Willemsen[9] studied the absorption and single scattering of radium gamma-rays through thin targets of lead and iron. They were able to make theoretical calculations agreeing perfectly with their experimental data by taking into account the exact spectral distribution of the primary beam and using the same cross sections for Klein-Nishina scattering, the photoelectric effect, and pair production which we use in the present report. Our theoretical treatment should be accurate for both the unscattered and the singly scattered beams since no approximations are made once the cross sections have been chosen. Thus the work of Sizoo and Willemsen guarantees that our absorption coefficients are valid for thin targets of less than two mean free paths.

The authors know of an unpublished experiment[10] in which the mass absorbtion coefficient for Ra$(B+C)$ gamma-rays passing through 7 cm of lead is 0.047. For 1-Mev gamma-rays we calculate 0.048; for 3-Mev gamma-rays we calculate 0.030. According to Roberts,[11] the spectral distribution of gamma-rays from a Ra$(B+C)$ source is very complex with the energies ranging from 0.5 Mev to 3.0 Mev so that it is difficult to make any sort of comparison. Furthermore, 7 cm of lead correspond to a reduction of the energy flux by a factor of only ten; i.e., $I/A=0.1$, and for this attenuation, 90 percent of the flux is in the form of either the unscattered or the singly scattered rays. Thus, if an accurate comparison were possible it would only check the approximations which we make in estimating the remaining 10 percent of the rays which are multiple scattered. Thus it is clear that very thick targets, such as 15 or more cm of lead, are required to provide an adequate check of our results.

There is more than academic interest in both experimental and theoretical considerations of multiple scattering, since it is the total radiation which is physiologically important.

The authors regret that John L. Magee and M. H. Hull were unable to participate in this present report, although they had a great deal to do with the methods used here. The basic idea for the sequence of differential equations was suggested by John von Neumann. The calculations were carried out by Jean Patterson, Ruth Shoemaker, and Wallace Spaulding.

This report is an extension of work which was originally undertaken at the laboratories of the University of California under Government Contract W-7405-eng-36. The Los Alamos work was published in the form of LADC-70(MDDC-348), and the Los Alamos Laboratory was credited with the work performed under Part I of the present series. However, all work contained in Part II has been carried out at the University of Wisconsin, and therefore the University of Wisconsin should be credited with this publication.

TABLE V. Ratio of roentgens per unit time to energy flux.

		$(R/R_0)/(I/A)=\exp(cX/d+X)$	
		c	d
$\alpha=2$	Water	0.0345	11.20
	Concrete	0.0345	5.43
	Iron	0.0467	3.64
	Lead	0.0437	5.06
$\alpha=6$	Water	0.318	61.5
	Concrete	0.318	29.80
	Iron	0.340	9.99
	Lead	0.318	8.07
$\alpha=10$	Water	0.468	93.2
	Concrete	0.468	45.1
	Iron	0.556	15.50
	Lead	0.602	10.78

[8] K. W. F. Kohlrausch, Akad. Wiss. Wien Ber. 126 (4), 441 (1917); 683 (1917); (2a) 705 (1917); (2a), 887 (1917).
[9] G. J. Sizoo and H. Willemsen, Physica 5, 100 (1938).
[10] H. M. Parker, Clinton Laboratory Lecture Series (unclassified), Lecture V (May 1944).
[11] J. E. Roberts, Phil. Mag. 36, 264 (1945).

Sensitivity of Proton-Proton Scattering to Potentials at Different Distances

G. BREIT, A. A. BROYLES, AND M. H. HULL
*Yale University, New Haven, Connecticut**

(Received December 19, 1947)

Estimates are made of sensitivity of proton-proton scattering to assumed changes δV in theoretical potential energy. The energy range 0.15–9 Mev is considered for the incident protons. The changes in potential energy are taken to be small additions in small intervals at distance R. First-order perturbation theory is used. Combining the effect of δV at $R=3$ or 5 in units e^2/mc^2 with a change δD in the depth of a square potential well (width e^2/mc^2) the effects are made to neutralize at a preassigned energy $E_{\rm I}$ and the sensitivity of scattering to δV is estimated at a second energy E. Combination of these effects with a simultaneous change δr_0 in range of square well enables neutralization of effects at energies $E_{\rm I}$, $E_{\rm II}$ and adjustment to arbitrary small change in scattering at a third energy E. The sensitivity of observed scattering to δV for a few choices of pairs $E_{\rm I}$, $E_{\rm II}$ is worked out as a function of E. It is found that the region 200 kev–600 kev should be valuable in determining values of δV for preassigned R. The relative importance of the smaller energies increases with R on account of shielding of the smaller R by the Coulomb barrier. Neutralization of effects at two energies $E_{\rm I}$, $E_{\rm II}$, with simultaneous adjustment to changes in scattering at energies E_1, E_2, is also considered in terms of simultaneous potential energy changes at two values of R combined with δr_0, δD. An experimental accuracy of 1 percent in scattering is found to correspond to the possibility of detecting as little as 1 kev for δV through a distance e^2/mc^2 at $R=5e^2/mc^2$ and 10 kev at $R=3e^2/mc^2$.

I. INTRODUCTION

THE most accurate experimental material[1,2] on proton-proton scattering is in the energy range from about 700 to 2400 kev. There are, in addition, observations[3] at low energies (150–320 kev) and more recent material[4] at 7, 9, 10, 15 Mev. The present note contains estimates concerning the relative usefulness of measurements at different energies for the determination of the shape of the effective potential energy curve between two protons.

It is realized that the concept of potential energy as a definite function of distance is only approximate,[5,6] and that a velocity dependence of nuclear forces would vitiate conclusions regarding both the range of force and the shape of the potential energy curve. There is probably some meaning to the shape of the potential energy-distance curve, especially if the energies dealt with are confined to a region small compared with the rest mass energy of the meson. For this reason it is better to determine the effective shape from observations which do not extend over a too wide energy range. The estimates reported on below show that it would be possible to detect the presence of interaction energies acting in addition to the Coulomb energy, if they were located at distances of the order of 10^{-12} cm by means of observations in the low energy range from about 200 to about 500 kev. The development of electron multiplier and counter techniques should make it possible to make improved measurements in this energy range and to ascertain small interactions outside of the region of 3×10^{-13} cm within which the potential energy is mainly seated. It is clear intuitively that the low energy region should be good for detection of deviations from the inverse square law of potential at larger distances. This potential is small for two protons and is relatively ineffective beyond about 500 kev in keeping the protons apart. The regions of 3×10^{-13} cm and 10^{-12} cm are nearly equally accessible to protons of the higher energy. At 200 kev, however, the Coulomb potential shields the smaller distance region, and the higher distances have, therefore, a greater relative weight for giving phase shifts.

* Assisted by Contract N6ori-44, Task Order XVI, of the Office of Naval Research.

[1] R. G. Herb, D. W. Kerst, D. B. Parkinson, and G. J. Plain, Phys. Rev. 55, 998 (1939).

[2] N. P. Heydenburg, L. R. Hafstad, and M. A. Tuve, Phys. Rev. 56, 1078 (1939).

[3] G. L. Ragan, W. R. Kanne, and R. F. Taschek, Phys. Rev. 60, 628 (1941).

[4] R. R. Wilson and E. C. Creutz, Phys. Rev. 71, 339 (1947); R. R. Wilson, Phys. Rev. 71, 384 (1947); R. R. Wilson, E. J. Lofgren, J. R. Richardson, B. T. Wright, and R. S. Shankland, Phys. Rev. 71, 560 (1947); A. N. May and C. F. Powell, Proc. Roy. Soc. 190, 170 (1947).

[5] G. Breit, H. M. Thaxton, and L. Eisenbud, Phys. Rev. 55, 1018 (1939), compare p. 1062. This paper is referred to as BTE in the text.

[6] G. Breit, University of Pennsylvania Bicentennial Conference, Pamphlet N-15-16, p. 5 (1941).

This effect is only a contributing factor to the high sensitivity at 400 kev which is found below. There is besides a strong effect of interference[7] between the Coulomb wave and the expected proton-proton interaction wave which enhances the sensitivity. The total scattering at 45° at these energies is a small fraction of the scattering due to each cause taken separately. A given percentage change in either of the contributions gives, therefore, a larger effect on the percentage change in scattering. It is realized that if the scattering is very small at 45°, then the experimental determination of scattering might be impossible to carry out with the same percentage error as is normally the case. There has been no intensity difficulty reported in the published experimental work because the Rutherford scattering is large at low energies. There might be some error introduced by multiple scattering when the scattering is close to a minimum (~400 kev) at a scattering angle of 45°. On account of this possible source of error the results reported on below are given also for 35° scattering. The effects will be seen to be present, although to a smaller degree, at this angle also.

An estimate of order of magnitude of sensitivity is of interest at this stage. By first-order perturbation calculations one finds that a potential change δV, located at a distance $R=3e^2/mc^2$ and spread through a distance ΔR, gives at 0.2 Mev a change δK, in the phase shift K, of amount

$$\delta K \cong -\frac{0.618}{(0.2)^{\frac{1}{2}}}\times 0.158q = -0.218q, \qquad (1)$$

where

$$q=(\delta V_{\text{Mev}})(\Delta R mc^2/e^2). \qquad (1.1)$$

Here 0.158 is the approximate value of $\mathfrak{F}^2$ in Eq. (2) below. In the notation of BTE[5] the sensitivity of the ratio to Mott's scattering expected at 0.2 Mev, for the phase shift known approximately from experiment, is

$$d\mathfrak{R}/dK \cong -3.8. \qquad (1.2)$$

The expected change in $\mathfrak{R}$ for 45° scattering at 200 kev is

$$3.8\times 0.58\times 0.218q = 0.47q. \qquad (1.3)$$

The value of $\mathfrak{R}$ is about 0.45 and hence

$$(\delta\mathfrak{R}/\mathfrak{R})_{45°,\ 0.2\ \text{Mev}} \cong 1.0q. \qquad (1.4)$$

Measurements to an accuracy of 1 percent at this energy would determine as small a value of q as $(e^2/mc^2)10$ kev, i.e., a lump of potential energy of 10 kev through a distance 2.8×10^{-13} cm. The factor 0.58 included in Eq. (1.3) takes into account an opposing change in the depth of the potential energy curve adjusted so as to keep the total scattering the same at 2 Mev. At 200 kev one is still far from the minimum of $\mathfrak{R}$ and only the difficulty of counting low energy protons is in the way in this energy region. The sensitive condition illustrated above is still stronger at 350 kev and is especially marked between 0.3 and 0.5 Mev. One of the objects of the present note is to point out the possible value of extending previous measurements into this energy region.

It would not be satisfactory to deal only with the sensitivity of scattering to a small potential lump because the effect of the lump can be compensated at any energy by an opposing effect in the depth of the potential well. The calculations are made, therefore, on the supposition that the effect of the potential extension is compensated by a well depth change at some energy and the fractional change in $\mathfrak{R}$ is estimated. The rate of change of scattering expressed in fractional amount of total scattering change is X_{I} of Eq. (13); the compensation by well depth change is supposed to take place at an energy $E=E_{\text{I}}$. A change in the potential energy curve, consisting in the introduction of a potential energy lump at R, and compensated at a conveniently chosen energy E_{I} by a well depth change, can be reproduced at another energy E_{II} by a change in the range of the potential energy well (range, according to custom, means here range of force) accompanied by a suitable change in well depth. If measurements were available at only two energies there would be no way of distinguishing between a change in range, which has to do with changes of the potential energy curve from $r=0$ to $r\cong 3\times 10^{-13}$ cm, and the effect of a potential energy lump at a larger distance R. The sensitivity to range is expressed to first order by the quantity $\delta_1 K+\delta_2 K$ in Eq. (6). Graphs giving the ratio of potential lump sensitivity to

[7] G. Breit, E. U. Condon, and R. D. Present, Phys. Rev. **50**, 825 (1936).

range sensitivity are given below in terms of the quantity Y of Eq. (9). This quantity has to be multiplied by $(\delta V)\Delta R/(D\delta r_0)$ where δr_0 is the change in range in order to give the ratio of phase shift changes caused by a potential change δV through ΔR at distance R and a change δr_0 in the radius of the potential well. Both changes are supposed to be compensated by suitable well depth changes as has been explained above. The graphs show that the ratio of sensitivity depends on energy even though both changes are made so as to produce no effect at one arbitrarily chosen value of E such as 1 Mev or 2 Mev. There remains, therefore, a possibility of distinguishing between effects of change of range and effects of potential energy lumps at larger distances. The sensitivity of scattering to changes in shape of potential energy curves can be estimated by means of the graphs.

The change in scattering caused by a potential energy change at the larger distances and compensated at energy E_{I} by a suitable well depth change can be combined with a change in range of force also accompanied by a well depth change compensating its effect at energy E_{I}. The combination of the two changes can be made in such a way as to have them compensate each other at energy E_{II}. The fractional rate of change of scattering with respect to q [see Eq. (1.1)] is the quantity $Z_{\mathrm{I,II}}(E)$ which is plotted below in a few cases. These graphs also show that the low energy region should be valuable in extending knowledge of the shape of the effective potential energy curve.

All calculations reported on are in the nature of estimates. They are subject to the following limitations and approximations. First-order perturbation theory for phase shift calculation is used. This means that the potential energy changes dealt with must be small in order that the result be applicable. The calculations have to do with additional information that can be derived from improved measurements rather than with indications from present measurements concerning the shape of potential energy curves. Radial wave functions for a "square well" of radius e^2/mc^2 and depth 10.5 Mev (without Coulomb potential inside well) have been used. This potential probably represents experiment imperfectly and an approximation is involved at this point. The values of the radial function at the larger R are determined, however, mainly by the phase shift K rather than by the potential well and this approximation is believed, therefore, to be harmless. Some of the Coulomb functions and other quantities at low energies were not computed directly but were interpolated for. No great numerical accuracy was aimed at. The methods employed are similar to some of the work of Hoisington, Share, and Breit,[8] but the present note has more to do with qualitative understanding of the relative importance of different energy regions than with an adjustment of potential energy curves to represent experimental data.

The object in dealing with compensated combinations is to enable fitting experiments at two energies by means of a potential well with orthodox range and later improving the over-all fit by adjusting q to agree with experiment at a third energy.

II. CALCULATIONS

The notation used is that of BTE. The subscript 0 is omitted for K. No confusion can result because only one K is dealt with. The first-order effect of a potential energy change, δV, is given by

$$\delta K = -\int (\delta V/E')\mathfrak{F}^2 d\rho = -\frac{0.618}{(E_{\mathrm{Mev}})^{\frac{1}{2}}}\int \delta V_{\mathrm{Mev}}\mathfrak{F}^2 d(rmc^2/e^2), \quad (2)$$

where $\mathfrak{F}$ is $r\times$the radial wave function and the energy of relative motion is E' so that

$$E = 2E'. \quad (3)$$

For a "square well" potential the first-order phase shift caused by a change in well depth, δD, is given by

$$\delta_1 K = \rho_0 \mathfrak{F}^2(\rho_0) J(z_0)\delta D/E, \quad (4)$$

where the quantity J is

$$J(z_0) = \int_0^{z_0} (\sin^2 z/\sin^2 z_0)dz = (z_0 - \sin z_0 \cos z_0)/(z_0 \sin^2 z_0). \quad (4.1)$$

[8] L. E. Hoisington, S. S. Share, and G. Breit, Phys. Rev. 56, 884 (1939).

In these formulas the quantity ρ is the distance expressed in wave-length/2π while z is the phase of the sine curve representing the wave function inside the potential well, counting the phase as 0 at $r=0$. Subscripts 0 in these formulas indicate that quantities are evaluated at the edge of the potential energy well for which $r=r_0$. A change in width of the potential energy well gives a similar change in phase shift:

$$\delta_2 K = 2\rho_0 \mathfrak{F}^2(\rho_0)(D/E)(\delta r_0/r_0), \tag{5}$$

where δr_0 is the change in range. The combined phase shift is given by

$$\delta_1 K + \delta_2 K = 2\rho_0 \mathfrak{F}^2(\rho_0)(D/E)(\delta r_0/r_0)[1+\lambda J(z_0)], \tag{6}$$

where

$$\lambda = (\delta D/2D)/(\delta r_0/r_0). \tag{6.1}$$

If the change in range has to be compensated by a change in depth at energy E_{I} one has to determine λ by

$$J(z_{0,\mathrm{I}}) = -1/\lambda_{\mathrm{I}}. \tag{6.2}$$

A potential energy lump extending through ΔR at distance R is

$$\delta_3 K = -2\mathfrak{F}^2(kR)(\delta V)k\Delta R/E. \tag{7}$$

If the effect of the potential energy lump is compensated for by a change in well depth at energy E_{I}, the remaining phase shift is given by

$$\delta_3' K = -2[\mathfrak{F}^2(kR) - a_{\mathrm{I}} J(z_0)\mathfrak{F}^2(kr_0)]k(\delta V)\Delta R/E, \tag{8}$$

where the energy independent number a_{I} is given by

$$a_{\mathrm{I}} = \mathfrak{F}^2(k_{\mathrm{I}}R)/[J(z_{0,\mathrm{I}})\mathfrak{F}^2(k_{\mathrm{I}}r_0)]. \tag{8.1}$$

The ratio of the phase shift produced by q to the phase shift produced by a change in r_0, if both are compensated at energy E_{I}, is given by

$$\frac{\delta_3' K}{\delta_1 K + \delta_2 K} = \frac{(\delta V)\Delta R}{D\delta r_0} Y, \tag{9}$$

where the quantity Y is

$$Y = -\frac{\mathfrak{F}^2(kR) - aJ\mathfrak{F}^2(kr_0)}{\mathfrak{F}^2(kr_0)(1+\lambda J)}. \tag{10}$$

The quantity Y has the meaning

$$Y = S'_{\mathrm{pot}}/S'_{\mathrm{range}}, \tag{11}$$

where

$$S' = \text{relative sensitivity}. \tag{11.1}$$

It follows from Eq. (2) and Eq. (8) that the fractional sensitivity of scattering to q of Eq. (1.1) is given by

$$X_{\mathrm{I}} = \frac{0.618}{(E_{\mathrm{Mev}})^{\frac{1}{2}}} \frac{\partial \mathfrak{R}}{\mathfrak{R}\partial K}[\mathfrak{F}^2(kR) - a_{\mathrm{I}} J\mathfrak{F}^2(kr_0)], \tag{12}$$

so that

$$X_{\mathrm{I}} = d_{\mathrm{I}}\mathfrak{R}/\mathfrak{R}d_{\mathrm{I}}q, \tag{13}$$

where d_{I} stands for differentiation for effect of δV when δV is compensated by δD at $E=E_{\mathrm{I}}$. If the potential lump effect is compensated for by well depth change at energy E_{I} and if, in addition, a change in range is made and also compensated for by a well depth change at energy E_{I}, and if the two changes are opposed in such a way as to compensate each other's effects at the energy E_{II}, then the fractional sensitivity to the quantity q at energy E is given by

$$Z_{\mathrm{I,II}}(E) = X_{\mathrm{I}}(E)[1 - Y_{\mathrm{I}}(E_{\mathrm{II}})/Y_{\mathrm{I}}(E)]. \tag{14}$$

In this formula the term 1 in the square brackets together with the factor X_{I} represents the sensitivity to q as in Eq. (12). The remaining term in square brackets together with the factor X_{I} is, on account of Eq. (11), the compensating fractional rate of change of scattering produced by the change in range. The proportionality factor $Y_{\mathrm{I}}(E_{\mathrm{II}})$ is adjusted so that the change in range compensates for the effect of the potential lump at energy E_{II}. This means that δr_0 in Eq. (9) is suitably chosen to give compensation at E_{II}. The quantity $Z_{\mathrm{I,II}}$ is symmetrical in I, II and one verifies that

$$Z_{\mathrm{I,II}} = Z_{\mathrm{II,I}} = 0.618(E_{\mathrm{Mev}})^{-\frac{1}{2}} \frac{\partial \mathfrak{R}}{\mathfrak{R}\partial K} \times \left\{ \mathfrak{F}^2(kR) + \frac{\mathfrak{F}^2(kr_0)}{J_{\mathrm{I}} - J_{\mathrm{II}}} \left[\frac{\mathfrak{F}^2(k_{\mathrm{II}}R)}{\mathfrak{F}^2(k_{\mathrm{II}}r_0)}(J - J_{\mathrm{I}}) + \frac{\mathfrak{F}^2(k_{\mathrm{I}}R)}{\mathfrak{F}^2(k_{\mathrm{I}}r_0)}(J_{\mathrm{II}} - J) \right] \right\}, \tag{15}$$

and $Z_{\mathrm{I,II}}$ = fractional sensitivity of scattering to

potential change (in Mev, and e^2/mc^2) compensated by potential depth and range changes at E_I and E_{II}. The calculation of $\partial\mathfrak{R}/\partial K$ was made by means of

$$\frac{\partial\mathfrak{R}}{\partial K}=-\frac{2X}{\eta\mathfrak{M}}\cos 2K+\left(\frac{4}{\eta^2\mathfrak{M}}+\frac{2Y}{\eta\mathfrak{M}}\right)\sin 2K. \quad (16)$$

Other formulas and tables in BTE were used. Additional Coulomb functions for higher energies were obtained from the paper by Thaxton and Hoisington[9] and a few additional Coulomb functions were computed directly.

III. RESULTS AND DISCUSSION

In Fig. 1 the quantity X is plotted against the energy for $R=5e^2/mc^2$, $E_I=1.994$, 1.001 Mev for the scattering angle $\Theta=45°$, 35°, 25°. The quantity X, it will be remembered, is the fractional sensitivity to the quantity q when the potential is put at distance R; it is understood that the effect of the potential lump is compensated by a suitable change in well depth. For $E_I=1.00$ Mev, the curve for $\Theta=45°$ crosses through 0 once. If, however, $E_I=2.00$ Mev, the curve for $\Theta=45°$ crosses the axis of $X=0$ not only at 2.00 Mev but also between 3 and 4 Mev. The second crossing is caused by a node of $\mathfrak{F}$ going through $r=5e^2/mc^2$. On account of the second crossing the much higher sensitivity of scattering to the exterior part of the potential is especially marked in this case. The sensitivity to q is seen to be higher at $\Theta=45°$ than at other angles. The effect is still pronounced at $\Theta=35°$. At $\Theta=45°$ the scattering as a function of angle is nearly a minimum, and sufficiently small angular apertures or receiving slits in a scattering chamber should be attainable for approximating the more favorable conditions close to $\Theta=45°$. In Fig. 2 the quantity X is plotted against E for $R=3e^2/mc^2$, $E_I=4.00$, 2.07 Mev, and $\Theta=45°$, 35°, 25°. Comparison of Fig. 2 with Fig. 1 shows that the sensitivity to q is smaller for $R=3e^2/mc^2$ than for $R=5e^2/mc^2$ at 1 Mev. The ratio is roughly represented by a factor of 2 or 3. In other respects the two values of R compared in Figs. 1 and 2 give similar behavior of X on E.

In Fig. 3 the quantity Z for $R=5e^2/mc^2$ is plotted against E. Here $E_I=1$ Mev while E_{II} has been given the values 2 Mev, 4 Mev, respectively, for the two sets of graphs. In this comparison the value of observations in the high energy range 5 Mev–9 Mev shows up to better advantage than in Figs. 1, 2. Nevertheless, it is seen that simultaneous compensation of change of range and addition of potential energy at $R=5e^2/mc^2$ at both 1 Mev and 2 Mev makes observations at 0.5 Mev and 0.3 Mev of about equal interest with those at 9 Mev. The required accelerating equipment is more modest for the lower energy range, although there are technical difficulties in counting low energy protons which are absent at the higher energies. For these there is only a slight difference in the effectiveness of scattering angles 45°, 35°, 25°, while for lower energies 45° is by far the more effective angle in detecting changes in scattering produced by q. As is well known, the scattering approaches spherical symmetry in the center of mass system of the two protons at the higher energies. There is, accordingly, no decrease of sensitivity towards the smaller angles. This advantage is present only if *absolute* measurements are made, i.e., if the yield of scattered protons per incident proton is determined. On the other hand, absolute measurements are usually more difficult than the determination of angular distributions. Checks on absolute measurements are also difficult, requiring repetition of experiments with different geometries. It is felt, therefore, that the apparent advantage of the availability of a wide angular range at high energies for testing the potential extension at R is partly offset by the necessity of drawing conclusions from absolute determinations of the scattered proton yield. There is also the added uncertainty of the effects of phase shifts corresponding to high angular momenta which enters at high energies more seriously than at the low ones. For the latter the consistency of ratios of observed scattering with expectation for a given K at a given energy is itself a test of the correctness of absolute yield determinations, as is well known.[5,7] The wave scattered by the Coulombian potential can be used as a reference standard for the wave scattered on account of the change in the s wave produced by the potential well. If one were to assume that phase shifts for angular momenta

[9] H. M. Thaxton and L. E. Hoisington, Phys. Rev. **56**, 1194 (1939).

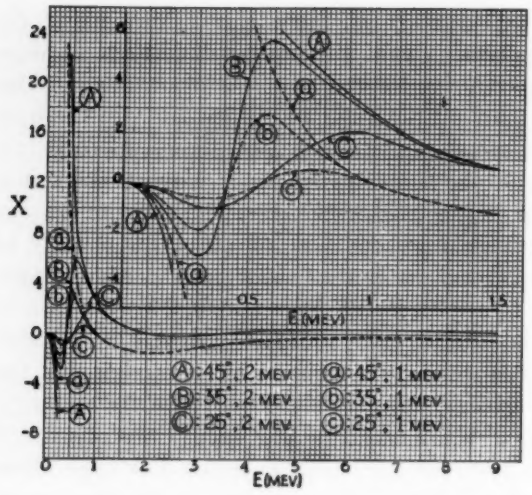

FIG. 1. X of Eqs. (12) and (13) as a function of energy for $R=5e^2/mc^2$. Here X is the fractional sensitivity of scattering to quantity q of Eq. (1.1) when the potential change is placed at R. Curves A, B, C are for compensation by potential well depth change at 2 Mev; curves a, b, c are for the same at 1 Mev.

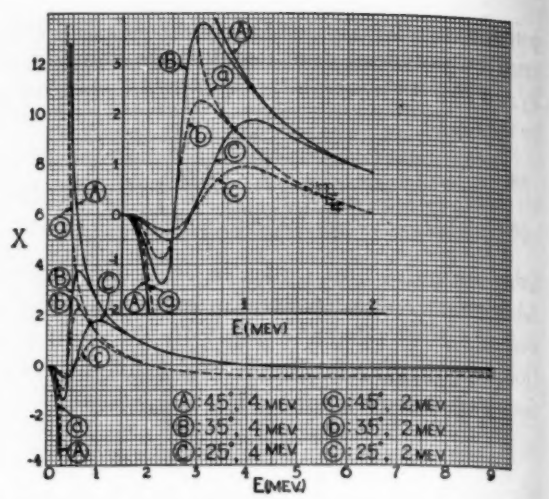

FIG. 2. X of Eqs. (12) and (13) as a function of energy for $R=3e^2/mc^2$. Curves A, B, C are for compensation by potential well depth change at 4 Mev, and curves a, b, c are for the same at 2 Mev.

higher than 0 are absent one could do away with absolute yield determinations in this region. It is seen, therefore, that the drop in sensitivity at $\Theta=35°$, 25° is not a disadvantage but can even be used. If compensation of potential extension, range, and well depth is made at 1 Mev and 4 Mev, the lower energy range shows up somewhat better in comparison with that between 7 and 9 Mev. In this case $\Theta=35°$ gives a peak sensitivity for differentiation between the two types of potential energy changes which is higher than that at 9 Mev. In Fig. 4 the quantity Z is plotted against E for $R=3e^2/mc^2$ with compensation at 1 Mev and 4 Mev. The higher energy range shows more effectiveness in giving changes in scattering than in the previous figures. This is to be expected because the potential lump is put at a smaller distance. Here also the usefulness of observations in the low energy range is seen to be definite.

Estimates of potential energy×distance which are detectable by experiments of given fractional accuracy can be made as follows. Both X and Z are fractional rates of change of scattering with respect to q of Eq. (1.1). For X this relation is described by Eq. (12). For Z one has

$$Z_{\mathrm{I,II}}=d_{\mathrm{I,II}}\mathfrak{R}/\mathfrak{R}d_{\mathrm{I,II}}q, \tag{17}$$

where $d_{\mathrm{I,II}}$ stands for differentiation with respect to q subject to the requirement of compensating the effect of q at energies E_{I}, E_{II} by changes in potential depth D and range of force r_0. If either Z or X has the absolute value 1 and if the experimental accuracy is 1 percent so that $\delta\mathfrak{R}/\mathfrak{R}=1/100$ then, according to Eqs. (12), (17), the detectable δq is 0.01 Mev=10 kev. For $r=5e^2/mc^2$, $E_{\mathrm{I}}=1$ Mev, $E_{\mathrm{II}}=4$ Mev, Fig. 3 shows values of Z at $\Theta=45°$ exceeding 10 which corresponds to the possibility of detecting with a 1 percent accuracy in the measured scattering of an interaction potential of less than 1 kev through a distance e^2/mc^2. This very high sensitivity is perhaps not fully attainable because it is mainly the result of the smallness of scattering at 45° when the interference between the Coulomb and non-Coulomb waves becomes pronounced. But even for $\Theta=35°$ for the distance R and compensation energies just mentioned Z takes on the value 2 and more corresponding to the possibility of detecting less than 5 kev through a distance e^2/mc^2. For $R=3e^2/mc^2$ the sensitivity to q is appreciably smaller. In order to detect 5 kev through e^2/mc^2 one needs, in this case, according to Fig. 4, measurements at $\Theta=45°$ close to 400 kev while $\Theta=35°$ gives at best the possibility of detecting 30 kev through a distance e^2/mc^2. The ordinates in Figs. 1 and 2 correspond to still higher sensitivities. Thus, according to Fig. 2, even for $R=3e^2/mc^2$ one can

detect $q=0.01$ Mev (e^2/mc^2). The possibility of doing so presupposes, however, that the range of the main part of the potential well is known in some other way. It is probable that Figs. 3 and 4 are more representative of what is attainable.

In the comparisons of sensitivity made so far it was supposed that the shape of the potential energy curve is known or decided on in some way except for the hypothetical addition to the potential described by q and the depth and range of the main part of the potential well. Such a procedure corresponds to fitting the experimental material by three parameters: depth and range of the potential well (for a preassigned shape of well), and in addition the quantity q for a preassigned R which adds essentially a tail to the potential well. Three energies are required in principle to determine the three parameters and, again in principle, a fourth energy could be used to determine a fourth parameter. In practice, however, the experimental accuracy will make it necessary to be more modest in the number of parameters derived from experiment.

If it is desired to distinguish between two alternative theories containing the three parameters in such a way as to have a short-range potential of unknown depth and width superposed on a long-range potential of known range but unknown depth or height the above estimates or their obvious extensions can be used for obtaining an idea of the possibility of determining the magnitude of the long-range part. The question arises as to what can be attempted to determine the range of the long-range part of the potential. To do this one has to adjust theory to experiment at 4 values of E.

In such a determination experimental information regarding the phase shifts for higher angular momenta may give valuable clues because these phase shifts are more easily produced by interaction potentials at larger distances. In principle, however, it is hard to exclude nearly unrelated potential energy curves for different angular momenta and it is desirable to be able to say something definite regarding sensitivity independently of any clues from other phase shifts than that of the s wave. The possibilities can be seen by comparing the values of Z for compensation at 1 Mev and 4 Mev for $R=5e^2/mc^2$ and $3e^2/mc^2$, respectively. The ratio of the sensitivities has the approximate values 1 at 9 Mev, 2 at 5 Mev, 5 at 2 Mev, 7.5 at 0.6 Mev, 8 at 0.35 Mev, 9.5 at 0.2 Mev. Accordingly, fitting at 0.2 Mev, 1 Mev, 4 Mev will not distinguish between a value q for $R=5e^2/mc^2$ and $q/10$ at $R=3e^2/mc^2$. On the other hand, an additional fit at say 9 Mev will distinguish between these possibilities determining essentially $q(3e^2/mc^2)+q(5e^2/mc^2)$, while the 0.2 Mev region determines approximately $q(3e^2/mc^2)+10q(5e^2/mc^2)$. The error of $q(3e^2/mc^2)$ is thus not decreased by

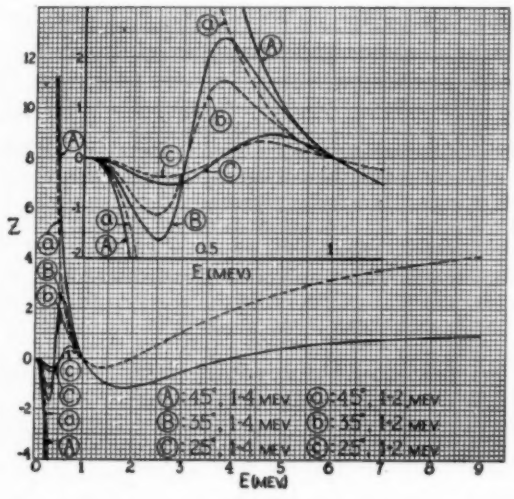

FIG. 3. Z of Eqs. (14) and (15) as a function of energy for $R=5e^2/mc^2$. Here Z is the fractional sensitivity of scattering to potential change at R compensated by potential well depth and range changes at energies E_I and E_{II}. For curves A, B, C, $E_I=1$ Mev, $E_{II}=4$ Mev. For curves a, b, c, $E_I=1$ Mev, $E_{II}=2$ Mev.

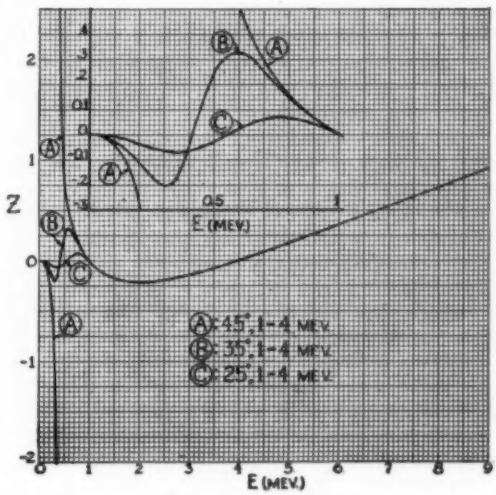

FIG. 4. Graph of Z of Eqs. (14) and (15) against energy for $R=3e^2/mc^2$. In this case, $E_I=1$ Mev, $E_{II}=4$ Mev.

the inclusion, in this case, of data at 0.2 Mev. The relations between errors in a fit of data at 4 energies can be expressed as follows. The quantity $Z_{I,II}$ is a function of energy E and of the distance R at which the potential change is made. For fixed E_I, E_{II}, the symbol ζ will be used for $Z_{I,II}$. The quantity ζ will be denoted by

$$\zeta_1(a),\quad \zeta_1(b),\quad \zeta_2(a),\quad \zeta_2(b),$$

for the pairs of values (E_1, R_a), (E_1, R_b), (E_2, R_a), (E_2, R_b) of E and R, respectively. It will be supposed that after the potential well has been adjusted there remain fractional deviations δ_1, δ_2 of experiment from theory at the energies E_1, E_2, respectively. The values of q at R_a, R_b will be denoted by q_a, q_b, respectively. There are then the equations

$$\begin{aligned}\zeta_1(a)q_a+\zeta_1(b)q_b&=\delta_1,\\ \zeta_2(a)q_a+\zeta_2(b)q_b&=\delta_2,\end{aligned}\tag{18}$$

that determine q_a, q_b as

$$\begin{aligned}q_a&=\frac{\delta_1/\zeta_1(b)-\delta_2/\zeta_2(b)}{\zeta_1(a)/\zeta_1(b)-\zeta_2(a)/\zeta_2(b)},\\ q_b&=\frac{\delta_1/\zeta_1(a)-\delta_2/\zeta_2(a)}{\zeta_1(b)/\zeta_1(a)-\zeta_2(b)/\zeta_2(a)}.\end{aligned}\tag{19}$$

The accuracy of the determination of q_a, q_b depends on the uncertainty in the values of δ_1 and δ_2. If through the use of the low energy region one makes $\zeta_1(a)$ and $\zeta_1(b)$ very large, one only renders the terms in δ_1 negligible and makes the terms in δ_2 the only important ones. For an extreme condition of entire suppression of δ_1 and for $\zeta_1(b)\gg\zeta_1(a)$ which corresponds to $R_b=5e^2/mc^2$, $R_a=3e^2/mc^2$, one has the following limiting form of the above equations

$$\begin{aligned}q_a&\cong+\delta_2/\zeta_2(a),\\ q_b&\cong-\zeta_1(a)\delta_2/[\zeta_1(b)\zeta_2(a)].\end{aligned}\tag{20}$$

The largeness of both $\zeta_1(a)$ and $\zeta_1(b)$ is supposed here to be a stronger condition than $\zeta_1(b)\gg\zeta_1(a)$. The accuracy in the knowledge of q_a is thus not helped at all by the high values of $\zeta_1(a)$, $\zeta_1(b)$ in this instance. The accuracy in the knowledge of q_b is, however, appreciably improved by having $\zeta_1(b)\gg\zeta_1(a)$. In fitting data at four energies, the usefulness of the high sensitivity in the low energy region is seen to be more limited. The weakest link in the chain counts most, and there is only a limited value in having one region of high sensitivity. Since, however, by increasing the energy beyond 9 Mev one may hope to obtain an improved sensitivity at the high energy end, the low energy region in the vicinity of 0.4 Mev should be a good one to combine with the high energy end since by doing so both ζ_1 and ζ_2 can be enlarged.

The calculations reported on here show that it may be just as important to improve counting techniques for measurements in the energy range 0.2 to 0.5 Mev in order to obtain additional information regarding the shape of the proton-proton potential energy curves as to be extending observations into the 10-Mev region. Questions of phase shifts for higher angular momenta are less troublesome and may be perhaps non-existent in the low energy range. Questions of velocity dependence of the interaction potential are reduced in importance and relatively modest proton accelerating equipment is required.

The Ultraviolet Spectrum of the Sun from V-2 Rockets*

JOHN J. HOPFIELD AND HAROLD E. CLEARMAN, JR.
Applied Physics Laboratory, Johns Hopkins University, Silver Spring, Maryland

(Received December 19, 1947)

Spectra of the sun have been obtained from V-2 rockets at heights up to 155 km. A grating spectrograph was used giving a dispersion of 34A/mm. The ultraviolet spectrum of the sun obtained extends down to λ2300A, and traces are evident as far as λ2230A. A tentative list of identified lines is given. The MgII resonance doublet at λ2800A is observed to have emission centers in both absorption components. The intensity of this emission is estimated as about 10 percent that of the adjacent continuum.

I. INTRODUCTION

ONE of the outstanding developments of World War II was the German V-2 rocket. The great loads it can carry (payload 2000 pounds), its relatively small acceleration while rising (about 5 g maximum) and the great altitudes it can attain make it an excellent vehicle for certain types of high altitude research.** The study of the ultraviolet spectrum of the sun, practically free from absorption in the earth's atmosphere, is one of these.

Further essentials to this type of research[1] are techniques for post-flight recovery of photographic film, for the telemetering of data from the rocket in flight, and for radar and theodolite tracking of the rocket.

The first attempt of this laboratory to obtain the spectrum of the sun from German V-2 rockets was made in October 1946. The spectrograph used then was one containing lithium fluoride lenses and prism. It was built for us by the Bausch and Lomb Optical Company. This attempt resulted in failure due to a light leak into the cassette of the spectrograph which fogged the film. This leak was caused by the shock of terminal impact of the warhead of the rocket with the ground.

To avoid some difficulties that were experienced with lithium fluoride lenses and prisms, we have subsequently used reflecting concave grating spectrographs. More nearly shock proof cassettes have been provided.

Two flights have been successful in obtaining sun spectrograms. These were on April 1, 1947, and July 29, 1947. These flights will be referred to as Flights A and B, respectively, in this report.

Flight A took place at noon approximately; and Flight B, while it was planned for sunset firing in order to obtain more detail of atmospheric absorption,[2] actually took place a little after sunrise of a following day.

Since after an initial period of roll-stabilized and nearly vertical flight, the rocket rolls and tumbles, it is necessary to devise some means of directing sunlight into the spectrograph during such angular motion of the rocket. Front reflecting surfaces were used for shining the sunlight into the slits of the spectrograph in both Flights A and B. Because there was little absorbing medium in the path of light from the sun to the spectrograph at the heights at which most of the sun spectrograms were taken and because all reflecting surfaces, mirrors, and gratings were front-aluminized and ultraviolet sensitive film was used, the light intensity and the ultraviolet limit reached should be limited only by the strength of the incident solar radiation. These ideal conditions, however, were not realized in practice. For aside from the decreasing reflecting power of aluminum toward shorter wave-lengths, the parallel decrease of the iron comparison spectrum and the solar spectrum in the region of λ2300A, Figs. 2, 3, and other data indicate a rapid decrease in film sensitivity be-

* This work was done under Navy Bureau of Ordnance Contract NOrd 7386.

** For description of the V-2, see H. S. Siefert, M. M. Mills, and M. Summerfield, Am. J. Phys. **15**, 1, 121, 255 (1947) and J. M. J. Kooy and J. W. H. Uytenbogaart, *Ballistics of the Future* (Technical Publishing Company, H. Stam, Haarlem, Holland, 1946).

[1] L. W. Fraser, R. P. Petersen, H. E. Tatel, and J. A. Van Allen, Phys. Rev. **72**, 173 (1947).

[2] J. J. Hopfield, "U.V. absorption of air," Astrophys. J. **104**, 208 (1946).

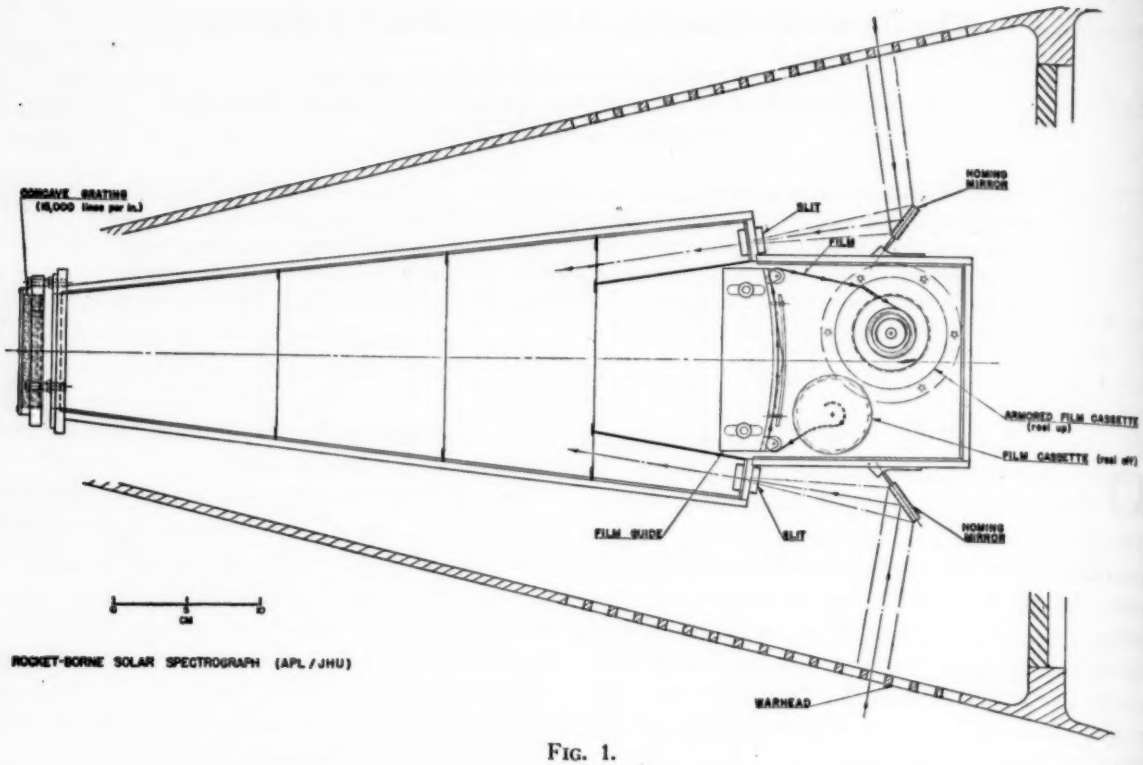

FIG. 1.

ginning at this point and extending to shorter wave-lengths.

Spectrograms of the sun using the V-2 rocket have also been obtained by a group at the Naval Research Laboratory[3,4]

II. SUN SPECTROGRAPHS

The sun spectrographs used in flights of April 1 and July 29 were alike in most details except for the illuminating devices used and the slits. It is the newer one which is shown in detail in the drawing Fig. 1. In this figure, the spectrograph is shown drawn to scale and in place in the nose of the rocket. Some of the special features of this spectrograph are the following: The spectrograph employed two slits, one on each side of the normal to the grating in order to use either side of the rocket which chanced to face the sun while the rocket was in rolling flight. One of these slits was slightly above and the other slightly below the Rowland circle of the grating, so that the two spectra obtained ran in opposite directions and side by side with a few millimeters space between them.

The slit jaws were made of hardened steel, and were fixed into threaded (40 threads per inch) tubes which could be screwed in and out for focusing the instrument. The slits were 0.025 mm wide and masked down to a 2-mm length. The grating was mounted on push-pull screws and the film cassette was movable. The final focusing was done by adjusting all three to give the best results.

The body of the spectrograph was made of $\frac{1}{4}$-in. aluminum plates fitted together with step lap joints and held by screws. The interior surfaces of the spectrograph and all light baffles were sandblasted and then painted a dull black to reduce light reflection. The spectrograph was fitted with a light trapped vent which permitted the air pressure in the spectrograph to be at approximately the ambient pressure at all times.

The grating was made at the Department of Physics, Johns Hopkins University. It was ruled on aluminized glass, with 15,000 lines/inch and had a radius of curvature of 50 cm. The rulings happened to be shaped to give much greater in-

[3] W. A. Baum, F. S. Johnson, J. J. Oberly, C. C. Rockwood, C. V. Strain, and R. Tausey, Phys. Rev. 70, 781 (1946).

[4] E. Durand, J. J. Oberly, and R. Tausey, Phys. Rev. 71, 827 (1947).

tensity in the spectrum from one side than from the other.

The spectra were photographed on 35-mm Eastman spectroscopic film, Type 103a–0, which is sensitive to the ultraviolet. The film platen and the film cassettes with the reel-off and reel-up spools are shown in Fig. 1. The armored film cassette (reel-up) was turned from a block of cold-rolled steel. It had a wall thickness of 1.8 cm, and provided with a screw cap of the same thickness. The entrance slot for the film was faced with black velvet to keep out the light. The reel-up spool was driven by a 24-v d.c. motor powered with batteries. The film change took less than 1 second.

The series of exposures was controlled by a switch, operated by a cam driven by a separate motor, which started automatically at rocket take-off. The cam was designed to make a series of 14 exposures of 5 seconds each during the rocket's powered flight while it was roll-stabilized, followed by a series of five exposures of 55 seconds each over the rest of the flight.

Shutters, operated by solenoids in parallel with this motor, shut off the light while the film was being changed. The warhead was blown off during the descent of the rocket thus reducing the landing speed from about 5000 feet per second, in which case all records are destroyed, to the order of two to three hundred feet per second. The film in the reel-up cassette was recovered in excellent condition.

TABLE I. Heights of exposures.

Spectrum no.	Flight	Altitude (km) Initial	Final	Weighted mean	Figure
A1	April 1	38	96	80	7
A2	April 1	103	123	115	
B1	July 29	64	116	95	
B2	July 29	116	148	135	
B3	July 29	148	159	155	
B4	July 29	159	148	155	6
B5	July 29	149	118	135	2, 3, 4, 5

III. ILLUMINATION

The sunlight was made diffuse by reflection from rough patterned glass in the spectrograph of April 1 and was directed into the spectrograph by plane mirrors before the slits. A sun "homing" device was used with the spectrograph of July 29. It was designed for sunset or sunrise firing and utilized a partially diffusing mirror before each slit. These mirrors consisted of two corrugated cylindrical concave mirrors placed back to back with their axes parallel and with the corrugations forming arcs of the cylinder normal to the plane of the incident and reflected light. The corrugated mirrors stretched the sun's image into a line about 5 mm wide and about 60° long in the plane of the paper (Fig. 1). The length of this beam, therefore, should compensate for a 30° tumble of the rocket. The mirrors rotated about shafts nearly coincident with the central elements of the cylinders. The shafts made angles of 45° downward from the axis of the rocket. The photoelectrically controlled rotation of these

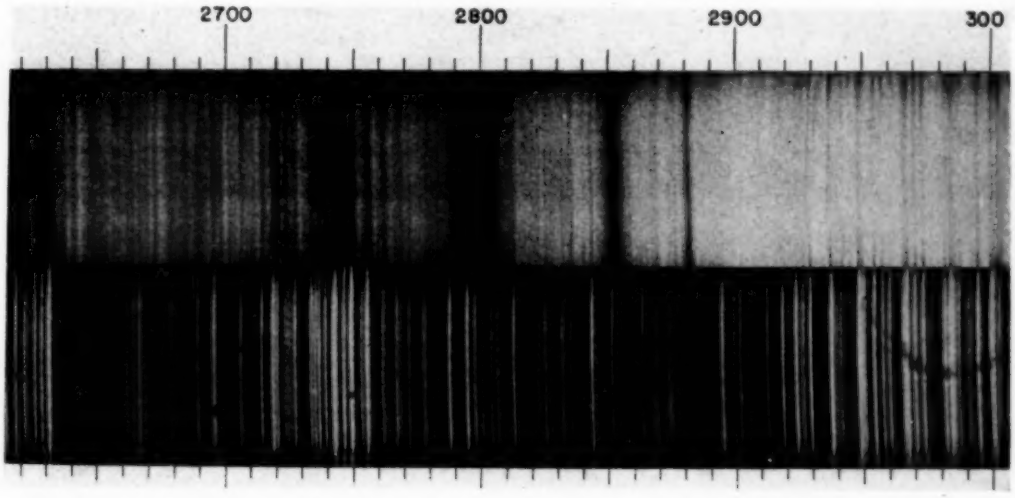

FIG. 2.

mirrors about their axes brought about by this light streak falling between the two midget photo-cells which were placed just above and below each slit constituted the control for the homing about this degree of freedom. This control was such that when the two photocells were equally illuminated by the light streak falling across them and the slit between them, the mechanism was in balance and the streak remained on the slit. When the spectrograph turned away from the sun, the motors turned the mirrors continuously in "hunting" until the sunlight returned. Independent homing systems were used for each slit.

As already mentioned, solenoid-operated shutters cut off the light while the film was being changed. A second pair of photo-cells near each slit was connected to a channel of the telemetering system and the time of illumination of the slits was recorded at the ground station. The voltage across the film drive motor, already mentioned, was also fed into the telemetering system. One could deduce the exposure of the various spectrograms from these combined records.

Because a single large hole in the side of the warhead for admitting the sunlight might be destructive to the mirror mechanism on account of the strong slip stream of the rocket, an array of ½-inch holes with about 50 percent over-all efficiency was used for admitting the sunlight to homing mirrors (see Fig. 1).

IV. RESULTS

The V-2 rocket with the spectrograph which was designed for vertical exposure was fired at 1:10 P.M. M.S.T. on April 1, 1947. The V-2 rocket with the spectrograph designed for horizontal exposure was fired a little after sunrise, 5:55 A.M., M.S.T. on July 29, 1947. The strong side of the grating in spectrograph B had been oriented for a sunset firing. However, trouble with other apparatus in the rocket changed the program to the above time so that the weak side of the grating now faced the sun while the rocket was in roll-stabilized vertical flight. Furthermore, the telemetering record shows that the "homer" on the sunrise side failed for the early part of the flight so that the spectra intended to measure the stratification of ozone and other absorbing gases of the earth's atmosphere were missed.

The height limits and the weighted mean heights of each exposure are given in Table I. This table lists the two spectra taken in the flight of April 1 and the five taken on July 29. The altitude data of Table I were calculated from the telemetered signals in connection with the trajectory as established by optical theodolite and radar tracking.

The spectra appearing in Figs. 2 and 3 show the sun spectrum above and the corresponding iron spectrum below it. The iron spectrum was made with the rocket spectrograph on separate film before the spectrograph was mounted in the rocket. The iron spectrum was then matched

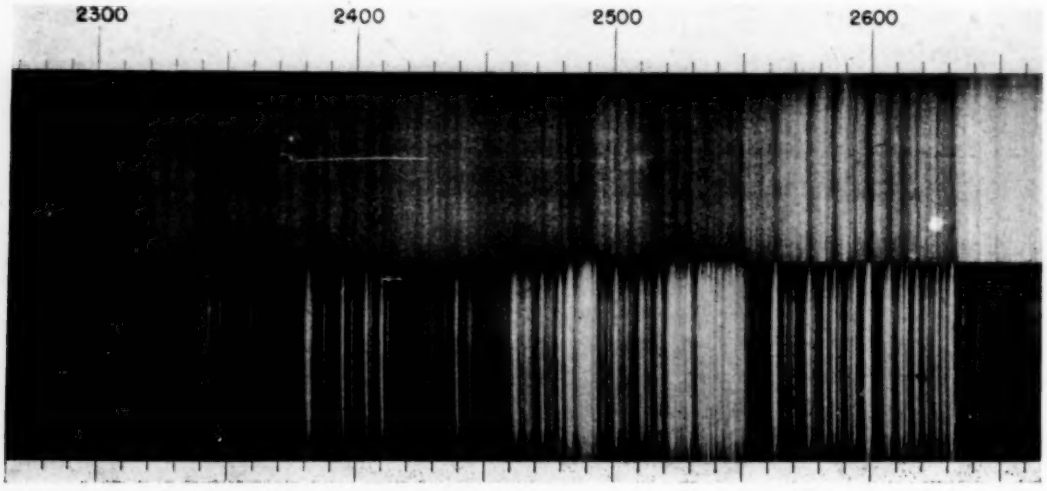

FIG. 3.

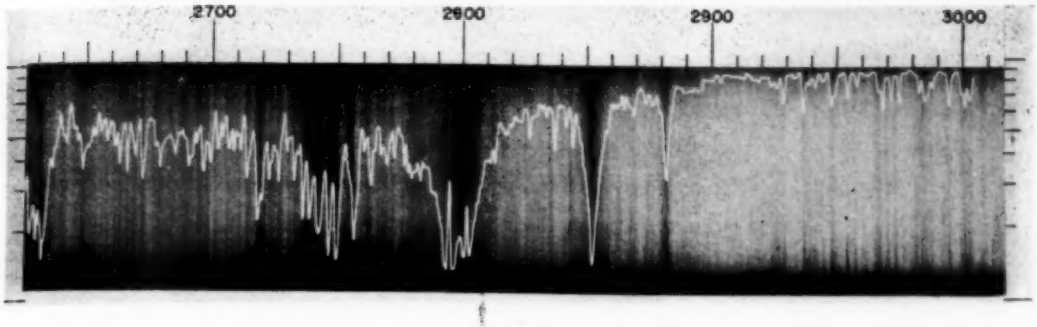

FIG. 4.

with Fraunhofer spectrum of the sun in the enlargement and the two mounted side by side. It is seen from these spectra that the iron spectrum is a dominant one in the sun in the region λ2300–3000A.

The spectra in Figs. 4 and 5 are the same sun spectrum pictures as those of Figs. 2 and 3, but with the microphotometer curve of intensity projected upon the spectra. It was not easily possible to position the intensity curves exactly on the spectrograms chiefly on account of the kind of recording microphotometer used. The slight shifts that exist, however, will cause the reader no confusion in the correlation of the curve and the features of the sun spectrum. The curves are uncalibrated traces, and the scales at the ends are arbitrary logarithmic scales, with the bottom lines marking the background intensity and top lines marking zero intensity.

The spectrum appearing in Fig. 6 shows the washed-out features resulting from underexposure in some parts, yet shows more details in parts where the spectra of Figs. 2 and 4 are overexposed. A comparison of the spectrum of Fig. 6 with those of Figs. 4 and 5 indicates a greater exposure in future flights will extend the sun spectrum and fill in more detail in the region λ2300–2600A. Such greater exposure is contemplated for succeeding "shoots" when "homing" in two degrees of freedom will be provided.

The spectra shown in Fig. 7 were taken on the April 1 "shoot." They do not have as good resolution as the other spectra and are shown only for comparison purposes.

Three sets of sensitometric exposures were made on film cut from the same roll as that used for the sun spectra. These exposures were made using a medium quartz spectrograph, a quartz mercury arc, and a step sector photometer. One of these sets was placed in the reel-up cassette of the rocket spectrograph; another was placed in a strong cylinder and bolted inside the warhead of the rocket; while the third set was held in storage at WSPG in New Mexico. On recovery of the film after the firing of the rocket, all film was processed together. Sets 1 and 2, therefore, had the same thermal, mechanical, and chemical history as the film of the sun spectrum except that the sensitometric exposures were made a few days earlier. The appearance of the background of all the developed films shows them to be alike.

Table II gives a preliminary list of identified

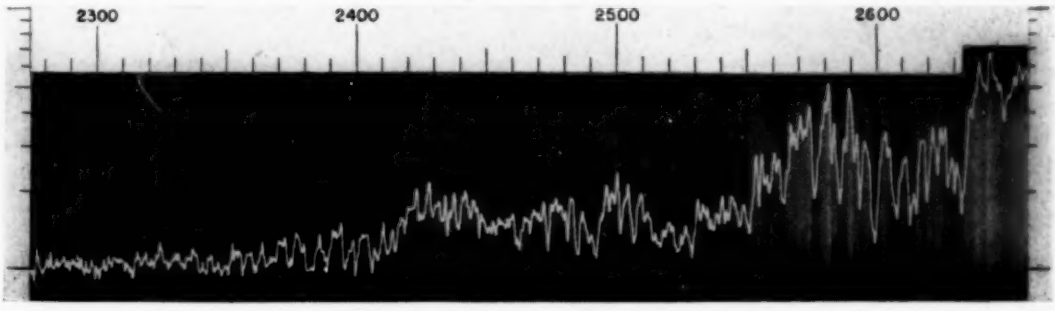

FIG. 5.

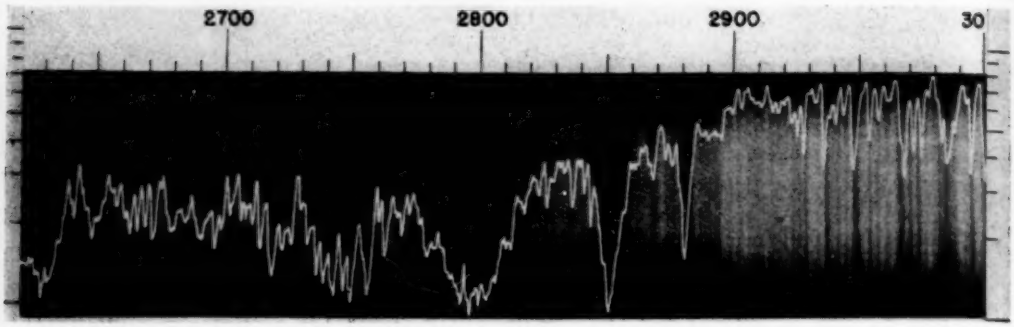

FIG. 6.

lines. As there was no provision for a comparison spectrum, a rough calibration of wave-lengths was made by matching the laboratory spectrum of iron against the solar spectrum. Further precision was attained by using internal standards of chosen iron lines of the solar spectrum. These were selected from among the least blended iron lines as indicated by a table of multiplets kindly furnished to us by Dr. C. M. Sitterly of the National Bureau of Standards. Because of blending, the scatter is large, so that wave-lengths are given to only 0.1A. All unidentified lines and lines identified as blends of several weak ones have been omitted from this preliminary table. The spectrum studied thus far extends to only λ2500A. The study of the lines on the short wave-length side of λ2500A is in progress.

One of the prominent features of the spectrum is the MgII doublet (3^2S-3^2P) at λ2796–λ2803A. This doublet is analagous to the H and K Fraunhofer lines of the solar spectrum due to CaII. The MgII lines are so wide that they overlap, yet each has an emission core located at the center of the line to within the limits of error of measurement. The intensity of the emission is estimated as about 10 percent of the neighboring continuum. A similar but weaker structure had already been observed in the CaII, H, and K Fraunhofer lines and is prominent in the *M*-type stars. An emission core of this type is possible for lines that show strongly in absorption such as the H and K lines due to CaII and which at the same time show strongly in emission in the flash spectrum which originated in the chromosphere of the sun. Solar eclipse data show that such is the case of the H and K lines, and may also be expected in the MgII lines λ2796, λ2803A when the flash spectrum of the sun is observed in this region. The origin of these emission cores is obviously in the high temperature luminous clouds which make up such features as the chromosphere and promi-

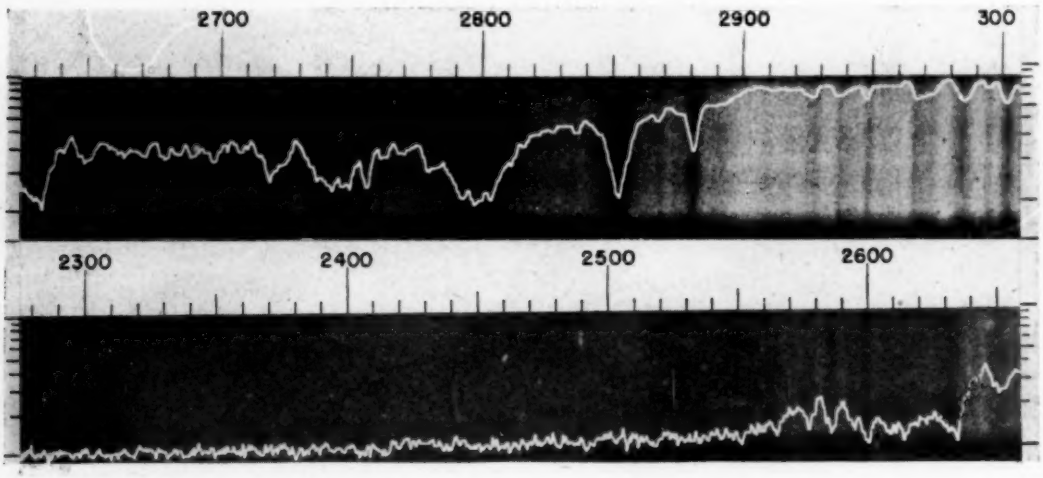

FIG. 7.

TABLE II. List of identified lines.

Wave-Length (A)	Identification		
2501.5	FeI	2501.13	$a^5D_4-x^5D_3^\circ$
03.7	FeII	03.32	$a^4G_{11/2}-z^2H_{11/2}^\circ$
	FeII	03.56	$a^4H_{9/2}-z^4I_{9/2}^\circ$
	FeII	03.87	$b^2G_{9/2}-x^2G_{9/2}^\circ$
06.7	SiI	06.89	$3p^2\ ^3P_1-4s\ ^3P_2^\circ$
10.7	FeI	10.83	$a^5D_3-x^5D_2^\circ$
11.7	FeII	11.76	$a^4F_{7/2}-z^4I_{9/2}^\circ$
14.0	SiI	14.32	$3p^2\ ^3P_0-4s\ ^3P_1^\circ$
16.3	SiI	16.11	$3p^2\ ^3P_2-4s\ ^3P_2^\circ$
19.0	SiI	19.20	$3p^2\ ^3P_1-4s\ ^3P_1^\circ$
23.6	FeI	22.84	$a^5D_4-x^5D_4^\circ$
	SiI	24.11	$3p^2\ ^3P_1-4s\ ^3P_0^\circ$
28.5	SiI	28.51	$3p^2\ ^3P_2-4s\ ^3P_1^\circ$
32.2	SiI	32.38	$3p^2\ ^1S-5s\ ^1P_1^\circ$
36.2	FeI	35.60	$a^5D_0-x^5D_1^\circ$
	FeII	36.67	$b^2H_{11/2}-x^4G_{11/2}^\circ$
40.9	FeII	40.67	$b^2D_{5/2}-w^2F_{7/2}^\circ$; $b^4F_{7/2}-y^4F_{9/2}^\circ$
	FeI	40.97	$a^5D_1-x^5D_2^\circ$
	FeII	41.10	$b^4F_{7/2}-y^4F_{5/2}^\circ$
45.6	FeI	45.97	$a^5D_2-x^5D_3^\circ$
	FeII	46.67	$b^4F_{7/2}-y^4F_{7/2}^\circ$
53.0	PI	53.28	$3p^3\ ^2P_{1/2}^\circ-4s\ ^2P_{1/2}$
55.2	PI	54.93	$3p^3\ ^2P_{3/2}^\circ-4s\ ^2P_{1/2}$
63.0	FeII	62.53	$a^4D_{7/2}-z^4P_{5/2}^\circ$
	FeII	63.47	$a^4D_{5/2}-z^4P_{3/2}^\circ$
67.6	FeII	66.90	$a^4D_{3/2}-z^4P_{1/2}^\circ$
	SiI	68.63	$3p^2\ ^1S-5s\ ^3P_1^\circ$
76.2	SiI	77.13	$3p^2\ ^1S-4d\ ^3D_1^\circ$
	FeII	77.92	$a^4D_{1/2}-z^4P_{1/2}^\circ$
82.3	FeII	82.58	$a^4D_{3/2}-z^4P_{3/2}^\circ$
85.6	FeII	85.87	$a^6D_{9/2}-z^6D_{7/2}^\circ$
91.2	FeII	91.54	$a^4D_{5/2}-z^4P_{5/2}^\circ$
93.7	NaI	93.82	$3^2S_{1/2}-7^2P_{3/2}^\circ$
	NaI	93.92	$3^2S_{1/2}-7^2P_{1/2}^\circ$
99.3	FeII	98.36	$a^6D_{7/2}-z^6D_{5/2}^\circ$
	FeII	99.39	$a^6D_{9/2}-z^6D_{9/2}^\circ$
2606.6	FeI	2606.83	$a^5F_4-x^5G_5^\circ$
	FeII	07.08	$a^6D_{5/2}-z^6D_{3/2}^\circ$
11.2	FeII	11.87	$a^6D_{7/2}-z^6D_{7/2}^\circ$
14.0	FeII	13.82	$a^6D_{3/2}-z^6D_{1/2}^\circ$
17.7	FeII	17.61	$a^6D_{5/2}-z^6D_{5/2}^\circ$
20.0	FeII	19.07	$b^4F_{9/2}-z^4G_{9/2}^\circ$
21.6	FeII	21.67	$a^6D_{1/2}-z^6D_{1/2}^\circ$
23.6	FeII	23.72	$b^4F_{5/2}-z^4G_{5/2}^\circ$
25.6	FeII	25.66	$a^6D_{7/2}-z^6D_{9/2}^\circ$
28.3	FeII	28.29	$a^6D_{1/2}-z^6D_{3/2}^\circ$
31.8	FeII	31.05	$a^6D_{3/2}-z^6D_{5/2}^\circ$
	FeII	31.32	$a^6D_{5/2}-z^6D_{7/2}^\circ$
64.1	FeII	64.66	$a^2F_{7/2}-y^2G_{9/2}^\circ$
66.5	FeII	66.63	$a^2F_{5/2}-y^2G_{7/2}^\circ$
80.7	NaI	80.33	$3^2S_{1/2}-6^2P_{3/2}^\circ$
	NaI	80.44	$3^2S_{1/2}-6^2P_{1/2}^\circ$
92.7	FeII	92.60	$b^2G_{9/2}-y^2H_{11/2}^\circ$
2702.1	VII	2702.18	$a^5D_3-z^3D_3^\circ$
03.5	FeII	03.98	$a^2F_{7/2}-z^2F_{7/2}^\circ$
06.8	VII	06.17	$a^5D_3-z^5F_4^\circ$
	VII	06.70	$a^5D_2-z^5D_2^\circ$
11.6	FeII	11.84	$a^4G_{11/2}-z^2I_{13/2}^\circ$
14.8	FeII	14.41	$a^4D_{7/2}-z^4D_{5/2}^\circ$
16.0	FeII	16.21	$a^2F_{5/2}-z^2F_{5/2}^\circ$
19.1	FeI	19.02	$a^5D_4-y^5P_3^\circ$
21.0	FeI	20.90	$a^5D_3-y^5P_2^\circ$
23.7	FeI	23.57	$a^5D_2-y^5P_1^\circ$
27.8	FeII	27.38	$a^4G_{11/2}-z^2G_{9/2}^\circ$
	FeII	27.54	$a^4D_{5/2}-z^4D_{3/2}^\circ$
30.8	FeII	30.87	$a^4D_{3/2}-z^4F_{3/2}^\circ$
33.8	FeI	33.58	$a^5F_5-w^5D_4^\circ$
37.2	FeI	37.31	$a^5D_1-y^5P_1^\circ$
39.8	FeII	39.54	$a^4D_{7/2}-z^4D_{7/2}^\circ$
42.3	FeI	42.26	$a^5F_3-w^5D_2^\circ$
	FeI	42.40	$a^5D_2-y^5P_2^\circ$
43.9	FeI	44.06	$a^5D_0-y^5P_1^\circ$
46.7	FeII	46.49	$a^4D_{3/2}-z^4F_{5/2}^\circ$
	FeII	46.98	$a^4D_{5/2}-z^4D_{5/2}^\circ$
	FeI	46.98	$a^5F_5-z^5H_6^\circ$
49.9	FeI	50.14	$a^5D_3-y^5P_3^\circ$
56.6	FeI	56.32	$a^5D_1-y^5P_2^\circ$
69.3	FeII	68.94	$a^4D_{3/2}-z^4D_{5/2}^\circ$
	FeII	69.15	$a^4G_{7/2}-z^4G_{9/2}^\circ$
	FeII	69.35	$a^4G_{11/2}-z^4I_{13/2}^\circ$; $b^2D_{5/2}-w^4F_{7/2}^\circ$
79.9	MgI	blend	$3p\ ^3P^\circ-p^2\ ^3P$
83.5	FeII	83.69	$b^2H_{11/2}-z^2G_{9/2}^\circ$
95.9	MgII	95.52	$3^2S_{1/2}-3^2P_{3/2}^\circ$
2802.9	MgII	2802.69	$3^2S_{1/2}-3^2P_{1/2}^\circ$
13.3	FeI	13.29	$a^5F_4-y^5G_5^\circ$
28.3	TiII	28.15	$z^4G_{11/2}^\circ-e^4H_{13/2}$
	TiII	28.89	$z^4G_{9/2}^\circ-e^4H_{9/2}$; $z^4G_{3/2}^\circ-e^4G_{3/2}$
32.3	FeI	32.44	$a^5F_5-y^5G_4^\circ$
36.0	FeII	35.72	$b^2P_{3/2}-z^4G_{3/2}^\circ$
38.3	FeI	38.12	$a^5F_2-y^5G_2^\circ$
52.2	MgI	52.12	$3s^1S_0-3p^1P_1^\circ$
58.8	FeI	58.90	$a^5D_1-z^5G_2^\circ$
73.2	FeII	73.40	$b^2G_{7/2}-z^2H_{5/2}^\circ$
76.6	FeII	75.34	$a^2F_{7/2}-z^2G_{9/2}^\circ$
	FeII	76.80	$a^2F_{7/2}-y^4F_{5/2}^\circ$
81.7	SiI	81.59	$3p^2\ ^1D_2-3p4s\ ^1P_1^\circ$
98.2	VI	99.21	$a^4F_{5/2}-v^4D_{7/2}^\circ$
	VI	99.60	$a^4F_{3/2}-v^4D_{1/2}^\circ$
2910.5	VII	2910.00	$a^5F_2-z^3D_2^\circ$
	VII	10.38	$a^5F_1-z^3D_1^\circ$
20.6	VII	20.37	$a^5F_2-z^5F_3^\circ$
23.7	VI	23.63	$a^4F_{9/2}-v^4D_{7/2}^\circ$
	VII	24.63	$a^5F_4-z^5F_4^\circ$
26.5	FeII	26.58	$a^4D_{7/2}-z^4F_{9/2}^\circ$
28.7	MgII	28.62	$3\ ^2P_{1/2}^\circ-4\ ^2S_{1/2}$
	FeII	29.00	$a^5D_3-y^5F_2^\circ$
33.0	MnII	33.05	$4s\ ^5S_2-4p\ ^5P_1^\circ$
37.0	MgII	36.49	$3\ ^2P_{3/2}^\circ-4\ ^2S_{1/2}$
	FeI	37.50	$a^5D_4-y^5F_4^\circ$
39.4	MnII	39.31	$4s\ ^5S_2-4p\ ^5P_2^\circ$
	FeII	39.50	$a^4D_{5/2}-z^5F_{5/2}^\circ$
41.5	FeI	41.34	$a^5D_2-y^5F_1^\circ$
44.6	FeII	44.39	$a^4P_{3/2}-z^4P_{1/2}^\circ$
	VII	44.57	$a^5F_4-z^5F_3^\circ$

TABLE II.—(*Continued.*)

Wave-Length (A)	Identification		
47.9	FeII	47.66	$a^4P_{3/2}-z^4P_{3/2}^\circ$
	FeI	47.88	$a^5D_3-y^5F_3^\circ$
49.4	FeII	49.18	$b^2G_{9/2}-z^2F_{7/2}^\circ$
	MnII	49.21	$4s\ ^5S_2-4p\ ^5P_3^\circ$
	FeI	50.24	$a^5P_3-5^\circ$
54.0	FeII	53.77	$a^4D_{5/2}-z^6F_{7/2}^\circ$
	FeI	53.94	$a^5D_2-y^5F_3^\circ$
57.3	FeI	57.36	$a^5D_1-y^5F_1^\circ$
59.9	FeII	59.60	$a^2F_{7/2}-z^2D_{5/2}^\circ$
61.4	FeII	61.27	$a^4D_{3/2}-z^6F_{1/2}^\circ$
65.3	FeI	65.26	$a^5D_0-y^5F_1^\circ$
66.8	FeI	66.90	$a^5D_4-y^5F_5^\circ$
70.3	FeI	70.11	$a^5D_1-y^5F_2^\circ$; $a^5D_2-z^3P_2^\circ$
	SiI	70.35	$3p^2\ ^1D_2-3p4s\ ^3P_2^\circ$
	FeII	70.51	$a^4D_{3/2}-z^6F_{5/2}^\circ$
73.2	FeI	73.13	$a^5D_2-y^5F_3^\circ$
	FeI	73.27	$a^5D_3-y^5F_4^\circ$
76.2	FeI	76.12	$a^3P_2-u^3D_3^\circ$
	VII	76.20	$a^5P_1-y^5P_2^\circ$
	VII	76.52	$a^5P_2-y^5D_3^\circ$
79.1	FeII	79.34	$a^4D_{1/2}-z^6F_{3/2}^\circ$
81.4	FeI	81.44	$a^5D_3-z^3P_2^\circ$
83.6	FeI	83.57	$a^5D_4-y^5D_3^\circ$
84.8	FeII	84.83	$a^4P_{5/2}-z^4P_{5/2}^\circ$
85.8	FeII	85.55	$a^4P_{1/2}-z^4P_{3/2}^\circ$
	CrI	85.86	$a^5D_2-y^5D_2^\circ$
	CrI	86.00	$a^5D_3-y^5D_3^\circ$
	CrI	86.47	$a^5D_4-y^5D_4^\circ$
87.6	FeI	87.29	$a^5F_4-x^5F_5^\circ$
	SiI	87.65	$3p^2\ ^1D_2-3p4s\ ^1P_1^\circ$
94.5	FeI	94.42	$a^5D_3-y^5D_3^\circ$
	FeI	94.50	$a^5D_0-z^3P_1^\circ$
99.5	FeI	99.51	$a^5F_5-x^5F_5^\circ$
3000.8	FeI	3000.95	$a^5D_2-y^5D_1^\circ$

nences above the cooler reversing layer of the sun.

From a preliminary examination of the microphotometer traces, it is obvious that a determination of the blackbody curve will be difficult. There are a number of sudden drops in intensity such as those near λ2630A, λ2550A, and λ2410A due to multiplets of iron. There are step-wise drops of intensity such as one at λ2950A that might originate in band absorption in the reversing layer of the sun. Another feature of interest is the several bright "windows" that are seen in the spectrum of the sun. Two such are bright lines near λ2638A and λ2643A. The simplest hypothesis is that such windows represent the true intensity of the continuum of the sun and that others will be found when one uses sufficient resolution and exposure to resolve the narrow plateaus of the continuum from the canyons, the Fraunhofer lines. It appears at present that even these windows are less bright than those corresponding to a solar temperature of 5500°K. One should also look into the possibility of the origin of such "bright" lines in the spectrum of iron, calcium, and other elements known to exist in a highly ionized state in the solar corona. There are no systematic differences among exposures B1 to B5 of Table I showing that atomspheric absorption in all of them is small.

To photograph much more of the ultraviolet spectrum of the sun is our desire for future rocket flights, when sufficient exposure is obtained by complete homing on the sun. An important extension would be the Lyman series of hydrogen beginning at λ1215A. This series like the Balmer series so prominent in total eclipses, should be strong in the layer of the sun just outside the reversing layer.

In writing this report, the authors feel that they are only the spokesmen of the people and organizations that made the experiments possible. Among these organizations are the Army Ordnance Group at White Sands Proving Ground, Las Cruces, New Mexico, the General Electric Company through its representatives at White Sands, and the Department of Physics at Johns Hopkins which made the gratings.

We are greatly indebted to our associates at the Applied Physics Laboratory who helped in photometry and photography of the spectra and especially to Messrs. J. W. B. Barghausen, L. W. Fraser, A. V. Gangnes, R. S. Ostrander, and J. V. Smith whose help was indispensable in designing and constructing the homing and other equipment. Dr. Jesse L. Greenstein gave many useful suggestions during the early stages of this work. Dr. J. Allen Hynek, now of Ohio State University, contributed enthusiastically to early planning. We are especially fortunate in having the leadership of Dr. James A. Van Allen who, despite our failures, never despaired.

This work would have been impossible without the facilities and generous support of the Navy Bureau of Ordnance under Contract NOrd 7386.

A Study of the Breakup of Li^8 *

T. W. BONNER, J. E. EVANS, C. W. MALICH,** AND J. R. RISSER
Rice Institute, Houston, Texas

(Received January 2, 1948)

An experimental technique in which radioactive Li^8 atoms are introduced into the gas of a cloud chamber has been used to determine the energy distribution of the alpha-particles from the Li^8 breakup. The maximum of the distribution occurs at 3.3 Mev and the width of half-intensity is 1.2±0.2 Mev. The theoretical distribution

$$N_\alpha dE_\alpha = [P_{\alpha J}(Q-2E_\alpha)^5/(E_0-2E_\alpha)^2+\tfrac{1}{4}\Gamma^2]dE_\alpha$$

with $E_0=3.1$ Mev, $\Gamma=0.8$ Mev, and $J=4$, gives good agreement with experimental data. N_α is the relative number of alpha-particle pairs, E_α is the energy of one alpha-particle, $P_{\alpha J}$ is the penetrability of one alpha-particle from a Be^8 nucleus having J units of total angular momentum, and E_0 and Γ are, respectively, the mean energy and width at half-intensity of the excited level in Be^8. No evidence was found for a short-range group of alpha-particles which would correspond to the disintegration energy of the ground state of Be^8.

1. INTRODUCTION

RADIOACTIVE Li^8 was discovered by Crane, Delsasso, Fowler, and Lauritsen[1] by the observation of a short-period beta-ray activity produced by deuteron bombardment of lithium. The period of the delayed beta-particles has been measured accurately by Lewis, Burcham, and Chang[2] and found to be 0.88 sec. They also found delayed alpha-particles having a decay period of 0.88 sec. These activities result from the following reactions:

$$Li^7+H^2 \rightarrow Li^8+H^1-0.26 \text{ Mev}, \quad (1)$$

$$Li^8 \rightarrow He^4+He^4+e^-+\nu+16.0 \text{ Mev}. \quad (2)$$

In the excitation curve for reaction (1) in which Li^8 is produced, there are resonances at 0.65, 1.02, and 1.35 Mev.[3] The energy limit of the beta-ray spectrum has been found to be about 12.0 Mev.[4]

The exact process by means of which Li^8 decays into two alpha-particles and an electron is not known, but it is generally considered that the emission of the electron leaves a highly unstable Be^8 nucleus. Study by means of a mass spectrograph[5] has shown that the relative abundance of Be^8 in natural beryllium is less than 10^{-5}. Wheeler[6] concludes, upon consideration of the experiments of Laaff[7] and Fink,[8] that Be^8 is unstable with respect to two alpha-particles by about 125±25 kev.

In an attempt to determine the mechanism of the decay of Li^8 several investigators[2,9-13] have studied the energy distribution of the alpha-particles. Widely varying energy distributions have been found. Gamow and Teller[10,13] have derived an expression for the energy distribution of the alpha-particles to be expected if the breakup of Li^8 is a 4-body disintegration. Their expression is based on the Fermi theory of beta-neutrino decay and assumes that the two alpha-particles break apart at the same time the beta-particle and neutrino are emitted. The Gamow-Teller expression is as follows:

$$N_\alpha dE_\alpha = (Q-2E_\alpha)^5 E^{J+\frac{1}{2}} dE_\alpha, \quad (3)$$

where N_α is the relative number of alpha-

* A preliminary report of these results was made at the May, 1947 meeting of the American Physical Society [Phys. Rev. **72**, 163 (1947)].

** Now located at University of Pennsylvania, Philadelphia, Pennsylvania.

[1] Crane, Delsasso, Fowler, and Lauritsen, Phys. Rev. **47**, 971 (1935).

[2] Lewis, Burcham, and Chang, Nature **139**, 24 (1937).

[3] Bennett, Bonner, Richards, and Watt, Phys. Rev. **71**, 11 (1947).

[4] D. G. Bayley and H. R. Crane, Phys. Rev. **52**, 604 (1937).

[5] Alfred O. C. Nier, Phys. Rev. **52**, 933 (1937).

[6] John A. Wheeler, Phys. Rev. **59**, 27 (1941).

[7] O. Laaff, Ann. d. Physik **32**, 745 (1938).

[8] Kurt Fink, Ann. d. Physik **34**, 717 (1939).

[9] W. A. Fowler and C. C. Lauritsen, Phys. Rev. **51**, 1103 (1937).

[10] Rumbaugh, Roberts, and Hafstad, Phys. Rev. **51**, 1106 (1937).

[11] Smith and Chang, Proc. Roy. Soc. **A166**, 415 (1938).

[12] Bennett, Bonner, Mandeville, and Watt, unpublished data.

[13] Rumbaugh, Roberts, and Hafstad, Phys. Rev. **54**, 657 (1938).

particle pairs per unit energy range, Q is the total energy available for the disintegration, E_α is the energy of one alpha-particle, and J is the total angular momentum of the Be^8 nucleus. Wheeler[6] has developed a theory which gives the energy distribution of the alpha-particles which would be expected if the disintegration were a three-body disintegration. He assumes that the mechanism is the beta-neutrino decay of Li^8 according to the Fermi theory, followed almost immediately by the breakup of an excited state of Be^8 into two alpha-particles. The distribution is given by the following expression:

$$N_\alpha dE_\alpha = \frac{(Q-2E_\alpha)^5}{(E_0-2E_\alpha)^2+\frac{1}{4}\Gamma^2} dE_\alpha, \qquad (4)$$

where E_0 and Γ are, respectively, the mean energy and the width at half-intensity of the excited level in Be^8.

Lewis, Burcham, and Chang[2] found a continuous energy distribution of alpha-particles with combined energies as great as 12 Mev. As a matter of convenience, throughout the remainder of this paper we shall always refer to the combined energies of the two alpha-particles from the breakup of Li^8. Fowler and Lauritsen[9] found a maximum in the distribution curve at 2.6 Mev and a corrected width of about 1.0 Mev. Using counter techniques, Rumbaugh, Roberts, and Hafstad[13] found no maximum; however, using a cloud chamber, they found a maximum in the curve at 2.6 Mev. Smith and Chang,[11] using counter techniques, studied the energy distribution of the alpha-particles from 2.4 Mev up to the end point of 15.5±0.1 Mev and found no maximum in the distribution curve. Bennett, Bonner, Mandeville, and Watt[12] found a maximum in the distribution curve of 2.0 Mev. At the conclusion of their experimental work, however, it was discovered that they, and most of the previous investigators, had neglected to take into account the alpha-particle range correction due to the recoil of the Li^8 nuclei into the target. The failure to make this correction would cause the maximum of the distribution to occur at too low an energy value. Since the range energy relations for lithium nuclei are not known accurately, it was impossible to evaluate the exact amount of this effect. However, they did suggest a way to obviate this difficulty. The experimental arrangement used in the experiment to be described here was based on these suggestions. The experiment to be described was undertaken for the purpose of determining accurately this energy distribution curve of the alpha-particles from 0 up to about 5 Mev. It was also hoped that some pictures showing all three observable disintegration particles of the breakup of Li^8 atoms would be obtained. Analysis of such pictures could determine whether or not the neutrino hypothesis is necessary to conserve momentum in radioactive beta-decay.

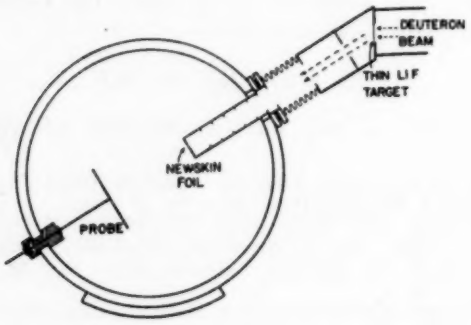

FIG. 1. Experimental arrangement of the cloud chamber and target holder. Some of the radioactive Li^8 atoms recoil from the LiF target and proceed along the evacuated tube in the direction of the arrows through the thin foil into the cloud chamber.

2. EXPERIMENTAL ARRANGEMENTS

The deuterons were accelerated to an energy of 1.3 Mev by means of the Rice Institute pressure Van de Graaff generator. The atomic beam was deflected through an angle of 90° by an annular ring-type magnetic energy selector. Targets were prepared by evaporating from a hot tungsten filament in a high vacuum about 0.2 mg/cm² of LiF on to an aluminum foil which weighed 0.22 mg/cm.² The foil was supported on an aluminum disk into which there had been cut a rectangular window 1 cm by 2 cm. This was mounted so that the incident deuterons penetrated the aluminum foil before reaching the deposit of LiF. Some of the Li^8 atoms formed had sufficient recoil energy and the correct direction to pass through a new-skin foil into the gas of a cloud chamber.

The cloud chamber used was 26 cm in diameter and 11 cm in depth. In order to keep nuclear scattering down to a low value, helium and water

vapor were used. A pressure of 1.7 atmospheres was used in an effort to render visible as many of the beta-rays as possible. Figure 1 shows the experimental arrangement of the cloud chamber and target holder used.

In order to keep the direct deuteron beam out of the cloud chamber, the cloud-chamber port was located at an angle with respect to the beam. Momentum considerations allow Li^8 atoms to recoil within a maximum angle of 35° for a bombarding energy of 1.3 Mev. In the early part of the experiment the cloud chamber was placed so that some Li^8 atoms, recoiling at an angle of 20° from the forward direction of the incident deuterons, would pass through the new-skin foil into the cloud chamber. Later the angle was changed to 30° in order to reduce, by a factor of 5, the Coulomb scattering of the incident deuterons by the target. Even with this improvement, the Coulomb scattering of the deuterons was a major problem. In the region directly in front of the new-skin foil, and out for a distance of about 4 cm, a fog was formed on nearly every expansion. Tracks, due to the breakup of Li^8 atoms late in the sensitive period of the chamber, sometimes had gaps of one to two cm in length in this region. Electron tracks were, for all practical purposes, completely obscured in this region. Alpha-particles from the decay of Li^8 atoms which had come to rest on the walls of the vacuum system between the target and the new-skin foil were prevented from getting into the cloud chamber by means of thin brass baffles shown in Fig. 1.

New-skin foils, which had stopping powers from 0.5 mm to 0.7 mm of air, were used. They were mounted on well-polished silver-plated microphone screen which had 20 percent of its area open and was 0.015 cm thick. In preliminary experiments it was found that the recoil ranges of the Li^8 atoms, after penetration of the new-skin foil, were generally not more than 1 cm out into the cloud chamber. Some of these Li^8 atoms moved approximately 1 cm farther out into the cloud chamber because of gaseous diffusion during the 1-second time interval between the short bombardment period and the expansion of the cloud chamber. There was a pronounced bunching of the tracks near the foil which was very undesirable. It was found that by means of an electrostatic probe, as shown in Fig. 1, some of the Li^8 ions could be pulled into the central region of the cloud chamber. A potential of 500 volts on the probe, with an accompanying 250 volts on the top and bottom of the cloud chamber, was sufficient to pull some of the Li^8 ions over to the probe; a considerable fraction of the Li^8 ions getting through the foil disintegrated near the center of the cloud chamber.

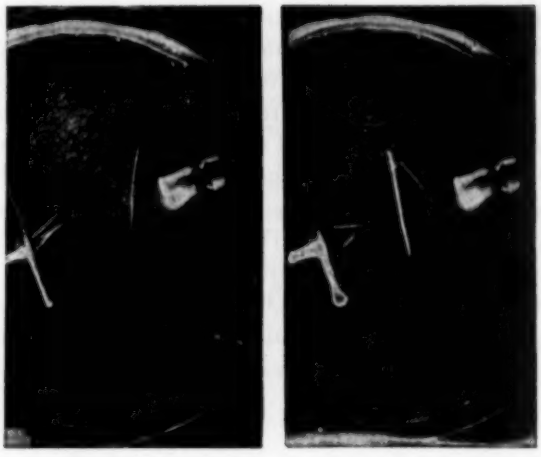

(a) (b)

FIG. 2. Representative cloud-chamber photographs for the breakup of Li^8. The bright object at the right of each picture is the collimating tube through which the Li^8 atoms enter the cloud chamber. The bright T-shaped object on the left is the electrostatic probe which pulls the Li^8 ions toward the center of the cloud chamber. The alpha-particle tracks near the probe are from the breakup of Li^8 atoms which have been pulled to the probe. (a) Photograph of an alpha-particle pair having a combined energy of about 3.5 Mev. The angular deviation between the paths of the two alpha-particles is 8.5°. (b) Photograph showing two alpha-particle pairs. Each pair has a combined energy of about 4 Mev, and the angular deviation between the paths of the two alpha-particles of a pair is about 2° for both of the pairs.

3. PROCEDURE

The operation of the cloud chamber and associated equipment was entirely automatic. The target was bombarded for a period of about 0.5 sec. During this time there was a strong horizontal pulling-out field. At the end of the bombarding period the horizontal field was turned off and the vertical clearing field was turned on again.

In the early stages of the experiment considerable difficulty was experienced with electron tracks produced by x-rays from the Van de Graaff generator. A chance coincidence of one of

these electron tracks and a Be^8 breakup might be misinterpreted as an electron from the decay of a Li^8 nucleus. Later on in the experiment the x-radiation was eliminated by turning off the ion source before the cloud chamber was expanded. This procedure also eliminated neutron recoils, which would otherwise be accepted as short alpha-particle tracks. The electron accelerating voltage in the ion source was turned off by a relay controlled by a photo-cell. The photo-cell was activated by an auto headlight unit located at one end of the pressure tank of the Van de Graaff generator.

In the analysis of the reprojected alpha-particle tracks only sharp tracks, whose directions were within 30° of a line drawn perpendicular to the plane of the stereoscopic system, were measured. Also, only those tracks whose centers (points of origin) were between the foil and the electrostatic probe were used. Tracks which had gaps of 1 cm or more where they had passed through a "foggy" region, were also rejected.

4. RESULTS

Four hundred and twenty-six tracks were measured, and in a large fraction of the cases, the two oppositely directed alpha-particle tracks were collinear within a few degrees. However, angles up to 10° were observed. No evidence was found that the two oppositely directed alpha-particles might have different energies. We observed no unmistakable electrons tracks starting in the gas at the midpoint of the alpha-particle tracks. However, several modifications of the equipment can be made which will increase the probability of observing such events. Representative cloud-chamber photographs are shown in Fig. 2.

The combined ranges of the two alpha-particles were divided by two in order to get the ranges of the single alpha-particles. These ranges

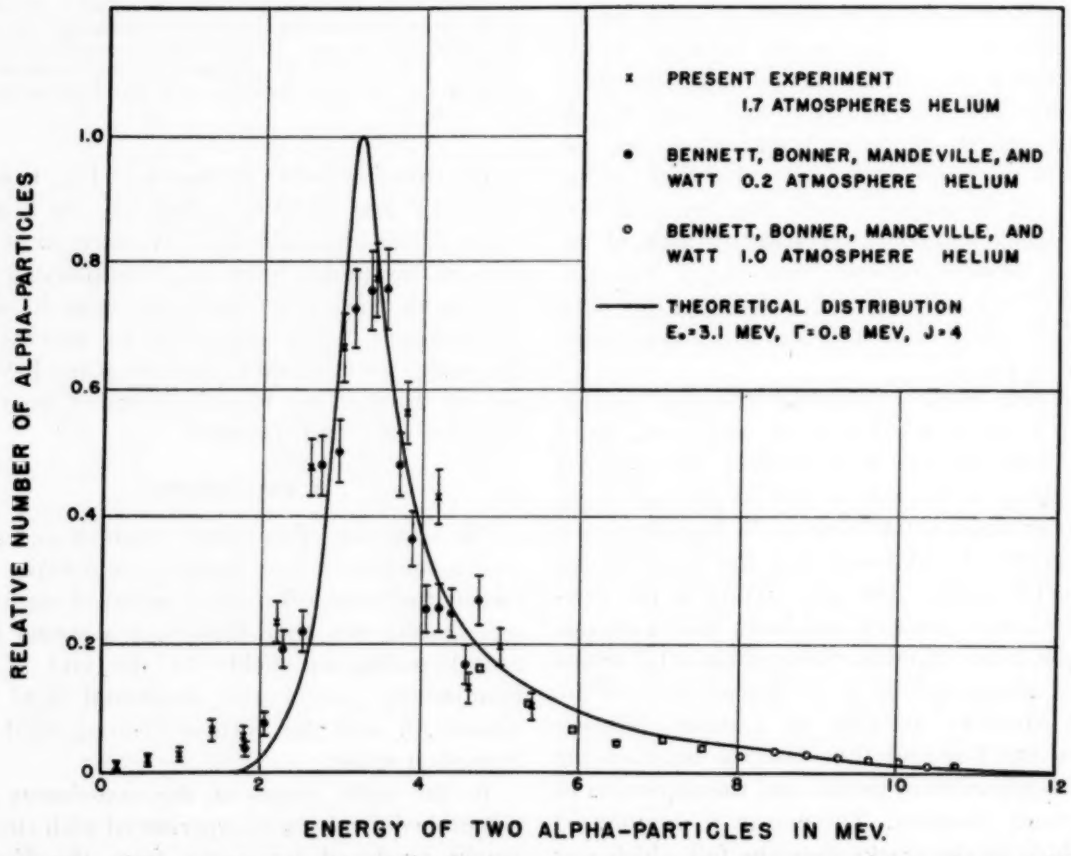

FIG. 3. The relative number of alpha-particle pairs as a function of their energy in the region of the maximum at 3.3 Mev. The statistical errors are shown by the vertical lines.

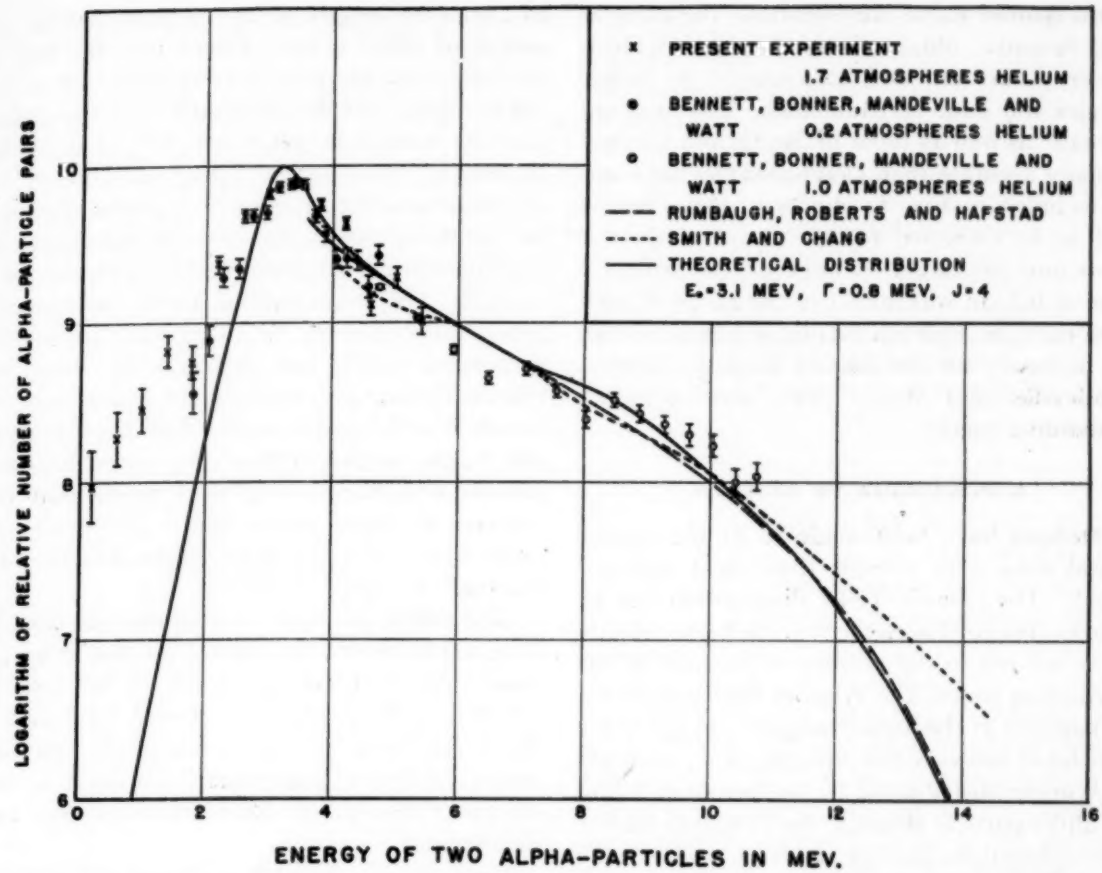

FIG. 4. The logarithm of the relative number of alpha-particle pairs as a function of their energy. Collected data of several authors are shown.

were converted to energy values and then grouped in equal energy intervals. The resulting distribution is shown by the crosses in Fig. 3. The value of the ordinates on this curve have been normalized so that the value of 1.0 corresponds to 108 tracks. The most probable energy of an alpha-particle pair is 3.3 Mev and the width at half-height is 1.2 ± 0.2 Mev. This width has been corrected for the finite energy intervals which were used. Some of the shorter tracks included in the distribution were undoubtedly neutron recoils; the control circuit, which turned off the ion source during expansion, was only used during about half of the experiment.

No evidence was found for a group of very short-range alpha-particles which would correspond to the disintegration energy of the ground state of Be^8. The combined track length of both alpha-particles, according to Wheeler's[6] estimate of the mass of Be^8, is about 5 mm. Tracks of half this length would certainly have been noticed in our experimental arrangement. Failure to observe a group of such particles is in agreement with the arguments based on selection rules that Be^8 in the ground state would not be formed in this reaction.[14,15]

The data of Bennett, Bonner, Mandeville, and Watt[12] can be compared to the present results if a suitable correction is made for the penetration of the Li^8 atoms into their target. 3.3 mm must be added to the range of each alpha-particle to make the maxima of the two curves coincide. These corrected data are shown in Fig. 3. For these data the values of the ordinates have been normalized so that the value 1.0 corresponds to 91 tracks. The width at half-height for this adjusted distribution is 1.0 ± 0.2 Mev. The two

[14] E. Wigner and G. Breit, Phys. Rev. **50**, 1191 (1936).
[15] Christy, Cohen, Fowler, Lauritsen, and Lauritsen, Phys. Rev. **72**, 698 (1947).

widths quoted above are essentially the same as that recently obtained by Christy, Cohen, Fowler, Lauritsen, and Lauritsen.[15] At higher energies the data of Rumbaugh, Roberts, and Hafstad[13] as well as those of Smith and Chang[11] are more accurate than cloud-chamber data and are included in Fig. 4. However, these results need to be corrected for the recoil of the Li^8 atoms into the target. A more or less arbitrary value of 0.2 cm was added to the range of each alpha-particle. This is a smaller adjustment than was necessary for the data of Bennett, Bonner, Mandeville, and Watt,[12] who used a higher bombarding energy.

5. DISCUSSION OF RESULTS

Attempts have been made to fit the experimental data with various theoretical distributions.[6,13] The Gamow-Teller distribution can be made to give good agreement at the higher energy values but not in the vicinity of the peak of the distribution curve. The Wheeler theory gives too few particles at the higher energies and too many particles at the very low energies. If we multiply the Wheeler distribution by the penetrability of one alpha-particle through the Coulomb barrier of the other alpha-particle, we have the following distribution:

$$N_\alpha dE_\alpha = \frac{P_{\alpha J}(Q-2E_\alpha)^5}{(E_0-2E_\alpha)^2+\frac{1}{4}\Gamma^2},$$

where $P_{\alpha J}$ is the penetrability of one alpha-particle through the Coulomb barrier of the other alpha-particle from the breakup of an excited state in Be^8 which has J units of total angular momentum. Formulae for $P_{\alpha J}$ have been given by Bethe.[16] This new distribution gives good agreement with experimental results when J is taken equal to 4, $E_0=3.1$ Mev, and $\Gamma=0.8$ Mev. The mean time of existence of such a level is about 8×10^{-22} sec. In this time an electron, traveling with essentially the velocity of light, could travel 2.4×10^{-11} cm. This is about equal to the wave-length of an electron having an energy of about 6 Mev. Hence the $*Be^8$ breaks up before the electron is completely out of its nuclear field, and the penetrability of the alpha-particles cannot be neglected. The peak of the theoretical distribution curve is allowed to extend above the experimental points since the use of finite energy intervals in obtaining the experimental distributions flatten and widen such a peak. The experimental points at energies below the maximum lie consistently above the theoretical curve, but this is what would be expected from the inclusion of a few neutron recoils. Further experiments, free from neutron effects, are needed in this same region for comparison with theory. Figure 4 shows that the theoretical curve agrees quite well with the experimental data of Rumbaugh, Roberts, and Hafstad[13] to about 14 Mev.

Note added in proof: Agreement can also be obtained from this theoretical relation if we assume that there are two levels in Be^8 (one at 3.2 Mev with $J=2$, and a broad level at 7–9 Mev) concerned in the breakup. In this case somewhat better agreement is obtained at low energies. Theoretical calculations predict two such levels.[6]

The energy and width of this level in $*Be^8$ is nearly the same as that found by Dee and Gilbert[17] in the reaction $B^{11}(p,\alpha)*Be^8$. They concluded that Be^8 was excited to a 3.0-Mev level which had a width of about 1 Mev. An analysis of the same data by Bethe[18] indicated a level at 2.8 Mev with a width of 0.8 Mev.

If the value of J is equal to 4 for $*Be^8$ and if the beta-decay of Li^8 involves a transition $\Delta J=\pm1$, it seems probable that the ground state of Li^8 has a value of $J=3$. Hence, in reaction (1) only deuterons having at least one unit of orbital angular momentum will be effective in producing Li^8.

We are indebted to the Office of Naval Research and the Research Corporation for financial support.

[16] H. A. Bethe, Rev. Mod. Phys. 9, 166, 178 (1937).

[17] Dee and Gilbert, Proc. Roy. Soc. 154, 279 (1936).

[18] H. A. Bethe, Rev. Mod. Phys. 9, 218 (1937).

The Production of High Velocity Mercury Vapor Jets by Spark Discharge

J. RICHARD HAYNES
Bell Telephone Laboratories, Murray Hill, New Jersey

(Received November 20, 1947)

Photographs of sparks of microsecond duration in hydrogen to a mercury electrode show high velocity jets from the mercury surface regardless of polarity. Spectroscopic examination shows that these jets are largely composed of mercury atoms which sweep away the hydrogen. Measurements of jet velocity demonstrate that it is independent of current and gas pressure over a wide range. While it decreases with distance from the source, the original velocity of the cathode jet is 1.9 (10^5) cm/sec., and that of the anode jet is 1.5 (10^5) cm/sec. The energy of the anode jet can be accounted for by positive mercury ions crossing the anode drop. It appears that the energy of the cathode jet cannot be accounted for unless it is assumed that, in addition to positive ions striking the cathode and rebounding as neutral atoms, many mercury atoms leave the cathode as negative ions.

SECTION I

Introduction

THE experiments of many investigators show that a migration of atoms of the metal composing the electrodes of a gap occurs in either an arc or spark discharge. There is, however, considerable disagreement in the results published by various investigators on the velocity of migration found with spark discharge, and the results obtained with arc discharge are approximately an order of magnitude higher than those obtained with sparks.

Spark Discharge

The earliest work appears to be that of Schuster and Hemsalech.[1] Using a spectrometer and moving film arrangement they showed that, during an oscillatory spark in air, radiation characteristic of the electrode material is found at increasingly greater distances from the electrodes with increasing time. Although the accuracy of their experiments was not very great, they were able to conclude that the atoms of the electrode materials migrated with a velocity of from 1.9 (10^5) to 0.4 (10^5) cm/sec. The velocity determined in this way was dependent on the electrode material and was found to decrease with distance from the electrodes. Mohler[2] photographed a spectrum of an electric spark along the line of discharge, then reversed the electrodes and took another spectrogram. From the observed Doppler shift he calculated an average velocity of the "particles" from the electrodes of 0.37 (10^5) cm/sec. Lawrence and Dunnington[3] through the use of a Kerr cell and spectrograph showed that the luminosity of the metallic vapors of the electrodes spread from the electrodes with a velocity which, using zinc, had an average value of 2.1 (10^5) cm/sec. On the assumption that the broadening of the zinc spectrum was due to the Stark effect of interatomic fields, they calculated that a third of the molecules in the discharge paths were ionized. Assuming that their measured velocity was that of the migration of positive ions from the anode, they estimated that approximately $\frac{1}{2}$ of the current was carried by positive ions.

Arc Discharge

Using a "vacuum" arc with copper electrodes Tanberg[4] found that a pressure is exerted on both the cathode and a vane suspended in front of it. On the assumption that the measured force was that caused by the force of reaction of evaporating copper atoms, he calculated a velocity of 16 (10^5) cm/sec. for these copper atoms. Tanberg supposed this high velocity to be caused by a high temperature of the cathode spot and calculated that the required temperature was 500,000°. Compton,[5] objecting to the postulation of such a high temperature, thought it much more likely that the force was due to the rebounding of

[1] A. Schuster and G. Hemsalech, Proc. Roy. Soc. **64**, 331 (1899).
[2] J. F. Mohler, Astrophys. J. **15**, 125 (1902).
[3] E. O. Lawrence and F. G. Dunnington, Phys. Rev. **35**, 396 (1930).
[4] R. Tanberg, Phys. Rev. **35**, 1080 (1930).
[5] K. T. Compton, Phys. Rev. **36**, 706 (1930).

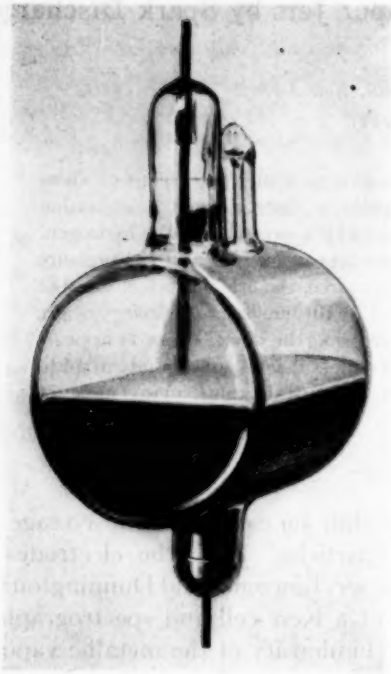

FIG. 1. Spark gap tube provided with flat glass window.

neutralized positive ions from the cathode with energy $(1-\alpha)$, where α is the accommodation coefficient of the positive ions. The force on the cathode of a mercury vacuum arc was measured by Kobel.[6] Again assuming that this force was due to the reaction of mercury vapor on the cathode he calculated a velocity very similar to that obtained by Tanberg.

That this high velocity could not be accounted for by an accommodation coefficient theory was shown by Slepian and Mason,[7] since the velocity calculated by Tanberg required energies of 70 volts, or considerably more than the cathode drop.

Tanberg and Berkley[8] then showed that the temperature of the cathode was only of the order of 3000°K and concluded that the high speed of the vapor stream cannot be caused by the temperature of the cathode itself. They suggested that the vapor gained a high velocity thermal agitation in a region just outside the cathode. Ludi and Risch[9] have suggested that there may be a large number of atoms ionized five or six times. Easton, Lucas, and Creedy[10] measured a force on the anode of the vacuum arc and, using the assumption of Tanberg that this force was the force of reaction of particles leaving the anode, calculated a velocity of the anode vapor of 10^6 cm/sec. They concluded that a thermal origin was indicated. Robertson[11] showed that the force on the cathode of a vacuum arc is a function of gas pressure, and Risch[12] showed that this was the expected result of a jet caused by the unbalanced gas pressure on the back of the cathode.

Considerable doubt that the calculations of vapor velocities in the vacuum arc are valid was expressed by Tonks[13] who calculated that a force of the order measured could be accounted for by the partial pressure of the electron gas. Loeb[14] showed that even if this correction were small the calculated velocity would be too high because of a difference between the number of atoms "evaporated" and those which actually escape into the vapor stream, since a large number of atoms is returned to the cathode as positive ions.

During the war an extensive study of fixed spark gaps has been made because of their importance in radar circuits. These studies have shown that, at least in air and hydrogen and using a wide variety of cathode material, a spark having a peak current greater than 100 amperes has a cathode and anode drop of the same order

FIG. 2. Photograph of five individual sparks showing cathode mercury vapor jets. The mercury pool (cathode) is at the bottom. (Retouched.)

[6] E. Kobel, Phys. Rev. **36**, 1636 (1930).
[7] J. Slepian and R. C. Mason, Phys. Rev. **37**, 779 (1931).
[8] R. Tanberg and W. E. Berkley, Phys. Rev. **38**, 297 (1931).
[9] F. Ludi and R. Risch, Zeits. f. Physik **75**, 812 (1932).
[10] E. C. Easton, F. C. Lucas, and F. Creedy, Elect. Eng. **53**, 1454 (1934).
[11] R. M. Robertson, Phys. Rev. **53**, 578 (1938).
[12] R. Risch, Phys. Rev. **57**, 1181 (1940).
[13] L. Tonks, Phys. Rev. **46**, 278 (1934).
[14] L. B. Loeb, *Fundamental Processes in Electrical Discharge in Gases* (John Wiley and Sons, Inc., New York, 1939), p. 633.

as that measured in a steady arc.[15] It is therefore reasonable to suppose that the mechanism of vapor jet production is the same in both arc and spark discharge. Indeed, it would be amazing if even much difference of a quantitative nature exists, and it appears likely that most of the large reported difference between the vapor velocities in sparks and those in arcs is due to the lack of proper corrections of vacuum arc velocities, making these calculated values too high, and to the use of average velocities in spark measurements, making these values comparatively low, especially in the Doppler measurements of Mohler.

SECTION II

Spark Photographs

At one stage in the investigation of fixed spark gaps used as switches in radar modulator circuits a mercury pool was used as one electrode in a tube, such as that shown in Fig. 1. These spark gaps consist simply of a rod of molybdenum, 1.5 millimeters in diameter, brought within 7 millimeters of a mercury pool in a tube containing purified hydrogen at a pressure of 90 centimeters of mercury. When tubes of this type were operated as a switch, sparks occurred between the tip of the molybdenum rod and the mercury pool at the rate of several hundred per second. The current in these sparks is a unidirectional pulse having a constant value of a few hundred amperes and a duration adjustable from 0.25 to 5 microseconds. It was found that regardless of polarity a jet of mercury vapor was ejected from the mercury pool during the time of discharge.

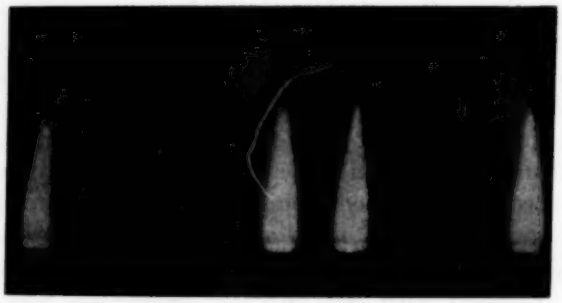

FIG. 3. Photograph of four individual sparks showing anode mercury vapor jets. The mercury pool (anode) is at the bottom. (Retouched.)

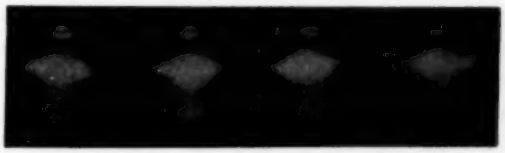

FIG. 4. Photograph of four individual sparks showing the effect of mercury on both electrodes. The mercury pool (anode) is at the bottom. (Retouched.)

There is no doubt whatever about the physical reality of these jets. Perhaps the simplest and most striking proof is that obtained from Kodachrome photographs of individual sparks. These photographs were taken by reflecting the image of the spark from a rotating first surface mirror prior to focus on the Kodachrome film. A black and white reproduction* of a Kodachrome film obtained in this way, using the mercury pool as the cathode, is shown in Fig. 2. This is a photograph of five individual sparks, having a current of 230 amperes, which is constant for 5 microseconds. The images of the molybdenum anode are at the top and those of the mercury cathode at the bottom. A red positive column (dominated by the hydrogen α-line) reaches from the anode to the cathode. A well defined jet of the blue-green color characteristic of excited mercury vapor extends from the cathode spot into the positive column. It has been suggested that perhaps these are not real jets but are produced by the propagation of a high energy pulse along the spark column. That this is not the explanation is demonstrated in the first spark of Fig. 2 since the jet extends outside the spark column.

If the polarity of the mercury and molybdenum rod be reversed, so that the mercury is now the anode, similar jets are obtained as shown in Fig. 3. These sparks were obtained without changing the pulse conditions. In each spark photograph an anode jet may be seen extending from an anode spot on the mercury into the positive column. Again in the first spark photograph the anode jet is seen to pass outside the spark column.

If mercury is splashed on the molybdenum rod

[15] F. S. Goucher, J. R. Haynes, W. A. Depp, and E. J. Ryder, "Spark gap switches for radar," Bell Sys. Tech. J. 25, 594 (1946); Tech. Pap. Bur. Stand. **25** (October, 1946).

* These photographs have been retouched to restore the contrast lost in black and white reproduction.

it wets the surface and, in this way, a drop of mercury may be hung from its tip. Under these conditions jets are obtained from both electrodes which are oppositely directed. The result is shown in Fig. 4. The gap between the rod and the mercury pool has been reduced so that the jets will collide while retaining a high energy. When the jets meet they splay out, giving the effect that one obtains by directing the streams of two garden hose against each other. This is a proof of the physical reality of these jets since they obviously have momentum.

The anode and cathode jets are always found to leave the mercury in a direction normal to the surface and proceed in a straight line regardless of the path of the spark. The apparent deviations from this rule, shown in Fig. 2, are produced by ripples on the mercury surface which are clearly visible during sparking. In extreme conditions with a mercury drop hung on the tip of the molybdenum rod the cathode spot may be produced on the side of the drop. When this occurs the jet still leaves in a direction normal to the mercury surface proceeding in a straight line which is nearly 90° from the average path of the spark.

A "dark" space of about 0.05 centimeter may be observed in Fig. 2 between the cathode spot and the jet. A similar dark space between the anode spot and jet, of much the same thickness, is clearly visible in the original Kodachrome of Fig. 3. The width of these dark spaces increases with current and time and is a function of the jet diameter. These spaces cannot be regions of cathode and anode drop since, from the space-charge law and existing voltage, the current density would be many orders of magnitude less on this assumption than that actually measured. It seems far more likely that these dark spaces constitute the distance required for the mercury atoms in the jet, all originally moving in the same direction with much the same velocity, to acquire a sufficiently random velocity by impact with hydrogen molecules to produce a high probability of excitation on mutual impact.

Analysis of spark photographs taken with peak currents ranging from 90 to 440 amperes and pulse durations of 0.25, 1, 2, and 5 microseconds, shows that the current density at the cathode is independent of current but decreases with time. An empirical formula for the current density ρ, at the cathode which fits the data closely, is given simply by

$$\rho = 10^6/(14.8+7.7\log_e t), \qquad (1)$$

where t is in microseconds. Thus, for a 0.25-microsecond pulse the enormous current density of 2.4 (10^5) amperes/cm² is obtained. Since in these experiments the current is maintained constant during the time of pulse, it follows that the cathode spot area is increasing rapidly.

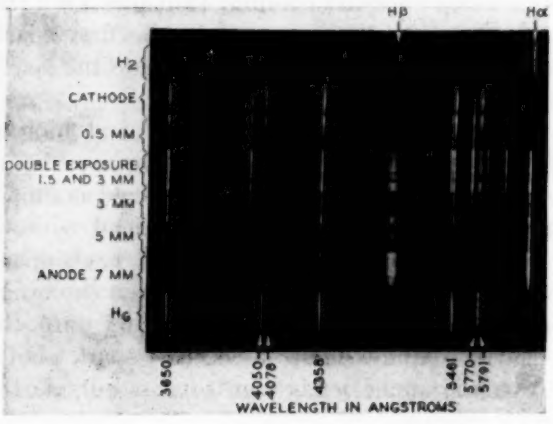

FIG. 5. Spark spectra of the light originating at progressively greater distances from a mercury cathode. At the extreme top and bottom are comparison spectra of hydrogen and mercury.

SECTION III

Spectroscopic Examination

Examination with a spectrograph shows that the jets are composed largely of mercury atoms. A spectrogram obtained with the light from portions of sparks at progressively greater distances from a mercury cathode is shown in Fig. 5. These sparks were obtained with current pulses having a constant value of 300 amperes for two microseconds. At the top is a comparison spectrum of hydrogen and at the bottom a mercury spectrum obtained from a General Electric H4 lamp. Many of the lines which appear with increasing intensity near the cathode are easily identified with the mercury comparison spectrum. The additional strong lines are included in the spark spectrum of mercury. It is evident that the light near the cathode and hence from the jet is very largely that of excited mercury vapor.

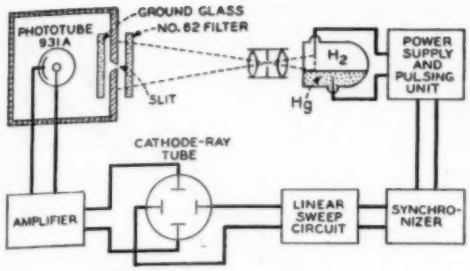

FIG. 6. Schematic diagram of apparatus used to measure mercury vapor jet velocities.

It will be observed that hydrogen β-line is quite broad. Its half-width at 6 millimeters from the mercury cathode was measured with a microphotometer and was found to be 99 angstroms. It has been shown by Finkelnburg[16] that this broadening is chiefly due to the Stark effect. Calculation shows that the implied interatomic field requires an ionization of the positive column of approximately 25 percent. This value agrees well with that of 33 percent, obtained by Lawrence and Dunnington, in the early stages of an electric spark in air. Since both of these calculations are based on the assumption that the density of the gas in the discharge path remains unaltered during the time of discharge, it follows that the gas density in the positive column cannot have decreased more than a factor of 3 or 4 at the most, since more than this would lead to greater than 100 percent ionization.

SECTION IV

Jet Front Velocity Measurements

It was obvious that an accurate measure of these mercury vapor jet velocities could be obtained by measuring the time required for the excited mercury atoms in the jet to go a known distance. Accordingly, an apparatus was constructed which enables these quantities to be determined. The light from sparks produced in the tube shown in Fig. 1 is focused on a horizontal slit by means of a lens provided with a diaphragm, as shown in Fig. 6. The horizontal slit allows only the light from a small segment of the spark column to reach a multiplier phototube. A No. 62 Wratten and Wainwright filter (mercury monochromat) is placed in the path of the light beam to limit the radiation reaching the photo-tube largely to that of the green line of mercury, and a ground glass screen is interposed to diffuse the light. The output of the photo-tube is amplified by a broad band amplifier and then placed on the vertical plates of a cathode-ray oscilloscope, the horizontal plates being connected to a fast linear time sweep synchronized to the pulsing circuit. It was shown that the deflection of the oscilloscope spot was closely proportional to the light reaching the photo-tube and that the time constant of the circuit was of the order of 0.02 microsecond. The dimensions of the slit and magnification of the image are such that the light reaching the photo-tube comes only from a section of the spark column a hundredth of a millimeter thick. It is therefore possible to place the slit across the spark image at any desired distance from the image of the mercury surface and to measure the time of arrival of the excited mercury atoms composing the jet by the consequent increase of light intensity passing through the mercury green line filter.

Typical characteristics obtained with this equipment are shown in Fig. 7. The current pulse shown in Fig. 7(b) was obtained on the oscillo-

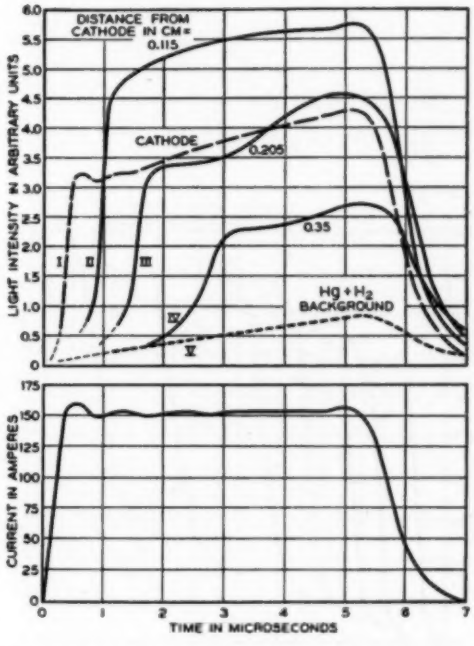

FIG. 7. (a) Typical characteristic of light intensity as a function of time, at various distances from a mercury cathode. (b) Current through the discharge on the same time scale.

[16] W. Finkelnburg, Zeits. f. Physik **70**, 375 (1931).

scope tube by well-known radar pulse technique using a nominal 5-microsecond pulse network. The current rises rapidly to a little over 150 amperes and remains substantially constant for approximately 5 microseconds. The consequent characteristics obtained from the light from the spark are shown in Fig. 7(a). When the slit is placed across the spark image so that the light reaching the photo-tube comes only from the cathode, or from its immediate vicinity, an approximate analog of the current pulse is obtained (curve I). However, close inspection of these curves shows that on the initial rise the light lags behind the current by about 0.15 microsecond. This delay time between the light and the current corresponds to the time required to initiate the arc discharge since it is known that currents in excess of 50 amperes are required to produce an arc (instead of a glow). A time delay of this same magnitude was found by Lawrence and Dunnington in the time required to produce zinc lines in a spark in air between zinc electrodes.

When a slit is placed so that the light reaching the photo-tube originates at a distance of 0.115 centimeter from the mercury cathode, an additional time delay of 0.6 microsecond is observed, as shown in curve II. At further distances longer time delays are observed, and the intensity rise due to the arrival of the jets diminishes so that a position of the slit is reached, near the anode,

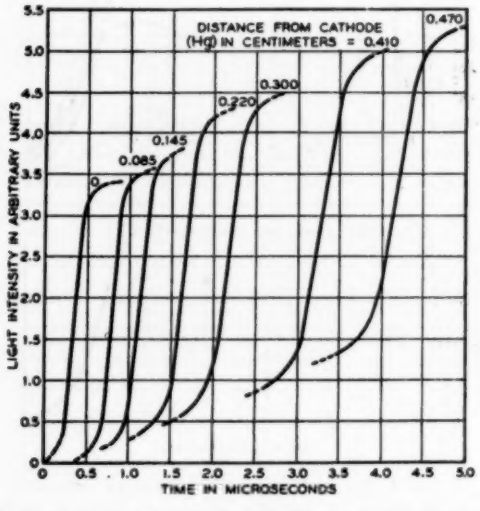

FIG. 8. Typical characteristics of light intensity as a function of time, used for obtaining jet velocity.

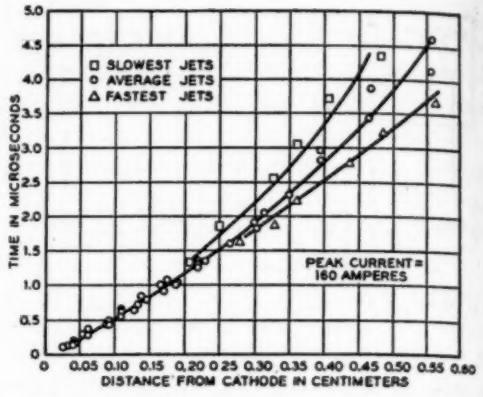

FIG. 9. Time of arrival of cathode jet front as a function of distance from mercury cathode.

where no effect of the jet can be found. In such a position the intensity varies with time, as shown in curve V. This is evidently the variation of the light from the positive column, already shown (Fig. 5) to be the mercury vapor and hydrogen spectrum characteristic of the gas in regions not reached by the jet.

The difference in time between any two analogous points on the light intensity rise characteristic, due to the arrival of the jet front and, at two different distances from the mercury cathode, might be used as a measure of the average velocity of the jet from between these distances.

The characteristics are seen to rise sharply to a fairly definite maximum after which the intensity increases much more slowly. Half of this maximum intensity was chosen as the comparison point.

The characteristics shown in Fig. 7 were made without changing the lens diaphragm and, therefore, show the relative maximum intensities. For the purpose of making measurements of the jet front velocity it is much more convenient to change the lens diaphragm aperture so that the change in intensity, due to the arrival of the jet, is maintained nearly constant. This also serves to reduce any errors due to non-linearity of the amplifier or cathode-ray tube. Typical characteristics obtained in this way are shown in Fig. 8. Only the initial rise of the characteristics are drawn and used as data. In the characteristics the upward shift with increasing time is produced by the mercury and hydrogen background light, shown in curve V, Fig. 7 (a).

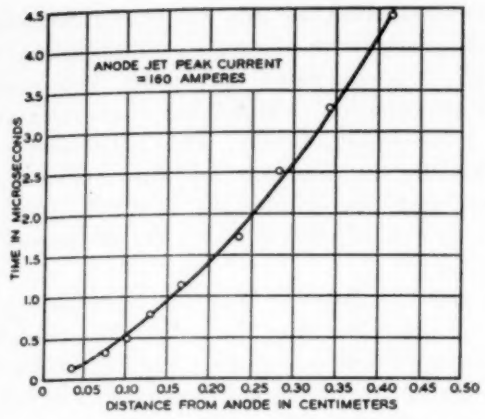

FIG. 10. Average time of arrival of anode jet front as a function of distance from mercury anode.

The characteristic obtained on the oscilloscope from light originating at the mercury cathode is a sharp line since the time uncertainty of synchronization of the apparatus is less than 0.02 microsecond. As the distance from the cathode is increased, the characteristics due to individual pulses (produced at the rate of 300 per second) have an increasing variation on the time axis of the oscilloscope tube and appear as a band of increasing width. This band width is evidently produced by variations in jet front velocity. It is possible, therefore, to trace the characteritics through points corresponding to jets having average velocities, as was done in obtaining data shown in Fig. 8, or through characteristics corresponding to the slowest or fastest jets. All three of these were done in order to obtain some idea of the distribution of jet velocities and the results are plotted in Fig. 9, where the time of arrival of a half-intensity point of a cathode jet front is plotted as a function of distance from the cathode. It will be observed that the maximum difference in jet front velocities is negligible at less than 0.2 centimeter from the mercury surface. Since all jets, therefore, have closely the same velocity near the cathode, it appears that the spread of jet velocities at greater distances is due to variations in density of the hydrogen produced by the previous spark.

Reversing the polarity of the mercury pool gives characteristics which are very similar to those shown in Fig. 8. Measurement of the delay in time of arrival of the half-intensity point at two known distances from the mercury anode, therefore, also gives a measure of the velocity of the front of the anode jet between these distances. Data obtained in this way are shown in Fig. 10 for average anode jets.

The velocity of the jet fronts may be derived from the curves of Figs. 9 and 10. This velocity for both cathode and anode jet fronts is plotted in Fig. 11. The velocities of each decrease linearly with distance from the mercury surface. This decrease is due to the mass reaction of the hydrogen with the jets. Extrapolation to the anode gives an initial velocity of the anode jet of 1.55 (10^5) cm/sec., and an initial velocity of the cathode jet of 1.9 (10^5) cm/sec. This initial velocity is found to be independent of hydrogen pressure from 5 to 153 centimeters of mercury and independent of current from 70 to 400 amperes. It has been shown[15] that both the electrode voltage drops and column voltage gradient are independent of current. As shown in Section III, the current density at the cathode is independent of current. Therefore, the initial jet velocity should be independent of current on any theory of the mechanism of jet production. The independence of jet velocity of gas pressure can be explained if the mechanism of jet production lies close to the electrode surface. Here the hydrogen is quickly swept away by the jet and the gas density is determined solely by the rate of mercury vaporization, so that the pressure of the surrounding hydrogen is of no consequence.

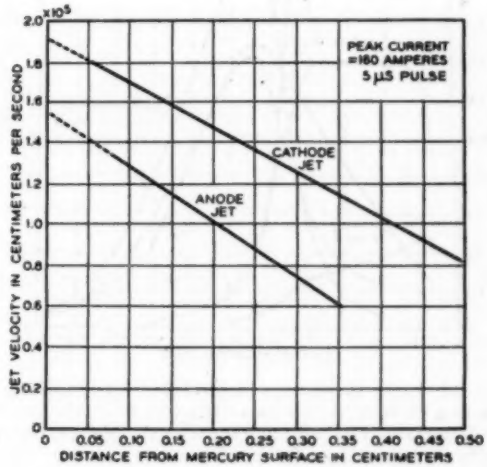

FIG. 11. Velocity of cathode and anode jet fronts as a function of distance from mercury surface.

SECTION V

Intensity Variation of Individual Lines

The variation of intensity of individual spectrum lines with time was investigated by a combination of the photo-tube and the spectrograph. The No. 62 filter was removed and the slit of the spectrograph substituted for the horizontal slit shown in Fig. 6. The usual photographic plate of a spectrograph was replaced by a metal plate provided with a narrow slot at the appropriate position to allow only the light from the chosen spectrum line to pass to the photo-tube. In this way the intensity of any chosen line could be investigated as a function of time and distance from the mercury surface.

When the spectrograph slit is so placed that the light reaching the photo-tube comes from a distance of 0.6 centimeter from the mercury cathode, the solid line characteristic, shown in Fig. 12, is obtained. This same solid line was obtained with three different wave-lengths. The diaphragm of the lens system was adjusted so that the peak intensities of the three lines examined (mercury 5461A, hydrogen 6563 and 3861A) had the same value. When this was done, it was found that the entire characteristic fell on the single solid line that was drawn. Since this radiation originates in a region not influenced by the jet, it is concluded that under these conditions all radiation in this band of energies rises and falls simultaneously. This conclusion was checked by showing that this same curve is obtained with the total light emitted from the spark in this region (to which the photo-tube is sensitive).

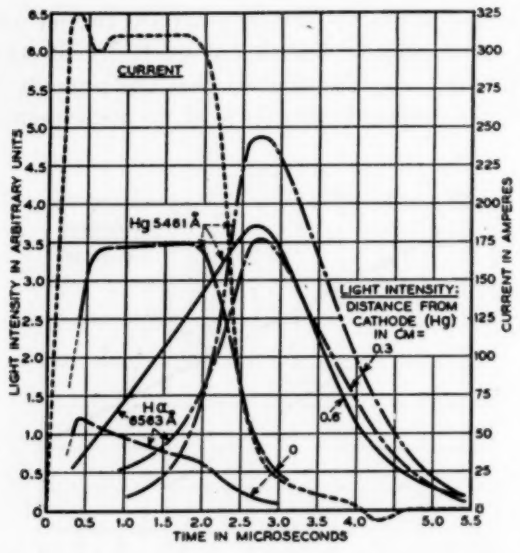
CURRENT
Hg 5461 Å
Hα 6563 Å
LIGHT INTENSITY: DISTANCE FROM CATHODE (Hg) IN CM=
0.3
0.6
0
LIGHT INTENSITY IN ARBITRARY UNITS
CURRENT IN AMPERES
TIME IN MICROSECONDS
0 0.5 1.0 1.5 2.0 2.5 3.0 3.5 4.0 5.0 5.5
0 0.5 1.0 1.5 2.0 2.5 3.0 3.5 4.0 4.5 5.0 5.5 6.0 6.5
0 25 50 75 100 125 150 175 200 225 250 275 300 325

FIG. 12. Light intensity of individual spectrum lines as a function of time, at various distances from the mercury cathode surface. The solid line is the characteristic obtained by light originating at 0.6 cm from the mercury surface, the dash-dot lines at 0.3 cm, and the dash lines at 0.0 cm. The current through the discharge as a function of time is also dotted in for reference.

It will be observed that the light persists a considerable time after the pulse. This afterglow in hydrogen first recorded by Lord Rayleigh has been studied by numerous investigators including Meek and Craggs[17] with a photo-tube and cathode-ray oscilloscope arrangement. All of these investigations show that the afterglow in hydrogen persists for a much longer time than the calculated 10^{-8} second average life of an excited hydrogen atom. It has been suggested[17] that this long afterglow is caused by the persistence of a high temperature in a spark column, so that excitation persists as long as temperature permits. The fact that the variation of intensity of the green line of mercury is the same as hydrogen α and hydrogen β tends to confirm this "temperature" theory.**

It will also be observed that the peak of the light intensity time characteristic occurs after the current pulse, or more precisely some $\frac{3}{4}$ of the microsecond after the current has started to drop. On the "temperature" theory of excitation this implies that the "temperature" of the positive column continues to increase after the current drops. A time delay in sparks of this order of magnitude was predicted by Loeb[18] for conversion of the energy from ions and electrons to a velocity distribution of the gas molecules to something approaching a temperature. Thus, although the average kinetic energy of ions and electrons is decreasing, more impacts have energies above that required for ionization.

---

[17] J. M. Meek and J. D. Craggs, Nature **152**, 538 (1943); Proc. Roy. Soc. **A186**, 241 (1946).

** As Loeb points out, it is very loose to use the word "temperature" to describe the condition of the gas in a spark column, since equilibrium is not established. "Temperature" is used here in quotation marks to represent the kinetic energy of agitation of the gas molecules since it is clear that the molecules do not attain a Maxwellian distribution of velocities in these times.

[18] L. B. Loeb, *Fundamental Processes of Electrical Discharge in Gases* (John Wiley and Sons, Inc., New York, 1939), p. 539.

If the spectrograph slit is placed to receive the light originating nearer the mercury cathode (0.05 centimeter from the mercury surface) the jet appears after a time and alters the characteristics so that the time variation of mercury and hydrogen lines is no longer the same. The characteristics obtained under these conditions are shown in Fig. 12 (dash-dot lines). The intensity of the mercury radiation at 5461A is relatively low before the appearance of the jet. When the jet arrives the intensity of this mercury line increases about 25-fold. The hydrogen radiation at 6563A also increases on jet arrival but only 3.5-fold. No significance is to be placed on the relative magnitudes of intensities of these two radiations since they depend on the optical system and relative response of the photo-tube. The difference in increase of intensity found on appearance of the jet is significant, however, since it shows that the composition of the gas in the discharge path changes on jet arrival and, therefore, constitutes still another proof of jet reality. The increase in intensity of the hydrogen α-line on jet arrival may be partly due to excitation of hydrogen by excited mercury atoms through collisions of the second kind, but it probably is largely due to high collision excitation probability of the hydrogen near the jet surface.

When the spectrograph slit is placed so that the light reaching the photo-cell originates at the cathode, the characteristics are again quite different, as shown in Fig. 12 (dashed lines). The radiation of the mercury green line (5461A) is a fair analog of the current, but the radiation from the hydrogen α-line is not. It quickly reaches a peak and then decreases, in accord with the postulate that the hydrogen in front of the cathode is completely swept away by the jet. Some radiation from hydrogen remains, probably because the cathode spot is expanding so that hydrogen atoms are being constantly excited on the cathode spot periphery.

SECTION VI

Velocity of Jet Front, Center, and Back

In Section IV the velocity of the jet front was determined by measuring the increase in intensity of the light passing through a No. 62 filter as a function of time. By using short pulses, it is possible, in this way, not only to measure this velocity of the front of the jet but also, by measuring the decrease in intensity, the velocity of the back of the jet. This has been done with both 0.25- and 1-microsecond pulses. The results obtained with both pulse durations are quite consistent but the data obtained with the 0.25-microsecond pulse are more easily interpreted since, because of the circuit used, the current cuts off much more rapidly. The apparatus was used as shown in Fig. 6. The current pulse obtained with the nominal 0.25-microsecond pulse network is shown in Fig. 13(b). The consequent intensity time variation obtained with light originating at the mercury cathode is shown in Fig. 13(a), (CATHODE). This curve is a fair analog of the current pulse with a time delay of about 0.15 microsecond as before.*** When the hori-

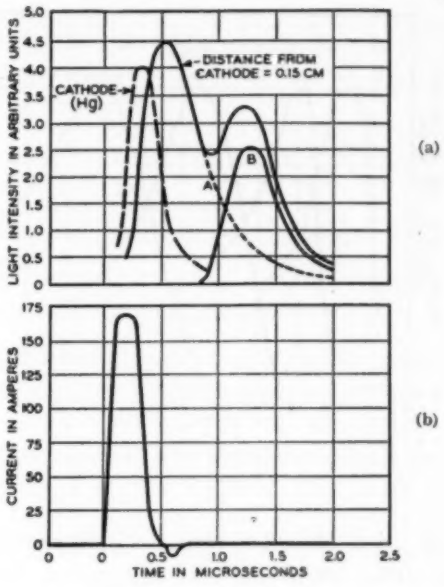

FIG. 13. (a) Light intensity as a function of time, I at the mercury cathode surface, and II at 0.15 cm from mercury surface. (b) Current through the discharge as a function of time.

*** The pulse of light obtained from the cathode with these sparks is of considerable interest since it has a far faster decay than can be obtained with the usual gas discharge tubes used in high speed photography. The reason for the sharp decay in the light from the cathode is doubtless that the excited atoms are swept out of the cathode region by the jet.

Another interesting fact is the enormous intrinsic brightness of the cathode spot. Calculations based on either the effect of Kodachrome film or the average current through a photo-tube agree that the cathode spot of these 0.25-microsecond sparks has an intrinsic brilliancy of 10^6 candles/cm^2. This is some 500 times the intrinsic brilliancy

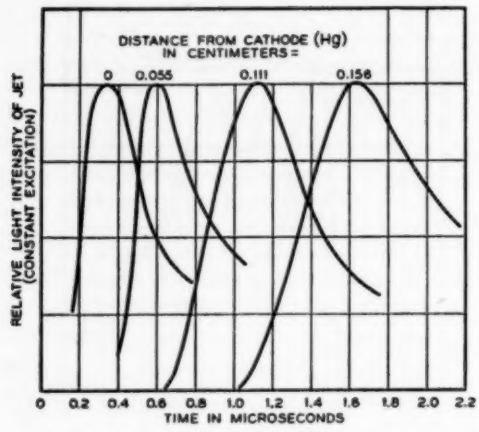
DISTANCE FROM CATHODE (Hg) IN CENTIMETERS =
0
0.055
0.111
0.156
RELATIVE LIGHT INTENSITY OF JET (CONSTANT EXCITATION)
0 0.2 0.4 0.6 0.8 1.0 1.2 1.4 1.6 1.8 2.0 2.2
TIME IN MICROSECONDS

FIG. 14. Corrected relative light intensity of jet as a function of time.

zontal slit is placed so that the light reaching the photo-tube originates 0.15 centimeter from the mercury surface, the light intensity is greatly decreased. In order to compensate for this decrease the diaphragm of the lens was opened, giving the characteristics shown in Fig. 13(a). This curve has two peaks. If the slit is moved so that the light reaching the photo-tube comes from a region of the positive column not reached by the jet, the first part of this curve is retraced but the second peak disappears, the characteristic dropping along the dotted line *A*. Evidently, then, the first peak is due to the background light of the positive column and only the second peak is due to the jet. In order to obtain the intensity variation of the jet alone, the radiation due to the positive column (first peak and the dotted line) is subtracted from the original characteristic. The result is curve *B*.†

Curve *B* is evidently due to the jet but its profile is not due entirely to a change in number of mercury atoms in the spark since the intensity of radiation of the excited atoms is decreasing rapidly with time because the current has been cut off. This decrease in intensity with time was measured and it was found that for 0.25-microsecond pulse, the intensity of light from the jet, after the current is cut off, follows closely an exponential decay which can be written $i = i_0 e^{-2.8t}$, where t is the time in microseconds. Therefore, by multiplying curve *B* by $e^{+2.8t}$ a profile is obtained that is due to a change in the number of mercury atoms only.

Such profiles, obtained at four different distances from the mercury cathode, are shown in Fig. 14. For comparison, the peaks of the four curves were arbitrarily made to have the same relative light intensity. The time of arrival of any analogous points on these curves might be plotted as a function of distance. In this manner one obtains the velocity of the corresponding part of the jet. The points chosen are those corresponding to the time required for the number of mercury atoms to reach the half-maximum, the maximum, and the half-minimum. These points, therefore, give a measure of the velocity of the mercury atoms at the front of the jet, at the maximum jet density, and at the back of the jet. The times of arrival of these parts of the jet are plotted in Fig. 15. It is obvious that near the mercury cathode all parts of the jet move with much the same velocity. The jet spreads out as the distance from the mercury surface increases, since the jet front apparently travels faster than the back. The dotted line is that of Fig. 9 obtained for the cathode jet front and a constant supply of energy, since a current of 160 amperes was maintained during the time recorded. The

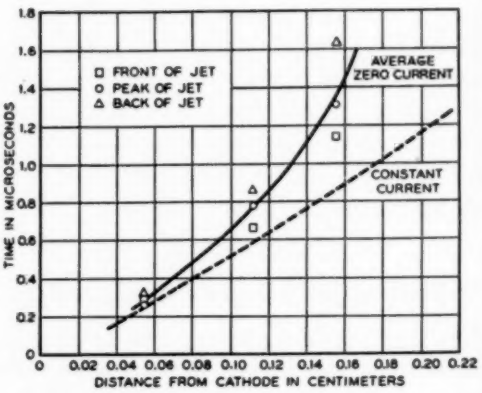
□ FRONT OF JET
○ PEAK OF JET
△ BACK OF JET
AVERAGE ZERO CURRENT
CONSTANT CURRENT
TIME IN MICROSECONDS
0 0.2 0.4 0.6 0.8 1.0 1.2 1.4 1.6 1.8
0.02 0.04 0.06 0.08 0.10 0.12 0.14 0.16 0.18 0.20 0.22
DISTANCE FROM CATHODE IN CENTIMETERS

FIG. 15. Time of arrival of specified parts of the cathode jet as a function of distance from the mercury surface.

of tungsten at 3100°K and more than 10 times the brilliancy of the crater of a high intensity d.c. arc. These cathode spots are, in fact, apparently brighter than the surface of the sun (1.6×10^9 candles/cm²) or even the star Algol (0.8×10^9 candles/cm²). This enormous intrinsic brilliancy decreases with pulse duration since the cathode spot area increases with time, in accordance with Eq. (1), while the total light from the cathode remains substantially constant, as shown in Fig. 7.

† This is a permissible procedure since it has been shown in Section V that, even though some change in gas composition may exist as a function of distance from the mercury surface, the intensity variation of all the radiation to which the photo-cell is sensitive follows the same relative time variation in the absence of a jet.

solid curve is that for the average of the points. This curve, which closely approaches the dotted line near the mercury cathode, bends away at greater distances, in accordance with expectation, since no energy is being supplied to the jet column from external sources.

SECTION VII

Summary of Experimental Facts

The following experimental facts concerning the discharge in these tubes appear to have been established:

1. A jet of mercury vapor is ejected from a mercury cathode or anode during the time of discharge.

2. Jets are ejected in a direction always normal to the electrode surface (Section II).

3. Spectrograms show the jets are largely composed of mercury vapor (Section III).

4. At the cathode all parts of the jet move with approximately the same velocity (Section VI).

5. Jet velocity decreases with distance but the initial velocity of the cathode jet is $1.9\times(10^5)$ cm/sec., and that of the anode jet is $1.5\times(10^5)$ cm/sec. (Section IV).

6. These initial velocities are independent of current and gas pressure (Section IV).

7. The gas density in the positive column decreases little during the short discharge time (Section III).

8. The anode and cathode drop is 40 ± 5 volts[15] (the column drop is 300 volts/cm at 0.2 microsecond and 100 volts/cm at 1 microsecond).

Mechanism of Jet Production

These facts are incompatible with a "temperature" theory of jet production not only from a consideration of magnitudes but also because the jets are highly directive. If a "temperature" of the electrode were responsible one would expect a cosine distribution of direction of particles, leading to a diffused appearance of the jet at the electrodes. If the jets gain their energy thermally in a high energy region just in front of the electrodes, the velocity of the particles would be distributed at random and the jet would not be directive at all.

The facts are equally incompatible with a high ionic mobility for the following reasons:

1. From the known order of gas density in the positive column (Section III), mobility would have to increase a hundredfold under these conditions to reach the velocities recorded.

2. It is found experimentally that substitution of an oscillatory current pulse for the unidirectional pulse produces a little change in jet front velocity and, therefore, reversal of the field has a negligible effect.

3. Positive ions in the cathode jet would be moving the wrong way.

4. The jet direction may be removed nearly 90° away from the direction of the column gradient.

Since the jets always leave the electrodes in a direction normal to the surface, it is reasonable to attribute their energy to the anode and cathode drop. The energy of the anode jet can be accounted for by positive ions crossing the anode drop. From the laws of conservation of energy and momentum, the velocity of the anode jet, v_+ can be written

$$v_+=(M_+/M)[M/(M+M_h)][(2eV_a)/m]^{\frac{1}{2}}, \quad (2)$$

where M_+ is the effective mass of mercury atoms per unit time that cross the entire anode drop as positive ions, M is the mass of mercury atoms in the jet, M_h is the effective mass of hydrogen involved per unit time, e is the electronic charge, V_a the anode drop, and m the mass of the mercury atom. For the ratio of M_+/M to be as large as unity, every mercury atom vaporized from the anode would necessarily be immediately ionized by collision with an incoming electron. Since a large fraction of atoms may not be ionized until an appreciable portion of the anode drop has been crossed and others never ionized at all, M_+/M is considerably less than one. It is also evident that $M/(M+M_h)$, the fraction due to the mass reaction of the hydrogen, is less than unity. In any event, since V_a must be at least as great as the ionization potential of mercury (10.4 volts), substitution of this value in Eq. (2) shows that $(M_+/M)[M/(M+M_h)]=f$ must be less than 0.5, for otherwise v_+ becomes larger than the measured value $(1.5\times(10^5)$ cm/sec.).

Using the accommodation coefficient theory of cathode jet production,[5] the velocity of the cathode jet, v_-, may be written similarly:

$$v_-=(M_+/M)[M/(M+M_h)]\times[2eV_c(1-\alpha)/m]^{\frac{1}{2}}, \quad (3)$$

where M_+ is the effective mass of mercury atoms

which are positively ionized at the anode end of the cathode drop and escape into the jet by rebounding from the cathode, retaining an average fraction of their incident energy of $(1-\alpha)$. V_c is the cathode drop and M, M_h, and e are the same as before. Both fractions M_+/M and $M/(M+M_h)$ are again certainly less than unity for exactly the same reasons. In fact, there is no reason to expect either to be greatly different numerically from those obtained with the anode jet. Since $V_a+V_c=40$ volts[18], V_c cannot be greater than 30 volts. The value of α for positive mercury ions on mercury has not been determined. From consideration of known values of α it is, however, unreasonable to assume that the average value of α in this case is less than 0.90 and it is probably very close to the 0.93 measured by Arnot and Milligan[19] for 50-volt positive mercury ions on tungsten. Substituting the value of $V_c=30$ volts and $\alpha=0.90$ in Eq. (3), one obtains

$$v_-=1.7\ (10^5)\ f\ \text{cm/sec.}$$

Using the maximum value of f obtained from the anode jet (0.5) as an approximation, $v_-=0.85\times10^5$ cm/sec. which is approximately half the velocity or a quarter of the energy required.

The same conclusion is reached by use of the measured loss of mercury from the cathode with a current pulse of 200 amperes for 2 microseconds and a repetition rate of 300 per second. This value, corrected for the gross evaporation at the mercury surface, is 17 (10^{-4}) grams/coulomb. This measurement was made by simply weighing a small cup of mercury before and after sparking in hydrogen for one hour and making a small correction for vaporization at the mercury surface. This correction was made by measuring the temperature of the mercury surface with a thermocouple during sparking and repeating the experiment with the mercury surface held at the same temperature by means of a heating coil instead of sparks. Since it has been shown in Section VI that ejection of mercury from the cathode spot stops abruptly with the current, the result obtained in this way should be reasonably accurate. Tonks[20] obtained 2.5 (10^{-4}) grams/coulomb by extrapolating to zero current using an anchored spot and small currents. The value of 17 (10^{-4}) grams/coulomb may be too high, but it is believed nearer the true value for unanchored spots and these high current densities than the value obtained by Tonks.

Using a mercury loss of 17 (10^{-4}) grams/coulomb of the cathode, it is easily shown that $M_+/M=1.2(i_+/i)$ where i_+/i is the ratio of the positive ion currents to the total currents at the cathode. Also, using this value of mercury loss $M/(M+M_h)\approx0.90$. Therefore, if $i_+/i=\frac{1}{2}$, which is certainly as large as one would like to assume, $f=0.54$ and $v_-=0.9$ (10^5) cm/sec. (maximum).

It therefore appears necessary to assume that in addition to positive ions striking the cathode and rebounding as neutral atoms, a large number of other particles leave the cathode drop with higher energies. This could be true if many mercury atoms leave the cathode as negative ions. That negative mercury ions can be produced at the cathode has been shown by Arnot and Milligan.[19] Under the conditions of their experiments, however, the probability of production of negative mercury atoms was extremely small. If it is assumed that this small probability is greatly increased due to the high field at the cathode surface under these conditions, the cathode jet velocity can easily be accounted for, since Eq. (3) can be rewritten as

$$v_-=(M_+/M)[M/(M+M_h)]\times[2eV_c(1-\alpha)/m]^{\frac{1}{2}}+(M_-/M)[M/(M+M_h)]\times[2e(V_c-\phi)/m]^{\frac{1}{2}},\quad(4)$$

where M_- is the mass of negative ions and ϕ is the effective work function for a negative ion. Using the more probable values of $V_c=22$ volts, $\alpha-0.93$, and $\phi\approx4$ volts, when $M_+/M=0.40$ and $M_-/M=0.36$, $V=1.9$ (10^5) cm/sec., and the measured velocity of the cathode jet is attained.

If this theory is correct one would expect the cathode jet to carry a high net negative charge and the anode jet to carry a high net positive charge. This condition appears to exist as shown by the direction in which the jets are bent in a magnetic field. In a field of approximately 2000 gauss it is observed that both the anode and cathode jets are bent out of the positive column in opposite directions corresponding to the net charges expected. The anode jet is bent some-

[19] F. L. Arnot and J. C. Milligan, Proc. Roy. Soc. **A156**, 538 (1936).
[20] L. Tonks, Phys. Rev. **54**, 634 (1938).

what less than the cathode jet, which has a mean radius of curvature of about a centimeter, implying a net charge to mass ratio for the jet of about -40 e.m.u./gram.

SECTION IX

Conclusion

The existence of mercury vapor jets in sparks, which have been shown to be arcs of short duration, appears to have been proven beyond reasonable doubt. The velocity of the jets is such that neither the positive nor negative ions in the arc column can reach the electrodes since the ion velocities are considerably less than the jet velocities and are oppositely directed. From consideration of the literature of vapor velocities in both sparks and arcs, it is certain that these vapor jets occur with a wide variety of electrode materials. An obvious test of the theory of the mechanism of jet production would be to obtain the initial jet velocity as a function of the atomic weight of the electrode material. Since the program of peacetime research prevents further work in this organization, it is hoped that the study will be carried on elsewhere.

It is a pleasure to acknowledge the advice and the assistance of many persons in this organization, particularly Drs. F. S. Goucher, W. Shockley, J. Bardeen, and C. H. Townes.

PHYSICAL REVIEW VOLUME 73, NUMBER 8 APRIL 15, 1948

On the Calculation of Self-Energies in Quantum Theory by Analytic Continuation

S. BERTIL NILSSON
Institute of Mechanics and Mathematical Physics, University of Lund, Sweden

(Received July 23, 1947)

Riesz's method of solving hyperbolic differential equations by analytic continuation has been used by Gustafson to eliminate infinities in quantum theory. Treating the one-electron case, he found finite values of the self-energy integrals in the second approximation, also for those integrals for which the λ-limiting process fails* (without the further assumption of negative-energy photons). In the present paper it is shown that the general result of Gustafson's procedure is to remove all divergences normally appearing in self-energy expressions, except logarithmic divergences. Thus the total self-energy of the electron, to the second approximation, is found to be zero on the one-electron theory if calculated by this method, whereas in the hole theory the logarithmically divergent expression of Weisskopf is retained. A proposal by Pauli to alter the commutation rules in a certain way gives essentially the same results.

I. INTRODUCTION

WE are going to investigate the general effect of evaluating self-energies in quantum theory by the method used by Gustafson in the case of the second approximation.[4–8]* Before entering on the problem we set down a few notations to be employed in the following.

A point in space-time is denoted by $x=x^\nu$ ($\nu=0, 1, 2, 3$; $x^0=ct$), and a metrical tensor with $-g_{00}=g_{11}=g_{22}=g_{33}=1$ is used. The length $r(x)$ of a vector x is defined by

$$-r(\mathbf{x})^2=g_{\mu\nu}x^\mu x^\nu=x_\nu x^\nu=(\mathbf{x},\mathbf{x}),$$

so that r^2 is positive for a time-like vector. Further, we write $\Box$ for the wave operator $-\partial^2/\partial x^\nu \partial x_\nu$, and $\vec{x}$ for a vector (x^1, x^2, x^3) in ordinary space. Then $(x,y)=x_\nu y^\nu=\vec{x}\vec{y}-x^0y^0$.

Now, to form an expression for the self-energy of an electron or of a nucleon, one may start with the equations giving the interaction with the electromagnetic field and the meson field, respectively. Here we use the formulation of the theory in which the dynamic variables are operators satisfying field equations analogous to those of the classical theory. The specific state of the system is then characterized by a normalized and time-independent state vector C. A variable represented by an operator F has the expectation value $\langle F\rangle=C^*FC$.

* Numbered references will be found at the end of the text.

To fix our ideas, consider the case of quantum electrodynamics. The interaction between electrons, of mass m and charge $-e$, and the electromagnetic field is described by the equations[a]

$$\left(-i\alpha^\nu\frac{\partial}{\partial x^\nu}+\beta m\right)\psi=-eA_\nu\alpha^\nu\psi,$$
$$\Box A^\nu=-4\pi es^\nu\,(=-4\pi e\psi^*\alpha^\nu\psi), \tag{1.1}$$

where the expression in brackets holds in the one-electron theory, and where the vector $\boldsymbol{A}$ and spinor ψ fulfill well-known commutation and anticommutation relations. α^ν and β are Dirac matrices ($\alpha^0=1$).

Using perturbation theory we expand $\boldsymbol{A}$ and ψ, and hence $\boldsymbol{s}$, in power series in e,

$$\mathbf{A}=\mathbf{A}^{(0)}+e\mathbf{A}^{(1)}+\cdots,$$

etc. The second approximation of the self-energy of the electron is then given by

$$W=\frac{e^2}{2}\int(dx)^3\langle(\mathbf{s}^{(0)},\mathbf{A}^{(1)})+(\mathbf{s}^{(1)},\mathbf{A}^{(0)})\rangle$$
$$=(W_{\text{st}}+W_{\text{sp}})+W_{\text{fluct}}. \tag{1.2}$$

(see Weisskopf[14]). Here $\boldsymbol{A}^{(1)}$ satisfies

$$\Box\mathbf{A}^{(1)}=-4\pi\mathbf{s}^{(0)}, \tag{1.3}$$

so that the solution of the inhomogeneous wave equation is of importance for the first part of W, that of the Dirac equation playing a corresponding role for the second part (in the case of a nucleon the meson equation takes the place of the wave equation). As is well known, simple insertion of these solutions into 1.2 as in the ordinary treatment gives rise to divergent integrals. In Gustafson's papers use is made of the method of solving normal hyperbolic differential equations given by Riesz[11,12] and employed by him and Fremberg[2,3] to eliminate divergences in the classical theory of point electrons.

II. RIESZ'S SOLUTION OF HYPERBOLIC EQUATIONS

A. To solve the wave equation

$$\Box u(\mathbf{x})=f(\mathbf{x}) \tag{2.1}$$

by analytic continuation, we form with Riesz[11,12] an expression u^α (the "α-solution") depending analytically on a parameter α. In the following we are not interested in special boundary conditions[b] and can then take u^α as

$$u^\alpha(\mathbf{x})=I^\alpha f(\mathbf{x})=\int_{D^\mathbf{x}}V^\alpha(\mathbf{x}-\mathbf{y})f(\mathbf{y})(dy)^4, \tag{2.2}$$

where

$$V^\alpha(\mathbf{x})=\frac{r(\mathbf{x})^{\alpha-4}}{H(\alpha)},\quad H(\alpha)=\pi 2^{\alpha-1}\Gamma\left(\frac{\alpha}{2}\right)\Gamma\left(\frac{\alpha-2}{2}\right).$$

The integration element is $(dy)^4=dy^0dy^1dy^2dy^3$, and the domain of integration $D^\mathbf{x}$ is the whole interior of the retrograde light-cone $r(x-y)^2=0$ with its vertex at the point $\boldsymbol{x}$. Under certain conditions on f the integral $I^\alpha f$ converges for $\alpha>2$ or in some interval $A>\alpha>2$; for other values of α it has to be defined by analytic continuation.

We can now assert that $u^{(2)}$ is a solution of the wave equation 2.1. That a solution is indeed obtained for $\alpha=2$ is seen from the relation

$$\Box V^\alpha=V^{\alpha-2},\quad\text{whence}\quad\Box I^\alpha f=I^{\alpha-2}f,$$

(which is an immediate consequence of the definitions above) together with the fact that I^0 is an identity operator,[c]

$$I^0f=f.$$

B. The solution of the "meson equation" (Klein-Gordon's equation),

$$(\Box+\kappa^2)u(\mathbf{x})=f(\mathbf{x}), \tag{2.3}$$

can be obtained in an exactly analogous way. We have only to replace the integral operator I^α in (2.2) by a similar operator I_κ^α in which the new kernel V_κ^α has to satisfy

$$(\Box+\kappa^2)V_\kappa^\alpha=V_\kappa^{\alpha-2}.$$

The further condition that $V_\kappa^\alpha\to V^\alpha$ as $\kappa\to 0$ now determines V^α completely:

$$V_\kappa^\alpha=\sum_{k=0}^{\infty}\binom{-\alpha/2}{k}\kappa^{2k}V^{\alpha+2k}=\frac{(r/\kappa)^{(\alpha/2)-2}J_{(\alpha/2)-2}(\kappa r)}{\pi 2^{(\alpha/2)+1}\Gamma(\alpha/2)},$$

where J is a Bessel function.[12,3]

We may note that, owing to the form of $H(\alpha)$, the contributions to the integral from the

[a] In natural units, $\hbar=c=1$.

[b] The solution of the general Cauchy problem in any number of dimensions is to be found in references 3 and 12.

[c] For proofs see references 1 and 3.

interior of the cone are cancelled in $I^2 f$ (Huygens's principle: retarded potentials), but not in $I_\kappa^2 f$ for $\kappa \neq 0$.

C. The Dirac equation may be written

$$(\nabla + im)\psi(\mathbf{x}) = g(\mathbf{x}), \tag{2.4}$$

where $\nabla = \gamma^\nu(\partial/\partial x^\nu)$ $(\gamma^\nu = \beta\alpha^\nu,\ \gamma^\mu\gamma^\nu + \gamma^\nu\gamma^\mu = -2g^{\mu\nu})$. Multiplying on the left by $\nabla - im$ we get

$$(\Box + m^2)\psi = (\nabla - im)g,$$

which is solved, as in the case of (2.3) above, by $I_m^2(\nabla - im)g$.[d]

D. As a special case, which will be of importance in the applications below, let us choose for $f(x)$ a plane wave of the form $e^{i(K,x)}$. Then f does not vanish for $x^0 = -\infty$, and the integrals $I^\alpha f$ and $I_\kappa^\alpha f$ over D^x will not converge for any value of α. However, for $\alpha > 2$ they are oscillating and can be defined in the usual way by first letting iK_0 have a real positive part, which is then made to tend to zero. In this way we get, assuming $\boldsymbol{K}$ to be a time-like vector and choosing a suitable set of coordinate axes,

$$\int_{D^x} r(\mathbf{x}-\mathbf{y})^{\alpha-4} \exp[iK_0 y^0](dy)^4$$

$$= \exp[iK_0 x^0] \int_0^\infty dz^0 \exp[-iK_0 z^0] \times \int_0^{z^0} 4\pi\rho^2 d\rho ((z^0)^2 - \rho^2)^{(\alpha-4)/2}$$

$$= \exp[iK_0 x^0](iK_0)^{-\alpha} H(\alpha),$$

(where $\boldsymbol{z} = \boldsymbol{x} - \boldsymbol{y}$, $|\vec{z}| = \rho$), whence generally,

$$\int_{D^x} V^\alpha(\mathbf{x}-\mathbf{y}) \exp[i(\mathbf{K},\mathbf{y})](dy)^4 = \exp[i(\mathbf{K},\mathbf{x})] r(i\mathbf{K})^{-\alpha}.$$

From the expansion of V_κ^α we now obtain for $I_\kappa^\alpha \exp[i(\mathbf{K},\mathbf{x})]$ a binomial series giving

$$\int_{D^x} V_\kappa^\alpha(x-y) \exp[i(\mathbf{K},\mathbf{y})](dy)^4 = \frac{\exp[i(\mathbf{K},\mathbf{x})]}{(K_\nu K^\nu + \kappa^2)^{\alpha/2}}, \tag{2.5}$$

which holds, provided the denominator does not vanish, whether $\boldsymbol{K}$ is time-like or not (also for $\kappa = 0$).

With this form of $f(x)$, and with $g(x) = f(x)u$ (u a spinor independent of x), (2.5) is the α-solution of (2.3) or of (2.1) ($\kappa = 0$), that of the Dirac equation (2.4) being given by

$$\psi^\alpha(\mathbf{x}) = \frac{i(K_\nu\gamma^\nu - m)u}{(K_\nu K^\nu + m^2)^{\alpha/2}} \exp[i(\mathbf{K},\mathbf{x})]. \tag{2.6}$$

The actual solutions are obtained for $\alpha = 2$.

III. FORMATION OF SELF-ENERGY INTEGRALS GENERAL DISCUSSION

A. Returning to the self-energy (1.2) with a view to establishing what types of integral to expect in such expressions, we can content ourselves for the moment with studying one typical term, e.g., the electrostatic energy

$$W_{sl} = -\frac{e^2}{2} \int \langle s_0^{(0)} A_0^{(1)} \rangle (dx)^3. \tag{3.1}$$

We introduce the α-solution for $A_0^{(1)}$ (from (1.3) and (2.2)),

$$A_0^{(1)\alpha} = -4\pi I^\alpha s_0^{(0)}(\mathbf{x}).$$

In evaluating the integral we write $\psi^{(0)}$ as a Fourier series,

$$\psi^{(0)} = V^{-\frac{1}{2}} \sum_n a_n u_n \exp[i(\mathbf{p}_n,\mathbf{x})],$$

where V is a periodicity volume, $\boldsymbol{p}_n$ is the momentum four-vector of an electron in state n, u_n is a certain spinor, and the a_n's are Jordan-Wigner matrices.

The one-electron theory (cf. (1.1)) will then give for an electron with the momentum vector $\boldsymbol{q}$,

$$\langle s_0^{(0)} A_0^{(1)\alpha} \rangle = -4\pi V^{-2} \sum_n u_q^* u_n u_n^* u_q \times \exp[i(\mathbf{p}_n - \mathbf{q},\mathbf{x})] I^\alpha \exp[-i(\mathbf{p}_n - \mathbf{q},\mathbf{x})].$$

If this is inserted into W_{sl} and the sum over the momenta is written as an integral, the resulting expression reads (with $p = |\vec{p}|$, $z = y - x$)

$$W_{sl}^\alpha = -\frac{e^2}{2} \int \langle s_0^{(0)} A_0^{(1)\alpha} \rangle (dx)^3$$

$$= \frac{e^2}{\pi} \oint \frac{d\omega}{4\pi} \int_0^\infty p^2 dp \sum_{(u)} \Big| u_q^* u u^* u_q \times \int_D V^\alpha(-\mathbf{z}) \exp[-i(\mathbf{p}-\mathbf{q},\mathbf{z})](dz)^4 \Big|. \tag{3.2}$$

[d] This remark is sufficient for our present purpose. A more detailed treatment of the Dirac equation, also taking certain boundary conditions into consideration, is given by Gustafson (reference 8).

The summation here is over the four states belonging to a fixed momentum $\vec{p}$, $d\omega$ is a solid-angle element, and D the retrograde light-cone from the origin.

So far everything is straightforward and no new hypotheses have been made, the usual infinite value of W_{st} being obtained by putting $\alpha=2$ after the integration over D has been performed. However, in the form given above, $W_{st}{}^{\alpha}$ can be computed also for other values of α and is not necessarily infinite everywhere. In the domain of convergence it is then, as $A_0{}^{(1)\alpha}$, an analytic function of α, which can be continued analytically to $\alpha=2$ (just as, e.g., the Eulerian integral for $\Gamma(x)$ converges only for $x>0$, the function having to be defined by analytic continuation for $x<0$).

Gustafson's procedure consists in taking this $W_{st}{}^{2}$ as the significant value of W_{st}, corresponding definitions being used for other quantities. A certain justification for defining physical quantities by means of analytic continuation can be given in the classical case, where the whole theory, as shown by Fremberg,[2,3] can be built up with general α-quantities in place of the ordinary ones, and satisfying the same equations. Such a procedure does not seem adapted to the quantum theory. Instead, we must there lay down as a rule that all the equations should be solved by Riesz's method, then all physical quantities are first to be defined as functions of the parameters entering into these solutions, and afterwards calculated by analytic continuation. In this way an unambiguous scheme is obtained. It means a redefinition, but if we want to have some means of eliminating divergences without changing the fundamental equations, it is a rather natural one.

B. In connection with the expression (3.2) for $W_{st}{}^{\alpha}$ we can now make some general observations. Using Fourier analysis, it is evident from (2.5) and (2.6) that self-energies involving a solution of the wave or meson equation, or of the Dirac equation, can always be expressed as a sum of terms of the same general form, *viz.*

$$\text{const.}\oint d\omega\int_0^{\infty} f_1(p)dp \times\int_D V_s{}^{\alpha}(-\mathbf{z})\exp[-i(\mathbf{K},\mathbf{z})](dz)^4$$

($\kappa=0$ for the wave equation), where $\boldsymbol{K}$ is linear in $\boldsymbol{p}$. The integral over D equals

$$(K_\nu K^\nu+\kappa^2)^{-\alpha/2}=f_2(p)^{-1-\beta}, \tag{3.3}$$

where we have introduced $\beta=(\alpha/2)-1$, so that $\beta\to 0$ as $\alpha\to 2$. Thus, apart from an integration over the directions[*] and from a constant factor, the terms of interest are of the form

$$Q^{\beta}=\int_0^{\infty}\frac{f_1(p)}{f_2(p)^{1+\beta}}dp. \tag{3.4}$$

The functions f_1 and f_2 are rational in p or may contain square roots. For large values of p $f_1/f_2{}^{1+\beta}$ can then be supposed to behave essentially as $p^{n-r\beta}$, where r is the degree of f_2 (1 or 2).

The ordinary result is obtained by setting $\beta=0$ in the integrand. A possible infinity is presupposed in the following to arise only from the upper limit of the integral (i.e., if $n\geqslant -1$), so that we have no convergence difficulties at the origin for $\beta=0$. It may happen, however, that new singularities are in some cases introduced here for other values of β. To exclude this contingency we may agree always to let the lower limit of the integrals over the momenta be some small positive value ϵ, which is allowed to approach zero only after the analytic continuation of the integral has been performed. Thus

$$\underset{\beta\to 0}{\text{anal. cont.}}\int_{\epsilon}^{\infty} p^{n-\beta}dp\to 0 \text{ as } \epsilon\to 0\ (n>-1) \tag{3.5}$$

(we may also choose $\epsilon=$ const. β). However, we will continue to write 0 for the lower limit, understanding it to be reached only in the final result if this is necessary for the convergence.

To calculate Q^0 by analytic continuation assuming that the integral Q^{β} does exist for some β's, we split it up into

$$Q^{\beta}=\left(\int_0^{P}+\int_P^{\infty}\right)\frac{f_1}{f_2{}^{1+\beta}}dp =Q^{\beta}(0,P)+Q^{\beta}(P,\infty). \tag{3.6}$$

The two parts are both analytic in β with some domain of convergence in common and, consequently, Q^0 is obtained by performing the

[*] This integration does not give rise to any new infinities, so that we can pass to $\beta=0$ before carrying it out.

continuation of each integral separately. In fact, the same procedure can always be used for a general Q^β if we have first a lower integration limit $\epsilon>0$ as above.

If P is chosen large enough, $f_1/f_2^{1+\beta}$ can be expanded into a series of falling powers of p in the interval (P, ∞), so that for $\beta>(n+1)/r$

$$Q^\beta(P,\infty)=\int_P^\infty p^{n-r\beta}\sum_{m=0}^\infty a_{n-m}(\beta)p^{-m}$$

$$=-\sum_{m=0}^\infty a_{n-m}(\beta)\frac{P^{n-m+1-r\beta}}{n-m+1-r\beta},$$

and as $\beta\to 0$ by analytic continuation

$$Q^0(P,\infty)=-\sum_{n-m\neq -1} a_{n-m}\frac{P^{n-m+1}}{n-m+1}$$

$$+\left[a_{-1}\frac{P^{-r\beta}}{r\beta}+\frac{a_{-1}(\beta)-a_{-1}}{r\beta}\right]_{\beta=0},$$

where $a_{n-m}=a_{n-m}(0)$.

In the first integral of (3.6), with the limits 0 and P, β may be set equal to zero under the integration sign. We determine the dependence upon P by expanding f_1/f_2 as before and making an indefinite integration:

$$Q^0(0,P)=\sum_{n-m\neq -1} a_{n-m}\frac{P^{n-m+1}}{n-m+1}$$

$$+a_{-1}\log P+\bar{Q}, \quad (3.7)$$

where $\bar{Q}$ does not depend on P.

Thus we get by addition

$$Q^0=\bar{Q}+\frac{1}{r}\frac{d}{d\beta}a_{-1}(0)+a_{-1}\left[\log P+\frac{P^{-r\beta}}{r\beta}\right]_{\beta=0}$$

which is, as it must be, independent of P, the last term equaling $a_{-1}(1/r\beta)_{\beta=0}$. If we let P tend to infinity in this term before $\beta\to 0$, the result may be written as

$$Q^0=\bar{Q}+\frac{1}{r}\frac{da_{-1}}{d\beta}+\lim_{P\to\infty} a_{-1}\log P. \quad (3.8)$$

(Nothing is changed in this formula if Q^β is a sum of terms of the form (3.4).)

So, if $a_{-1}\neq 0$ the value is logarithmically infinite in P, and otherwise finite. The general result, then, of defining self-energy terms by means of analytic continuation as above is that logarithmic divergences are retained, whereas all other types are eliminated. For the analytic function Q^β this means that in the presence of logarithmically divergent integrals Q^β has, and otherwise has not, a pole at $\beta=0$.

The result is an improvement on the λ-limiting process of Wentzel and Dirac, which is only able to remove the singularities of uneven orders if it is not combined with Dirac's assumption of negative-energy photons.**

IV. EXAMPLES—SELF-ENERGY OF THE ELECTRON

The calculation of the self-energy (1.2) of the electron by means of analytic continuation has been carried out by Gustafson[4,8] when neglecting the retardation in the solution of the equations (i.e., putting $y^0=x^0$ in $f(y)$ in (2.2), etc.). As an application of the formalism developed above, the continuation of the exact integrals is given here.

A. The electrostatic energy is expressed in the one-electron theory by (3.2).† We make the calculation also for a $\kappa\neq 0$ (meson theory) and get for the integral over D, in the case of a particle at rest: $q=(m, 0, 0, 0)$,

$$[p^2-(p^0-m)^2+\kappa^2]^{-\alpha/2}$$

$$=\left[2m\left(p^0-m+\frac{\kappa^2}{2m}\right)\right]^{-\alpha/2},$$

where $p^0=\pm(p^2+m^2)^{\frac{1}{2}}$. If we let p_0 stand for the positive square root, the result of performing the

---

** In the classical case, the λ-limiting process and the Riesz method have been shown by Ma[15] to be equivalent.

† This is not the usual expression for the electrostatic energy, E_{st} (obtained, e.g., by eliminating the longitudinal waves). Indeed, E_{st} can be obtained from our W_{st} by neglecting the retardation, which is equivalent to letting the time component of the vector $\mathbf{p}-\mathbf{q}$ in (3.2) be zero. Then we get, instead of (4.1) and (4.2),

$$E_{st}^\alpha=e^2/\pi\int_0^\infty [p^2dp/(p^2+\kappa^2)^{1+\beta}]\to -e^2\kappa/2$$

(cf., reference 5). So our separation into 'W_{st}' and 'W_{sp}' is not identical with that in reference 14.

summation over u in (3.2) can then be written

$$W_{st}^{\alpha}=\frac{e^2}{4\pi m}\frac{1}{(2m)^{\beta}}\int_0^{\infty}\frac{p^2dp}{p_0}\left\{\frac{p_0+m}{\left(p_0-m+\frac{\kappa^2}{2m}\right)^{1+\beta}}-\frac{p_0-m}{\left(-p_0-m+\frac{\kappa^2}{2m}\right)^{1+\beta}}\right\}=\frac{e^2}{\pi}Q^{\beta} \quad (4.1)$$

($\beta=\alpha/2-1$). The integral converges for $\beta>2$. As in the last section the analytic continuation to $\beta=0$ is conveniently carried out by dividing the integration interval into two parts. After putting $\beta=0$ directly in the first part and simplifying the integrand, we obtain

$$Q^0(0,P)=b\int_0^P\frac{p^2dp}{p^2+\kappa^2b}=bP-\kappa b^{\frac{1}{2}}\left(\frac{\pi}{2}-\arctan\frac{\kappa b^{\frac{1}{2}}}{P}\right),$$

with $b=1-\kappa^2/4m^2$. The last term can be expanded in descending powers of P. Comparing with (3.7) we have $a_{-1}=0$, and since $da_{-1}/d\beta$ is found to be a pure imaginary and so has no physical significance, (3.8) gives

$$Q^0=\bar{Q}=-(\pi/2)\kappa b^{\frac{1}{2}},$$

i.e.,

$$W_{st}=-\frac{e^2\kappa}{2}\left(1-\frac{\kappa^2}{4m^2}\right)^{\frac{1}{2}}, \quad (4.2)$$

which is zero for $\kappa=0$ (electrodynamics).[g]

The effect of assuming the hole theory is to substitute a plus sign for the minus sign between the terms in (4.1); the result is then logarithmically divergent, *viz.* essentially (for $\kappa=0$)

$$W_{st}=\frac{9e^2m}{8\pi}+\lim_{P\to\infty}\frac{3e^2m}{4\pi}\log\frac{2P}{m}.^{h} \quad (4.3)$$

B. The α-expression for the "spin energy" W_{sp} (obtained from the product $\vec{s}^{(0)}\vec{A}^{(1)}$ in (1.2)) is found to be ($\kappa=0$)

$$W_{sp}^{\alpha}=-\frac{3e^2}{4\pi m}\frac{1}{(2m)^{\beta}}\int^{\infty}\frac{p^2dp}{p_0}\times[(p_0-m)^{-\beta}\mp(-p_0-m)^{-\beta}],$$

where the upper and lower signs refer to the one-electron theory and hole theory, respectively. In the former case we get the result zero immediately by setting $\beta=0$, while the hole theory gives, by analytic continuation,

$$W_{sp}=-\frac{3e^2m}{8\pi}+\lim_{P\to\infty}\frac{3e^2m}{4\pi}\log\frac{2P}{m}.$$

C. The last energy term W_{fluct} in (1.2) contains the solution of Dirac's equation for $\psi^{(1)}$. If $A^{(0)}$ and $\psi^{(0)}$ are written as Fourier series, this solution is expressed as a sum of terms of the form (2.6) with $K=q-k$, q being the momentum vector of the electron and k that of an emitted photon. For an electron at rest $q=(m,0,0,0)$, and then

$$K_\nu K^\nu+m^2=2mk, \quad (4.4)$$

where $k=|\vec{k}|=k^0$. Comparing with (3.3), (3.4), and with the ordinary result,[13] we see that we must have

$$\dot{W}_{\text{fluct}}^{\alpha}=\frac{e^2}{\pi m}\frac{1}{(2m)^{\beta}}\int_0^{\infty}k^{1-\beta}dk.$$

(Waller's result is obtained for $\beta=0$; this holds also in the hole theory.[14]) If the integral is interpreted as in (3.5) the continuation to $\beta=0$ gives the value zero.[i]

D. Collecting our results, we obtain for the second approximation of the total self-energy of the electron,

$$W=W_{st}+W_{sp}+W_{\text{fluct}}(=E_{st}+E_{\text{dyn}}),$$

in the one-electron theory

$$W=0,$$

and in the hole theory

$$W=\frac{3e^2m}{4\pi}+\lim_{P\to\infty}\frac{3e^2m}{2\pi}\log\frac{2P}{m}.^{j}$$

[g] If $\kappa=0$ at the outset we must use an $\epsilon>0$, as in (3.5), in order to make the integral (4.1) convergent (for $\beta>2$). For another device serving the same purpose see reference 4.

[h] For E_{st} Weisskopf's result is obtained, i.e., it is only the logarithmic term in (4.3) that is retained, with the factor $\frac{3}{4}$ replaced by unity.[9]

[i] Neglect of the retardation results in changing the denominator $2mk$ as given by (4.4) into k^2+m^2, the numerical value then becoming $-e^2m$.[8]

[j] The value of the finite term is really immaterial.

Consequently, the singularities have been removed in the one-electron case[k] by using analytic continuation, but the situation in the hole theory is not improved as compared with the usual treatment.[14]

V. PAULI'S MODIFICATION—CONCLUSION

An alternative formulation of quantum electrodynamics which leads to the elimination of the same divergences as above in a simplified manner, by likewise making use of analytic continuation, has been proposed by Pauli.[l] In this method the commutation rules for the Fourier components of the electromagnetic potentials are changed by introducing a factor $\varphi_\beta(k)$ (corresponding to the factor $\cos(\boldsymbol{k},\lambda)$ in the λ-limiting process, see, e.g., reference 10, p. 193), chosen in such a way that $\varphi_\beta(k)\to 1$ as $\beta\to 0$, and that

$$\underset{\beta\to 0}{\text{anal. cont.}} \int_0^\infty k^n \varphi_\beta(k)dk = 0 \text{ for } n > -1.$$

From (3.5) it is seen that we may choose

$$\varphi_\beta(k) = k^{-\beta}.$$

To avoid having to introduce a lower integration limit $\epsilon > 0$ as in (3.5), we may define φ_β to be constant, equal to $l^{-\beta}$, for $k \leqslant l$.

In this modification of the theory[m] the function φ_β will enter as a factor under the integration sign in all self-energy terms (cf. the corresponding expressions obtained with the λ-process). Then the considerations of Section III can be repeated, again giving the result (3.8), with the difference that the term containing $da_{-1}/d\beta$ is no longer present. Consequently, the same divergences are removed as when Riesz's solution is used, though there may in some cases be a difference in the numerical results.

To sum up, we have seen that by admitting analytic continuation and not only ordinary limit transition it is possible in quantum theory to extend the class of divergent integrals that can be made finite by formal mathematical methods, though the difficulties of the logarithmic divergences cannot be overcome in this way. It is true, however, that if Pauli's method is formulated with several parameters (as done for the λ-process by Pomeranchuk), these divergences can be removed too, but the result can then be made wholly arbitrary.

In conclusion, I want to thank Professor T. Gustafson cordially for suggesting an investigation of problems within this sphere and for valuable discussions and suggestions. My thanks are also due to Professor W. Pauli for instructive criticism of the procedure and especially for permission to mention his alternative method.

[k] However, in the higher approximations logarithmic singularities appear also in the one-electron theory. The calculations by analytic continuation (using Pauli's modification below) have been made in the e^4 approximation, and will be published before long (the result is infinite).

[l] I am indebted to Professor Pauli for permission to mention his method here.

[m] The theory is consistent for a finite β, but is seen to be relativistically invariant only in the limit $\beta = 0$.

BIBLIOGRAPHY

(1) N. E. Fremberg, Fysiogr. Sällsk. i Lund Förh. **15**, No. 27 (1945).
(2) N. E. Fremberg, Proc. Roy. Soc. **A188**, 18 (1946).
(3) N. E. Fremberg, "A Study of Generalized Hyperbolic Potentials," Medd. Lunds Univ. Mat. Sem. **7** (1946), thesis.
(4) T. Gustafson, Fysiogr. Sällsk. i Lund Förh. **15**, No. 28 (1945).
(5) T. Gustafson, Fysiogr. Sällsk. i Lund Förh. **16**, No. 2 (1946).
(6) T. Gustafson, Nature **157**, No. 3996, 734 (1946).
(7) T. Gustafson, Nature **158**, No. 4008, 273 (1946).
(8) T. Gustafson, Arkiv f. Mat., Astr. o. Fys. **34A**, No. 2 (1947).
(9) S. B. Nilsson, Fysiogr. Sällsk. i Lund Förh. **16**, No. 24 (1946).
(10) W. Pauli, Rev. Mod. Phys. **15**, 175 (1943).
(11) M. Riesz, C. R. du Congrès internat. d. math. (Oslo, 1936) II, p. 44.
(12) M. Riesz, Conférence à la Réunion internat. d. Math. tenue à Paris en Juillet 1937, p. 153 (1939).
(13) I. Waller, Zeits. f. Physik **62**, 673 (1930).
(14) V. F. Weisskopf, Phys. Rev. **56**, 72 (1939).
(15) S. T. Ma, Phys. Rev. **71**, 787 (1947).

On the Formal Extension of Dirac's Equation under Continuous Transformation Groups

E. L. HILL
Department of Physics, University of Minnesota, Minneapolis, Minnesota
(Received January 14, 1948)

The theory of equations of the Dirac type which are form-invariant under general finite continuous groups of point transformations in space-time is developed. The possible equations invariant under a given group depend on the structure of the group, but in each case the required invariance imposes a set of linear homogeneous relations on the β-operators with which any assumed algebra must be consistent. It is shown that the algebra appropriate to the general equation possessing form-invariance under the inhomogeneous Lorentz group is necessarily of infinite order.

1. INTRODUCTION

THE success of the Dirac equation for the electron and the positron and, to a lesser extent, that of the Proca equation for the meson[1,2] in providing a basis for the theory of elementary particles has led to an interest in more general equations of the same type which possess form-invariance under the Lorentz group, L_4, of the special theory of relativity.[3-5] A similar concern has arisen from the related study of possible quantum-mechanical equations in cosmological spaces.[6-8] Apart from the importance of these studies in the formulation of a theory of spin forces, it seems that considerable mathematical exploratory work of this nature will need to be carried out if effective progress is to be made in reconciling the divergent aims of quantum mechanics and of the general theory of relativity in the pursuit of a unified theory of matter.

The work to be detailed here had its origin in the writer's interpretation of the conformal group of transformations in space-time,[9] and in the desire to extend the consequences of that discussion into the domain of quantum mechanics. We shall be concerned with the generalization of equations of the Dirac-Proca type under finite continuous transformation groups in space-time, and shall show that such a generalization exists for an arbitrary group G. The form of the equation which is proposed is not specified uniquely by the group, but the invariance under G imposes on the β-operators a set of relations with which any assumed algebra must be consistent. It is found, for example, that the algebra for the general equation having form-invariance under the inhomogeneous Lorentz group is necessarily of infinite order. This must then also be the case for the conformal group as well as for the more extended groups which contain L_4 as a subgroup. The infinite algebras appropriate to these equations are as yet undeveloped, so that for the present we are forced to leave our discussion incomplete on the side of actual physical applications.

Earlier treatments of possible quantum-mechanical equations having form-invariance under the conformal group have been given by Dirac[10] and by Bhabha.[11] In this work the number of independent variables was extended in such a manner that the transformations of the conformal group become linear and homogeneous, a procedure which is equivalent to the use of the so-called hexaspherical coordinates. We do not follow this method in the present work, but base our procedures on the use of the basis operators of a finite continuous group as a linear vector space under the transformations of the group. In this way we are enabled to achieve a precise and manageable mathematical technique, and at the

[1] H. C. Corben and J. Schwinger, Phys. Rev. **58**, 953 (1940).
[2] J. H. Bartlett, Phys. Rev. **72**, 219 (1947).
[3] W. Pauli, Rev. Mod. Phys. **13**, 203 (1941).
[4] H. J. Bhabha, Rev. Mod. Phys. **17**, 200 (1945).
[5] Harish-Chandra, Phys. Rev. **71**, 793 (1947).
[6] A. H. Taub, Phys. Rev. **51**, 512 (1937).
[7] E. Schrödinger, Proc. Roy. Irish Acad. **A46**, 25 (1940).
[8] L. Infeld and A. Schild, Phys. Rev. **70**, 410 (1946).
[9] E. L. Hill, Phys. Rev. **67**, 358 (1945); **72**, 143 (1947).
[10] P. A. M. Dirac, Ann. Math. [2] **37**, 429 (1936).
[11] H. J. Bhabha, Proc. Camb. Phil. Soc. **32**, 622 (1936).

same time to leave the way open for a possible later treatment of more general types of canonical transformation groups which are of such great importance even in the elementary theory of classical and quantum mechanics, but which at present find no place in the general theory of relativity.

Another feature of the present approach which is of some interest is the manner in which it provides for the introduction of the "kinematical forces" associated with the transformations of reference systems between equivalent observers.

2. THEORY

We consider a finite continuous group, G, of point transformations on the space-time variables ($x^1=x$, $x^2=y$, $x^3=z$, $x^4=i\tau=ict$), having n essential parameters $a^1, \cdots, a^n$. The general transformation of the group will be designated as S_a; the parameters will be supposed to take the values $(a_0{}^a)$ for the identity transformation, S_0, and the values $(\bar{a}^a)$ for the inverse transformation, $S_a{}^{-1}$. We shall consider the group to be defined in terms of a set of basis operators[12]

$$X_a \equiv \xi_a{}^k(x)p_k, \tag{1}$$

where Greek indices take values from 1 to n, and Latin indices from 1 to 4, and where we employ the usual dummy index summation notation for both types of indices. The fundamental differential operators are taken in the quantum-mechanical form

$$p_k = -ih\partial/\partial x^k, \tag{2}$$

and the functions $\xi_a{}^k(x)$ will be considered to be *real* functions of the variables (x^k).

The general infinitesimal transformation of the group is then given by the formula

$$\delta x^k = \delta a^\beta [X_\beta, x^k] = -ih\xi_a{}^k(x)\delta a^\alpha, \tag{3}$$

where $[A,B]=AB-BA$ is the usual commutator symbol. Corresponding to Eq. (3), we define an infinitesimal transformation of the basis operators by the formula

$$\delta X_a = \delta a^\beta [X_\beta, X_a]. \tag{4}$$

It follows from the fact that we are dealing with a *group* of transformations that

$$[X_\beta, X_a] = -ihc_{\beta a}{}^\gamma X_\gamma, \tag{5}$$

where the quantities $c_{\beta a}{}^\gamma = -c_{a\beta}{}^\gamma$ are the *structure constants* of the group. Our definition of Eq. (4) thus reduces to the form

$$\delta X_a = ihc_{a\beta}{}^\gamma X_\gamma \delta a^\beta. \tag{4'}$$

It is readily verified that this definition is equivalent to that to be found directly from Eq. (3). For, if we write the infinitesimal transformation corresponding to Eq. (3) as

$$x'^k = x^k - ih\xi_a{}^k(x)\delta a^\alpha, \tag{6}$$

we obtain for the differential operators

$$\begin{aligned} p_k' &\equiv -ih\partial/\partial x'^k \\ &= -ih[\partial/\partial x^k + ih\delta a^\alpha(\partial \xi_a{}^m/\partial x^k)\partial/\partial x^m] \\ &= p_k + ih(\partial \xi_a{}^m/\partial x^k)p_m \delta a^\alpha, \end{aligned}$$

to first orders, and so have, correspondingly,

$$\delta p_k \equiv p_k' - p_k = ih(\partial \xi_a{}^m/\partial x^k)p_m \delta a^\alpha.$$

Similarly, we have

$$\delta \xi_a{}^k \equiv \xi_a{}^k(x') - \xi_a{}^k(x) = -ih(\partial \xi_a{}^k/\partial x^m)\xi_\beta{}^m \delta a^\beta.$$

By combining these expressions we find

$$\begin{aligned} \delta X_a \equiv \delta(\xi_a{}^k p_k) &= \delta \xi_a{}^k \cdot p_k + \xi_a{}^k \cdot \delta p_k \\ &= +ih[\xi_a{}^m(\partial \xi_\beta{}^k/\partial x^m) \\ &\quad - \xi_\beta{}^m(\partial \xi_a{}^k/\partial x^m)]p_k \delta a^\beta. \end{aligned} \tag{7}$$

But it follows from the group properties of G that

$$\xi_a{}^m(\partial \xi_\beta{}^k/\partial x^m) - \xi_\beta{}^m(\partial \xi_a{}^k/\partial x^m) = c_{a\beta}{}^\gamma \xi_\gamma{}^k,$$

and on substitution of this condition into Eq. (7) we again obtain the result of Eq. (4').

We now consider the formal operator

$$\mathfrak{M} \equiv \beta^\alpha \xi_a{}^k(x)[p_k - \epsilon A_k/c] + im_0 c, \tag{8}$$

in which ϵ, c, and m_0 are the usual absolute constants. We require of the four functions $A_k(x)$ only that they transform as the covariant components of a 4-vector. The properties of the β-operators are to be determined in such a manner that the operator $\mathfrak{M}$ is formally invariant under the group G.

[12] L. P. Eisenhart, *Continuous Groups of Transformations*, (Princeton University Press, Princeton, 1933).

We have for the transformation of the 4-vector A_k,

$$\delta A_k \equiv A_k'(x') - A_k(x) = ih(\partial \xi_\alpha{}^m/\partial x^k) A_m \delta a^\alpha.$$

If we let

$$\Pi_k \equiv p_k - \epsilon A_k/c,$$

we obtain

$$\delta \Pi_k = ih(\partial \xi_\beta{}^m/\partial x^k)\Pi_m \delta a^\beta,$$

so that, finally,

$$\delta(\xi_\alpha{}^k \Pi_k) = ihc_{\alpha\theta}{}^\gamma(\xi_\gamma{}^m \Pi_m)\delta a^\theta.$$

For the variational equation of $\mathfrak{M}$ we now find

$$0 = \delta \mathfrak{M} = \delta\beta^\alpha \cdot (\xi_\alpha{}^k \Pi_k) + \beta^\alpha \cdot \delta(\xi_\alpha{}^k \Pi_k)$$
$$= [\delta\beta^\gamma + ihc_{\alpha\theta}{}^\gamma \beta^\alpha \delta a^\theta]\xi_\gamma{}^k \Pi_k. \quad (9)$$

By virtue of the independence of the quantities $\xi_\gamma{}^k \Pi_k$ we require that

$$\delta\beta^\gamma = -ihc_{\alpha\theta}{}^\gamma \beta^\alpha \delta a^\theta = ihc_{\theta\alpha}{}^\gamma \beta^\alpha \delta a^\theta. \quad (10)$$

Equations (10) constitute the necessary and sufficient conditions which we must impose on the β-operators in order to secure formal invariance of the operator $\mathfrak{M}$ under the group G. In view of the fact that we have considered only the infinitesimal transformations of G in the neighborhood of the identity transformation, we interpret Eqs. (8) as differential equations to be integrated along some definite path in the space of the parameters $a^1, \cdots, a^n$. If we let

$$a^\alpha = \rho^\alpha a,$$

where $\rho^1, \cdots, \rho^n$ are specified, but arbitrarily chosen, constants, and a is the running group parameter, we have the differential equations.

$$d\beta^\gamma/da = ihc_{\theta\alpha}{}^\gamma \rho^\theta \beta^\alpha. \quad (11)$$

Since Eqs. (11) are linear and homogeneous in the β's, with constant coefficients, they can be integrated without specification of the algebraic properties of the β's.

An alternative discussion of this mathematical theory, which yields the integrated form of Eqs. (11), is given in Appendix A.

Our extension of the Dirac equation is now given by

$$\mathfrak{M}\Psi \equiv \{\beta^\alpha \xi_\alpha{}^k(x)\Pi_k + im_0 c\}\Psi = 0. \quad (12)$$

In order that Eq. (12) shall constitute a true system of differential equations for the components of the wave function, we must subject the β's to a set of algebraic relations compatible with Eqs. (11), and must then find a suitable representation of this algebra. Furthermore, to give assurance that the equations so obtained will be completely form-invariant under G, the assumed algebra must lead to the condition that Eq. (11) is equivalent to a similarity transformation, that is, a non-singular operator (matrix) V_a, dependent on the transformation S_a, must exist such that

$$\beta^\alpha(a) = V_a \beta^\alpha(a_0) V_a{}^{-1}. \quad (13)$$

If we let

$$V_a = 1 + v_a \delta a^\alpha, \quad V_a{}^{-1} = 1 - v_a \delta a^\alpha, \quad (14)$$

for infinitesimal transformations, then we have from Eqs. (10) and (13) the conditions

$$[v_\alpha, \beta^\gamma] = ihc_{\alpha\theta}{}^\gamma \beta^\theta, \quad (15)$$

as the determining relations for the n operators v_α.

The reality conditions to be imposed for a general group of transformations are somewhat obscure. However, it is expected on the basis of present theory that the representation of the algebra of the β-operators will be by Hermitian matrices, and the nomenclature of this paper has been chosen to conform to this premise. This property is lost, of course, under the transformations of Eqs. (11) and (13), but is restored on making a transformation on the representation space of the wave function, according to the relation

$$\Psi = V_a \Psi',$$

exactly as is the case for the Dirac equation for which the transformation matrix for the specifically Lorentz transformations, as distinguished from the three-dimensional rotations, is Hermitian rather than unitary.

We note that Eq. (12) is also form-invariant under a gauge transformation of the 4-vector, for if the latter is subjected to the transformation

$$A_k = A_k' + \partial\omega/\partial x^k,$$

Eq. (12) preserves its form if we make the replacement

$$\Psi = \exp(i\epsilon\omega/hc)\Psi'.$$

On the other hand, if we interpret the functions A_k as the components of the electromagnetic 4-vector, and require also the form-invariance of the Maxwell field equations, then the largest group under which both Eq. (12) *and* the Maxwell field equations have form-invariance is the conformal group, C_4.

It is of importance to observe that if the group G is not simple, but contains an invariant subgroup of order $m<n$, then, with a proper ordering of the basis operators, one can set $\beta_{m+1}=\cdots=\beta_n=0$, and so can obtain an equation in place of (12) containing only m operators, but one which still is form-invariant under the full group. The consistency of this procedure with Eqs. (10) follows from the properties of the table of structure constants.[13] This circumstance is of paramount importance in the case of the Lorentz group, within which the translations form an invariant subgroup, and is responsible for the fact that the Dirac and Proca equations can have form-invariance under the full inhomogeneous Lorentz group. Under more general transformation groups this simplifying property may be lost.[14]

3. THE LORENTZ GROUP

The basis operators for the inhomogeneous Lorentz group may be taken conveniently in the form

$$X_1\equiv p_1,\quad X_2\equiv p_2,\quad X_3\equiv p_3,\quad X_4\equiv p_4, \tag{16a}$$

$$X_5\equiv yp_3-zp_2,\quad X_6\equiv zp_1-xp_3,$$

$$X_7\equiv xp_2-yp_1, \tag{16b}$$

$$X_8\equiv -i\tau p_1+xp_4,\quad X_9\equiv -i\tau p_2+yp_4,$$

$$X_{10}\equiv -i\tau p_3+zp_4. \tag{16c}$$

In writing out the expansion of Eq. (12) we shall drop the summation notation, lower the indices on the β-operators, and introduce the new symbols

$$\gamma_1=\tfrac{1}{2}(\beta_5+\beta_8),\quad \gamma_2=\tfrac{1}{2}(\beta_6+\beta_9),$$

$$\gamma_3=\tfrac{1}{2}(\beta_7+\beta_{10}), \tag{17a}$$

$$\omega_1=\tfrac{1}{2}(\beta_5-\beta_8),\quad \omega_2=\tfrac{1}{2}(\beta_6-\beta_9),$$

$$\omega_3=\tfrac{1}{2}(\beta_7-\beta_{10}). \tag{17b}$$

[13] Reference 12, Section 35.

[14] The translations do not form an invariant subgroup of the conformal group, C_4.

The latter quantities can be written formally as two vector operators $\boldsymbol{\gamma}$ and $\boldsymbol{\omega}$. We then obtain from Eq. (12) the result

$$\left\{\sum_{k=1}^{4}\beta_k\Pi_k+im_0c+\boldsymbol{\gamma}\cdot\left[\mathbf{M}-\frac{\epsilon}{c}(\mathbf{r}\times\mathbf{A})\right.\right.$$

$$\left.-\mathbf{r}\left(\frac{\hbar\partial}{\partial\tau}+\frac{i\epsilon}{c}\phi\right)-i\tau\boldsymbol{\Pi}\right]+\boldsymbol{\omega}\cdot\left[\mathbf{M}-\frac{\epsilon}{c}(\mathbf{r}\times\mathbf{A})\right.$$

$$\left.\left.+\mathbf{r}\left(\frac{\hbar\partial}{\partial\tau}+\frac{i\epsilon}{c}\phi\right)+i\tau\boldsymbol{\Pi}\right]\right\}\Psi=0, \tag{18}$$

in which we have introduced the usual notation

$$\mathbf{M}=\mathbf{r}\times\mathbf{p},\quad \boldsymbol{\Pi}=\mathbf{p}-\epsilon\mathbf{A}/c,\quad A_4=i\phi.$$

It will be convenient at this point to change the definition of the parameters of the group from that implied in Eq. (6) in such a manner that all of the parameters shall be real. The required transformation is given by the table

$$\mu_1=iha_1,\quad \mu_2=iha_2,\quad \mu_3=iha_3,\quad \mu_4=ha_4,$$

$$\mu_5=iha_5,\quad \mu_6=iha_6,\quad \mu_7=iha_7,\quad \mu_8=ha_8,$$

$$\mu_9=ha_9,\quad \mu_{10}=ha_{10}.$$

If we now let $\rho_1,\cdots,\rho_{10}$ be a set of arbitrary real constants, the differential equations (11) take the form

$$d\beta_1/d\mu=-(\gamma_3+\omega_3)\rho_2+(\gamma_2+\omega_2)\rho_3$$

$$-i(\gamma_1-\omega_1)\rho_4-\beta_3\rho_6+\beta_2\rho_7+i\beta_4\rho_8, \tag{19a}$$

$$d\beta_2/d\mu=(\gamma_3+\omega_3)\rho_1-(\gamma_1+\omega_1)\rho_3$$

$$-i(\gamma_2-\omega_2)\rho_4+\beta_3\rho_5-\beta_1\rho_7+i\beta_4\rho_9, \tag{19b}$$

$$d\beta_3/d\mu=-(\gamma_2+\omega_2)\rho_1+(\gamma_1+\omega_1)\rho_2$$

$$-i(\gamma_3-\omega_3)\rho_4-\beta_2\rho_5+\beta_1\rho_6+i\beta_4\rho_{10}, \tag{19c}$$

$$d\beta_4/d\mu=(\gamma_1-\omega_1)\rho_1+(\gamma_2-\omega_2)\rho_2$$

$$+(\gamma_3-\omega_3)\rho_3-i\beta_1\rho_5-i\beta_2\rho_9-i\beta_3\rho_{10}, \tag{19d}$$

$$d\gamma_1/d\mu=-\gamma_3\rho_6+\gamma_2\rho_7-i\gamma_3\rho_9+i\gamma_2\rho_{10}, \tag{20a}$$

$$d\gamma_2/d\mu=\gamma_3\rho_5-\gamma_1\rho_7+i\gamma_3\rho_8-i\gamma_1\rho_{10}, \tag{20b}$$

$$d\gamma_3/d\mu=-\gamma_2\rho_5+\gamma_1\rho_6-i\gamma_2\rho_8+i\gamma_1\rho_9, \tag{20c}$$

$$d\omega_1/d\mu=-\omega_3\rho_6+\omega_2\rho_7+i\omega_3\rho_9-i\omega_2\rho_{10}, \tag{21a}$$

$$d\omega_2/d\mu=\omega_3\rho_5-\omega_1\rho_7-i\omega_3\rho_8+i\omega_1\rho_{10}, \tag{21b}$$

$$d\omega_3/d\mu=-\omega_2\rho_5+\omega_1\rho_6+i\omega_2\rho_8-i\omega_1\rho_9. \tag{21c}$$

It can be verified directly from Eqs. (20a-21c) that the γ's and ω's can be subjected separately to the Pauli algebra

$$\gamma_1^2=\gamma_2^2=\gamma_3^2=1, \quad \gamma_1\gamma_2=-\gamma_2\gamma_1=i\gamma_3, \text{ etc.,} \quad (22a)$$

$$\omega_1^2=\omega_2^2=\omega_3^2=1, \quad \omega_1\omega_2=-\omega_2\omega_1=i\omega_3, \text{ etc.} \quad (22b)$$

A study of Eqs. (19a–d) shows, however, that unless we set

$$\gamma_1=\gamma_2=\gamma_3=\omega_1=\omega_2=\omega_3=0, \quad (23)$$

we cannot find a *finite* algebra which is compatible with all of these conditions under the full group L_4. This simplification is just that ordinarily made, and depends on the fact that the translations form an invariant subgroup of L_4, as pointed out in Section 2.

In order to show that the operator algebra defined by Eqs. (19a–21c) must be of infinite order, unless Eqs. (23) are separately imposed, we consider the effects of translations alone, and so set

$$\rho_5=\rho_6=\rho_7=\rho_8=\rho_9=\rho_{10}=0.$$

Under translations the γ's and ω's are invariant, while the equations for the β-operators are immediately integrable in the form

$$\beta_1(\mu)=\beta_1(\mu_0)+\{-(\gamma_3+\omega_3)\rho_2+(\gamma_2+\omega_2)\rho_3 -i(\gamma_1-\omega_1)\rho_4\}(\mu-\mu_0), \quad (24)$$

with similar relations for the remaining β's. Now, since the transformation (24) must be a similarity transformation, the eigenvalue spectrum of the matrix representations of the β's is preserved. But since the ρ's have indeterminate numerical values, while the group parameter μ can take all real values, both positive and negative, the eigenvalues of the matrix representations of $\beta_1, \cdots, \beta_4$ must vary continuously, and furthermore must be unbounded numerically, both above and below. It is clear that these conditions cannot be satisfied by representations with finite matrices. The writer has not yet found it possible to establish an algebra which is consistent with Eqs. (19a–21c) when Eqs. (23) are not satisfied.

When Eqs. (23) are imposed, the reduced forms of Eqs. (19a–d) furnish a relatively easy starting point for the generalization of the Dirac and the Duffin-Kemmer algebras. However, since this question has been examined in detail by Bhabha[4] and by Harish-Chandra[5] it will not be considered further here.

The writer is indebted to Professors C. Critchfield and J. Weinberg for helpful discussions of this and related topics.

APPENDIX A

In the interest of clarity it is of value to restate the invariance property of Eq. (12) by an interpretation of Eq. (6) as a change of reference coordinates in space-time. Under a general change of reference system, the basis operators X_α are interpreted as formal invariants,[12] so that the functions $\xi_\alpha{}^k(x)$ transform as the contravariant components of a set of 4-vectors, the index α specifying the vector, while the index k specifies the components. Designating the new coordinates by the transformation formula

$$y^k=Tx^k=f^k(x),$$

the transformations of the group, expressed in terms of the new coordinates will be given by the expressions

$$TS_\alpha T^{-1}.$$

The basis operators, expressed in terms of the new coordinates, take the form

$$Y_\alpha \equiv \eta_\alpha{}^k(y)(-ih\partial/\partial y^k), \quad \text{with} \quad \eta_\alpha{}^k(y)=\xi_\alpha{}^m(x)(\partial y^k/\partial x^m). \quad (25)$$

If this change of coordinate system is effected by means of a transformation $T=S_b$ of the group G itself, Eq. (25) takes the simpler form

$$\eta_\alpha{}^k(y)=\xi_\gamma{}^k(y)D_\alpha{}^\gamma(b),$$

where the n^2 functions $D_\alpha{}^\gamma(b)$ depend on the parameters defining the transformation S_b, but not on the space-time coordinates.

The transformation of the basis operators under the group is therefore such that

$$Y_\alpha=D_\alpha{}^\gamma(b)X_\gamma',$$

where X_γ' has exactly the same functional form as does X_γ, but is expressed in terms of the y-variables. If we now perform the transformation S_b on the space-time coordinates, we have

$$\beta^\alpha X_\alpha \rightarrow \beta^\alpha Y_\alpha=\beta^\alpha D_\alpha{}^\theta(b)X_\theta'.$$

In order to return this to the original form, but expressed in terms of the new variables, we have only to define the transformation on the β-operators

$$\beta'^{\theta}=D_{\alpha}{}^{\theta}(b)\beta^{\alpha}. \tag{26}$$

As was discussed in Section 2, this transformation must be equivalent to a similarity transformation in order that the algebraic properties of the operators may be preserved, and the form-invariance of the equations for the components of the wave function assured.

Equations (26) give the integrated form of Eqs. (11), from which the latter can be obtained by consideration of the infinitesimal transformations in the neighborhood of the identity of the group.

Although Eqs. (11) are more useful for practical computations than are Eqs. (26), it is of interest to know the formulation of the coefficients $D_{\alpha}{}^{\beta}(b)$ in terms of the properties of the group. If S_a, S_b, and S_c are three transformations of the group such that

$$S_c=S_bS_a,$$

the corresponding functional relations among the parameters are expressed by the *group functions*

$$c^{\alpha}=\varphi^{\alpha}(a,b).$$

Considering these as functions of the $2n$ independent variables, we define the derived functions

$$\lambda_{\beta}{}^{\alpha}(a,b)=\partial\varphi^{\alpha}/\partial a^{\beta}, \quad \Lambda_{\beta}{}^{\alpha}(a,b)=\partial\varphi^{\alpha}/\partial b^{\beta}.$$

From these, making use of the general notation of Section 2, we define the sets of functions

$$A_{\beta}{}^{\alpha}(a)=\lambda_{\beta}{}^{\alpha}(a_0,a), \quad B_{\beta}{}^{\alpha}(a)=\Lambda(a,a_0),$$
$$\bar{A}_{\beta}{}^{\alpha}(a)=\lambda_{\beta}{}^{\alpha}(a,\bar{a}), \quad \bar{B}_{\beta}{}^{\alpha}(a)=\Lambda(\bar{a},a).$$

It can be shown from these relations that

$$D_{\beta}{}^{\alpha}(a)=\bar{B}_{\gamma}{}^{\alpha}(a)A_{\beta}{}^{\gamma}(a),$$

and

$$\bar{D}_{\beta}{}^{\alpha}(a)=\bar{A}_{\gamma}{}^{\alpha}(a)B_{\beta}{}^{\gamma}(a),$$

where

$$D_{\alpha}{}^{\gamma}(a)\bar{D}_{\gamma}{}^{\beta}(a)=D_{\gamma}{}^{\beta}(a)\bar{D}_{\alpha}{}^{\gamma}(a)=\delta_{\alpha}{}^{\beta}.$$

For transformations in the neighborhood of the identity we have the series expansions

$$D_{\beta}{}^{\alpha}=\delta_{\beta}{}^{\alpha}-ihc_{\beta\gamma}{}^{\alpha}\cdot(a^{\gamma}-a_0{}^{\gamma})+\cdots,$$
$$\bar{D}_{\beta}{}^{\alpha}=\delta_{\beta}{}^{\alpha}+ihc_{\beta\gamma}{}^{\alpha}\cdot(a^{\gamma}-a_0{}^{\gamma})+\cdots.$$

The relation with the method of Section 2 now follows on making the definition

$$\delta X_{\alpha}\equiv X_{\alpha}'-X_{\alpha},$$

for an infinitesimal transformation.

The Identification of the Surplus Gamma-Radiation from Granite

VICTOR FRANCIS HESS AND J. DONALD ROLL
Fordham University, New York, New York

(Received March 8, 1948)

IN a previous paper[1] we expressed the opinion that a new and direct determination of Eve's constant for the gamma-rays from potassium would be necessary in order to find out whether the surplus gamma-radiation from Quincy granite, found experimentally by one of us, could be ascribed to the effect of the gamma-rays from potassium in the granite.

The existing data on the intensity and the penetrating power of gamma-rays from potassium are meager and rather conflicting. The intensity of the gamma-rays from potassium expressed in terms of the equivalent amount of radium (RaC), according to various authors, is given in Table I, together with the calculated mass absorption coefficients.

TABLE I.

Author	1-g potassium equivalent to:	Mass absorption coefficient of gamma-rays from potassium
W. Kolhörster*	5.10×10^{-11} g Ra	0.0250 cm²/g
W. Mühlhoff**	3.34×10^{-11} g Ra	0.0520 cm²/g
F. Bêhounek***	1.30×10^{-10} g Ra	0.0513 cm²/g
L. H. Gray and G. T. P. Tarrant†	1.60×10^{-11} g Ra	0.0477 cm²/g
E. Gleditsch and T. Gráf††	1.23×10^{-10} g Ra	0.0513 cm²/g

* W. Kolhörster, Zeits. f. Geophys. **6**, 340 (1930).
** W. Mühlhoff, Ann. d. Physik **7**, 205 (1930).
*** F. Bêhounek, Zeits. f. Physik **69**, 654 (1931).
† L. H. Gray and G. T. P. Tarrant, Proc. Roy. Soc. **A143**, 681 (1934).
†† See reference 4.

Since the latest determination (Gleditsch and Gráf) indicated the correctness of Bêhounek's value, which was heretofore considered as the least reliable, we decided to test the intensity of the gamma-rays from two potassium salts (KCl and K_2SO_4) with the same apparatus that was used in the studies of the surplus gamma-radiation from granite.[2,3]

After the densities of both KCl and K_2SO_4 in powdered form were determined, bags filled with these salts were arranged so as to fill completely one or two quadrants of the space located concentrically between the outer lead cylinder (1 cm thick) surrounding the ionization chamber and the inner wall of our "iron house." This iron house, having a wall thickness of four inches, served only the purpose of excluding the local gamma-rays coming from the walls of the room. A quantity of 50 lb. of KCl and about 75 lb. of K_2SO_4 was sufficient to fill one quadrant of this space.

We also made a series of experiments where two of the quadrants were filled with potassium chloride while the other two were filled with dunite, a material which is practically free of uranium, thorium, and potassium and therefore inactive, as direct gamma-ray tests had shown previously.[1] This experiment showed that the scattering of gamma-rays from the potassium-filled quadrants in the inactive dunite enhanced the effect very little: by only $0.2I$ (ion pairs/cm³/sec.), as compared with the total ionization of $6.7I$ given by the two potassium-filled quadrants.

For KCl two determinations, consisting of about 50 individual observations, gave, after subtracting the background ($2.7I$), values of $3.68I$ and $3.72I$, respectively. An experiment with two quadrants gave $7.0I$, which is a little lower than $2\times3.7I$ because the material at hand was not quite sufficient to fill the second quadrant completely. We, therefore, took the value for one quadrant (q_1) filled with KCl (and also later with K_2SO_4) and obtained the gamma-ray effect of the concentric layer 15.78 cm thick around the ionization chamber by multiplying the value by four ($4q_1$). A slight correction is necessary since the "open cone" (angle subtended by the electrometer head of the chamber) is not filled with the salt. This correction amounts to $C=0.89$. Extrapolation for an infinite layer of salt is obtained by dividing the corrected value $4q_1/C$ by $(1-e^{-\mu d})$, where μ is the linear absorp-

[1] V. F. Hess and J. D. Roll, Phys. Rev. **73**, 592 (1948).
[2] V. F. Hess, Phys. Rev. **72**, 609 (1947).
[3] V. F. Hess, Trans. Am. Geophys. Union **27**, 670 (1946); V. F. Hess, Norsk Geologisk Tidsskrift **27** (Jan. 1947).

TABLE II.

		KCl	K_2SO_4
Ionization with one quadrant filled with salt,	q_1	$3.70I$	$3.87I$
density of the salt,	ρ	1.125 g/cm³	1.576 g/cm³
thickness of salt layer,	d	15.78 cm	15.78 cm
linear absorption coefficient,	μ	0.0578 cm^{-1}	0.0809 cm^{-1}
exponential factor,	$e^{-\mu d}$	0.402	0.279
potassium content per gram,	M	0.523 g/g KCl	0.448 g/g K_2SO_4

for KCl: $K=\dfrac{3.70\times0.0513}{\pi 0.89(1-0.402)0.523}=0.217I$

for K_2SO_4: $K=\dfrac{3.87\times0.0513}{\pi 0.89(1-0.279)0.448}=0.220I.$

tion coefficient of gamma-rays from potassium in the salt, and d is the thickness of the layer.

Thus the ionization due to an infinite concentric layer is given by

$$q_\infty=[4q_1/C(1-e^{-\mu d})].$$

On the other hand, Eve's formula for a concentric layer of infinite thickness gives

$$q_\infty=4\pi K/(\mu/\rho)\cdot M,$$

where K is Eve's constant for potassium, M the amount of potassium per gram of the salt used, and μ/ρ the mass absorption coefficient. Equating the two expressions for q_∞, we get Eve's constant

$$K=[q_1(\mu/\rho)]/[\pi C(1-e^{-\mu d})M].$$

We took for μ/ρ the most recent value of Gleditsch and Gráf[4] 0.0513 cm²/g for gamma-rays from potassium, while our own direct determination with concentric lead shields of 1 cm and 2 cm around the chamber gave 0.0523 cm²/g, which is identical within the limits of experimental error.

The results of the two independent determinations of Eve's constant for the gamma-rays of potassium, for a brass chamber shielded by 1 cm of lead from all sides, are shown in Table II.

A slight correction is necessary due to the fact that the radiating source is neither point shaped nor at a considerable distance, but distributed throughout a relatively large volume quite close to the ionization chamber. As a result, most of the gamma-rays follow oblique paths as they pass through the lead shield around the chamber. The amount by which the ionization within the chamber is reduced by this effect was evaluated by a graphical method and the correction was made as follows:

For KCl: $K=0.217\times1.184=0.257I$,
for K_2SO_4: $K=0.220\times1.184=0.260I$.

The corrected values of Eve's constant agree quite satisfactorily. Since in our apparatus Eve's constant for gamma-rays from radium (RaC) was found to be $2.90\times10^9 I$/g Ra/cm, we find that the intensity of the gamma-rays from 1 g of potassium is equivalent to $0.2585/2.90\times10^9=0.89\times10^{-10}$ g Ra. This value is somewhat lower than the most recent value of Gleditsch and Gráf, but it shows clearly that this latter value is essentially correct.

We are now in a position to compute the total ionization produced by gamma-rays from Quincy granite with these revised data at hand and compare it with our experimental findings. For the radium and thorium component we can use our previously published values,[2] taking Eve's constant for radium $K_1=2.90\times10^9$, for thorium $K_2=440$, and for potassium our own new value $K_3=0.2585$.

(a) Radium component:

$M_1=1.02\times10^{-12}$ g Ra/g granite;
$\mu_1/\rho=0.045$ cm²/g,

$$q_a=\frac{12.56\times2.90\times10^9\times1.02\times10^{-12}}{0.045}=0.832I.$$

[4] E. Gleditsch and T. Gráf, Phys. Rev. **72**, 640 (1947).

(b) Thorium component:

$$M_2 = 8.1\times10^{-6} \text{ g Th/g granite};$$
$$\mu_2/\rho = 0.041 \text{ cm}^2/\text{g},$$
$$q_b = \frac{12.56\times440\times8.1\times10^{-6}}{0.041} = 1.094I.$$

(c) Potassium component:

$$M_3 = 0.038 \text{ g K/g granite};$$
$$\mu_3/\rho = 0.0513 \text{ cm}^2/\text{g},$$
$$q_c = \frac{12.56\times0.2585\times0.038}{0.0513} = 2.41I.$$

The total ionization to be expected from an infinite layer of Quincy granite is, therefore,

$$q_a + q_b + q_c = 4.34I$$

if the chamber is shielded by 1 cm of lead.

Our experiments with the same shielded chamber in an underground station and at Fordham, when the iron house was filled with Quincy granite, gave an ionization of $2.70I$. Correction for the "open cone" (explained above) brings this up to

$$2.70/0.89 = 3.03I,$$

and the extrapolation to an infinite layer of granite (assuming the absorption coefficient of gamma-rays in granite $= 0.057$ cm^{-1}, as previously determined[2]) is

$$q_\infty = \frac{3.03}{1-e^{-\mu d}} = \frac{3.03}{0.590} = 5.13I.$$

This is somewhat higher than the computed value. However, the agreement is now quite satisfactory if we consider the uncertainties involved in the determination of the three radioactive components. Furthermore, if instead of using our own experimental value of 1-g potassium equivalent to 0.89×10^{-10} g Ra we would take either one of the two values reported by Gleditsch and Gráf (1.06×10^{-10} or 1.23×10^{-10}), the agreement between the computed value of ionization for Quincy granite and our experimental value would be even better.

We therefore believe that the surplus radiation found by one of us is now satisfactorily explained and identified as coming from the potassium in the rock. It is regrettable that the intensity of the gamma-rays from potassium was underestimated to such an extent by some of the authors in the past. Our investigation confirms preliminary statements of E. Gleditsch and T. Gráf[4] with regard to the consequences involved in the estimates of the contribution of the gamma-rays from potassium in the rocks to the production of heat in the interior of the earth.

The contribution of the gamma-rays from potassium to the ionization of the atmosphere, as estimated by one of us[5] as early as 1934, seems now essentially correct, and it is important to note that this contribution, as seen from our data, exceeds the sum of the ionization by gamma-rays from the uranium-radium and the thorium series.

This work has been carried out with the financial aid of a grant from the American Philosophical Society.

[5] V. F. Hess, "Jonisierungsbilans der Atmosphaere", Ergebn. Kosm. Physik 2, 95 (1934).

Letters to the Editor

PUBLICATION of brief reports of important discoveries in physics may be secured by addressing them to this department. The closing date for this department is five weeks prior to the date of issue. No proof will be sent to the authors. The Board of Editors does not hold itself responsible for the opinions expressed by the correspondents. Communications should not exceed 600 words in length.

Magnetic Moment of He^3 *

H. L. ANDERSON** AND A. NOVICK***
Argonne National Laboratory, Chicago, Illinois
February 27, 1948

THE nuclear magnetic resonance apparatus used previously in the measurement of the magnetic moment of tritium[1] was improved so that it could detect the nuclear magnetic moment of He^3. With this equipment we were able to find a resonance which we attribute to He^3 at a nuclear g value 0.763 ± 0.007 times that of the proton.

The He^3 was obtained from the radioactive decay of tritium.[2] For purposes of the present experiment it was first separated from tritium and then mixed with an equal volume of oxygen to reduce the relaxation time. This mixture of gases was compressed to a total pressure of 20 atmospheres into a small Pyrex bulb placed in the center of the 1-inch gap of an electromagnet whose pole pieces were 5 inches in diameter.

Transitions in the nuclear spin orientations were induced by the radiofrequency magnetic field produced in a small coil inside of which the sample was situated. At a frequency of 28.02 mc the nuclear magnetic resonance due to the hydrogen in the polystyrene insulation of the coil was found at 6590 gauss, while a new resonance at 8640 gauss was found which we attribute to He^3. No other resonances were detected between 8400 and 10,000 gauss at this frequency.

In order to observe this He^3 resonance it was necessary to improve the sensitivity of our apparatus 100-fold over what was needed in the case of tritium. A large signal to noise advantage was obtained by using a selective amplifier**** looked in to the 30-cycle modulation of the field of the electromagnet and having a band width of $\frac{1}{4}$ cycle.

The slow response time of such an amplifier required that the magnetic field be regulated to a precision of 1 part in 10^5. This was done with hard vacuum tubes, since the magnet was provided with a high voltage winding and required less than 1 ampere for its excitation. The search for the resonance was made by varying the magnetic field at the rate of 3 gauss per minute with a motor-driven potentiometer in the regulator circuit.

The present preliminary result provides strong evidence for the existence of charge exchange currents in nuclei. These currents serve to augment the magnitude of the magnetic moment of He^3 over that of the neutron by roughly the same amount as they augment the magnetic moment of H^3 over that of the proton. This follows the prediction of Villars.[3]

The relatively large error in the present experiment is due to the fact that a comparison of magnetic fields was made at fixed frequency. A precise measurement is in progress in which frequencies will be compared at fixed magnetic field.

* This document is based on work performed under Contract No. W-31-109 eng-38 for the Atomic Energy Commission at the Argonne National Laboratory. Submitted for declassification January 5, 1948.
** Member of the Institute for Nuclear Studies.
*** Member of the Institute of Radiobiology and Biophysics.
[1] H. L. Anderson and A. Novick, Phys. Rev. 71, 372 (1947).
[2] Aaron Novick, Phys. Rev. 72, 972 (1947).
**** Kindly provided us by Dr. Arthur Roberts and Mr. Tom Brill of this laboratory. Much of the electronic equipment was built by Mr. E. Yasitis.
[3] Felix Villars, Phys. Rev. 72, 256 (1947).

The Magnetic Exchange Moment for He^3 and H^3

HERBERT L. ANDERSON
Institute for Nuclear Studies, The University of Chicago, Chicago, Illinois
February 27, 1948

THE recent measurements of the nuclear magnetic moments of H^3 [1] and He^3 [2] may be interpreted as evidence for the existence of a magnetic exchange moment in these nuclei.

Sachs and Schwinger[3] have shown that the sum of the moments of H^3 and He^3 can be directly related to the amount of admixture of the ^2P, ^4P, and ^4D eigenfunctions with the ^2S eigenfunction. They obtained the formula,

$$\mu(He^3)+\mu(H^3)=\mu_n+\mu_p - \tfrac{3}{4}(\mu_n+\mu_p-\tfrac{1}{2})(3^4D^2-{}^4P^2+2^2P^2), \quad (1)$$

where μ_n and μ_p are the magnetic moments of the neutron and proton in nuclear Bohr magnetons, respectively, and the amount of admixture is designated by the square of the term symbol for the state. This formula is based on the assumption that the wave functions of these two nuclei are identical. It should hold even if exchange currents contribute to the moment since these contributions should be equal and opposite for the two nuclei.

The observed values of the moments[1,2,4,5] when referred to an electronic spin g value[6] of $[2+(\alpha/\pi)]$, where α is the fine structure constant, are

$$\mu_p=+2.7928,$$
$$\mu_n=-1.9125,$$
$$\mu(H^3)=+2.9791,$$
$$\mu(He^3)=(-)2.131\pm0.020.$$

(The minus sign for $\mu(He^3)$ has not been verified experimentally.) Inserting these values in (1) we obtain,

$$3^4D^2-{}^4P^2+2^2P^2=0.127 \quad (2)$$

with an experimental uncertainty of ±0.080.

If, following Gerjuoy and Schwinger,[7] we take $^4P=^2P=0$, this result gives $^4D^2=0.042\pm0.026$, in good accord with their predictions based on the assumption that the same tensor interaction acts between the particles as is

required to account for the observed quadrupole moment of the deuteron.

The large moments which are observed for H^3 and He^3 could be accounted for *without* exchange provided the extreme assumption is made that the admixture for the ground state is $^2P^2=0.383$ and $^4P^2=0.617$, while $^2S^2=^4D^2=0$. These values were calculated using the formula for the moment of H^3 given by Sachs.[8] This would mean that the ground state of H^3 and He^3 is essentially a P state rather than an S state. This seems extremely improbable on almost any assumption as to form of the nuclear forces, as has already been pointed out by Mayer and Sachs.[9]

It appears much more reasonable to accept Villars[10] explanation that the excess magnetic moment is caused by exchange currents and to accept the Gerjuoy-Schwinger admixture. If this is done, one finds for the part of the magnetic moment due to the exchange currents approximately 0.27 nuclear magneton, positive for H^3 and negative for He^3.

[1] H. L. Anderson and A. Novick, Phys. Rev. 71, 372 (1947); F. Bloch, A. C. Graves, M. Packard, and R. W. Spence, Phys. Rev. 71, 373 (1947).
[2] H. L. Anderson and A. Novick, Phys. Rev. 73, 919 (1948).
[3] R. G. Sachs and J. Schwinger, Phys. Rev. 70, 41 (1946).
[4] S. Millman and P. Kusch, Phys. Rev. 60, 91 (1941).
[5] W. R. Arnold and A. Roberts, Phys. Rev. 71, 878 (1947).
[6] P. Kusch and H. M. Foley, Phys. Rev. 72, 1256 (1947) and 73, 412 (1948); J. Schwinger, Phys. Rev. 73, 416 (1948).
[7] E. Gerjuoy and J. Schwinger, Phys. Rev. 61, 138 (1942).
[8] R. G. Sachs, Phys. Rev. 72, 312 (1947).
[9] M. G. Mayer and R. G. Sachs, Phys. Rev. 73, 185 (1948).
[10] F. Villars, Phys. Rev. 72, 256 (1947).

The Conductivity of Metals at Microwave Frequencies

A. B. PIPPARD,
Royal Society Mond Laboratory, Cambridge, England,
G. E. H. REUTER,
The Mathematics Department, Manchester University, England,
AND E. H. SONDHEIMER,
Trinity College, Cambridge, England
February 9, 1948

A NOTE by B. Serin under the above title has recently appeared in The Physical Review.[1] The formulation given by him is, however, not in accordance with the physical nature of the problem and, under certain conditions, the solution which he obtains is mathematically unsound. The problem of metallic conductivity at microwave frequencies is much more complicated than is suggested by Serin's account; a more exact formulation has already been given by one of us,[2] and the full solution is in course of publication.[3,4]

Serin assumes at the outset that the electric field in the metal must take the form of a damped simple harmonic wave. This is clearly correct for an unbounded metal *provided that wave propagation is possible at all;* we shall show, however, that no wave propagation in the ordinary sense is, in fact, possible when the mean free path of the electrons exceeds a certain critical value.

Following Serin (and using his notation), we write the Boltzmann equation for the distribution function of the electrons:

$$\frac{\partial f}{\partial t}-\frac{e}{\hbar}E(z)e^{2\pi i\nu t}\frac{\partial f}{\partial k_z}+v_z\frac{\partial f}{\partial z}=-\frac{f-f_0}{\tau}. \tag{1}$$

In order to simplify the discussion, we shall assume that $\nu\tau\ll 1$, so that the term $\partial f/\partial t$ may be neglected. Equation (1) is to be solved *for an arbitrary field distribution* $E(z)$, taking into account the boundary conditions appropriate to the problem under consideration. For an unbounded metal, the correct solution is easily shown to be

$$f=f_0-\frac{e}{\hbar v_z}\frac{\partial f_0}{\partial k_z}\exp\left(-\frac{z}{\tau v_z}\right)\int_z^\infty E(z')\exp\left(\frac{z'}{\tau v_z}\right)dz', \quad (v_z<0), \tag{2}$$

$$f=f_0+\frac{e}{\hbar v_z}\frac{\partial f_0}{\partial k_z}\exp\left(-\frac{z}{\tau v_z}\right)\int_{-\infty}^z E(z')\exp\left(\frac{z'}{\tau v_z}\right)dz', \quad (v_z>0).$$

$E(z)$, of course, must be such that the integrals converge; the physical interpretation of this obvious mathematical requirement is discussed below. The expressions (2) may now be used to calculate the current density as a function of $E(z)$, and, on combining the resulting expression with Maxwell's equations, the following equation for $E(z)$ is obtained:

$$\frac{d^2E(z)}{dz^2}=\frac{3i}{2l\delta^2}\int_{-\infty}^\infty k\left(\frac{z-z'}{l}\right)E(z')dz', \tag{3}$$

where $l=\tau v$ = mean free path, δ = classical skin depth, and

$$k(u)=\int_1^\infty\left(\frac{1}{y}-\frac{1}{y^3}\right)e^{-y|u|}dy.$$

Equation (3) belongs to a well-known type of integral equation, and it may be shown[5] that the only solutions are of the form

$$E(z)=\sum_j A_j\exp\left(-\frac{s_jz}{l}\right), \tag{4}$$

where the s_j's are the solutions of the equation

$$s^2=\frac{3il^2}{2\delta^2}\int_{-\infty}^\infty k(u)e^{-su}du=i\alpha K(s) \quad \text{(say)} \tag{5}$$

in the region in which the integral converges.

Examination[4] of the function $K(s)$ reveals that it is regular in the strip $|\Re s|<|$, and that Eq. (5) has two roots $\pm s_1$ in this strip if $\alpha(=\frac{3}{2}l^2/\delta^2)$ is less than $\alpha_0(\simeq 2.63)$, i.e., if l is less than 1.32δ, but none otherwise. For $\alpha<\alpha_0$ then, an exponential solution exists, and on substituting

$$E(z)=E_0\exp\left(-\frac{s_1z}{l}\right)=E_0\exp\left(-\frac{2\pi i\nu Mz}{c}\right) \quad \text{(say)}$$

in Eq. (2), Serin's result is obtained.

The absence of solutions for $\alpha>\alpha_0$ may be interpreted physically as follows. The exponential wave given by Serin's solution under these conditions is attenuated by a factor e in a distance smaller than the mean free path of the electrons. In this case the current at any point may be contributed by electrons which, though few in number, have come without collision from a region of the wave where the electric field is very great; indeed, the further the electrons have traveled in the wave direction the greater will be their total contribution to the current,

although their number will be diminishing. This physical picture is confirmed by substituting Serin's solution in (2) when it is found that the integrals diverge for $\alpha > \alpha_0$. This point was not noticed by Serin, since, in assuming at the outset that the field was exponential, he, in effect, wrote down a finite particular solution of the Boltzmann equation and neglected infinite terms in the general solution (2).

It is therefore clear that if any solution is to be found for $\alpha > \alpha_0$, the surface of the metal must be specifically taken into account in the calculation. If this is done, solutions may be found for all values of α. There is thus a fundamental physical difference in the nature of the electric field for values of α less or greater than α_0. In the former case the field in the metal, at sufficient distances from the surface, is unaffected by the presence of the surface, which simply acts as a means for exciting a damped traveling wave. In the latter case, however, the form of the excitation is conditioned at all points by the presence of the surface and never approximates to an exponential form, being, in fact, a true surface excitation. For further details we refer to the work already quoted.[3-4]

[1] B. Serin, Phys. Rev. 72, 1261 (1947).
[2] A. B. Pippard, Proc. Roy. Soc. A191, 385 (1947).
[3] G. E. H. Reuter and E. H. Sondheimer, Nature, in press.
[4] G. E. H. Reuter and E. H. Sondheimer, to be published.
[5] E. C. Titchmarsh, *Introduction of the Theory of Fourier Integrals* (Oxford University Press, London, 1937), Section 11.2.

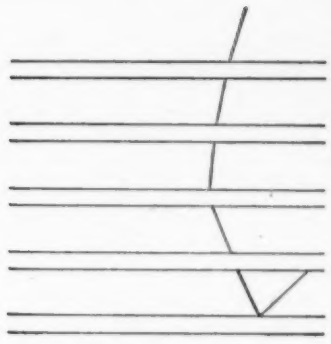

PICTURE NUMBER 7049

FIG. 1.

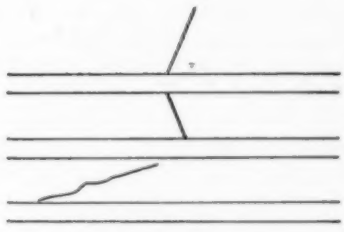

PICTURE NUMBER 7811

FIG. 2.

Mesotron Decay*

J. G. RETALLACK
Department of Physics, University of California, Berkeley, California
March 2, 1948

THE cloud-chamber pictures obtained in the experimental study of the mass of the mesotron[1] have been examined for evidence of charged decay particles. The radius of curvature of the track of the mesotron was measured in one cloud chamber placed in a magnetic field of 4750 gauss. The range in lead for the same mesotron was measured in a cloud chamber placed immediately below the first. It contained 15 horizontal lead plates 0.27 inch thick, both surfaces of which were covered with 0.001-inch aluminum foil. Sixteen positive mesotrons appear to have stopped in the lower chamber. In five of these cases a lightly ionized track is seen to leave the plate in which the mesotron stopped. Of the 27 negative mesotrons which appear to stop in the lower chamber, only one is accompanied by a possible decay track. In two cases, two particles are seen leaving the plate in which the mesotron stopped. It is possible that the decay electron initiated a cascade of which two particles are able to get out of the lead plate. Two of these events are illustrated by drawings made from measurements on the pictures. (See Figs. 1 and 2.) The width of the line represents roughly the density of ionization of the track. In each case the increase in the density of ionization of the mesotron track can be seen and the track of the decay particle is near minimum ionization. In the stereoscopic view the mesotron track and the track of the decay particle seem to be associated in space and time for all cases. In several pictures a delay in the reduction of the clearing field voltage has resulted in a separation of the track and the time association was checked by measurement. For the negative mesotron the decay particle comes out of the bottom of the lead plate in which the mesotron stops, and the space association of the tracks may be doubtful. The two tracks are of the same age. It seems very unlikely that the mesotron could have stopped and decayed in the thin aluminum foil. The scattering and density of the track do not suggest that the mesotron stopped in the top foil. If it stopped in the lower foil, one would expect the decay electron to have an energy of approximately 50 Mev. The scattering of the electron suggests that its energy is very much less than 5 Mev.

The data on these events are summarized in Table I.

Using curves given by Rossi and Greisen[2] one can make a rough estimate of the range of electrons in lead. Using this range with the assumption that the mesotron might have stopped anywhere in the lead plate and that the decay electrons are emitted with spherical symmetry, one can calculate the probability that a decay electron will get out of the lead plate and produce a track in the cloud chamber. For 50-Mev electrons the probability calculated in this way for the experimental arrangement used here is 0.52; for 25-Mev electrons the probability is 0.16. The experimental value found here for those cases which are identified as positive mesotrons is 0.31. Decay electrons which barely get out of the lead plate or which stay close to the plate, especially in a backward or forward direction,

TABLE I.

Picture number	Sign	Mass
7049	+	211±20
7811	+	207±27
7821	+	222±26
8818	+	240±28
9860	can be identified as positive but the picture in the upper cloud chamber is too faint to be measured.	
7362	−	240±31

would be difficult to find, and one might expect the experimental value to be lower than the calculated probability. Thus, the data are not inconsistent with the assumption of a decay electron of approximately 50 Mev from positive mesotrons.

The suggestion has been made by Valley and Rossi[3] and discussed by Piccioni[4] that perhaps negative mesotrons are not captured by nuclei but that their decay is accelerated. If this were true for lead, in the present experiment one would expect to see the tracks of decay electrons from 10 of the 27 negative mesotrons which stop in the lower cloud chamber. Only one picture gives evidence for the decay of a negative mesotron.

* This work was supported in part by the Office of Naval Research.
[1] To be published soon.
[2] Rossi and Greisen, Rev. Mod. Phys. 13, 240 (1941), see Fig. 9.
[3] Valley and Rossi, Phys. Rev. 73, 177 (1948).
[4] O. Piccioni, Phys. Rev. 73, 411 (1948).

A Note on the Paper "On the Possibility of Observing Beat Frequencies between Lines in the Visible Spectrum!"

L. R. GRIFFIN
University College, Swansea, Wales
January 5, 1948

IN a recent communication[1] the authors proposed an experiment to demonstrate the occurrence of beats with light radiations of slightly different frequencies.

Now, the variation of the intensity of the electric vector associated with either line at any point in space may be represented by a sine wave whose amplitude and phase vary continuously and discontinuously with time. The Fourier integral analysis of this variation gives the line spectrum and would be carried out automatically by a spectroscope. A Fourier integral analysis of a non-linear detector's response at this point will have no predominant frequency present as we may assume that the frequency equal to twice the incident frequency is so high that the detector is unable to respond. When there are two lines present there will be large fluctuations of amplitude and of phase of their combined electric vector. In this case the Fourier integral analysis of the detector's response gives a predominant frequency equal to the frequency difference Δ of the two lines, and this beat frequency could be detected by a suitable resonant circuit. It is interesting to note that there is no need to place any restriction upon the rapidity of the phase variations, except so far as it affects the sharpness of the response at the beat frequency. These conclusions are in general agreement with those of the authors.

However, we have so far restricted our discussion to one point in space, whereas in practice the detector must have dimensions large compared with the wave-length of the radiations present, in order that sufficient energy may be received. Therefore our analysis must be extended into three dimensions. Now obviously, at each point of our three-dimensional space, we shall have a predominant beat of frequency Δ, but the question of greatest interest is whether the beats will be in phase throughout the detector medium. If there is a phase variation, then it at once follows that the beat frequency will not be detected. There will be fluctuations of the detector's total response but these will be very irregular and have no relation to the beat frequency. A Fourier integral analysis of this response fluctuation would have a small predominant maximum at the frequency Δ, but this is not the beat in the sense implied in the paper, and in any case it would seem likely that its amplitude would be so small as to make it undetectable.

There would be well defined beats if the spatial beats were in phase, but this would mean that if at any time we construct the surfaces of equal phase for the two lines, they must be members of the same family of surfaces. This would seem to be impossible to attain in practice because the finite width of the slit alone is a prohibitive factor.

It thus appears unlikely that the proposed experiment will be successful in the detection of beats between light radiations.

[1] Forrester, Parkins, and Gerjuoy, Phys. Rev. 72, 728 (1947).

Signal-to-Noise Ratio in Photoelectrically Observed Beats

EDWARD GERJUOY, A. THEODORE FORRESTER AND WILLIAM E. PARKINS
University of Southern California, Los Angeles, California
January 24, 1948

THE discussion by Griffin[1] of the effect of phase variations on the possibility of observing beats between lines in the visible spectrum is, in our opinion, not wholly correct. Calculations made by us prior to our previous communication,[2] but omitted because of the space limitations, show that phase variations do reduce the beat frequency signal relative to what would be obtained for the same light intensity if the beats at all points on the cathode were in phase. However, the beat frequency signal is by no means extinguished merely because phase variations occur.

The electric current per unit area $i(r,t)$ from any point r on the cathode is proportional to the square of the electric vector at that point, provided the assumptions discussed in reference 2 are valid. Fourier analysis of $i(r,t)$ yields terms $i_f(r)$ representing the components of the beat frequency f in the photo-current. We now note that the photoelectrons originate so close to the surface of the

cathode that the phase of $i_f(r)$ does not vary with depth, so that the cathode can be considered two dimensional. Thus if the cathode is so small that the phase of $i_f(r)$ is practically constant everywhere on its surface, the amplitude of the beat frequency component of the total current I_f from the cathode is proportional to the area of the cathode, and the power activating the resonant cavity (Fig. 1, reference 2) is proportional to the square of the area. If the cathode is large, its surface can be subdivided into small regions of area $\sim\lambda^2/\Omega$ (defined below), in each of which the phase of i_f is constant, while the resultant currents I_f from separate regions are random in phase. In this case the total power activating the cavity is proportional to the number of subdivisions, i.e., to the area of the cathode.

These qualitative results are borne out by a more rigorous evaluation, using the exact phases at various points on the cathode. It should be emphasized that the received signal at the cavity increases with increasing cathode area. The limitation on the experiment is provided not by phase variations over the cathode, but by a phenomenon inherent in the emission process, namely, shot effect. The exact formula for the signal-to-noise ratio P is

$$P=2.11\cdot 10^{-3}\frac{Rg^2W^2\lambda^2S\Omega/\delta}{(RegWS\Omega/4\pi)+kT}, \qquad (1)$$

where W is the power radiated per unit area of the source into both lines, whose mean wave-length is λ. δ is the width of each line in cycles/sec., g the photoelectric efficiency, S the area of the cathode, Ω the solid angle included in the incident bundle of waves falling on the cathode, and R the shunt resistance of the resonant cavity. The first term in the denominator is the energy in the resonant cavity caused by shot noise in the photo-current, and the second term is the thermal noise in the cavity. Except for very small cathodes, the kT term is negligible. For larger cathodes the signal-to-noise ratio is independent of cathode area or of Ω.

A scheme developed by Dicke,[3] who measured signals only 0.0015 of noise, is applicable to this problem; in making estimates we assumed a signal-to-noise ratio of 0.01 could be detected. Using $g=0.04$ ampere/watt at $\lambda=4000$A (commercial S-4 photo-surface) makes the required value of W one watt/cm^2. This is a larger value than is ordinarily obtainable, but may be feasible because the source need be operated only for intervals longer than the response time of the detecting equipment ($\sim$1 second). Where the average heat dissipation is the factor limiting the power output of the source, continuous operation for an interval no longer than one second should permit using a peak power considerably larger than is possible with steady operation. An experimental program is now under way here to determine the spectral intensity obtainable in a source so operated.

It is expected that the details of the derivation of Eq. (1) will be presented in a paper to be submitted to this journal.

[1] L. R. Griffin, Phys. Rev. **73**, 922 (1948).
[2] A. T. Forrester, W. E. Parkins, and E. Gerjuoy, Phys. Rev. **72**, 728 (1947).
[3] R. H. Dicke, Rev. Sci. Inst. **17**, 268 (1946).

On the Presence of Neutrons in the Extensive Cosmic-Ray Showers*

VANNA TONGIORGI
Laboratory of Nuclear Studies, Cornell University, Ithaca, New York
March 2, 1948

AN experiment has been performed in order to find out whether or not neutrons are present in the extensive showers of the cosmic radiation.

For studying neutrons associated with showers one has to record the coincidences between some Geiger counters struck by the electrons of the showers and a neutron detector: a BF_3 proportional counter surrounded by paraffin seems to be the simplest and most reliable one. However, a serious difficulty arises from the fact that, when an extensive shower falls on the recording system, the neutron counter is struck by such a large number of electrons that a pulse may occur as large as the pulse due to the α-particles produced in the BF_3 by the neutrons; also stars and slow protons associated with the showers may give rise to confusing records. By experimenting with and without cadmium screens on the BF_3 counter, one is able to select only the neutrons, but one has to deal with a small effect superimposed on a large background.

We attempted to face the problem by taking advantage of the fact that neutrons have a quite long mean lifetime in paraffin ($\sim$200 μsec.). If one records the coincidences between the pulses of the neutron counter and the pulses of the electron counters delayed by several microseconds, all particles but neutrons are cut off; the number of neutrons lost, however, is very small (<5 percent for delays smaller than 10 μsec.).

The experimental arrangement used is drawn in Fig. 1. The extensive showers were detected by the counter trays, a, b, and c, each consisting of four G-M counters in parallel (area of each tray 2000 cm^2). They were placed in a horizontal plane at the vertices of an equilateral triangle of 4-m sides.

Two identical neutron detectors N_1 and N_2 were used, each consisting of a paraffin box (45×45×50 cm^3) in which four BF_3 proportional counters connected in parallel were embedded. Boxes N_1 and N_2 were placed 1.3 meters apart. The experiment was performed under a deck of few g/cm^2 of light material, practically at sea level.

All neutron counters (surface 2.5×45 cm^2) were provided with Kovar guard ring seals and were filled to 100 cm Hg with enriched BF_3 (96 percent B^{10}), plus argon to 20 cm Hg. For all of them the operating voltage was about 5000 volts. Their calculated efficiency[1] was about 30 percent.

Figure 2 is the schematic diagram of the recording circuit. Pulses from N_1 and N_2, through cathode followers placed inside the paraffin boxes, were fed into Mod. 100 amplifiers, pulse discriminators, and blocking oscillator outputs (pulse width, 1.5 μsec.). Both N_1 and N_2 were put in coincidence with the coincidences $(a+b+c)$ delayed by 7 μsec. and shaped in a square pulse of 150-μsec. duration. Delayed coincidences $abc+N_1$, $abc+N_2$, and $abc+N_1+N_2$ were recorded.

Thus far have been recorded, in 482 hours, 25,901 extensive showers ($\sim$53 showers/hour) and 117 coinci-

FIG. 1.

dences of the types $abc+N_1$ or $abc+N_2$ (~0.25 neutron associated with showers/hour). Taking into account the efficiency of the counters and the geometrical efficiency of the system (a rough calculation yields about 0.1 for the probability that a neutron slowed down in the paraffin box should strike the counters), the actual frequency of neutrons associated with extensive showers becomes greater than 8/hour. In 482 hours only one coincidence $abc+N_1+N_2$ was recorded.

In order to ascertain that the delayed coincidences were caused only by neutrons, tests have been made with cadmium foils (0.75 mm thick) surrounding all neutron counters: in 157 hours no coincidences $abc+N_1$ or $abc+N_2$ were recorded. These results demonstrate the existence of neutrons in the extensive air showers.

From the data, the ratio of neutrons to electrons may be evaluated. Assuming for the extensive showers the density spectrum determined in reference 2 and assuming that the ratio of neutrons to electrons is constant throughout the showers, we find that there are in the extensive showers at sea level about one neutron for every 30–40 electrons. Roughly the same figure has been found[3] for the penetrating ionizing particles (likely mesons) present in the extensive showers. The above-mentioned ratio refers, of course, only to those neutrons which our paraffin is able to slow down, i.e., neutrons of energies not bigger than 5–10 Mev. But it is reasonable to assume that faster neutrons, if they exist, are only a small fraction of the neutron component associated with the extensive showers.

During the performing of this experiment the total number of neutrons (associated or not with extensive showers) was also recorded with and without cadmium on the counters. The frequency of the Cd difference is in good agreement with the figures given by other authors[4] for the neutron component of cosmic radiation at sea level.

Experiments are in progress to investigate the mechanism of production of the neutrons associated with extensive air showers.

The author wishes to express thanks to Mr. J. Bistline for filling the BF_3 counters, to Mr. D. Hudson for help in the earlier stage of the experiment, and to Professor K. Greisen, Professor H. A. Bethe, and Mr. J. Levinger for helpful discussions on the problem.

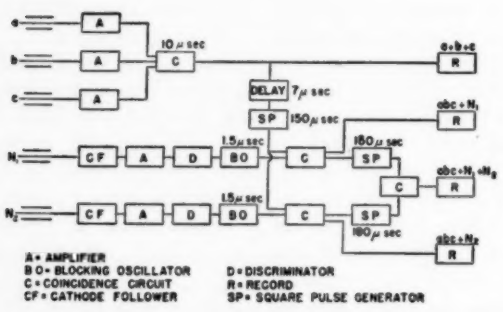

FIG. 2.

* This work was supported in part by the Office of Naval Research.

[1] S. A. Korff, Rev. Mod. Phys. 11, 211 (1939).
[2] G. Cocconi, A. Loverdo, and V. Tongiorgi, Phys. Rev. 70, 846 (1946).
[3] G. Cocconi, A. Loverdo, and V. Tongiorgi, Phys. Rev. 70, 852 (1946).
[4] C. G. Montgomery and D. D. Montgomery, Phys. Rev. 56, 10 (1939); M. Kupfenberg and S. A. Korff, Phys. Rev. 65, 253A (1944).

On the Magnetic Moment of H^3 and He^3 in the Møller-Rosenfeld Theory of Nuclear Forces†

ARMIN THELLUNG AND FELIX VILLARS
Swiss Federal Institute of Technology, Department of Physics, Zurich, Switzerland
February 25, 1948

A SYSTEMATIC investigation has been carried through to see whether the M-R model of nuclear forces is able to account for the magnetic moment M of the H^3 nucleus. M is composed of three parts:

1. The sum of the proper moments of all nucleons:
$$M_p=\Sigma_A \sigma^A\{\mu_p[(1+\tau_3{}^A)/2]+\mu_n[(1-\tau_3{}^A)/2]\}.$$
2. The orbital moment: $M_{orb}=\Sigma_A[(1+\tau_3{}^A)/2]\cdot l^A$.
3. The exchange moment, which is the sum of the contributions from the vector and the pseudoscalar field:
$$M_{ps}=-(e/2\hbar c)(f\mu)^2\sum_{A<B}(\tau^A\times\tau^B)_3 \times\{(1/\mu)[(\sigma^A\times\sigma^B\cdot r_{AB})(r_{AB}/r_{AB}{}^2)((1/\mu r_{AB})+1) -(\sigma^A\times\sigma^B)]e^{-\mu r_{AB}}-(r_A\times r_B)V_{AB}{}^0\}$$
$$M_v=-(e/2\hbar c)\sum_{A<B}(\tau^A\times\tau^B)_3\{(f\mu)^2[(1/\mu)(\sigma^A\times\sigma^B) \times((1/\mu r_{AB})-1)e^{-\mu r_{AB}}-(r_A\times r_B)V_{AB}{}^1] -(g\mu)^2(r_A\times r_B)(e^{-\mu r_{AB}}/r_{AB})\}$$
where $V_{AB}{}^0$ and $V_{AB}{}^1$ are the interaction energies of the corresponding fields.

According to the absence of tensor forces in the M-R model, the total spin S and the total orbital angular momentum L are good quantum numbers, and also the total isotopic spin T and the charge number $T_3(|T_3|\leq T)$. The ground state of the three-body system belongs to $S=T=\frac{1}{2}$, $L=0$ and may be considered, in a first approximation, as symmetrical in the space coordinates. The orbital symmetry class, however, is not a good quantum number, and a closer investigation shows that the deviation from space symmetry, taken in connection with the exclusion principle, may change the expectation value of M to an amount which is of the same order of magnitude as the exchange effect.

To give a more precise description of the investigation, let us introduce the two ortho-normal spin states ξ_1 and ξ_0,

belonging to $S=S_z=\frac{1}{2}$, and also the two corresponding isotopic states η_1 and η_2, belonging to $T=\pm T_3=\frac{1}{2}$ ($-$:H³, $+$:He³). Then $\chi_A=1/\sqrt{2}(\xi_1\eta_2-\xi_2\eta_1)$ represents an antisymmetric spin-charge state, and in a first approximation the H³(He³) ground state eigenfunction may be written as

$$\varphi_{\rm I}=F_{\rm symm}(r_1,r_2,r_3)\cdot\chi_A.$$

In a next step we may take into account the two states

$$\chi_1=1/\sqrt{2}(-\xi_1\eta_1+\xi_2\eta_2),\quad \chi_2=1/\sqrt{2}(\xi_1\eta_2+\xi_2\eta_1).$$

(χ_1,χ_2) have the same symmetry properties as (ξ_1,ξ_2) or (η_1,η_2). Together with a set of two space functions (F_1,F_2) of the same symmetry as (χ_1,χ_2) we may build up the antisymmetric state

$$\varphi_{\rm II}=F_1\chi_2-F_2\chi_1.$$

A convenient choice of (F_1,F_2) is

$$F_2=2(q_1\cdot q_2)\cdot G,\quad F_1=(q_1^2-q_2^2)\cdot G,$$
$$G=\text{symmetrical in } (r_1r_2r_3)$$

and

$$q_1=(3/2)^{\frac{1}{2}}(r_1-r_2),\quad q_2=1/\sqrt{2}(r_1+r_2-2r_3).$$

The normalization condition is

$$\int dv(|F_S|^2+2|F_1|^2)=N_S+2N_1=1.$$

The expectation value of M_p turns out to be:

$$(M_p)_{Ni}=\mu_{pr}-4/3\cdot(\mu_{pr}+|\mu_n|)\cdot N_1 \text{ for H}^3,$$
$$(M_p)_{Ni}=\mu_n+4/3\cdot(\mu_{pr}+|\mu_n|)\cdot N_1 \text{ for He}^3.$$

The numerical evaluation was carried through with Gauss error functions for both F and G:

$$F_s\sim\exp\left(-\frac{\alpha}{2}(q_1^2+q_2^2)\right),\quad G\sim\exp\left(-\frac{\beta}{2}(q_1^2+q_2^2)\right).$$

α was determined by minimizing the energy in the first approximation: $\mu^2/\alpha=2.24$. With this value, E was then minimized with respect to β and the amplitude of G in the second approximation. Taking the force constants from the work of Fröhlich,[1] we find $\beta=1.54\alpha$, $2N_1=0.33$ percent, and, accordingly, $(M_p)_{Ni}=\mu_{pr}-0.010$ n.m. (H³).

To calculate the expectation value of the exchange moment, only the contribution from $\varphi_{\rm I}$ was taken into account, since there are no interference terms between $\varphi_{\rm I}$ and $\varphi_{\rm II}$. Hence, all terms in $M_{\rm exch}$ which are antisymmetric in space vanish. Denoting by γ the ratio of nucleon to meson mass, we obtain

$$(M_{\rm vect})_{Ni}=8\gamma(\mu f)^2\cdot T_3\int dv|F_s|^2\left(\frac{1}{\mu r_{12}}-1\right)e^{-\mu r_{12}}$$
$$=8\gamma(f\mu)^2\cdot T_3J_v,$$
$$(M_{ps})_{Ni}=8/3\gamma(f\mu)^2\cdot T_3\int dv|F_s|^2\left(\frac{1}{\mu r_{12}}-2\right)e^{-\mu r_{12}}$$
$$=8/3\gamma(f\mu)^2\cdot T_3J_{ps},$$

and, therefore,

$$(M_{\rm exch})_{Ni}=\pm4\gamma(f\mu)^2(\tfrac{1}{3}J_{ps}+J_v)\quad\begin{matrix}+:\text{He}^3.\\ -:\text{H}^3.\end{matrix}$$

The values of J_{ps} and J_v as functions of μ^2/α may be taken from Fig. 1. Together with Fröhlich's values, $\gamma=8.35$ and $(f\mu)^2=0.071$, we have

$$(M_{\rm exch})_{Ni}=\mp0.023 \text{ n.m.}$$

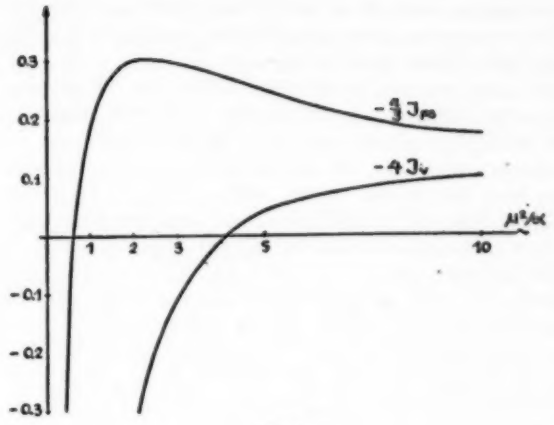

FIG. 1.

and, finally,

$$M(\text{He}^3)_{Ni}=\mu_n-0.013 \text{ n.m.},\quad M(\text{H}^3)_{Ni}=\mu_{pr}+0.013 \text{ n.m.}$$

Thus for H³ we obtain a value which is incompatible with the experiment, which gives $\mu_{pr}+0.186$ n.m.[2]

It should be noted that the present calculation is inconsistent insofar as any additional interaction (relativistic corrections) give rise to admixtures of D and P states, which, on one hand, reduce the value of $M_p+M_{\rm orb}$ and, on the other hand, introduce the contributions of non-diagonal elements of $M_{\rm exch}$. In any case, it can be said that the static M-R interaction represents a model of nuclear forces which is not sufficient to account for the magnetic moments of the lightest nuclei.

† Compare F. Villars, Phys. Rev. **72**, 256 (1947).
* The sign of this expression is in accordance with M-R's paper, but in contradiction with that of Ma and Yu (reference 4).
[1] H. Fröhlich, Kun Huang, and I. N. Sneddon, Proc. Roy. Soc. **A191**, 61 (1947).
[2] F. Bloch, A. C. Graves, M. Packard, and R. W. Spence, Phys. Rev. **71**, 373 and 551 (1947); H. L. Anderson and A. Novick, Phys. Rev. **71**, 372 (1947).
[3] C. Møller and L. Rosenfeld, Kgl. Danske Vid. Sels. Math.-Fys. Medd. **20**, No. 12 (1943).
[4] S. T. Ma and F. C. Yu, Phys. Rev. **62**, 118 (1942).

Mass Spectrometer Analysis of Mercury Made by Neutron Attachment to Gold

PAUL BRADT AND FRED L. MOHLER
National Bureau of Standards, Washington, D. C.
February 27, 1948

RECENTLY a sample of gold was submitted to prolonged neutron bombardment at Clinton Laboratory to produce Hg^{198} for spectroscopic purposes. The mercury is formed by the reaction

$$Au^{197}+n\rightarrow Au^{198}\rightarrow Hg^{198}+\beta \text{ (2.7 days)}.$$

Forty ounces of gold were used and about 60 mg of mercury extracted by heating the gold in vacuum. Spectroscopic observations showed that the mercury lines were quite free from any fine structure arising from polyisotopic composition,[1] but it seemed worth while to make a mass

spectrometer analysis of the mercury. This was made on a Nier-type mass spectrometer by first carefully measuring the unavoidable small background of ordinary mercury with seven isotopes in the range 196 to 204. Then vapor was admitted from a small droplet of Hg^{198} by breaking an internal break-off seal. Measurements indicated no ordinary mercury in the sample and it is estimated that less than 0.1 percent of the 198 peak comes from this source. However, in addition to the large 198 peak there was a measurable increase in the 199 peak amounting to 0.16 percent±0.06 of the 198 peak. In our experience, mercury hydride peaks have not been observed in mercury mass spectra, and it may well be that 199 comes from a secondary nuclear reaction. Neutron attachment to Au^{198} or Hg^{198} could produce the Hg^{199}. Inghram, Hess, and Hayden[2] have studied the isotopic constitution of ordinary mercury submitted to intense neutron irradiation and have established that most of the neutron absorption of mercury comes from the 199 isotope which is converted by an (n, γ) reaction to 200. This leaves the origin of 199 in our experiment open to question.

The mass spectrometer results indicate that the technique used in purifying the gold and recovering the mercury is excellent. The trace of 199 observed is too small to introduce any observable complexities of spectrum lines.

[1] "Light wave of mercury 198 as ultimate standard of length," Nat. Bur. of Stand. Tech. News Bull. **31**, 133 (1947).
[2] Inghram, Hess, and Hayden, Phys. Rev. **71**, 561 (1947).

On the Rate of Sintering of Metal Powders

A. J. Shaler and J. Wulff
Massachusetts Institute of Technology, Cambridge, Massachusetts
February 19, 1948

Kê has reported recently[1] on experimental confirmation of Snoek's hypothesis[2] that, under stress, interstitially dissolved atoms in metals tend to become preferentially distributed in the lattice of the solvent metal. C. Zener[3] has also observed this phenomenon in the case of a substitutional solid solution (70–30 alpha-brass). In this case the larger zinc atom distorts the copper lattice elastically. If two zinc atoms become neighbors, the distortion no longer has cubic symmetry; a stress is then able to orient the axis of the zinc pair in the direction of stress.

Frenkel[4] has shown that the presence of a vacancy in a lattice introduces an elastic distortion which is the opposite of that introduced by adding a large solute atom. It is evident that a preferential distribution of pairs of vacancies should be observable under stress just as is a preferential distribution of solute atoms. In the case of zinc atoms some time is required for the establishment of the orientation, and the relaxation time of the phenomenon is related to the activation energy for diffusion of zinc in alpha-brass. Similarly, the rate of orientation of vacancy pairs must be related to the heat of activation for self-diffusion. The relaxed orientation of vacancy pairs is perpendicular to a tensile stress.

It is believed that this mechanism may provide the atomistic explanation for the observation of Shaler and Wulff[5] that the rate of sintering of copper powder can be predicted on the basis of a viscous flow of metal under the influence of surface tension, the viscosity being that resulting from the preferential self-diffusion of vacancies in the lattice under stress.

[1] T'ing Sui Kê, Phys. Rev. **73**, 267 (1948).
[2] Snoek, Physica **8**, 711 (1941).
[3] C. Zener, Trans. A.I.M.E. **152**, 122 (1943); Phys. Rev. **71**, 34 (1947).
[4] Frenkel, *Kinetic Theory of Liquids* (Clarendon Press, Oxford, 1946).
[5] Shaler and Wulff, Phys. Rev. **72**, 79 (1947)

The Energies of Alpha-Particles from Pu^{238} and Pu^{239}

William P. Jesse and Harold Forstat
Argonne National Laboratory, Chicago, Illinois
February 24, 1948

A STANDARD method for comparing the energies of two alpha-particles has been by comparison of the total ionization produced by each in an ion chamber. We find that the use of the vibrating-reed[1] electrometer can greatly increase the precision of such a method. In our apparatus the two samples to be compared are mounted on a turntable, so that by means of a magnetic control either may be brought into the active region of the ion chamber. The alpha-particles, by means of a collimating system consisting of holes in a thin plate, are directed parallel to the central electrode in a cylindrical ion chamber. The latter is connected to the vibrating-reed electrometer and a Brown strip-chart recorder. The sudden jump of the pen on the latter, produced by the ionization in the chamber from a single alpha-particle, may be of the order of four to five inches. Such jumps are very reproducible and may be read on the chart with good precision.

Some idea of the self-consistency of the method is given in Table I from an intercomparison of three samples of Po^{210}, Pu^{238}, and Pu^{239}. These samples were prepared by evaporation of solutions on platinum disks. For the preparation of these we are indebted to Miss Sylvia Warshaw and Mr. George Reed of our chemistry division. A detailed comparison of Pu^{239} against Po as a standard is shown in the first three columns of the table. For each run the samples were measured in turn in the chamber until more than a hundred electrometer jumps had been recorded for each sample. The counting rate was about two counts per minute. The ratio of the alpha-particle energies for the two samples was taken to be the ratio of the mean respective electrometer deflections. This assumption is probably justified within the narrow range of energies involved. On this basis, the values in column three for Pu^{239} were derived, the Po alpha-energy being taken as 5.298 Mev. The value of 5.137 for Pu^{239} includes a small correction of 0.002 for the energy lost in the collimating system. A comparison of Pu^{238} with Po in

TABLE I. Energy Comparisons.

Run	Gas in chamber	Comparison Pu^{239} with Po^{210} (5.298 Mev) Energy for Pu^{239} in Mev	Energy for Pu^{239} from comparison with Po^{210}	Energy for Pu^{239} from comparison [b]with Pu^{23} (5.13$_7$ Mev)
1	N_2	5.13$_8$		
2	N_2	5.13$_3$		
3	Argon	5.13$_8$		
4 Samples reversed	Argon	5.13$_9$		
5 Original position	Argon	5.14$_0$		
6	Argon	5.14$_0$		
7	Argon	5.13$_9$		
Mean		5.13$_7$	5.49$_8$	5.49$_8$

argon gave the value in column four. This is the result of one extended run in argon. Finally, a cross comparison of Pu^{239} with Pu^{235} is shown in column five. This is the mean of two runs in argon. Here the alpha-energy for Pu^{239} was assumed to be 5.137 Mev, the value previously determined by comparison with Po. Although the almost exact agreement shown by the last two columns is undoubtedly somewhat fortuitous, the general consistency throughout the table cannot be considered so, since it is easily duplicated.

A series of runs with other samples, some deposited by electroplating instead of evaporation, is in good accord with the runs above. A weighted mean for all samples gives for Pu^{239} 5.140 Mev and for Pu^{235} 5.493 Mev. The consistency of the readings would indicate an error of about 0.1 percent. The ranges in air derived from these values and a range-energy curve[2] are 3.67 cm and 4.07 cm for Pu^{239} and Pu^{235}, respectively. The agreement is good between these values and the values 3.68 cm and 4.08 cm from previous[3] direct measurement of the ranges in air.

Measurement of the energies of various (n,p) reactions by this method are now in progress.

[1] Palevsky, Swank, and Grenchik, Rev. Sci. Inst. **18**, 298 (1947).
[2] Holloway and Livingston, Phys. Rev. **54**, 18 (1938).
[3] Chamberlain, Gofman, Segrè, and Wahl, Phys. Rev. **71**, 529 (1947).

Phase Determination with the Aid of Implication Theory

M. J. BUERGER
Massachusetts Institute of Technology, Cambridge, Massachusetts
March 3, 1948

SINCE the implication diagram[1,2] provides the locations of atoms in crystals, there must be a close similarity between a Fourier representation of the implication diagram and the Fourier representation of the projection of electron density of the crystal on the same plane. The relation between the coefficients of the two series can be ascertained in several ways. A straightforward way, which is not difficult in cases of low symmetry, is to expand $FF^*(hkl)$ and then separate $F(h'k'l')$ from the rest of the expansion. For symmetries other than $\bar{1}$ it is then possible to eliminate most (if not all) of the unsymmetrical components. This is illustrated here for symmetry 2 parallel to c. By a simple manipulation, the expansion of $FF^*(hkl)$ can be arranged in the following form:

$$F^2_{hkl}=\sum_j n_j f^2_{j,hkl}+F_{hkl}(P_0)+F_{hkl}(P_s)$$
$$\text{(a)}\qquad\text{(b)}\qquad\text{(c)}$$
$$+\left(\frac{f^2_{1,hkl}}{f_{1,2h2k0}}\right)F_{2h2k0}+\sum_j\left(\frac{f^2_{j,hkl}}{f_{j,2h2k0}}-\frac{f^1_{1,hkl}}{f_{1,2h2k0}}\right)F'_{2h2k0}. \quad (1)$$
$$\text{(d)}\qquad\qquad\text{(e)}$$

The expansion consists of five parts, which can be described in terms of the contribution of this term to the Patterson synthesis. (a) is a contribution to the origin peak, (b) represents the contribution on the Harker level to a non-Harker peak, and (c) represents a contribution on a non-Harker level to a general Patterson peak.

Term (c), which represents a very large part of the expansion, can be eliminated by the following manipulation: All terms are summed over l from $l=-L$ to $+L$, and each side of the equation is multiplied by $\cos 2\pi(hx+ky)$. The left side of (1) then represents the hk contribution to a Harker synthesis on level zero, and the parts of the right side of (1) represent the hk contributions to Fourier syntheses of quasi-electron density representations. In the complete syntheses, (c) vanishes because it represents a section on level zero, where there is no "density." The only way for this to occur is for each term $\Sigma_l F(P_s)$ to vanish independently. This eliminates the term $\Sigma_l F_{hkl}(P_s)\times\cos 2\pi(hx+ky)$. All terms are now divided by $\cos 2\pi(hx+ky)$. There remains

$$\sum_{l=-L}^{L}F^2_{hkl}=\sum_{l=-L}^{L}\sum_j n_j f^2_{j,hkl}+\sum_{l=-L}^{L}F_{hkl}(P_0)$$
$$\text{(a)}\qquad\qquad\text{(b)}$$
$$+\left(\frac{\sum_{l=-L}^{L}f^2_{1,hkl}}{f_{1,2h2k0}}\right)F_{2h2k0}$$
$$\text{(d)}$$
$$+\sum_j\left(\frac{\sum_{l=-L}^{L}f^2_{j,hkl}}{f_{j,2h2k0}}-\frac{\sum_{l=-L}^{L}f^2_{1,hkl}}{f_{1,2h2k0}}\right)F'_{2h2k0}. \quad (2)$$
$$\text{(e)}$$

When non-Harker peaks can be recognized on the implication map, for example, by the non-appearance of satellites in certain symmetries,[1] term (b) can be allowed for. Relation (2) then provides the relation of F's to F^2's for twofold symmetry. The last term is a correction term which arises because all atoms do not scatter with the same power. When all atoms have about the same scattering power, as in many organic compounds and in many silicates, this term vanishes. In other cases, it can be evaluated from special position information or, more generally, from the locations of certain atoms provided by the implication diagram. Where these do not apply, then this term can be evaluated for its maximum value, in which case it sets determinable limits on the part of (2) which cannot be directly computed. Since the absolute values of the F's are known, it should not be difficult in most cases to decide on phases of the F's with the aid of (2).

Equalities of a similar nature exist for each Harker level of each symmetry. It should be noted that the phases of

only a fraction of the coefficients of the electron density series can be determined in this way. The fraction is $\frac{1}{4}$, $\frac{1}{3}$, $\frac{1}{2}$, or 1, corresponding, respectively, to the implication ambiguity of 4, 3, 2, and 1. Therefore, if an electron density map is computed using the terms whose coefficients are determined in this manner, n possible positions appear for each atom in the crystal structure, where n is the ambiguity coefficient of the implication. The wrong positions can only be removed by supplying the electron density series with the missing terms.

[1] M. J. Buerger, "The interpretation of Harker syntheses," J. App. Phys. 17, 579–595 (1946).
[2] M. J. Buerger, "The solution of ambiguities arising in crystal structure analysis," Am. Soc. for X-Ray and Elec. Diff., abstracts of papers given at the 1947 summer meeting, Ste. Marguerite Station, Quebec, pp. 21–23.

The East-West Asymmetry of the Hard Component of the Cosmic Radiation*

MARCEL SCHEIN, VICTOR H. YNGVE, AND HENRY L. KRAYBILL
Department of Physics, University of Chicago, Chicago, Illinois
March 3, 1948

THE east-west asymmetry of the total cosmic radiation at altitudes above 5 cm Hg was found by Johnson[1] to be only about 7 percent. From this it was concluded that the primary radiation consisted of nearly equal numbers of positive and negative particles. On the basis of the experiments of Schein, Jesse, and Wollan,[2] it was proposed in 1941 that the majority of the primaries consist of protons. Arley,[3] combining these ideas, suggested that the primaries consist of equal numbers of positive and negative protons. To test whether or not most of the hard component, which has a small asymmetry at sea level, is actually produced by positive primaries, we measured the east-west asymmetry of particles penetrating more than 22 cm of Pb over a considerable latitude range at a high altitude.

The counter telescopes were mounted in a B-29 airplane in such a way that the zenith angle could be adjusted. In flight, the plane flew back and forth over the same course, with each telescope pointing alternately to the east and to the west so as to average out any systematic differences in their counting rates. The counters were connected both in threefold and in fourfold coincidence. However, only the fourfold data were used here in computing the asymmetry. An estimate of the correction required for the shower counting rate was obtained by counting the showers which tripped four counters with one counter moved out of line. The asymmetry was corrected by using this value of the shower rate. According to Johnson,[4] the showers show no asymmetry. A shower counting rate higher than that actually observed would decrease the observed value of the asymmetry. Dead time and resolving time measurements were made and the single counting rates of the counters were checked in flight. Errors in the asymmetry due to these causes were found to be negligible. The ground counting rate was determined between flights as a check on the operation of the equipment.

Flights were made between the geomagnetic latitudes of 27° 18′ North and 58° 30′ North with the telescopes at a 45° zenith angle. The results are shown in Table I. The asymmetry increases from a low value at the northern end to a value of over 45 percent at the southern end of the flights.

A flight was made to 27° 30′ North geomagnetic latitude to explore the effect at other zenith angles. The telescopes were at a zenith angle of 60° on the way south and at 30° on the way back. The results are given in Table II.

Table II shows that the east-west asymmetry undergoes large fluctuations with zenith angle at a latitude near 33° North. This effect is of considerable interest in connection with the problem of the primary radiation. It is planned to continue these measurements in the near future.

The latitude effect of mesotrons passing through 21 cm of Pb as a function of altitude was measured by Gill, Schein, and Yngve.[5] Using the observed value of the latitude effect, the large asymmetry of 46 percent detected for a zenith angle of 45° between latitudes of 27° and 32° is in general agreement with the theory of Lemaitre and Vallarta,[6] provided that all of the primaries which produce mesotrons of energies greater than about 6×10^{9} ev are positively charged. The lower limit of the mesotron energy is derived from the ionization loss in the atmosphere between the average height of their production[7] and the pressure altitude of 31,000 feet.

TABLE I. Latitude dependence of the east-west asymmetry at 45° zenith angle.

Geomagnetic latitude range	27° 18′ 32° 00′	31° 00′ 35° 40′	35° 00′ 40° 25′	39° 30′ 43° 00′	45° 00′ 50° 00′	50° 00′ 54° 00′	54° 00′ 58° 30′
Pressure altitude	34,500 ft.	32,000 ft.	31,000 ft.	37,000 ft.	31,000 ft.	31,000 ft.	31,000 ft.
East-west asymmetry $\frac{E_w-E_e}{1/2(E_w+E_e)}$	0.46±0.07	0.27±0.07	0.14±0.06	0.17±0.03	0.09±0.05	0.13±0.05	0.01±0.06

TABLE II. East-west asymmetry at 30° and 60° zenith angle for a pressure altitude of 31,000 feet.

Geomagnetic latitude range	27° 55′ 31° 05′	31° 05′ 35° 35′	35° 35′ 41° 00′	27° 30′ 32° 07′	32° 07′ 35° 35′	35° 35′ 40° 10′
Zenith angle	30°	30°	30°	60°	60°	60°
East-west asymmetry $\frac{E_w-E_e}{1/2(E_w+E_e)}$	0.4±0.1	−0.02±0.09	0.003±0.07	0.02±0.13	0.2±0.1	−0.06±0.1

We wish to thank the United States Navy and Army Air Force personnel at Inyokern, California for their cooperation in carrying out the airplane flights.

* This research was supported in part by Navy Contract N6ori-20, Task Order XVIII.

[1] T. H. Johnson and J. G. Barry, Phys. Rev. **56**, 219 (1939).
[2] Marcel Schein, W. P. Jesse, and E. O. Wollan, Phys. Rev. **59**, 615 (1941).
[3] N. Arley, Kgl. Danske Vid. Sels. Math.-Fys. Medd. **23**, 42 (1945); Physica **12**, 177 (1946).
[4] T. H. Johnson, Phys. Rev. **47**, 318 (1934).
[5] P. S. Gill, Marcel Schein, and V. H. Yngve, Phys. Rev. **72**, 733 (1947).
[6] G. Lemaitre and M. S. Vallarta, Phys. Rev. **49**, 719 (1936).
[7] Marcel Schein and J. Steinberger, Phys. Rev. **72**, 734 (1947).

Erratum: Natural Radioactivity of Rhenium

[Phys. Rev. **73**, 487 (1948)]

S. N. NALDRETT AND W. F. LIBBY
Institute for Nuclear Studies, University of Chicago, Chicago, Illinois

THREE numbers in the recent article on the natural radioactivity of rhenium are erroneous. They are contained, respectively, in the last three paragraphs of the article, and in each case in the last sentence of the paragraph. The changes are, in order:

2.6×10^{12} years to be changed to 5.3×10^{12} years.
3.1 counts per minute to be changed to 31 counts per minute.
3×10^{12} years to be changed to 4×10^{12} years.

The Interactions of Nucleons with Meson Fields

F. J. DYSON
Cornell University, Ithaca, New York
February 25, 1948

FOR a nucleon field Ψ interacting with a pseudoscalar field ψ there are available two forms of interaction, the pseudovector

$$H_1=g\int\Pi(\sigma\cdot\nabla\psi-(1/c)\gamma_4\pi)\Psi d\tau,$$

and the pseudoscalar

$$H_2=G\int\Pi\beta\gamma_5\psi\Psi d\tau.$$

These, and the corresponding two interactions with the scalar, the vector, and the pseudovector meson fields, were systematized by Kemmer.[1] Following Kemmer, several investigators have carried out calculations with the pseudoscalar field, using the interaction H_1 without the term in γ_4, justifying this procedure with the remark that the term in γ_4 in H_1 and the entire interaction H_2 would be negligible in problems concerning nucleons with non-relativistic velocities. That this argument is unsound Bethe[2] discovered by calculating nuclear potentials and scattering effects, using the complete interactions H_1 and H_2 in turn, and finding that either interaction gave the same form for these effects. Moreover, one can see directly that the matrix elements of $\nabla\psi$ for processes involving small momentum transfer are small, just as are those of γ_4, so that one may expect both parts of H_1 and H_2 to be of the same order of magnitude.

The purpose of this letter is to point out that the interactions H_1 and H_2 are, in fact, *completely equivalent for first-order radiative processes* and for many higher order processes as well. This fact was long ago noted by Nelson,[3] but it seems worth while to put forward the following derivation of the equivalence as in some ways more comprehensive than Nelson's. Let

$$H_0=\tfrac{1}{2}\int(\pi^2+c^2|\nabla\psi|^2+\mu^2c^2\psi^2)d\tau$$

$$-c\int\Pi(\alpha\cdot\nabla+iM\beta-V)\Psi d\tau$$

be the Hamiltonian of the meson field and the nuclear field with an external potential V, without interaction between the two fields. The total Hamiltonian $H=H_0+H_1$ may be transformed by a contact transformation to the form $H'=e^{iS}He^{-iS}$, with

$$S=-(g/\hbar c)\int\Pi\gamma_5\psi\Psi d\tau.$$

This transformation is a gauge transformation of conventional type, and after some reduction we obtain $H'=H_0+H_1'$, where

$$H_1'=c\int\Pi(iM\beta(1-e^{-2(g/c)\gamma_5\psi}))\Psi d\tau-\tfrac{1}{2}(g^2/c^2)\int(\Pi\gamma_5\Psi)^2d\tau.$$

The reason why the exponential survives in H_1' only in the term involving β is that γ_5 commutes with α and σ but not with β. The last term in H_1' represents a δ-function interaction (which has no physical meaning) between nucleons. Hence the interaction H_1 is equivalent to the first term of H_1' alone. Expanding the exponential, this gives (i) the interaction H_2 with $G=2iMg$ and (ii) higher order terms, most of which appear to be merely of the nature of "mass effects."[4]

In view of this result and the greater simplicity of the interaction H_2, it is recommended that H_2 be used exclusively in future calculations.

The same method may be used when the meson field is either *charged* or *symmetrical*; in this case, additional terms appear in H_1', but only of the second and higher orders in the meson field. Further, the result is true when V is either an ordinary or a spin-exchange potential, but not when V is a charge-exchange potential.

When ψ is a scalar field, there is the usual scalar form of interaction, and also a vector form

$$g\int\Pi(\alpha\cdot\nabla\psi+(1/c)\pi)\Psi d\tau.$$

Using a contact transformation with

$$S=(g/\hbar c)\int\Pi\psi\Psi d\tau,$$

it is easy to show that the vector interaction disappears entirely, except for a δ-function interaction between nucleons as before. Thus, the vector interaction leads to no physical processes in any order.

For vector and pseudovector meson fields, the corresponding gauge transformations lead only to the elimination of the longitudinal parts of the fields. As is well known, a nucleon may have two distinct couplings with the electromagnetic field, the first characterized by its charge and the second by its anomalous magnetic moment.[4] Thus a vector or pseudovector field has two distinct forms of interaction with a nucleon, as given by Kemmer, but a scalar or a pseudoscalar field has essentially only one.

[1] N. Kemmer, Proc. Roy. Soc. 166, 127 (1938).
[2] Unpublished.
[3] E. C. Nelson, Phys. Rev. 60, 830 (1941).
[4] See H. W. Lewis, Phys. Rev. 73, 173 (1947).
[5] W. Pauli, *Handbuch der Physik* 24/1, p. 221.